12-4-2015

Spectroscopic and Theoretical Characterization of Retinylidene Proteins and Biological Chromophores for Use in Biophotonic Applications

Jordan A. Greco
University of Connecticut - Storrs, jordan.greco@uconn.edu

Spectroscopic and Theoretical Characterization of Retinylidene Proteins and Biological Chromophores for Use in Biophotonic Applications

Jordan Alan Greco, Ph.D.

University of Connecticut, 2015

Retinylidene proteins are found in all domains of life and perform diverse biological functions, including light-induced ion transport and phototransduction in visual systems. One such protein, bacteriorhodopsin (BR), is the light-activated proton pump that produces chemical energy for the *archaeon*, *Halobacterium salinarum*. In recent years, a branching reaction from the photocycle of BR has been discovered to produce a stable photoproduct, the **Q** state, using a sequential multiphoton process. The **Q** state has optical properties that enable the use of BR in bioelectronic technologies, however, the native protein has limited access to this photoproduct. A review is presented on the associative processors and optical memories that are based on BR mutants with enhanced photochemical properties. The BR mutant, V49A, is identified as an efficient **Q**-forming mutant, and the pH-dependent mechanism that governs the photochemistry of V49A is investigated. This mutant is also characterized in the context of a protein-based retinal implant. Moreover, this thesis includes two reports involving the spectroscopic and theoretical analysis of various porphyrinoids for application in optically driven biotechnologies. The first is an analysis of the two-photon absorptivities of tertraphenyl-porphyrins and -chlorins, which reveal that the nonlinear optical properties are sensitive to macrocycle distortion. Secondly, absorption spectroscopy and excited state calculations describe the relationship between the structural features of trithienyl-corrole and the resulting optical properties. Lastly, low-temperature trapping of the rhodopsin E181Q mutant is investigated to elucidate the role of residue Glu-181 during the early photostationary states of the photobleaching sequence.

Spectroscopic and Theoretical Characterization of Retinylidene Proteins and Biological Chromophores for Use in Biophotonic Applications

Jordan Alan Greco

B.S., University of Connecticut, 2010

A Dissertation

Submitted in Partial Fulfillment of the

Requirements for the Degree of

Doctor of Philosophy

at the

University of Connecticut

2015

Approval Page

Doctor of Philosophy Dissertation

Spectroscopic and Theoretical Characterization of Retinylidene Proteins and Biological Chromophores for Use in Biophotonic Applications

Presented by

Jordan A. Greco, B. S.

Major Advisor ______________________________
Robert R. Birge, Ph.D.

Associate Advisor ______________________________
Harry A. Frank, Ph.D.

Associate Advisor ______________________________
José A. Gascón, Ph.D.

University of Connecticut

2015

Acknowledgements

This work would not have been possible without the guidance, love, and support of many individuals, both during my life as a graduate student and all the years leading up to this academic endeavor. First and foremost, I would like to dedicate this work to my incredible wife, Shelby Greco. Shelby has been an unyielding source of strength and comfort throughout this challenging period, and I am forever grateful to have had a companion that is so thoughtful, caring, and generous with her love and encouragement. Our life together has so far been wholly entwined with the efforts that have produced this dissertation, and it is safe to say that I would not be here today without Shelby's influence and steadying presence.

Equally deserving of the credit for the completion of this work are close family members who have given me the strength and the tools that have proven to be invaluable along this journey. My mother, Patricia Greco, is the strongest person that I know, and her moral support and advice over many years have been a constant source of encouragement. Above all others, her grit and determination opened a world of opportunities for me and ultimately led me down this path. Thank you, Mom, for instilling in me all of the qualities that I have needed for my achievements. I also owe a very special thank you to my grandmother, Nannette Prue, for always being there for me when I needed her. She has always taught me to be honest, kind, and diligent, and I am lucky to have such a positive role model that I could count on to put things into perspective. Her love and support have made all of the difference throughout my life. I would also like to acknowledge the role of Dorothy Polselli in making this possible. While she has been gone now for almost 15 years, I would not be where I am today without the generous support and encouragement that she had provided throughout the course of my education.

Moreover, I have had the great fortune of being surrounded by wonderful family and friends who have all contributed to this work in several ways. My brother, Justin, has been by my side through the good and the bad, and I would like to express my thanks for his support and sense of humor. I would also like to thank Victor Biondi and Joyce Biondi for their generosity and support, and for the richness of their friendship that I have come to rely on over the years. Importantly, Anthony Perillo, Jamie Perillo, and Jesse Liska have all surrounded me with such warmth and kindness, and I am truly a lucky man to have been welcomed into this family. Also, I would like to give my deepest gratitude to Tom Prue, whose larger-than-life personality and gumption continues to influence me on a daily basis. I will spend this life trying to carry on his spirited approach to living.

I would like to give my most sincere thanks to my research advisor, Dr. Robert Birge, who has been a wonderful mentor and friend. I could not have asked for a more rich and incredible graduate school experience than what was provided to me in his research group. As an advisor, Dr. Birge allowed me to explore my creativity and develop as an independent researcher, while also providing strong support and guidance along the way. This balance has been an incredible gift. I will be forever grateful for the opportunities that he has given me and for the immeasurable influence that he has had on me as a scientist and as a person. I would also like to thank Connie Birge for her unconditional support and friendship, which was a very important aspect of my time in the Birge group. Connie has an extraordinarily kind and giving heart, and is always willing to put the needs of others in front of her own. These features do not go unnoticed by anyone who gets to know her. The influence of Dr. Birge and Connie has significantly shaped my life in profound ways, and no words can truly express my gratitude.

Furthermore, I would like to express my appreciation to my committee members, Dr. Harry Frank, Dr. José Gascón, Dr. Christian Brückner, and Dr. Mark Peczuh, for their generous time and support. I consider myself lucky to have had access to their guidance and wisdom during my time as a graduate student. Two chapters in this dissertation are the result of a collaboration with Dr. Brückner, and I thank him for allowing me the freedom to explore entirely new systems outside of my own research projects. Similarly, it has been wonderful getting to know Dr. Frank, in addition to his group members Nikki Magdaong and Amy LaFountain, and I appreciate the opportunities granted by collaborating on his fascinating research projects.

During my time as a graduate student in the Birge research group, I was extremely fortunate to have such wonderful mentors, colleagues, and friends by my side. I am forever indebted to Dr. Matthew Ranaghan for taking an illogical leap of faith by accepting me into the group during the twilight of my undergraduate career. I consider myself so lucky to have had the opportunity to work under Matt's guidance during my first year in the Birge group, and I still find that I, sometimes unwittingly, emulate his approach as a researcher. I know that if I continue this approach, success is all but guaranteed. I also owe an enormous debt of gratitude to Dr. Nicole Wagner. Through thick and thin, Nicole has been a constant source of wisdom, inspiration, laughter, and sisterly camaraderie. I have learned so much from Nicole over the years, and I have also been lucky to share in the rewards of her extraordinary success as CEO of LambdaVision, Inc. Thank you, Nicole, for your friendship and endless support. While there are many other influential graduate students from the Birge group that have preceded my time at UConn, I would also like to specifically thank Dr. Megan Sandberg and Dr. Daniel Sandberg for their encouragement and positive example during my first year as a graduate student.

Additionally, my experience in the Birge group has provided me with a lifelong friend in a visiting researcher from Norway, André Fernandes. André is the most positive person that I have ever met and I am very grateful for his friendship. I would also like to acknowledge Dr. Trevor Hamlin, a true friend whose passion for science and determination to achieve a well-rounded understanding of chemistry is an example that I will always strive to live up to. Importantly, I am very grateful to have had the pleasure of learning from and getting to know Matthew Guberman-Pfeffer, whose energy and resolve are truly inspiring.

As a graduate student, it has been a privilege to be able to mentor a number of talented undergraduate students, from whom I have learned so much. I would like to specifically express my appreciation to Ed Courchaine and Clancy Emanuel for their exceptional work and friendship. I have no doubt that both will achieve many great things throughout all of their endeavors. I have also had the fortune of getting to know many other outstanding individuals, including Angelica Messana, Caroline Rogi, Erin Duffy, Megan Gillespie, Alex Minge, Nandan Pandit, Maschal Mohiuddin, Chris Godin, Terianna Wax, and Molly Zgoda. I could spend an exorbitant amount of time listing the wonderful qualities of each of these individuals, but will have to settle for thanking the collective for their hard work, dedication, and camaraderie. I would be remiss not to recognize Sierra Drevline, as well, who played a crucial role in my stumbling upon the golden ticket that provided a world of delightful opportunities in the Birge research group.

In addition to the aforementioned collaboration with Dr. Brückner, some of the work outlined in this dissertation is the result of fruitful collaborations with the laboratories of Dr. Erik Johannessen, Dr. Philip Häfliger, and Dr. Barry Knox. I sincerely appreciate the expertise and assistance from these individuals, which has, by and large, made this dissertation possible. A

special thank you is reserved for Dr. Johannessen, who generously hosted my wife and me during an unforgettable trip to Norway.

A heartfelt thank you is in order for the main office staff and the entirety of the Department of Chemistry for providing a nurturing environment for me to grow as a scientist, educator, leader, and person. There are many faculty, staff, and students who have made these years an amazing and memorable experience, and I will always look back at my time as a member of this department in fondness. Furthermore, I have valued my time as a participant and leader of Phi Lambda Upsilon and hope that my service has made a positive impact on the department, however small.

Dr. Edward Neth has also been an invaluable resource as a mentor, and as an aspiring educator in chemistry, I thank him for the chance to absorb his knowledge through my experience as his teaching assistant.

Finally, I would like to express my sincere gratitude to Roberta Downer for her guidance and honest counsel during a time that has proven to be a turning point in my career in research.

Table of Contents

List of Contributions

Chapter 1:

JAG: Performed the Kramers-Kronig analysis and prepared the manuscript.
NLW: Assisted in preparing the manuscript.
MJR: Assisted in preparing the manuscript.
RRB: Performed complex Fourier association analysis and assisted in preparing the manuscript.

Chapter 3:

JAG: Collected one-photon absorption spectra, determined fluorescence quantum yields of the standards and samples for the calculation of absolute two-photon absorptivities, performed ground state and excited state calculations, analyzed data to develop models for our predictions, and prepared the manuscript.
SS: Collected two-photon excitation spectra.
NLW: Assisted in performing ground and excited state calculations for the analysis.
JRM: Synthesized all porphyrin and chlorin molecules.
KA: Performed preliminary excited state calculations.
CB: Supervised the synthesis and spectroscopic investigations and assisted in preparing the manuscript.
RRB: Designed and implemented the two-photon apparatus, determined theoretical two-photon absorptivities using excited state calculations, and assisted in preparing the manuscript.

Chapter 4:

JAG: Performed all ground state and excited state calculations and prepared the manuscript.
AR: Synthesized all corroles used in this study and collected absorption spectra of the samples.
CB: Supervised the synthesis and spectroscopic investigation and contributed to the preparation of the manuscript.
RRB: Assisted in the analysis of the computational experiments and contributed to the preparation of the manuscript.

Chapter 5:

JAG: Performed all quantum mechanical calculations and photocalorimetric analyses and prepared the manuscript.
MNS: Assisted in preparing the manuscript.
NLW: Assisted in preparing the manuscript.
TA: Collected low-temperature spectra of rhodopsin and E181Q.
LAR: Assisted in all spectroscopic measurements.
MHC: Generated the E181Q rhodopsin mutant.
BEK: Supervised the mutagenesis efforts and supplied all rhodopsin samples.
RRB: Contributed to the spectroscopic and computational analyses and assisted in preparing the manuscript.

List of Figures

Chapter 1:

Chapter 2:

List of Schemes

List of Tables

Chapter 2:

Chapter 3:

Chapter 4:

Chapter 1

Biomolecular Electronics and

Protein-Based Optical Computing

Selected portions of the material presented in this chapter are published in: Greco, J. A., Wagner, N. L., Ranaghan, M. J., Rajasekaran, S., Birge, R. R. Biomolecular Electronics and Protein-Based Optical Computing. In *Molecular and Supramolecular Information Processing: From Molecular Switches to Unconventional Computing*, E. Katz, ed. Wiley-VCH: Weinheim, Germany, 2012; pp. 33-59; Greco, J. A., Wagner, N. L., and Birge, R. R. Fourier Transform Holographic Associative Processors Based on Bacteriorhodopsin. *Int. Journ. Of Unconventional Computing* **2012**, *8*, 433-457.

1.0. Abstract

Consumer demand for fast computing speeds and smaller device interfaces has prompted the necessary reevaluation of the long-term sustainability of modern computing paradigms. Computer scientists responsible for designing and developing emerging computing systems will soon be forced to imagine novel ways to store and process information due to the projected limitations of lithographic manipulation. Molecular and biomolecular approaches offer unique solutions to the impending issues of scalability and energy efficiency by using innovative architectural motifs. Biomolecular devices exploit the natural evolutionary processes that have serendipitously provided biomolecules that are able to function within an electronic and/or optical domain. One such biomolecule is bacteriorhodopsin, the light-transducing, trans-membrane protein found in the halophilic archaeon, *Halobacterium salinarum*. Bacteriorhodopsin has long been considered an excellent material for optical applications due to inherent photochemical efficiency and stability, and has served as an archetypal candidate for these applications for a number of decades. Upon light absorption by the retinal chromophore of bacteriorhodopsin, the protein undergoes a proton-pumping mechanism that is characterized by a series of spectrally and conformationally discrete photointermediates. This reaction is known as the bacteriorhodopsin photocycle. We describe here the implementation of the protein within two unique optical computing systems: Fourier transform holographic associative processors and three-dimensional optical memories. The real-time holographic associative processors employ Fourier transform optical loops and rely on the transient change of refractive index throughout the photocycle. The three-dimensional memories use the unique photochemistry of a branching reaction from the main photocycle for long-term data storage. The conception and design of prototypes for each bioelectronic device will be presented in detail. We also explore advances in

genetic engineering and directed evolution, which have allowed for the further enhancement of the optical properties of bacteriorhodopsin for use in these biomolecular device applications.

1.1. Introduction

Molecular electronics explores the encoding, manipulation, and retrieval of information at the molecular or macromolecular level. Biomolecular electronics (or bioelectronics) is a subfield of molecular electronics that investigates the use of both native and modified biological molecules as media, in place of molecules synthesized in the laboratory. Bioelectronics has shown significant promise because of the sophisticated control and manipulation that is obtainable through self-assembly mechanisms and genetic optimization of large macromolecules. The ability to explore new architectures unique to biomolecular-based systems enhances the value of bioelectronics beyond the materials realm and opens up new possibilities that reflect the creative processes inherent in nature and revealed through natural selection.

Semiconductor electronics are the cornerstone for a majority of the recent and developing computing and processing systems. We do not propose that biomolecular electronic systems can replace these semiconductor-based devices; rather, we believe that bioelectronics can provide new options that can ultimately yield improved energy efficiency or unique architectures. The continuous push towards miniaturization and high-speed computing will inevitably succumb to the limits of lithographic manipulation of bulk materials, as reflected in Moore's Law.[1] Experts in the industry have predicted that complimentary metal-oxide-semiconductors will soon reach scalable limits and will require new paradigms (i.e., new transistors) and new architectures to circumvent current device limitations in power and scalability.[2-4] As smaller transistors are crowded onto silicon chips, both power and heating issues start to dominate.[4] Biomolecular devices have the potential to operate at higher efficiencies. This chapter begins with a comparison of biomolecular and semiconductor electronics and highlights the exploration of these new architectures as the molecular limit is approached.

A bioelectronics material that has shown great potential in photonic devices is the protein bacteriorhodopsin (BR). The native organism, *Halobacterium salinarum*, uses this protein as a photosynthetic energy source that converts light energy into a proton gradient (chemical energy). The photochemistry involved in this conversion is inherent to its potential for biophotonic devices and facilitates complex optical data storage and information processing. Implementing BR as a medium for molecular computing has the potential to solve some of the problems unique to integrated circuits. Additionally, the architecture of these protein-based devices may serve as a model for scientists and computer engineers who are investigating other molecular media. Optical memories and processors will be discussed in this chapter and prototypes successfully implementing the proposed architectures will be described.

1.2. Biomolecular and Semiconductor Electronics

One of the best ways to introduce bioelectronic computing is to compare the potential advantages of these developing technologies with the current advantages of semiconductor-based electronics. The following sections elaborate on key characteristics of computing and serve as a sample of the technical advancements achieved by scientists and engineers over the past few decades. Similar discussions can be found in references [5,6]. We note that many of the same challenges faced by molecular engineers to achieve the goals of miniaturization and speed will soon be faced by semiconductor engineers as consumer technology advances. As the molecular level is approached, the problems involved in developing novel computational systems will unify independent of the technology used.

1.2.1. Size and Speed

The strength of molecular electronics is the potential capacity for using synthesized molecules that are of the nanometer scale. Additive synthesis allows a certain flexibility in creating a feasible material for these devices “from the bottom up”, starting with readily available organic compounds. Semiconductor devices are generated “from the top down” through the lithographic manipulation of bulk materials. A synthetic chemist can selectively add an oxygen atom to a chromophore with a precision that far exceeds a comparable lithographic step, in which electron beams or X-rays etch a semiconductor surface. Molecular-based gates approach a size that is hundreds of times smaller than lithographic components. Some investigations have even produced logic gates down to the atomic level,[7] while others have been shown to exploit the spin states of quantum dots as one- and two-quantum-bit gates.[8]

Figure 1.1[9-12] illustrates trends in bit size that have characterized the last few decades of computer memory development. The results indicate that the area per bit has decreased logarithmically for multiple technologies since the early 1970s. As a comparison, we also show the cross-sectional area per bit calculated for the human brain (assuming that one neuron is equivalent to one bit), for our proposed three-dimensional memory, and for generic molecular memories. Despite the fact that current technologies have surpassed the cross-sectional density of the human brain, the major advantage of the neural system is that information is stored in three dimensions and is capable of associative recall. Admittedly, it is a considerable stretch to compare the mind of a human being to digital technologies; however, the analogy emphasizes the fact that current computational technology is still far behind the complexity of the human brain. Figure 1.1 also demonstrates the rationale for and the potential of the development of

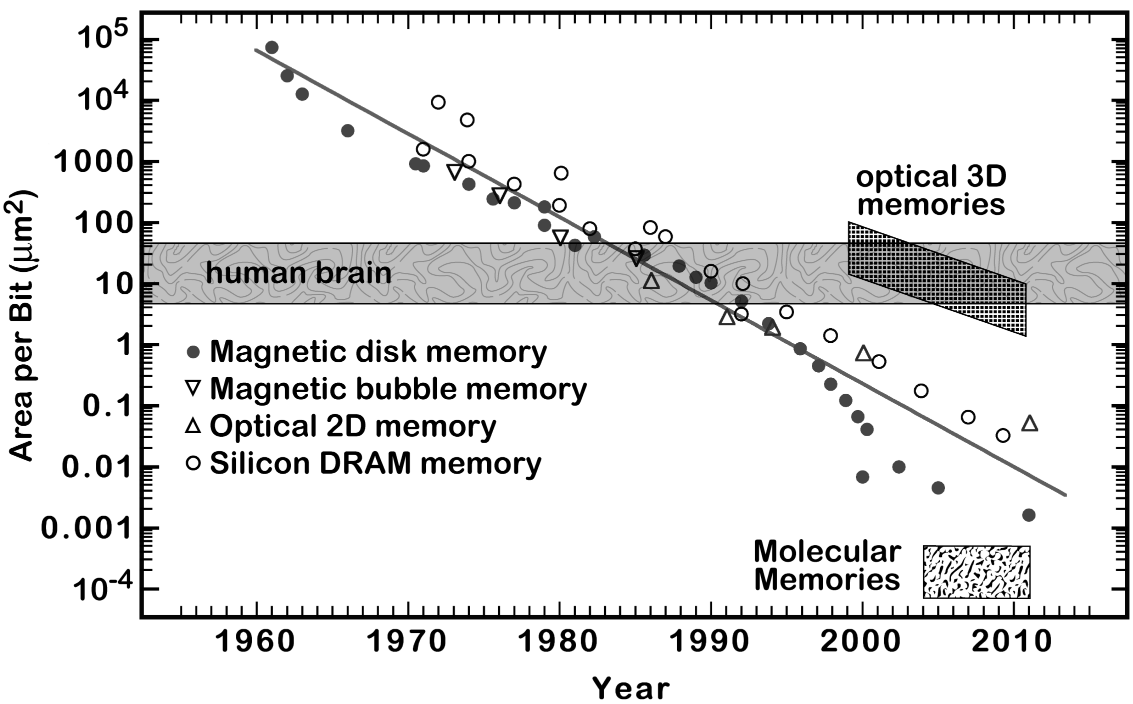

Figure 1.1. Analysis of the area in square microns required to store a single bit of information as a function of time (date in calendar years). The data for magnetic disk, magnetic bubble, optical 2D and silicon DRAM memories are taken from [9-11] and the references therein. These data are compared to the cross-sectional area per bit (neuron) for the human brain as well as anticipated areas and implementation times for optical three-dimensional memories and molecular memories.[12] Note that the optical 3D memory, the brain, and the molecular memories are three-dimensional and therefore the cross-sectional area (A) per bit is plotted for comparison. The area is calculated in terms of the volume per bit, V/bit, by the formula $A = (V)^{2/3}$.

three-dimensional memories based on BR, which will be discussed further in this chapter. We can conclude that the trend of memory densities will soon force the bulk semiconductor industry to address the approaching limitations that proponents for molecular electronics are beginning to solve.

The capability of rapid switching of molecular logic gates can largely be attributed to size. In general terms, gates operating either by electron transfer, electron tunneling, or conformational photochromism will increase in speed as there is a decrease in size of the material. This speed-versus-size tradeoff applies to all gates in use, whether they are already implemented or currently being envisioned. The mass of the carrier will limit how rapidly the conformational change can take place. In principle, one can argue that the generation of an excited electronic state in less than one femtosecond (10^{-15} sec) within a large chromophore-containing protein is an exception to this general statement. Nevertheless, the reaction of the system to the charge shift remains to be size-dependent and the direct relationship between the total size of the device and the response time remains valid.

The speed of molecular and biomolecular-based devices is limited in part by the Heisenberg uncertainty principle. The maximum frequency of operation of a monoelectronic or monomolecular device, $f_{\max}$, can be estimated by the following relationship:[13]

$$f_{\max} \cong \frac{0.00800801 \cdot \tilde{\upsilon}_s \cdot \pi^2}{hN\left[2\pi + 2\tan^{-1}(-2) + \ln\left(\frac{\tilde{\upsilon}_s^2}{4}\right) - \ln\left(\frac{5\tilde{\upsilon}_s^2}{4}\right)\right]} \tag{1.1a}$$

$$f_{\max}(\mathrm{GHz}) \approx \frac{0.963\tilde{\upsilon}_s}{N} \tag{1.1b}$$

where $\tilde{\upsilon}_s$ is the energy separation of the two states of the device in wavenumbers and N is the number of state assignments that must be averaged to achieve a reliable state assignment.

Equations 1.1a and 1.1b only apply to monoelectronic or monomolecular devices; however, Heisenberg's uncertainty principle permits higher frequencies for devices using ensemble averaging. For example, if a device requires 1000 state assignment averages to achieve reliability and $\tilde{\upsilon}_s$ =1000 cm^{-1}, the maximum operating frequency will be ~960MHz.[13] Almost all monomolecular or monoelectronic devices require $N > 500$ at ambient temperature, however, cryogenic devices (~1.2 K) can approach N=1. While quantum mechanics places constraints on the operating frequency at ambient temperatures, molecular devices may have an inherent advantage of faster data transfer and calculation speeds compared to current technologies.

1.2.2. Architecture

The fundamental building block of current computer gates and signal processing circuitry is the three-terminal transistor. Inherent in the ability to exploit this element of modern devices, lithography offers one advantage that none of the techniques available to bioelectronics can duplicate. Lithographic materials can be used to build ultra large-scale integrated devices that involve from 10^7 to 10^9 discrete components with complex interconnections. The true power of the integrated circuit does not come from the capability of fabricating a chip with millions of devices, but stems from the ability to interconnect the devices in a complex circuit. The replication of this particular architecture is near impossible using molecules and it should be noted that it is becoming more difficult to implement with semiconductor materials with the need to keep up with the increasing modern demands of computational power and energy efficiency.

Biomolecular electronics offers significant potential as a catalyst to explore completely novel architectures and represents one of the defining sources of enthusiasm for researchers in the field. The need for new architectures as devices approach the limits of lithographic materials should encourage the investigation and development of new designs based on neural, associative,

or parallel architectures and lead to hybrid systems with enhanced capabilities relative to current technology. For example, optical associative memories and three-dimensional memories can be implemented with unique capabilities based on photoactive proteins (see sections 1.4 and 1.5).[14,15] The incorporation of these architectures within hybrid systems is anticipated to have near-term application. Furthermore, the human brain, a computer with capabilities that far exceed the most advanced supercomputer, is an elegant example of the potential of molecular electronics and a hint into the future of computation and artificial intelligence.[12,16-19] Although the development of an artificial neural computer is beyond our current technology, it would be unreasonable to assume that such an accomplishment is impossible. Current research investigating molecular electronics should be viewed as an opening to new architectural opportunities that will lead to overall advances in computer and signal processing systems.

1.2.3. Nanoscale Engineering

During the evolution of computer technology, the feature size of high-speed semiconductor devices has decreased dramatically and still continues along this trend (see Figure 1.1). The informational revolution has driven the demand for higher speeds and densities, which has lead to submicron feature sizes in the most commonplace devices of today. Extreme ultraviolet lithography can provide modest improvement over the projected densities of current materials; however, there is a need for new light sources for the development of nanoscale feature sizes.[20] Such lithographic methods are well understood, although several challenges remain to be solved before the technology is successfully implemented.[21,22]

As we have noted above, organic synthesis provides a "bottom-up" approach that offers a 100- to 1000-fold improvement in resolution relative to the best lithographic methods. Two alternatives to organic synthesis that have made an impact on current efforts in biomolecular

electronics have been self-assembly and genetic engineering. The Langmuir-Blodgett technique that is used to prepare organized structures is the most known and best characterized example of self-assembly; however, self-assembly can also be used in the generation of membrane-based devices, microtubule-based devices, and liquid crystal holographic films.[23-29] Genetic engineering offers a unique approach to the manipulation of large biological molecules and is the described technique in this chapter. Specifically, here we discuss the enhancement and application of BR using mutagenesis and directed evolution for various bioelectronic devices (see section 1.6). Genetic engineering is crucial to the early success of implementing large and complex molecules into these devices. We note, however, that recent advances in DNA architectures for computing and processing information have been made and the reader is directed to relevant references for further discussions of these technologies.[16,17,30-32]

1.2.4. Stability

All electronic devices produce heat as a byproduct of their operation. The thermal stability of the biomolecular components must be considered because most organic-based molecules, including proteins, are irreversibly damaged at temperatures far lower than the operational temperature of the inorganic materials that are used in current semiconductors. However, there are examples of biological molecules that can operate at moderate to high temperatures for extended periods of time. Bacteriorhodopsin, for example, is stable to temperatures above 80 °C[33] and is often regarded as a viable material for optical computing (see section 1.3).[15,34-37]

When many write-read-erase cycles are required for biophotonic applications, such as holographic associative memories, concerns of stability are extended to the photochemical degradation of molecules. Photochemical stability is measured in terms of cyclicity and

approximates the ability to photochemically switch between functional states before becoming unreliable. There is no accepted definition of cyclicity, but it is often considered to be the number of events required to degrade (or denature) ~37% (1/e) of the material.[15] Bacteriorhodopsin is capable of $\geq 10^6$ conversions at ambient temperature[38-40] and, when paired with the thermal stability, is more stable than a majority of organic photochromic molecules.[41] Much of this stability is attributed to the protein structure,[42] which sequesters the photoactive chromophore within the protein core and protects it from oxidation and free radicals while simultaneously providing steric constraints that enhance stability.

The reliability of the protein-based device can also be implemented to ensure that no data is corrupted or lost if any protein denatures via thermal or photochemical stress during operation. One such method is ensemble averaging, whereby many molecules are simultaneously used to represent a single bit of information. This technique is implemented as a fail-safe to reduce the risk of molecular degradation affecting a device. Other methods have been designed and the reader is directed to articles by Lawrence *et al.*[43] and Lawrence and Birge[44] for further information about the topic. In summary, thermal and photochemical stability is an important issue to consider when implementing molecules into electronics; however, it has been shown that both native and redesigned biological molecules have stabilities sufficient for the operating conditions of the proposed technologies.[15]

1.2.5. Reliability

Advocates of semiconductor-based devices have cited the issue of reliability repeatedly as a reason to view molecular and biomolecular electronics as impractical. Some believe that the need to use ensemble averaging in optically coupled molecular gates and switches demonstrates the inherent unreliability of these devices. As a counterpoint, one must acknowledge that

transistors require more than one charge carrier to function efficiently. In fact, most ambient temperature molecular and bulk semiconductor devices use more than one molecule or charge carrier to represent a bit. This is simply because ensemble averaging improves reliability and permits higher speeds. The use of ensemble averaging does not, however, rule out the possibility of building reliable monomolecular or monoelectronic devices.

The probability of correctly assigning the state of a single molecule, p_1, is never unity. This seemingly flawed assignment capability is due to quantum effects and inherent limitations in the state assignment process for many technologies. The probability of an error occurring in a single state assignment, P_{error}, is a function of p_1 and the number of molecules, n, within the ensemble used to represent a single bit of information. P_{error} can be approximated by the following formula:[13]

$$P_{\mathrm{error}}(n,p_1) \cong -erf\left[\frac{(2p_1+1)\sqrt{n}}{4\sqrt{2p_1(1-p_1)}};\frac{(2p_1-1)\sqrt{n}}{4\sqrt{2p_1(1-p_1)}}\right] \tag{1.2}$$

where $erf\,[Z_0;\,Z_1]$ is the differential error function defined by:

$$erf\left[Z_0;Z_1\right] = Erf[Z_1] - Erf[Z_0] \tag{1.3}$$

where

$$erf[Z] = \frac{2}{(\pi)^{1/2}}\int_0^Z \exp(-t^2)\,dt \tag{1.4}$$

Equation 1.2 is an approximate representation of the error involved in these processes and neglects the statistical error associated with the probability that the number of molecules in the correct conformation can stray from their expectation values. Nevertheless, these equations are sufficient to demonstrate the issue of reliability and ensemble size.

Let us define a logarithmic reliability parameter, ξ, that is related to the probability of error in the measurement of the state of the ensemble by the function, $P_{\text{error}} = 10^{-\xi}$. A value of ξ = 10 is considered a minimal requirement for reliability without the need for error correcting routines. If we assume that a single molecule can be correctly assigned with a probability of 90% ($p_1 = 0.9$), then 95 molecules are required to collectively represent a single bit to yield $\xi > 10$ [$P_{\text{error}}(95, 0.9) \approx 8 \times 10^{-11}$]. A value of $p_1 = 0.9$ is larger than what is normally observed. Ensembles larger than 10^3 are typically required for sufficient reliability, although this value diminishes if fault-tolerant or fault-correcting routines are built within the architecture. Analyses on specific molecular-based devices are discussed further by Tallent *et al.*[13]

The question next becomes whether or not a reliable processor can be designed that uses a single molecule to represent one bit of information. The answer is yes, provided that one of two conditions is met. First, the device can have fault-tolerant architectures that either recover from digital errors or operate reliably with sporadic error due to analog or analog-type environments. One example of digital error correction that is commonly used in semiconductor memories is the use of additional bits beyond the number required to represent a number. These architectures lower the required value of ξ to less than 4. Analog error tolerance is present in many optical computer designs that implement holographic and/or Fourier architectures to carry out complex functions. Second, it is possible to design molecular architectures that can probe the assigned state of a bit without disturbing the state of the molecule. For example, an optically coupled device can be read by using a wavelength that is absorbed or diffracted, but that does not initiate state conversion. Under these conditions, the variable n in Equation 1.2 can be defined as the number of read operations instead of the ensemble size. In the previous example, 95 molecules must be included in the ensemble to achieve reliability. Using this architectural system, a single

molecule can be used to assign a state provided that 95 nondestructive measurements are used to define the state. Multiple measurements are equivalent to integrated measurements, and a continuous read with digital or analog averaging can achieve the same level of reliability.

1.3. Bacteriorhodopsin as a Holographic Material for Bioelectronics

1.3.1. The Purple Membrane

Bacteriorhodopsin (MW = 26 kDa) is the light-transducing protein expressed in the purple membrane (PM) of the archaeon, *Halobacterium salinarum.*[45-47] This organism is native to salt marshes, which contain environments characterized by low oxygen levels and a salinity that is roughly six times greater than that of seawater. When dissolved oxygen concentrations are insufficient to support oxidative phosphorylation, BR is expressed throughout the plasma membrane of the native organism. Thus, production of metabolic energy occurs via a photosynthetic proton pumping mechanism that is coupled with the rapid synthesis of adenosine triphosphate (ATP) in the cell cytoplasm.[48]

The PM, coined as such due to the presence of a distinctive purple pigment, contains a two-dimensional, semi-crystalline lattice of hexagonal subunits made up of BR trimers. The structure of BR includes a seven transmembrane, α-helical motif that is functionalized with a long-chain polyene chromophore, all-*trans* retinal, via a protonated Schiff base linkage to Lysine-216.[42] The absorption of a single photon by the protein initiates a complex photochemical reaction, termed the BR photocycle, which is characterized by a cyclic series of conformational changes and the concurrent net translocation of a proton from the intracellular to the extracellular region (see Figure 1.2).[49-51] The photocycle of native BR has a lifetime of approximately 15 ms and contains transient, spectrally distinct photointermediates that span the entire visible region of

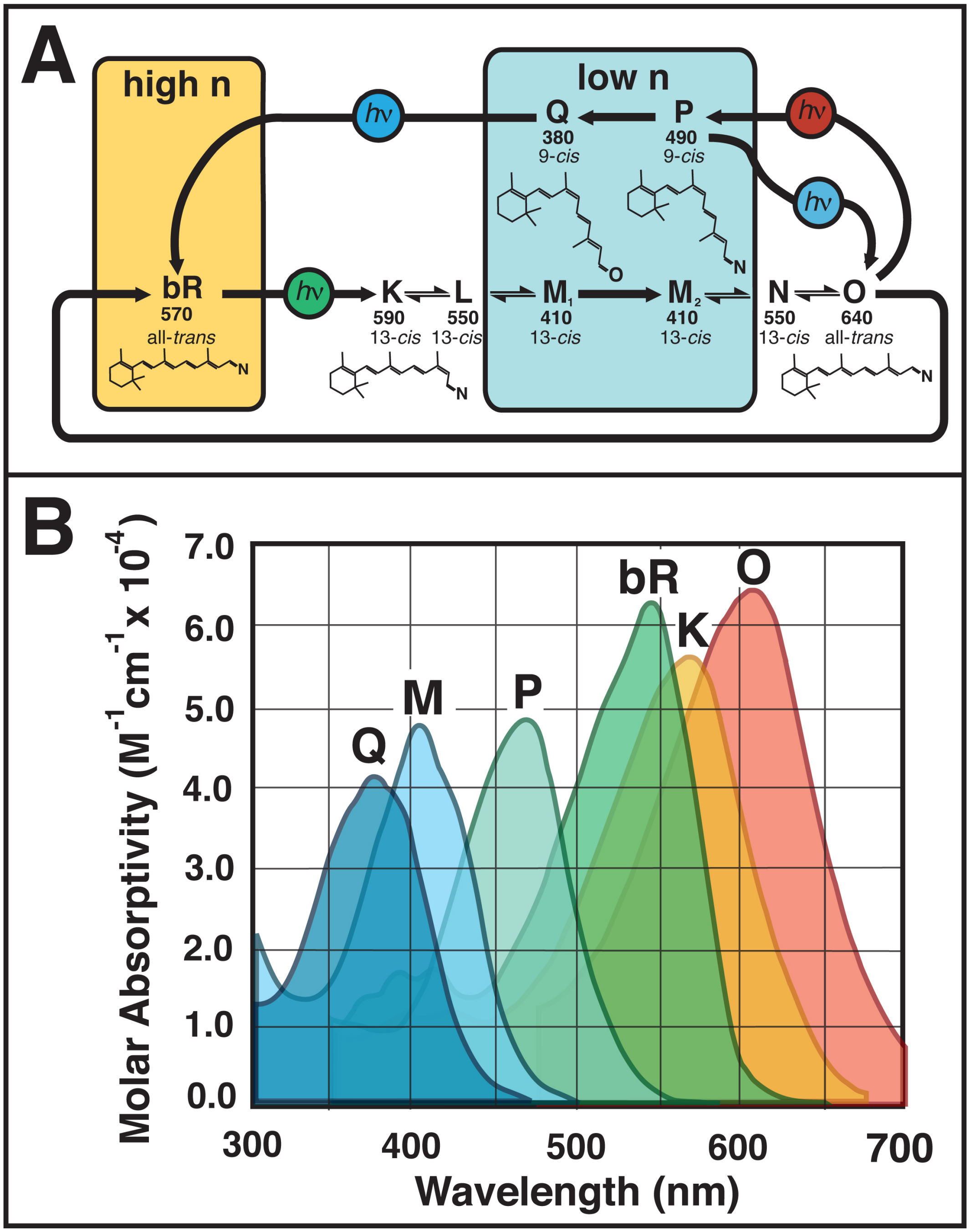

Figure 1.2. The photocycle and branched photocycle of native BR. (A) The absorption maxima (in nm) and the retinal conformation are provided below each corresponding photointermediate. The branched photocycle (the **P** and **Q** states) is reached via a sequential two-photon event, in which the protein is initially paged with an incident photon (~570 nm) and is subsequently driven by another (~640 nm) during the lifetime of the **O** state. The relative refractive index of key photointermediates are highlighted, and the absorption spectra of select photointermediates are provided in (B) (Based on Figure 2 from reference 15).

the electromagnetic spectrum. The unique photophysical properties of BR present an innate advantage for the development of photonic devices; however, the potential of this biomaterial is derived from the coupling of this photochemistry with robust structural and functional stability. In the PM, native BR has been shown to be stable at temperatures above 80°C,[33] and, once placed in a chemically altered environment, could withstand temperatures as high as 140°C.[52,53] In addition to thermal stability, BR exhibits high photochemical stability, which is defined as the number of times the protein can be photochemically activated before denaturing.[15] This cycling property exceeds 10^6 for BR at ambient temperature and is considerably higher than that of most photochromic organic molecules.[38,39]

1.3.2. The Photochromic Properties of Bacteriorhodopsin

For FT holographic associative processors, the spectral separation and the significant change in refractive index throughout the photocycle implicate the potential for use in the architectures described above. The absorption of a photon by all-*trans* retinal potentiates the formation of a Franck-Condon excited state and a near instantaneous shift of electron density down the polyene chain of the chromophore, thereby initiating an isomerization around the $C_{13}=C_{14}$ double bond to form 13-*cis* retinal (see Figure 1.2).[46] This 500 fs process is referred to as the primary photochemical event of BR (**bR→K**), and is followed by a cascade of thermally driven photointermediates (**L**, **M**, **N**, **O**, and back to **bR**).[54,55] The **M** state forms approximately 50 μs after the absorption of a photon and is associated with the transfer of a proton from the protonated Schiff base to Aspartic acid-85, which is the residue that serves as the primary counterion in the resting state.[56] This transition results in a dramatic hypsochromic shift in the absorption maximum (λ_{max}; 570 nm → 410 nm), which has a time constant of 10 ms. For real-time holographic associative processing, the blue light absorbing **M** state is the secondary

constituent in the **bR**/**M** photochromic pair. In addition to the thermal decay pathway of the **M** state back to the resting state, the **bR** state can also be regenerated from the **M** state through the absorption of blue light. This photoreversibility is described using the following equation,

$$bR(\lambda_{\max} \cong 570nm) \underset{\Phi_2 \leq 0.95}{\overset{\Phi_1 \sim 0.65}{\rightleftarrows}} M(\lambda_{\max} \cong 410nm) \quad , \tag{1.5}$$

where Φ_1 and Φ_2 are the quantum efficiencies of the forward (**bR→M**) and reverse (**M→bR**) reactions, respectively. Due to the unusually high quantum efficiencies of both reactions, BR has proven to be an ideal optical recording medium for holographic processors. However, this application relies on the manipulability of the **M** state time constant, which is prohibitively short in the native form of the protein. Norbert Hampp and colleagues have achieved success in designing a real-time holographic interferometer based on the chemically and mutationally modified BR mutant, which contains a long-lived **M** intermediate that persists on the order of seconds.[57-59] Despite this success, a system with pure photoswitching without a transient thermal decay has yet to be realized using the **M** state, thereby preventing applications in long-term data storage. Since the advent of this device, however, a long-term photoproduct of BR (the **Q** state) has been discovered and exploited to form a new prospect of photochromic equilibrium with two long-lived states.

A branching reaction of the main photocycle is accessed via a sequential two-photon event. The photocycle is first initiated through light absorption by the chromophore, and the branching reaction is obtained through the subsequent exposure to red light (~640 nm) while the protein is in the **O** state.[60] The **P** state, which contains a 9-*cis* chromophore and a λ_{max} of 490 nm, is the direct photochemical intermediate of this reaction pathway, and is followed by the hydrolysis of 9-*cis* retinal and the formation of the **Q** state (λ_{max} = 380 nm).[60,61] The **Q** state photoproduct is thermally stable for several years (requiring 190 kJ mol^{-1} to initiate a reversion)

and may be converted back to the **bR** resting state upon the absorption of a high-energy photon (~380 nm). The discovery of the branched photocycle of BR has yielded advances in the development of sequential two-photon volumetric memories based on the protein, where two stable products (**bR** and **Q**) are assigned to binary bit 0 and binary bit 1, respectively.[15]

The stability of this photoproduct and the ability to probe and manipulate the protein medium via differential absorptivity has lead to a dramatic increase of potential in biomolecular devices. The architectural requirements of the sequential two-photon stimulus parameters of BR in the PM are more suitable for three-dimensional memories,[15] and not for the FT holographic associative memories described here. Alternatively, a blue-shifted species analogous to the **P** and **Q** states can be exploited in the blue membrane (BM) form of the protein, in which the PM is transformed into a biphasic photochromic material capable of long-lived changes in the refractive index.

1.3.3. The Blue Membrane

The formation of the BM occurs through altering the electrostatic interaction of retinal with key residues using either chemical or mutational modification of the protein. Native BR contains 4 moles of calcium(II) and magnesium(II) per mole of protein at pH 6.0,[62,63] and the removal of these cations perturbs the retinal binding pocket, inducing a reversible color change from purple (λ_{max} = 570 nm) to blue (λ_{max}=605 nm).[63-67] Cation displacement is accomplished by either acidification of the PM [65,68,69] or through deionization methods at standard pH.[62,64,69-71] Despite the efficiency of these methods, both forms of chemical modification result in a destabilized form of the protein.[72,73] Mutational manipulation has proven to be effective at inducing localized changes to create a stable form of the BM. Amino acids that stabilize the

protonated Schiff base are often targeted for mutagenesis,[74,75] and these mutants have been successfully implemented into long-term holographic memory devices.[76,77]

Within the BM, the chromophore exists in both the all-*trans* and 13-*cis* conformations in the resting state (λ_{max} = 605 nm).[68,78] The primary photochemical event (all-*trans* → 13-*cis*) is still initiated upon the absorption of a photon, however, the reaction has a much lower efficiency ($\Phi \approx 0.10$) and contains a truncated photocycle that does not terminate with the net translocation of a proton.[79] Despite these altered photophysical characteristics, the BM is capable of forming blue-shifted intermediates that are similar to the **P** and **Q** states of the branched photocycle. Under sustained illumination with red light (~640 nm), a reversible photoconversion is initiated to form a species with a λ_{max} of 490 nm, which is often referred to as the pink membrane.[78] The pink membrane is characterized by the 9-*cis* conformation of retinal and is a long-lasting photoproduct of the BM form of BR, which can only be reverted back to the BM resting state (**bR**) via blue light (~400 nm) illumination.[68,69] The pink membrane has been shown to form two thermal decay products (λ_{max} = 450 nm and 380 nm), the latter of which is characterized by a hydrolyzed 9-*cis* retinal (**Q** state).[60,70,71,80] In application, blue←→pink photochromism is isolated in dehydrated polymer films.[71,81]

The application that includes the blue/pink photochromic pair differs in two ways from the **bR**/**M** pair. First, the pink membrane form is stable for weeks or months in contrast with the transient intermediates of the BR photocycle.[71] Secondly, the quantum efficiencies of the forward and back reactions are minute compared to the reactions of the PM.[78] The low sensitivity to incident light, however, is of little consequence and can even be advantageous. Low quantum efficiencies signify that thin films would be stable under ambient light conditions, which would elicit transferrable long-term holograms for data storage. Moreover, under write and read

conditions, the low efficiency is circumvented due to the widespread availability of high-energy diode lasers.

1.4. Fourier Transform Holographic Associative Processors

Associative processors based on holography present a unique advantage over conventional computers in the implementation of auto-correlation. These processors can be used to identify and optically compare real objects to an extensive holographic database and has shown potential for applications in optical computer architectures, robotic vision hardware, and generic pattern recognition systems.[58,82-84] Unlike the architectures of current integrated circuits in semiconductor-based computers, holographic associative processors mimic the neural associative activity of the human brain. Neural association processes allow for the fast and efficient identification of objects in real time and the capability of distinguishing between multiple objects of a similar form. Conventional computers lack the necessary architecture to complete associative recall. They are capable, however, of compensating through complex algorithms that involve the digitization of the input image, the comparison of the input data to all digital images, and the exploitation of correlation subroutines that identify the closest match.[85] Holography allows us to surpass these limitations and to create a data processor that competes with the complexity and efficiency of the human brain.

It has long been known that human associative recall can be simulated by using a Fourier transform (FT) holographic optical loop.[84,86-89] Before we discuss the use of protein-based holographic films and spatial light modulators, it is useful to describe the nature of FT optical association. This introduction is important to understanding the hybrid architecture we have implemented.

1.4.1. Computer Simulation of the Complex Fourier Association Process

Consider two gray-scale image planes of identical pixel dimensions. Each pixel is represented by an element in a matrix of identical dimension (a 1024 x 1024 image plane is represented by a 1024 x 1024 matrix of real numbers). A smaller sample image is copied into the sample plane at an arbitrary location, and a reference image is copied into the reference plane at an arbitrary location. If we assume that an image pixel has a value from 0.0 to 1.0, where 0.0 is pure black and 1.0 is pure white, the following algorithm will yield the complex Fourier association (CFA) between the two images.

Both images are Fourier transformed by using standard two-dimensional complex FT procedures. Our implementation is an internal function of MathScriptor 2.2.16, which is freely available from www.mathscriptor.org. The FT of the single matrix, representing the sample plane (onto which the sample image is imposed), is represented by a matrix, $\mathbf{\Psi}^a$, of cosine (real) components and sine (imaginary) components. We represent these elements as c_{ij}^a and s_{ij}^a, respectively. Similarly, the FT of the reference matrix yields $\mathbf{\Psi}^b$, with real and imaginary components, c_{ij}^b and s_{ij}^b. The CFA of these two image planes is calculated by using the following equation:

$$\left\langle \Psi^a \middle| \mathbf{A} \middle| \Psi^b \right\rangle = \frac{2\left\langle \Psi^a \middle| \mathbf{a} \middle| \Psi^b \right\rangle}{\left|\Psi^a\right|^2 + \left|\Psi^b\right|^2} \tag{1.6}$$

where

$$\left|\Psi^a\right|^2 = \sum_i \sum_j \left[\left(c_{ij}^a\right)^2 + \left(s_{ij}^a\right)^2 \right]^2, \tag{1.7}$$

$$\left|\Psi^b\right|^2 = \sum_i \sum_j \left[\left(c_{ij}^b\right)^2 + \left(s_{ij}^b\right)^2 \right]^2, \tag{1.8}$$

and

$$\left\langle \Psi^a \middle| \mathbf{a} \middle| \Psi^b \right\rangle = \sum_i \sum_j \left[\left(c_{ij}^a c_{ij}^b \right)^2 + \left(s_{ij}^a c_{ij}^b \right)^2 + \left(c_{ij}^a s_{ij}^b \right)^2 + \left(s_{ij}^a s_{ij}^b \right)^2 \right]. \tag{1.9}$$

The speed of the above algorithm is limited primarily by the time required to carry out a pair of two-dimensional complex Fourier transformations. High-resolution CFA on 3000 x 3000 images can take many seconds on array processors designed for the task, and thus, optical implementations are of value for real world applications. The key advantage of the above algorithm is two-fold: it allows us to explore the association process with digital precision and it reflects the same behavior as the optical associative memory that we explore below.

Translational Invariance: There are three variables that determine the relationship of a sample image with respect to a reference image: translation, rotation and size. If the sample and reference images are identical, the above equations calculate perfect association ($\left\langle \Psi^a \middle| \mathbf{A} \middle| \Psi^b \right\rangle = 1$) regardless of where the images are located on the sample and reference planes. Thus, CFA is translationally invariant in the mathematical domain. This observation is not necessarily true in the optical domain, but in our implementation, translational invariance is retained (see below).

Rotational Variance: Consider solid white rectangles of identical width and a variable aspect ratio, in which the aspect ratio equals the ratio of the long axis to the short axis. If we associate two identical rectangles that differ only in terms of rotation, we find that the CFA varies dramatically depending upon the relative angle of the sample and reference rectangles. The results are presented in Figure 1.3 for rectangles of aspect ratio 1 (squares) to 10 (rectangles of length 10 by 1). Thus, we are calculating the CFA (Equation 1.6) for two identical objects which have a relative rotation from 0° to 90°. The CFA value is invariant to the absolute rotation

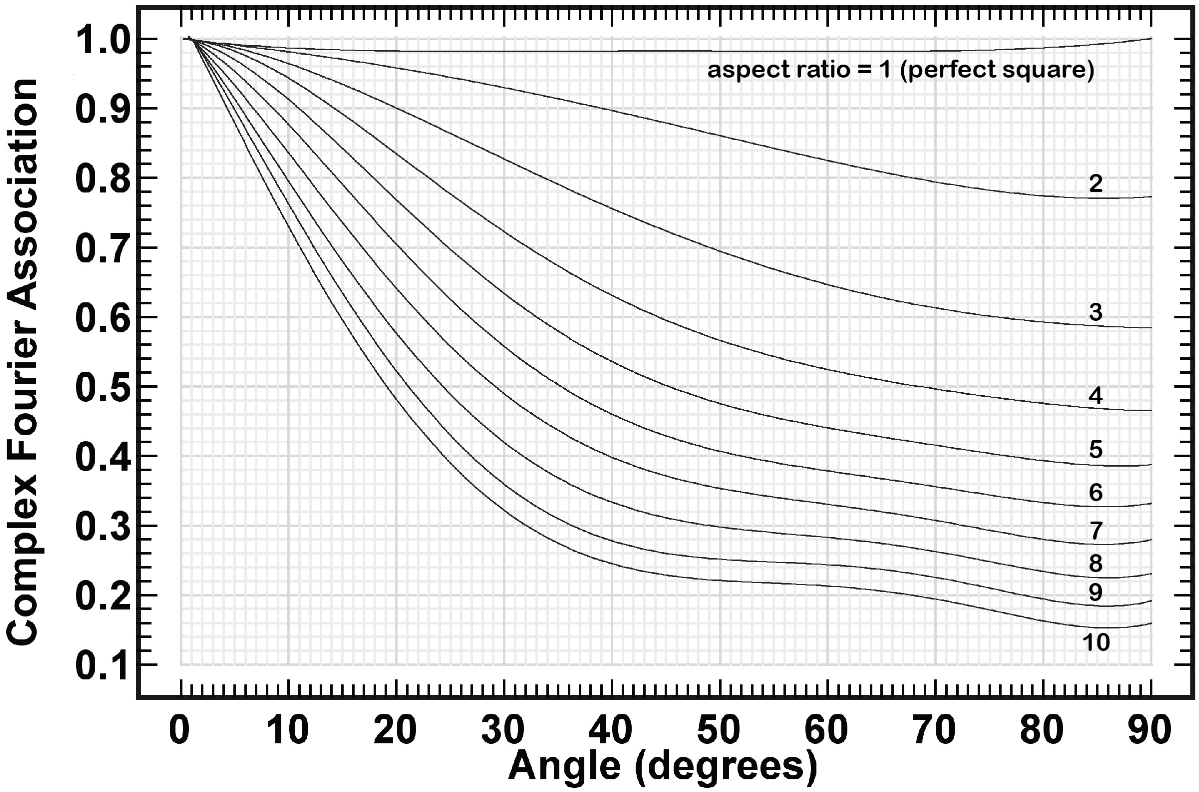

Figure 1.3. Complex Fourier association (CFA) is rotationally variant. The above graph displays CFA values for pairs of identical solid white rectangles as a function of relative angle and for various aspect ratios (= length/width). Pure squares (aspect ratio = 1) show only minor dependence on angle. Rectangles with lengths ten times longer than widths (aspect ratio = 10) must be aligned to within a fraction of a degree to register accurate CFA values.

of the samples, but very sensitive to the relative rotation. Higher aspect ratios lead to a more severe drop-off in CFA with relative rotation (Figure 1.3).

Size Variance: The problem of rotational variance is compounded due to the fact that two objects must be size coordinated to properly associate in Fourier space. As shown in Figure 1.4, however, the nature of the objects is of minor importance to the magnitude of the variance. Figure 1.4 displays the CFA for a variety of identical objects, from simple letters to human faces. It is surprising how similar the size dependence of the CFA is with regards to varying objects. The nature of the size variance (Figure 1.4) is quite different from the shape dependence of the rotational variance (Figure 1.3). Thus, when an unknown object is to be characterized via Fourier association, the first step is to optimize the relative size to yield a maximal CFA. The second step is to rotate the input object to maximize the CFA. This combination works well for the vast majority of problems, although it is not uncommon to follow this cycle through two optimization passes when high discrimination is desired (i.e. size→rotation→size→rotation).

Face Identification: The human brain is remarkably adept at facial recognition. The neural processes have been studied extensively,[90] but the complex architecture of the human brain is too unique to provide useful templates for computer-based face recognition.[91,92] Given the observation that FT optical associative memories mimic human memory recall (see above), it is appropriate to test the ability of CFA to differentiate human faces. A simple example based on four faces is presented in Figure 1.5. The two faces in the top quadrants are from different individuals. The two faces in the bottom quadrants are of the same individual, but differ in expression. Despite the different expressions, CFA yields a very high correlation between both faces (see Figure 1.6).

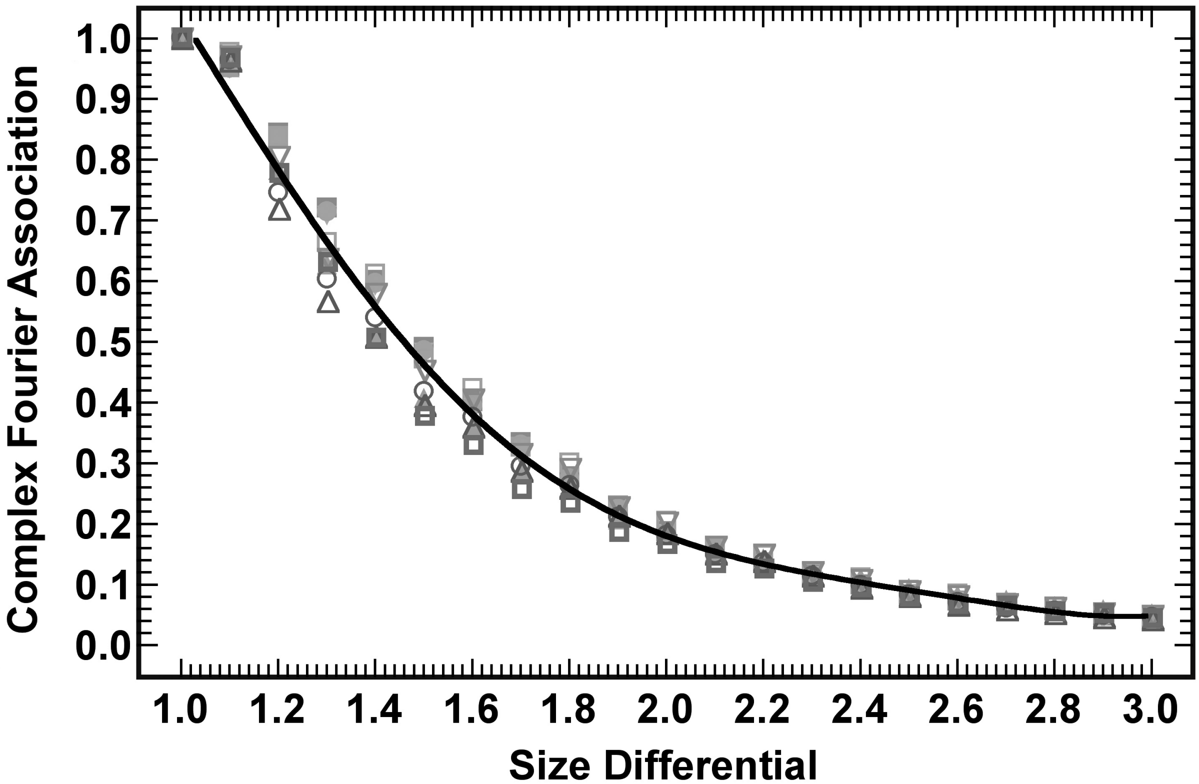

Figure 1.4. Complex Fourier association (CFA) requires that the two objects being compared have relative sizes that are shifted to an identical extent from the actual sizes of the objects. The above graph displays the CFA values for a set of identical objects, where the sample size has been changed relative to the reference size by a value of 1 (identical sizes) to 3 (sample image is three times larger than the reference image). Objects ranged from simple letters to complex objects, including human faces. Regardless of object complexity, the CFA varies with size differential by a similar magnitude.

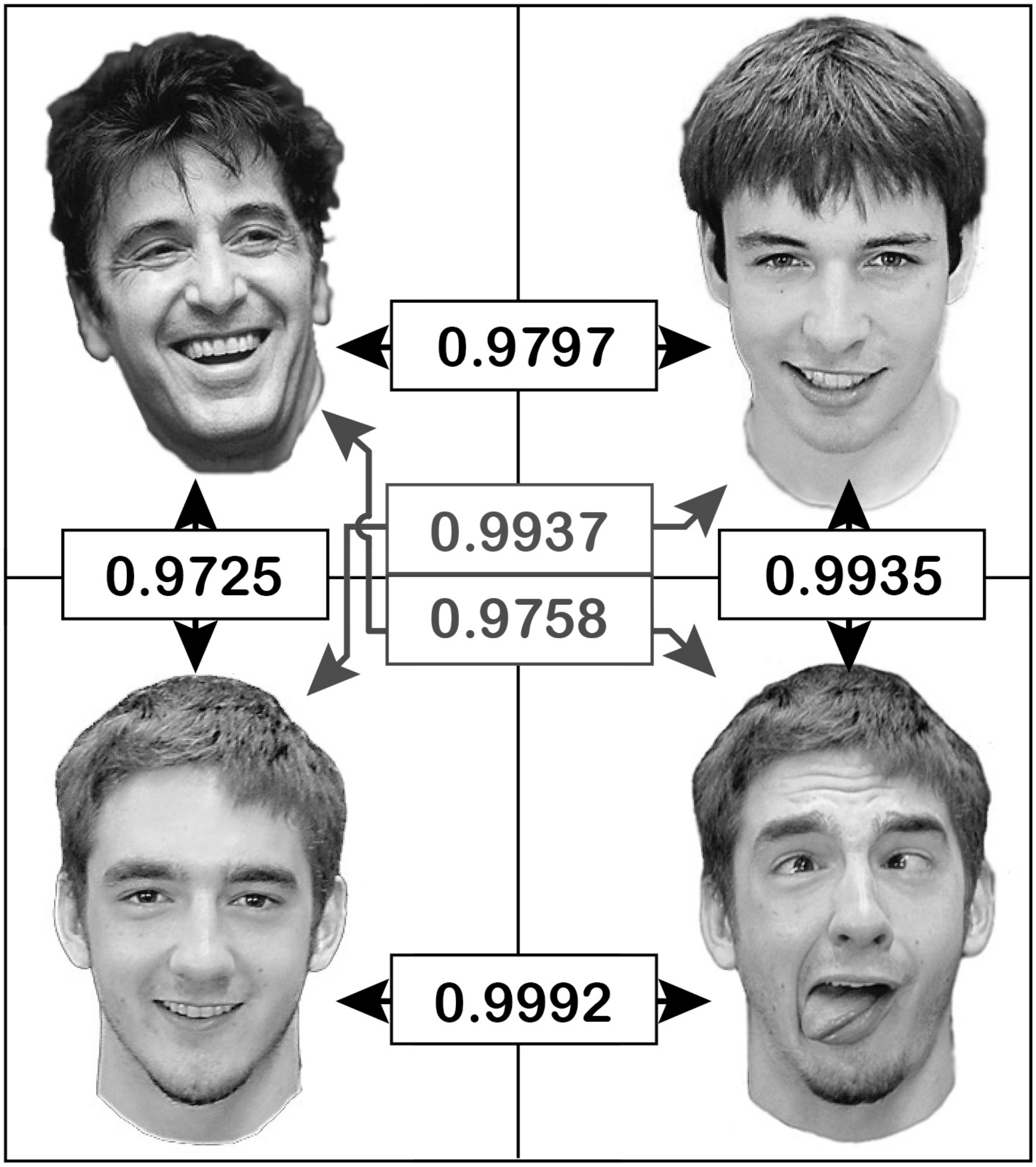

Figure 1.5. Comparison of four faces based on complex Fourier association (CFA). Each pair of faces are angle and size tuned to yield the listed maximal CFA value, which is displayed between all pairs as indicated by the arrows. Note that the bottom two faces belong to the same person, but differ significantly in expression. Nevertheless, the CFA value of 0.9992 indicates that a holographic associative memory would recognize that both images were associated with the same person. A key observation of this study is that facial recognition via CFA is accurate, but requires at least 3.5 significant digits of precision. This is an easy goal for a computer, but a non-trivial requirement for optical Fourier instrumentation.

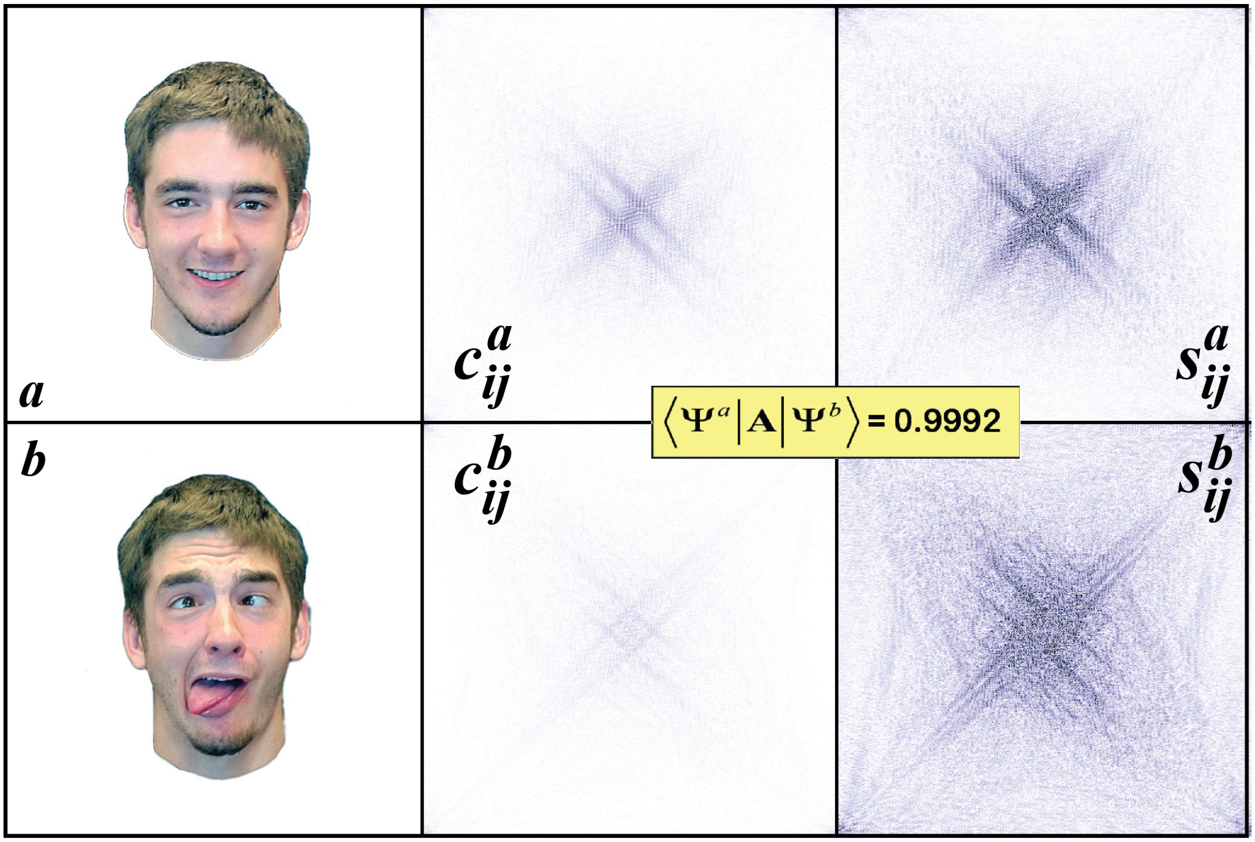

Figure 1.6. The remarkable ability of complex Fourier association (CFA) to recognize that two faces, with very different expressions, belong to the same individual. The complex Fourier transform of image *a* generates a cosine (c_{ij}^{a}) and a sine (s_{ij}^{a}) matrix, which are shown in the top three panels from left to right. The bottom three panels show the corresponding information for image *b*. The values of the matrix elements are represented by pixel darkness with white = 0.0 and relative magnitude being represented by darkness of the pixel. While the two complex transforms have significantly different cosine and sine matrices, the CFA calculated using Equation 1.6 is nevertheless capable of revealing a high associative correlation (0.9992). The key disadvantage of CFA algorithms is the computational expense. Hence, an optical approach (Figure 1.7), which is thousands of times faster, is to be preferred for real-time applications.

An important observation is that while CFA does a remarkably good job of differentiating faces, the process requires four digits of precision. In computer terms, this is a trivial requirement. When CFA is implemented in optics, however, the equivalent of four significant digits of precision can only be achieved by using high-quality Fourier lenses and vibration-free optical platforms. We explore an optical associative processor in the next section.

1.4.2. Fourier Transform Optical Associative Processors

Holographic associative loops were first described by Paek and Psaltis in 1987 and were revolutionary in their use of Fourier transformations to write and read reference planes using thin films.[84] In practice, these associative memories take an input data block and scan the entire memory for the data block that matches the input. In some implementations, the closest match will be found even if there is not a perfect match. The memory will then return the data block that satisfies the matching criteria. The most sophisticated associative memory hardware would permit data blocks of varying sizes for flexible association of input and output data. We have implemented the design proposed by Paek and Psaltis by using thin films made with BR as the photoactive material (Figure 1.7).[83] Modifications to this system have been made to facilitate the introduction of both input and reference images using a single active matrix spatial light modulator (AMSLM) and output using a charge-coupled detector (CCD). Because BR thin films are dynamic holographic media, new databases can be actively fed in through the AMSLM as needed. Database images are focused via Fourier lenses (FL) onto two hologram locations, H1 and H2, and then the input image is fed into the system. The image transverses the loop and is superimposed on H1 and H2, at which point an intensity enhancement is observed at the location of the closest match in the database array. The hologram stored at this location is preferentially selected and imaged at the CCD output. Figure 1.8 demonstrates the associative analysis of a

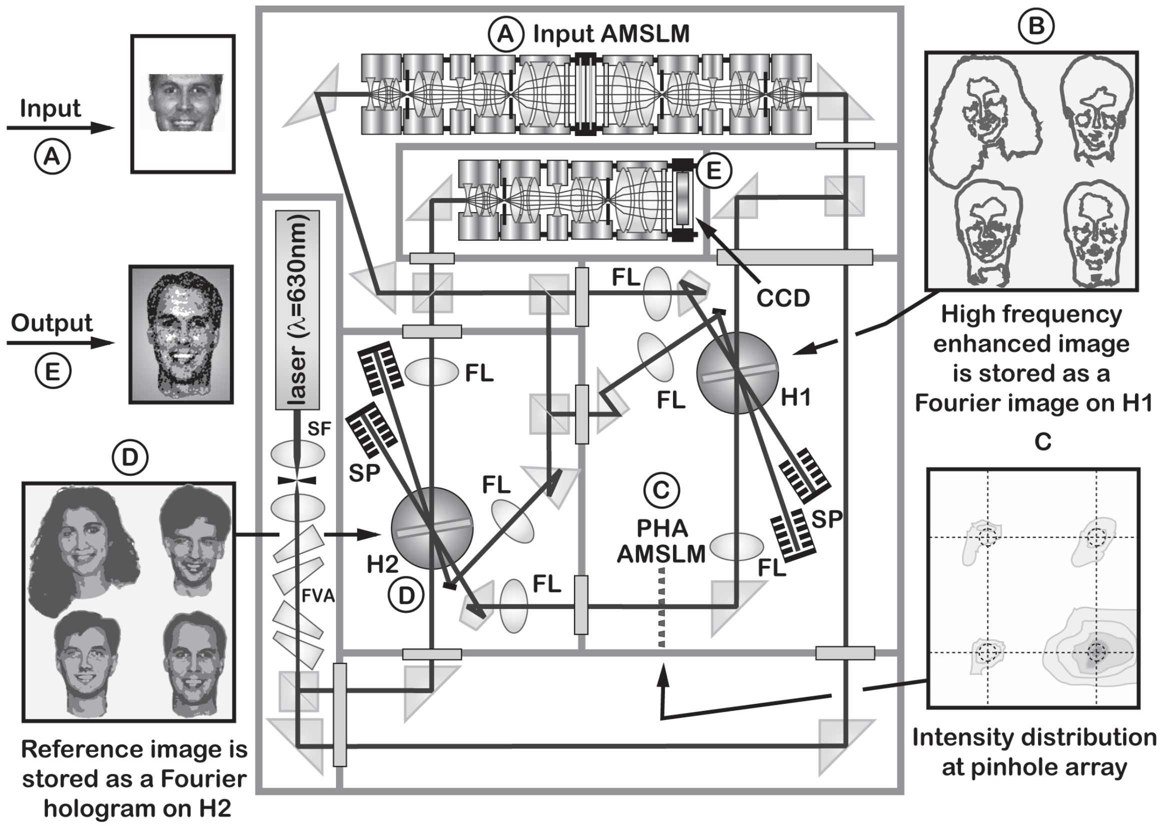

Figure 1.7. Schematic diagram of a Fourier transform holographic (FTH) associative memory. Thin polymer films of bacteriorhodopsin serve as media to create FTH reference planes for real-time storage of the holograms. A partial input image is enough to select and regenerate the entire associated image stored on the reference hologram. Although only four reference images are shown, the FTH associative memory can handle many hundreds or thousands of images simultaneously. This memory can also work on binary data by using redundant binary representation logic, and a small segment of data can be used to find which page has the largest association with the input segment. Selected components are labeled as follows: AMSLM, active matrix spatial light modulator; FL, Fourier lens; FVA, Fresnel variable attenuator; H1, H2, holographic films; PHA, pin-hole array; SF, spatial filter; SP, beam stop (adapted from Figure 9 from reference 15).

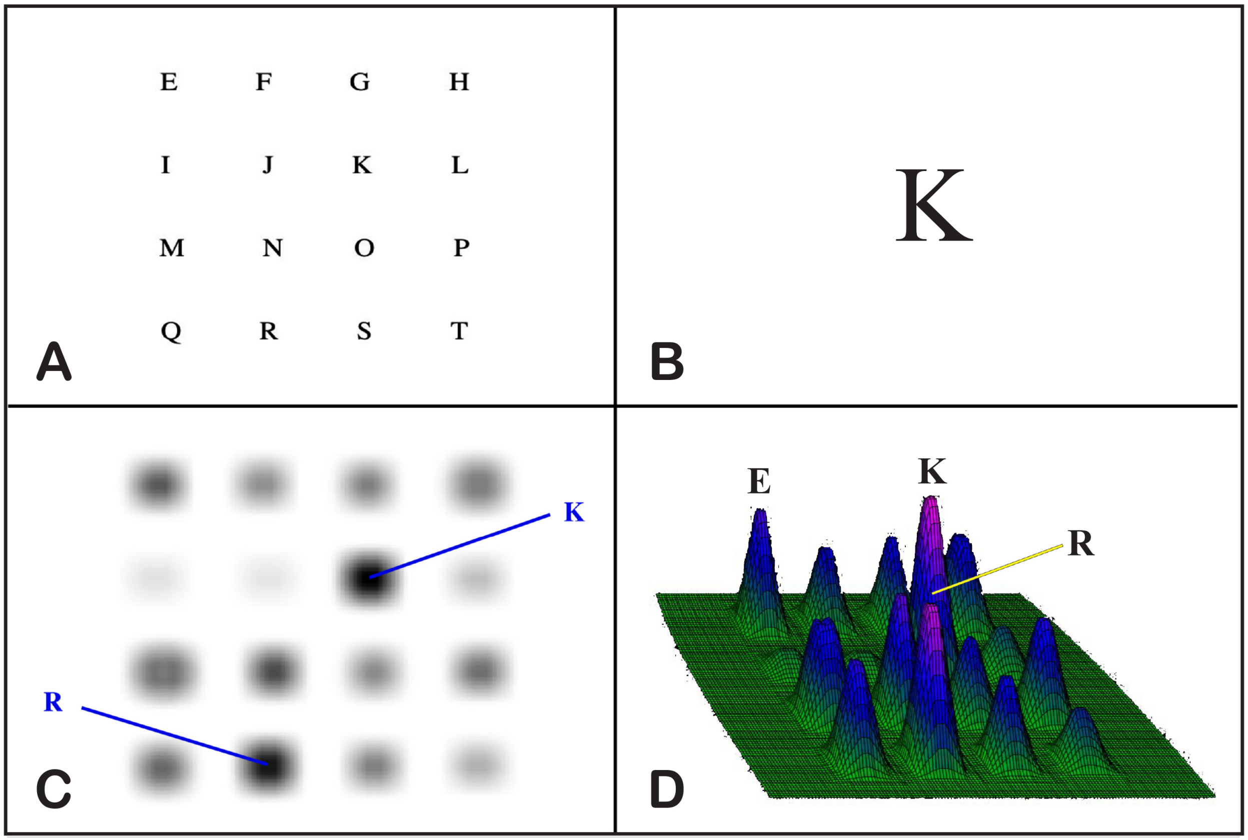

Figure 1.8. Demonstration of the importance of thresholding in the associative analysis of data sets with similar pages. A set of 16 pages each containing a single letter (**A**) is associated with a single letter, K, as input (**B**). The intensity of the Fourier association at each pinhole is shown in (**C**) and displayed as a profile at the CCD detector in (**D**). The letters R and K are so similar that either letter will strongly associate with the other, and without variable association, both letters would be displayed in the output. Associative memories work best when the pages contain more complex entities such as words, paragraphs, complex images or combinations of words and images. The higher the complexity, the more accurate is the associative recall.

data set using thresholding to obtain the closest match. Thresholding is handled electronically in this implementation; however, optical thresholding can improve the overall performance.[83,84,93] As shown in Figure 1.7, a partial input image is sufficient to generate a complete output image once a match is obtained within the database. For a more detailed discussion of associative loop technology and the architecture described above, the reader is referred to references [15,83,85,93], as well as further discussions by Paek and Psaltis.[82,84,94-97]

A data search within the associative memory can be enhanced significantly if the holographic reference pattern is rapidly changed via the single optical input. For this to remain true, feedback and thresholding must be maintained. In conjunction with solid-state hardware, a search engine of this type can be integrated into the hybrid computer architectures envisioned here. The diffraction limited performance and the high write and erase speeds associated with the excellent quantum efficiencies of these films represent key elements in the potential of this memory. The protein-based system described above provides the most efficient and cost-effective approach to developing large-scale associative processors for true artificial intelligence. Furthermore, the ability to genetically modify the protein (see section 1.6) or replace retinal with a modified chromophore analogue provides tremendous flexibility and control in enhancing the photophysical properties of the protein for such devices.[35,58,98]

1.4.3. Holographic Properties of Bacteriorhodopsin Thin Films

Bunkin and coworkers were the first to propose the use of BR in protein-based thin films as a holographic storage medium.[99] Bacteriorhodopsin has since been characterized as an efficient holographic material that exhibits significant potential in pattern recognition, optical filtering, and artificial neural networking.[39,40,57,89,100-102] Protein-based thin films are prepared by using an optically transparent polymer or polymer blend base to immobilize the PM (or BM),

thereby creating ordered protein-polymer assemblies. The thin films are tunable through the manipulation of concentration and chemical environment, genetic engineering, and read/write laser intensity, and have a resolution that is more than 5000 lines/mm.[102] Below, we discuss the holographic properties that enable BR-based thin films to be applied in associative memories.

Figure 1.9 provides a theoretical schematic describing the optical design necessary to record plane wave holograms onto a thin protein film and to read the resulting spatial light intensity distribution. This architecture is capable of recording volume transmission holograms, where the object and reference beams approach the recording medium from the same side of the film. Data recording is initiated using two identical laser beams that are derived from the same source and have a wavelength that couples sufficiently with the λ_{max} of BR (~570 nm). The two incident beams overlap at the plane of the film and are polarized perpendicular to the plane of incidence to make an angle (θ_w) with respect to the film normal. As a result of the coherence properties of emitted laser light, a three-dimensional interference pattern is recorded onto the film, which has a thickness (t) that is significantly greater than the recorded interference pattern induced by laser light. The periodic spatial light intensity distribution presented in Figure 1.9 can also be described mathematically in one dimension by

$$I(x) = (I_1 + I_2)\left[1 + V\cos\frac{2\pi x}{P}\right], \tag{1.10}$$

where I_1 and I_2 are the intensities of the individual beams, V is the contrast ratio of the interference pattern given by

$$V = \frac{2(I_1 I_2)^{1/2}}{(I_1 + I_2)}, \tag{1.11}$$

and P is the fringe spacing of the grating (see Figure 1.9), which can be calculated using

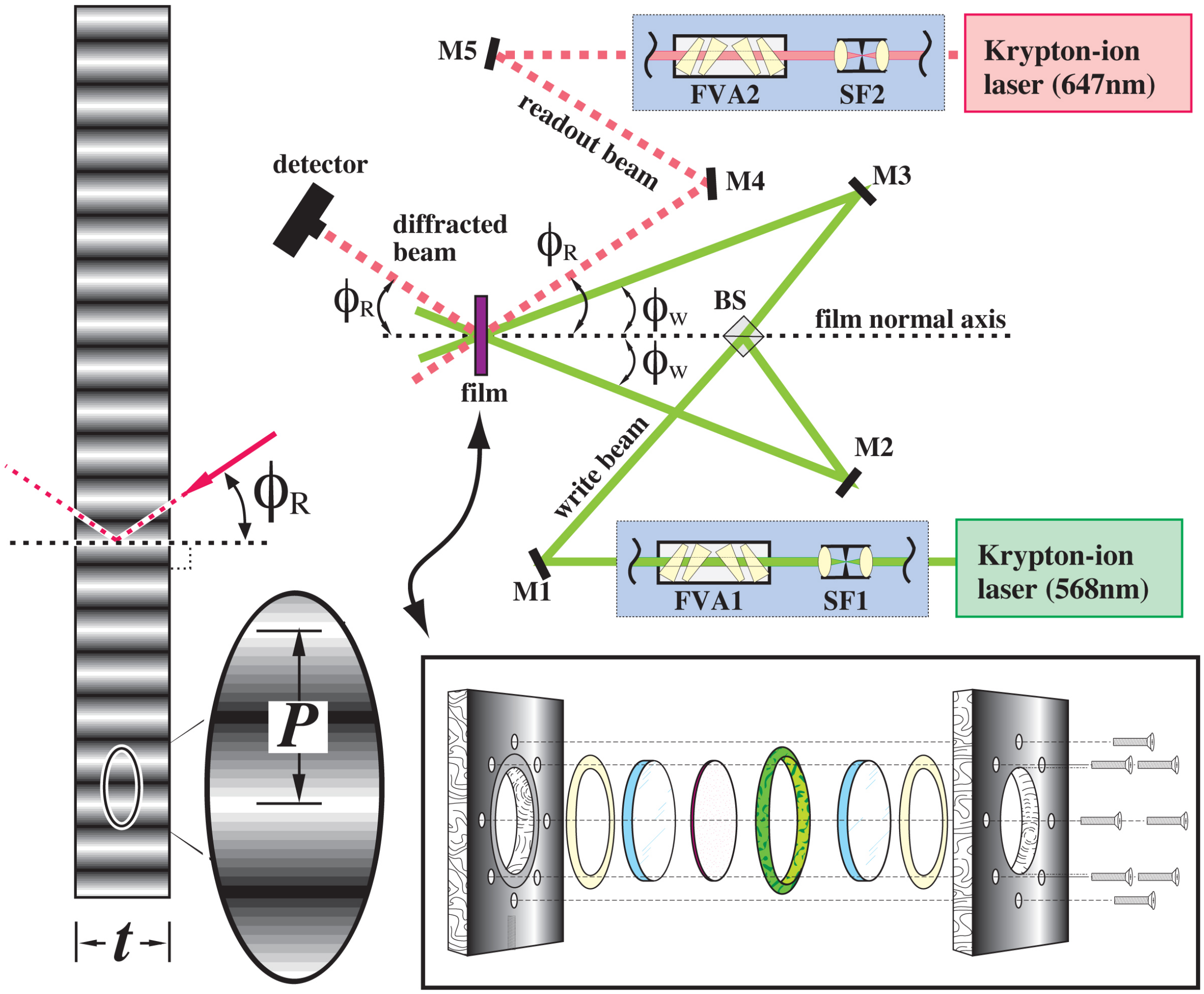

Figure 1.9. A schematic representation of the experimental set up used in writing and reading a volume transmission hologram. The volume transmission hologram (left) is representative of a BR-based thin film, wherein the dark and light lines represent regions of high (**bR**) and low (**M**) refractive index, respectively (see text). A BR hologram is written by overlapping beams derived from the same laser, and the hologram is non-destructively read using a probing beam at the Bragg angle (ϕ_R). See the text for further details on holographic properties. The inset depicts the general architecture of the formation of the BR-based thin film used in experiment. The following symbols are used: P (fringe spacing), t (film thickness), ϕ_W (writing beam angle), FVA (Fresnel variable attenuator), BS (beamsplitter), SF (spatial filter), M (mirror).

$$P = \frac{\lambda_w}{2\sin\phi_w} \quad (1.12)$$

In real-time holographic applications, the interference pattern can be defined as a periodic spatial concentration distribution of the **bR** and **M** states. The film is a recording of phase and amplitude information of the incident laser light and can be viewed as a spatial modulation of the absorption coefficients and the indices of refraction. In places of constructive interference, **bR** is driven to the **M** state and the associated volume has a lower refractive index than initially observed. Conversely, destructive interference does not initiate the photochemical reaction of BR and the relevant volumes remain in **bR** state, which has a relatively high refractive index. An accurate description of the relationship between absorption and refraction of a modulated BR thin film is achieved through the use of the Kramers-Kronig (KK) transformation.[103]

1.4.4. Application of the Kramers-Kronig Transformation

As light passes through any optically transparent medium, the material will absorb some portion of that incident light. The relationship between absorption and index of refraction (n) is fundamental to the diffraction or reconstruction processes in holographic processing applications. Thus, complex indices of refraction must be applied to accurately describe the behavior of these materials, using both real (n) and imaginary (κ) terms to indicate phase speed and loss of absorption, respectively.[88] These two terms are measured and correlated via the KK transformation.[103] The KK relation analyzes the complex index of refraction using the following integral relation:

$$\mathrm{n}(\omega) - \mathrm{n}(\omega_\infty) = \frac{2}{\pi}\mathrm{P.V.}\int_0^\infty \frac{\omega'\kappa(\omega')\mathrm{d}\omega'}{\omega'^2 - \omega^2}, \quad (1.13)$$

where κ is the absorption index, ω is the angular frequency, and P.V. is the Cauchy principal value of the succeeding improper integral. The absorption index can be related to the absorption coefficient using

$$\kappa = \frac{\alpha \mathrm{c}}{2\omega'}, \tag{1.14}$$

where α is the absorption coefficient in wavenumbers (cm^{-1}) and c is the speed of light in the centimeter-gram-second (CGS) system of units. The absorption coefficient can be linked to experimentally measured absorbance of the film by using the following equation:

$$\alpha(\lambda') = 2.3026\frac{\mathrm{A}(\lambda')}{t}, \tag{1.15}$$

where t is the thickness of the sample under investigation. Experimental absorbance can then be incorporated into Equation 1.13 to produce the following relationship:

$$\mathrm{n}(\omega) - \mathrm{n}(\omega_{\infty}) = \frac{2.3026}{2\pi^2 t}\mathrm{P.V.}\int_0^{\infty}\frac{\mathrm{A}(\lambda')\mathrm{d}\lambda'}{1-\frac{\lambda'^2}{\lambda^2}}. \tag{1.16}$$

Subsequently, this equation can be modified to include the specific photochemical conversion of interest, particularly the **bR→M** conversion observed in the transient BR photocycle or the formation of the pink membrane from the blue membrane:

$$\Delta\mathrm{n}(\lambda) = \frac{2.3026}{2\pi^2 t}\mathrm{P.V.}\int_0^{\infty}\frac{\mathrm{A_X}(\lambda') - \mathrm{A_{bR}}(\lambda')\mathrm{d}\lambda'}{1-\frac{\lambda'^2}{\lambda^2}}. \tag{1.17}$$

Here, X refers to either the **M** or **Q** states and **bR** refers to the resting state of native BR or of the BM. Figure 1.10 exhibits the overall change in refractive index of BR through a KK analysis of the **bR** and **Q** states of the BM mutant, D85E/D96Q (Figure 1.10, top) and an efficient **Q**-forming mutant, V49A (Figure 1.10, bottom). The D85E/D96Q mutant presents the highest

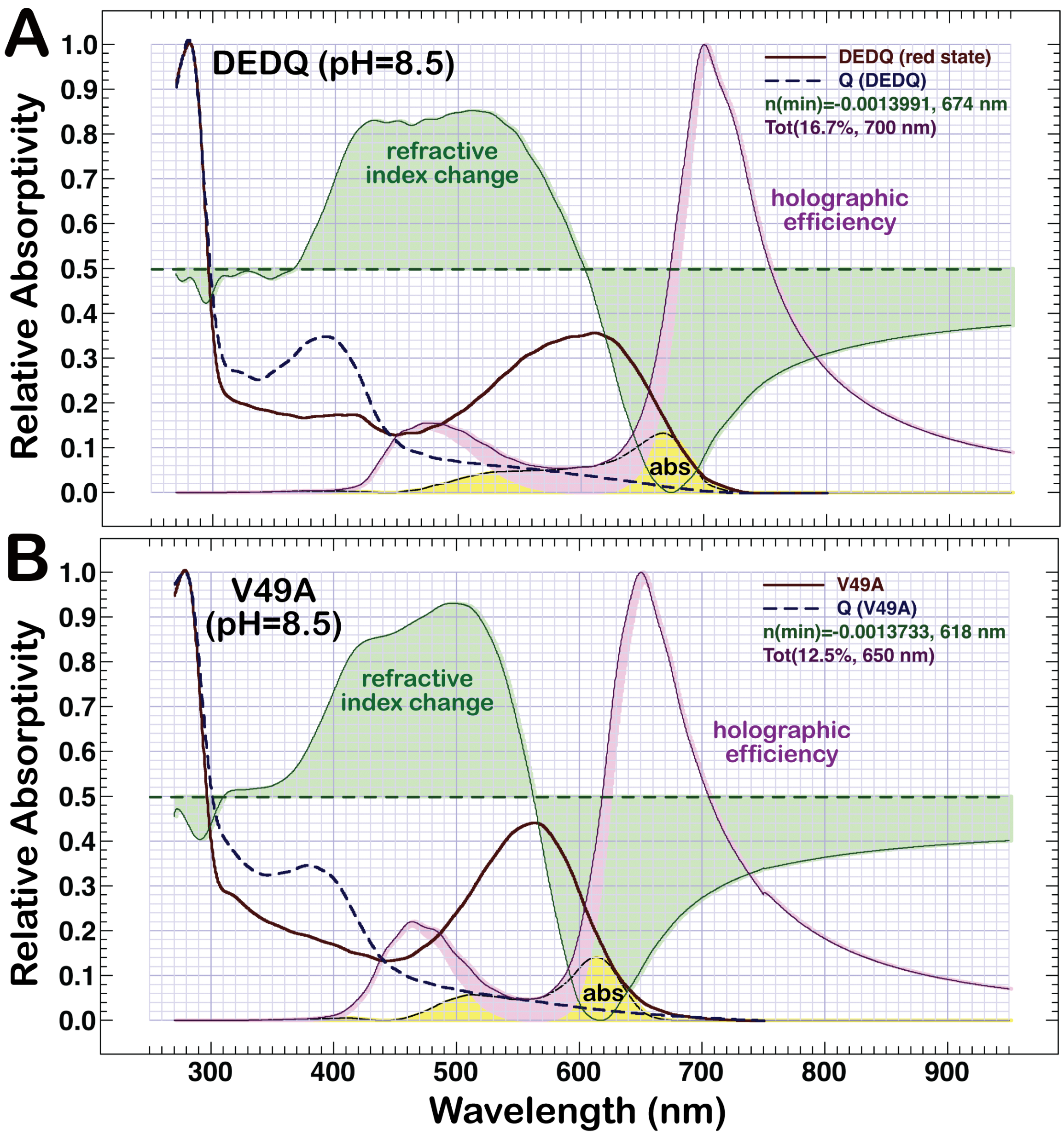

Figure 1.10. Calculated wavelength dependence of the holographic efficiency for D85E/D96Q (A) and V49A (B) BR using the Kramers-Kronig transformation and Kogelnik equations. The holographic efficiency (purple line) was calculated for 100% conversion of state 1 (**bR$_B$** or **bR**; thick red line) to state 2 (**Q**; dotted blue line) in a 0.01 cm thin film with an OD of 5 at 280 nm. A 10˚ write angle was used with a write wavelength of 532 nm. The refractive index change (shaded green line) and holographic efficiency are normalized to their maximal values. All spectra represent data collected at ambient temperature. This figure was adapted from Figure 7 from reference 104.

efficiency of any BR mutant to date (16.7%). The V49A mutant also demonstrates an improvement over that of native BR (6–8%), however, it is not as efficient as the BM mutant.[104]

1.4.5. Analysis of Diffraction Efficiency

The analysis of photodiffractive properties of volume transmission holograms has been established through Kogelnik's coupled wave theory.[105] Spatial modulations of the absorption coefficient and the index of refraction of BR thin films are described using the following truncated Fourier expansions:[83,105]

$$a(x) = a_{\text{avg}} + a_1 \cos(2\pi x / P)\,, \tag{1.18}$$

$$n(x) = n_{\text{avg}} + n_1 \cos(2\pi x / P)\,, \tag{1.19}$$

where $\alpha(x)$ and $n(x)$ are spatial dependent values, a_{avg} and n_{avg} are the average values, and a_1 and n_1 are the modulation amplitudes, all with respect to the absorption coefficient (α) and the index of refraction (n). These parameters contribute to the total diffraction of the system, with the absorption coefficient related to absorptive modulation and the index of refraction related to the phase (optical path) modulation of the light electric field amplitude.

The diffraction efficiency of a hologram stored in a BR thin film can be defined as the ratio of the diffracted light intensity, I_D, to the intensity of the reading beam, I_0. In a similar manner to the KK transformation, the diffraction efficiency has both an absorptive and a refractive component and can be explained using the following equations:[88]

$$\eta_{\text{total}} = \frac{I_D}{I_0} = \eta_{\text{abs}} + \eta_{\text{phase}}\,, \tag{1.20}$$

$$\eta_{\text{abs}} = \mathrm{D}^2 \sinh^2 \left\{ \frac{\Delta\alpha(\lambda_r)\mathrm{t}}{2\cos\phi_r} \right\} \tag{1.21}$$

$$\eta_{\text{phase}} = \text{D}^2 \sin^2 \left\{ \frac{\pi \Delta \text{n}(\lambda_\text{r})\text{t}}{\lambda_\text{r} \cos \phi_\text{r}} \right\} \tag{1.22}$$

$$\text{D} = \exp \left\{ \frac{-\alpha_{\text{ave}}(\lambda_\text{r})\text{t}}{\cos \phi_\text{r}} \right\} \tag{1.23}$$

where η_{total} is the total diffraction efficiency, η_{abs} is the diffraction efficiency due to absorption, η_{phase} is the diffraction efficiency due to refraction, *t* is the thickness of the film, λ_r is the wavelength of the read laser, and θ_r is the angle of incidence of the read laser. The read angle, θ_r, is an experimentally derived measurement that can be adjusted as needed, however, the optimal angle to achieve maximum efficiency can be found by using the Bragg condition:

$$\theta_\text{r} = \sin^{-1} \left\{ \frac{\lambda_\text{r} \sin \theta_\text{w}}{\lambda_\text{w}} \right\}, \tag{1.24}$$

where θ_w is the angle of the write beam relative to the film normal and λ_W is the wavelength of the write beam. The *a* and *n* terms in Equations 1.21 to 1.23 are related to the modulation amplitudes of the absorptive and refractive terms, respectively. The D term in the above equations is a measure of the amplitude of the spatial modulation and is included to restrict the maximum value of the absorptive component of the calculated total diffraction efficiency. This term requires that there is no spatial modulation of the refractive index, only modulation of the absorption constant. An upper limit for the amplitude of the sinusoidal modulation must be present, whereas the absorption modulation at the read wavelength is less than or equal to the average absorption. Thus, the highest diffraction efficiency for an absorption grating is of η_{abs} = 3.7%, which represents the case in which $a_1(\lambda_R)$ is equal to $a_{avg}(\lambda_R)$.[105] The η_{phase} term is entirely determined by the change of refractive index and can have diffraction efficiencies that approach

100%.[88] Therefore, devices that require diffraction efficiencies of 3.7% or higher must use phase holograms or mixed absorption and phase holograms.

1.5. Three-Dimensional Optical Memories

Many scientists and computer engineers interested in nanotechnology believe that the most likely architecture that will be used for molecular electronics and computer hardware will involve volumetric memory. Several optical architectures based on BR have been proposed in the literature, including those involving holography,[40,106-108] simultaneous two-photon,[109-111] and sequential two-photon[15,23,112] applications. Despite the variety of ways in which this architecture can be imagined, holographic media based on BR have not yet been successful due to the lack of a truly bistable **bR**/**M** system. Furthermore, simultaneous two-photon volumetric memories have shown to be problematic because of unwanted photochemistry induced by intense lasers and the subsequent need for cleanup operations.[112] The orthogonal sequential two-photon system has shown the greatest potential in recent years because the branched photocycle of BR and the presence of the long-lived **Q** state completely circumvent the major issues described above.

The sequential two-photon architecture minimizes unwanted photochemistry outside of the irradiated volume and provides a particularly straightforward parallel architecture. As discussed above, the discovery of the **P** and **Q** states add a considerable advantage to all BR-based devices with a possibility of a long-lived photoproduct other than the **bR** resting state. These devices rely on the potential for binary assignments of the two stable photoproducts, **bR** and **Q**, as bit 0 and bit 1, respectively. Because the **P** and **Q** states can only be accessed via a temporally separated dual pulse sequence, the protein operates like an optical AND gate in which data is written if and only if two conditions are satisfied. Under these terms, the two conditions

refer to the activation by a green paging laser, followed by a delay and a red data laser initiation during the **O** state of the protein (see Figure 1.2). The orthogonal laser excitation ensures that unwanted conversion to the **Q** state can be avoided in any given volume of the protein matrix. The exploitation of the photochemistry involved in driving BR to these desired photostates is based on the sequence shown in Figure 1.2, where the **K**, **L**, **M**, **N**, and **O** states are all transient intermediates within the main photocycle of the protein, and the **P** and **Q** states are intermediates in the branched photocycle. It is important to note that the **Q** state is the only photoproduct that is defined by hydrolyzed 9-*cis* retinal (i.e., retinal unbound to the protein). Figure 1.11 provides schematic representations of the write, read, and erase operations required for implementing the branched photocycle architecture, and the components of the devices are described in greater detail below.

1.5.1. Write, Read, and Erase Operations

The writing and the reading processes both start by "paging" a very thin region (~15 microns) inside the memory cuvette, initiating the photocycle in a select volume. Paging lasers must have a wavelength between 550 and 640 nm to efficiently induce photoexcitation of native BR and most BR mutants. The photocycle of native BR is over after approximately 10 ms, and it is within this window of time that the second red data laser (680 nm) must be activated orthogonally to the page to successfully write or read data within the medium. This process is ideally accomplished once the **O** state reaches a maximum concentration, at about 2-3 ms after initiation of the photocycle for native BR. If stimulation from the secondary laser is not present, the protein simply returns to the resting state in a nondestructive manner. To write data, information is spatially encoded in the incident red beam by a spatial light modulator (SLM), only orthogonally accessing your selection and completing the conversion from bit 0 to bit 1. As

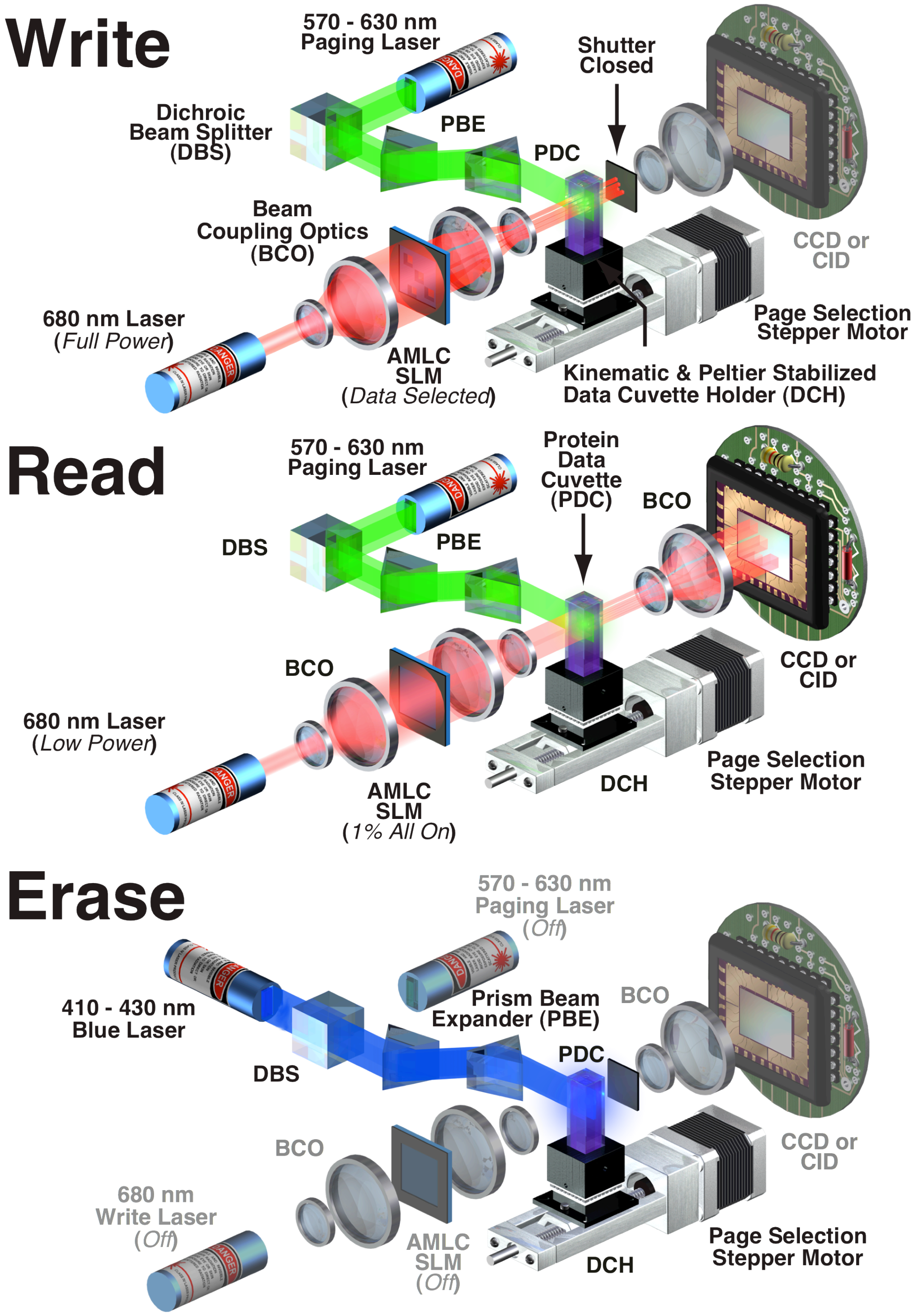

Figure 1.11. Schematic diagram of the branched photocycle three-dimensional memory. The write and read operations are illustrated in the top and center sections, respectively, and are based on a two-photon architecture in which the initiation of a paging laser is followed sequentially by an orthogonal write operation. The intensity of the data laser dictates whether bit assignments are designated or non-destructively probed. Data can then be erased, either globally or locally, by exposing the data cuvette to UV light (bottom) (adapted from Figure 12 from reference 15).

a result, volumetric pixels, or voxels, are encoded within the immobilized BR medium and remain until the erase operation is initiated.

In the center panel of Figure 1.11, the reading operation is illustrated. The first step is identical to the writing process via the paging action of the device. The difference here is that some volume in the page being probed is already written as the **Q** state, and is therefore transparent to the orthogonal paging and data beams. The page is exposed to orthogonal red light during the **O** state through data timing (DTS) and data read (DRS) shutters; however, this time the laser is fired at a much lower intensity (roughly 1% of nominal write intensity) and no SLM is used to encode information. A CCD array then images all light passing through the data cuvette. Only elements in the paged region that began in the bit 0 state cycle into the **O** state, and the CCD detector array observes differential absorptivity and the presence of bit 1. The selectivity described here allows for a reasonable signal-to-noise ratio, even with thick (1 cm) memory media containing more than 10^3 pages. The absorptivity of the **O** state within the paged region is more than 1000 times larger than the absorptivity of the remaining volume of the data cuvette, which allows for the relatively weak beam to generate a large differential signal. A protein with a photocycle of 10 ms completes one read cycle in that time, which leads to a rate of 10 megabytes per second. Each read operation must be monitored for each page in the cuvette, and a refresh operation is necessary after ~1000 reads. In practice, the three most recent pages are stored in semiconductor cache memory to reduce the number of refresh operations required.

The **P** and **Q** states can both be converted back to the **bR** resting state using blue light (~410 nm). Data erasure can be accomplished one of two ways. First, bit 1 can be converted to bit 0 by using a blue laser of coherent light with an output near 410 nm. Second, the cuvette can

be erased globally by using incoherent light in the 360 to 450 nm range. Both options are possible now with the availability of blue diode lasers at 405 nm to selectively erase pages; however, all prototypes thus far have used the global erasure option due to a decrease in complexity and expense. Figure 1.12 provides two views of a branched photocycle volumetric memory prototype. Prototype development is in its third stage and currently implements the orthogonal two-photon architecture using paging and data lasers coupled to fiber optics.

1.5.2. Efficient Algorithms for Data Processing

While the volumetric memories based on proteins offer significant advantages over traditional memories, a crucial issue remains with volumetric memories, namely, the diffraction problem. Protein-based memories require that the number of zeros and ones in the data stored be nearly the same. This issue presents an unreasonable demand for any user. To overcome this problem, many coding schemes have been proposed. One such option is to replace each zero in the data with 01 and every one with 10. In this case, the number of zeros and ones stored in the memory will be perfectly balanced. However, the memory utility (defined as the data size divided by the memory used) is only 50%. A series of coding techniques that can offer utility factors close to 100% have been proposed in references 113-118.

A common coding scheme employs novel compression algorithms (see e.g., [114,116-118]). The crucial insight here is that any data when compressed with the right algorithm tends to have nearly the same number of zeros and ones. Any efficient coding scheme should not only have a good memory utility but also the coding and decoding times should be small. Some of the coding algorithms presented in[113] are parallelizable (to run in $O(1)$ time, for example).

Volumetric protein-based memories also possess associative properties that make them ideal candidates for pattern recognition applications. In particular, we can think of protein-based

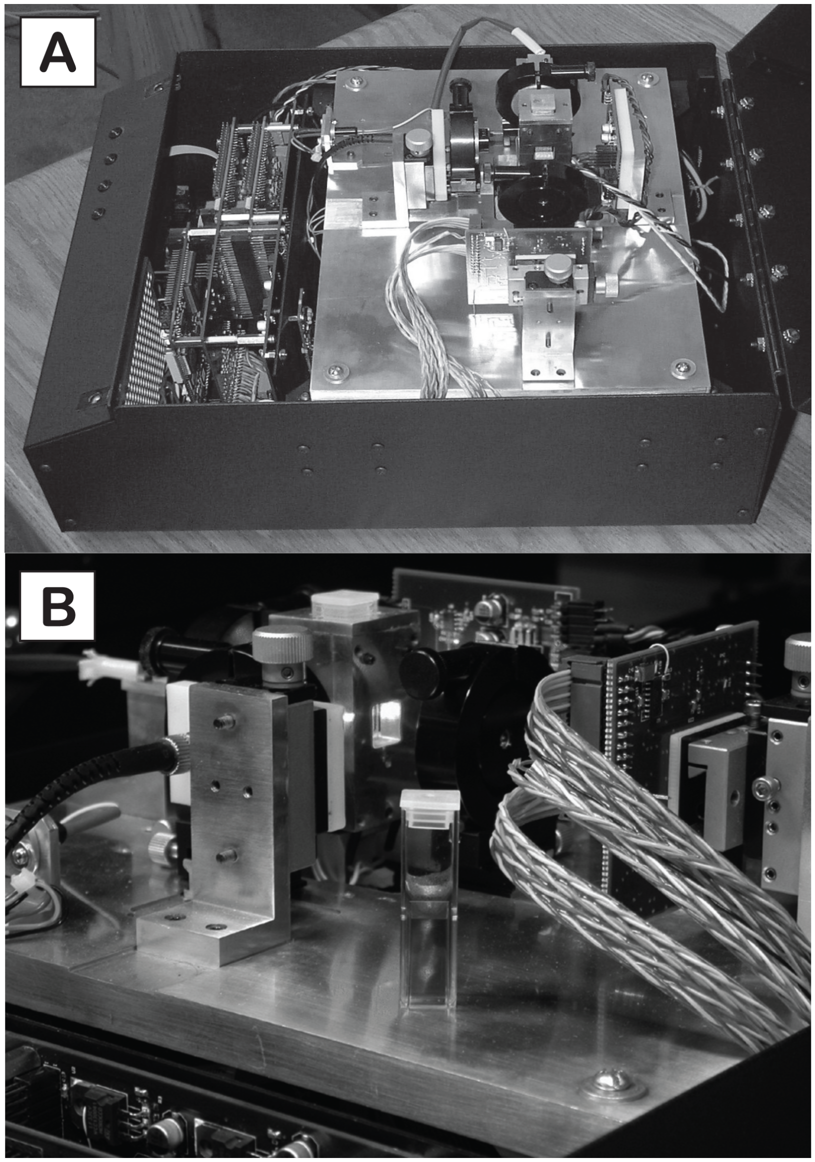

Figure 1.12. A prototype of the branched photocycle three-dimensional optical memory based on BR. This prototype currently implements the orthogonal two-photon architecture and contains paging and data lasers that are directed to the BR matrix via fiber optics (**A**). The data cuvette is placed into the cuvette holder on an x-y-z translation stage and high-speed linear actuators are employed to move the data cuvette relative to the fiber optic cables. The overall system measures 31cm x 38 cm x 23 cm. A close-up view of the optical platform is shown (**B**), with a polymer-based BR data cuvette in the foreground.

volumetric memory as a device that is capable of performing convolutions in $O(1)$ time. A computational model based on this observation has been defined as convolution-based parallel machine (CONV-PAR) in [113]. CONV-PAR is a parallel model where the convolution operation can be performed in $O(1)$ time. Through this model, it has been shown that various problems can be solved efficiently, including prefix computation, multiplying two polynomials, matrix multiplication, matrix inversion, string matching, sorting, motif search, and association rules mining. In particular, constant time algorithms have been devised for these problems. As an example, the sorting of n elements can be done in $O(1)$ time using n^2 processors, two given nxn matrices can be multiplied in $O(1)$ time using n^3 processors, and so on. Given that protein-based memories offer great parallelism, it is imperative that we develop efficient algorithms for various fundamental problems on the CONV-PAR model. Ideally, constant time algorithms will be preferred. Even when the run times are $O(1)$, it is essential to decrease the processor bounds as much as possible. For all the above problems, decreasing the processor bounds (or proving that these bounds are optimal) is an open problem. Devising better coding schemes to address the diffraction issue is also an open problem.

1.5.3. Multiplexing and Error Analysis

Polarization and gray-scale multiplexing of data in a three-dimensional memory can achieve higher storage densities of up to ten bits per voxel (Figure 1.13).[15] The importance of multiplexing for the proposed device lies in the ability to operate at or near the diffraction limit. The SLM and CCD in the prototypes are designed to provide 8-bit gray-scale capability, which is augmented to 16 bits into each voxel using polarization doubling. In practice, reliability limits and ensemble averaging permit that the writing and reading processes contain no more than 10 bits per voxel. Furthermore, the bits along the edges of the data cuvette must be allocated to

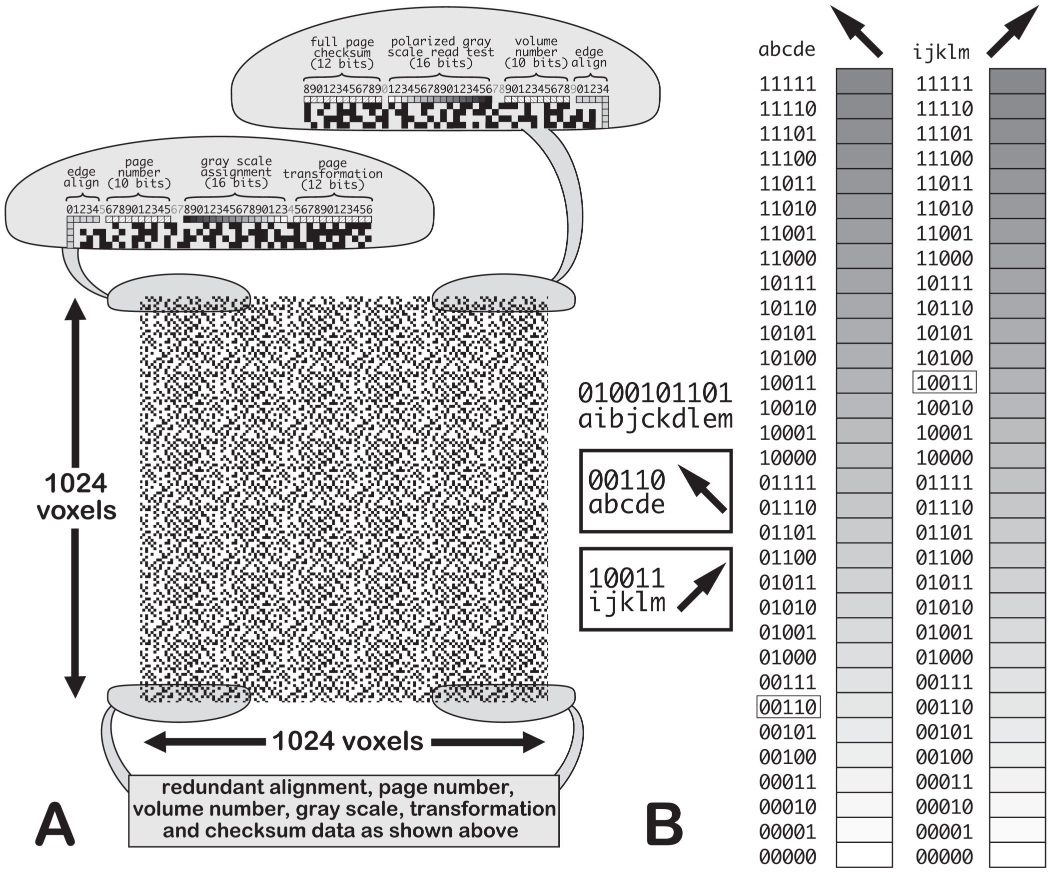

Figure 1.13. A polarization and gray scale multiplexing scheme in which each voxel can be assigned to store either a single bit or many bits of information. The current design includes voxels devoted to optical alignment, page number, volume number, gray scale, transformation, and checksum data along the edges (**A**). The multiplexing scheme envisioned here can store 10 bits per voxel, provided that two orthogonal polarizations and 16 density levels are implemented into the system (**B**) (adapted from Figure 15 from reference 15).

alignment and checksum information (Figure 1.13). With all of these features fully implemented, a standard 1 × 1 × 3 cm^3 data storage cuvette can store approximately 10 gigabytes of information, which translates into 10^4 to 10^5 protein molecules per bit for the average protein concentrations used for experimentation. This value yields a statistically relevant ensemble to compensate for potential error in the write, read, and erase operations.[13,15]

Error analysis can be carried out by measuring read histograms, which measure the separation between bit 0 and bit 1 and any overlap between the two.[15,43] A detailed discussion of error sources and error analysis for volumetric memories is beyond the scope of this chapter, and we direct the reader to Lawrence *et al*.[43] A read operation is carried out using differential absorption, which is based on a normalized scale where 0 is low intensity reaching the detector (bit 0, **O** state absorption) and 1 is high intensity reaching the detector (bit 1, **P** and **Q** state absorption). The differential read process allows the user to normalize the signals across the detector array so when no gray scaling is done, peaks are only observed at two locations (bit 0 and bit 1). When gray scaling is used, bit density increases and one observes peaks corresponding to each of the allowed levels.[15] Read errors increase the width of these peaks, which potentially creates a situation in which the peaks overlap. The overall goal is to keep such error at a level that limits the necessity of error-correcting codes within a device.

1.6. Genetic Engineering of Bacteriorhodopsin for Device Applications

Protein engineering of BR, or the design and construction of new BR mutants, is an essential process for the successful implementation of BR in biomolecular electronics. Although nature has provided a robust photoactive protein, the use of BR in applied technologies requires further enhancement of the native protein. Because the native protein is inherently stable,

mutagenesis of BR is often focused on the optimization of the photointermediates, primarily the **M** and **O** states, and the branched photoproduct, the **Q** state; however, mutagenesis of BR has also been employed to generate gold-binding BR mutants,[119,120] enhance the innate dipole moment of BR,[121] and to alter the photocycle lifetimes of the protein.[38,59]

Mutagenesis of the **M** and **Q** states is critical, particularly in holographic processors. Because the **M** state is not permanent, holograms made utilizing the **bR** to **M** state transition will only last as long as the **M** state lifetime, limiting the application of this state to real-time dynamic holography. Devices based on the **Q** state remove the time sensitive nature of holography because the **Q** state is a photoproduct of BR. Manipulation of these photostates allows for the generation of more efficient bioelectronic memory systems. In order to improve or lengthen the lifetime of the **M** state, mutagenesis usually targets residues involved in proton transfer from the intracellular milieu to the Schiff base.[35,59,98] Mutagenesis of the **Q** state is more involved because the **Q** state does not exist in nature, and is the result of a sequential two-photon event. Directed evolution (DE) has been used to improve the formation and reversion efficiencies of the **Q** state for BR for device applications.

Directed evolution, or the enhancement of a molecule toward a specific characteristic via repeated iterations of genetic mutation, screening, and differential selection, provides a cost-effective and time efficient method for the genetic and chemical manipulation of biological molecules.[122-125] The use of DE to optimize proteins is most useful when full organism selection is possible; however, organism selection is difficult to implement when a complex photochemical reaction needs to be optimized, particularly when variables such as thermal stability and pH require simultaneous enhancement.[122,125,126] Historically, DE has been used to modify the properties of enzymes for industrial and pharmaceutical applications;[127-130] however,

we implement DE to optimize the formation and reversion efficiencies of the **Q** state (Figure 1.14). In each case, a diversified genetic library is generated and screened to identify mutants with enhanced phenotypes, including efficient formation of the **Q** state. This molecular biological technique allows for the deliberate evolution of individual populations of molecules and proteins toward a specific trait.

The redesign and generation of new BR mutants is accomplished through site-directed, site-specific saturation, semi-random, and random mutagenesis. Site-directed mutagenesis (SDM) alters in the protein by strategically replacing or substituting single amino acid residues, thereby changing the structure or function of the protein. Semi-random mutagenesis (SRM) and random mutagenesis (RM) produce a large number of indiscriminant mutants through the use of doped oligonucleotides or error prone polymerase chain reaction (PCR). Lastly, site-specific saturation mutagenesis (SSSM), is a combination of SDM and SRM, and allows for the deliberate examination of multiple amino acid substitutions via the saturation of a key residue or residues at specific loci on the bacterio-opsin (*bop*) gene.

We use Type I DE to optimize the photochemical properties of BR by implementing automated screening and microgram protein characterization. In the first round of DE, mutants are generated via region-specific SRM and are screened and evaluated for altered photophysical properties, such as **M** state lifetime or **Q** state formation, using 96-well plates. Because the deliberate engineering of BR for devices requires several rounds of mutagenesis to identify a mutant that outperforms or exhibits enhanced photophysical properties, an *in-house* automated screening system was developed. At each stage in the DE process, the most efficient mutants are selected to serve as the parents to the next generation of genetic progeny, which are then produced via SDM, SSSM, and SRM. This process is reiterative and builds on successive

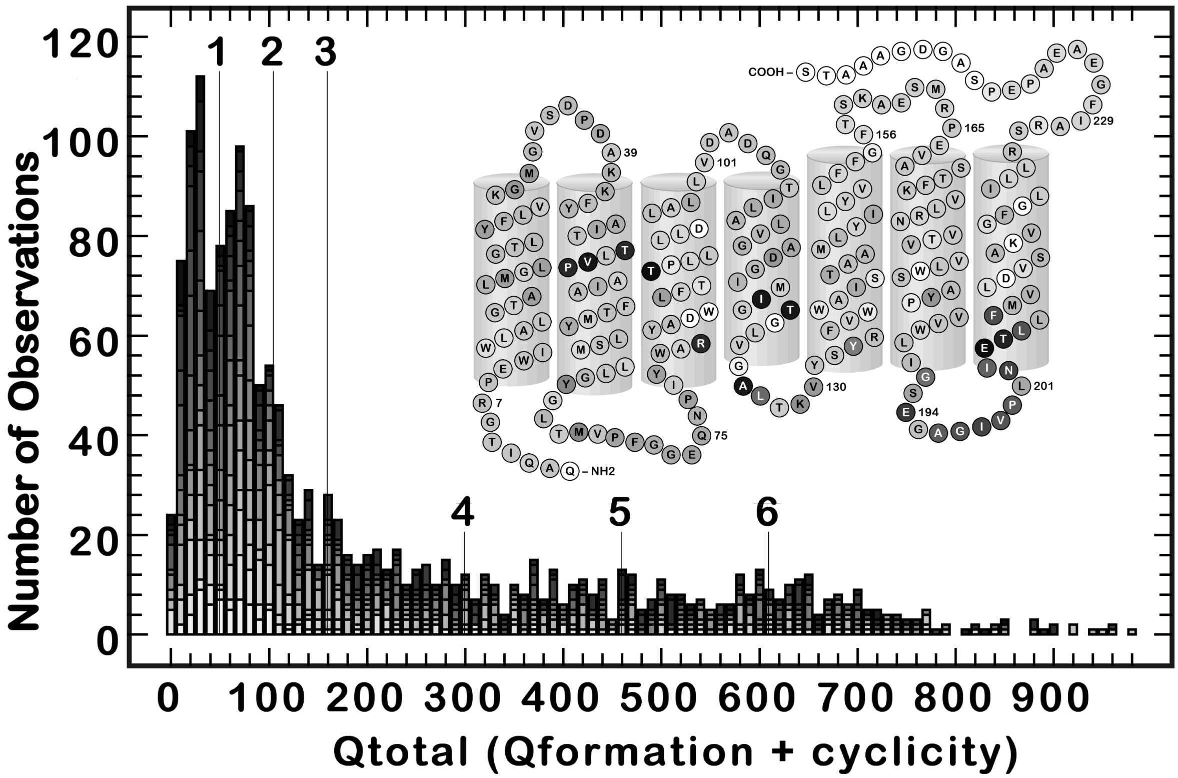

Figure 1.14. Histogram illustrating Type I directed evolution of BR to enhance the formation of the **Q** state. The vertical bars of the histogram represent the 1604 unique BR mutants that were sequenced throughout the six stages of directed evolution. The shade of the vertical bars indicate the regions of the protein that were targeted for mutagenesis, where the white bars indicate regions near the N-terminus of the protein and the black bars indicate the last region near the C-terminus. The vertical lines mark the average value of Q_{total} for each stage. The inset is a two-dimensional map of the primary sequence of native BR. Mutagenesis of the darkest residues had the most significant impact towards the enhancement of Q_{total}, while the light gray residues were less important to this enhancement. It should be noted that the shade of gray on the two-dimensional map does not correspond to the shade of the vertical bars within the histogram.

improvements to the protein. After six stages of mutagenesis, over ten thousand mutants have been generated and screened for the ability to serve in protein-based devices (Figure 1.14).

1.7. Future Directions

Bacteriorhodopsin has captured the attention of bioelectronic engineers for nearly four decades and has served as the quintessential medium for both general biophysical investigations and biomolecular device applications. In this chapter, two types of optical computing systems have been presented based on the photonic properties of BR. These architectures have been successfully implemented into numerous prototypes and address the issues central to interfacing biological molecules with inorganic materials. We envision that the first step in the evolutionary development of these technologies will be the design of hybrid computers that incorporate the best features of semiconductors and optical and molecular architectures. Limitations of the native protein have notably discouraged the development of commercially viable systems in recent years; however, advancements in random mutagenesis and directed evolution have reignited interest in implementing BR into optical memories and processors. Upon the discovery of BR mutants with enhanced photonic properties, the remaining issues lie in the development of materials capable of harnessing these proteins into electronic devices. We are currently in a third generation of prototyping and continue to improve upon the designs presented in this chapter. The prototypes will combine the past successes of architectural engineering with recent progress made using genetically engineered mutants, polarization and multiplexing schemes, and efficient algorithms to optimize these bioelectronic technologies. Molecular and semiconductor engineers have made dramatic advances in their respective fields using a wide variety of information processing media. BR and other biomolecules, however, offer a unique platform to investigate

microelectronics, holography, memory storage, artificial intelligence, and sensing while exploiting elegant natural processes like natural selection and evolution. The potential advantages of using biological materials in devices will continue to drive the development and optimization of these systems as the limitations of bulk material manipulation are approached

1.8 References

(1) Moore, G. Cramming More Components Onto Integrated Circuits. *Electronics* **1965**, *38*, 114-117.

(2) Meindl, J. D. Evolution of Solid-State Circuits: 1958-1992-20?? *IEEE ISSCC Commemorative Suppl.* **1993**, 23-26.

(3) Horowitz, M.; Alon, E.; Patil, D.; Naffziger, S.; Kumar, R.; Bernstein, K. Scaling, Power, and the Future of CMOS, Electronic Devices Meeting, Washington, DC, USA, December 5th, 2005.

(4) Esmaeilzadeh, H.; Blem, E.; St. Amant, R.; Sankaralingam, K.; Burger, D. Dark Silicon and the End of Multicore Scaling, Proceedings of the 38th International Symposium on Computer Architecture, San Jose, CA, USA, June 4–8, 2011.

(5) Vought, B. W.; Birge, R. R. Molecular Electronics and Hybrid Computers. In *Wiley Encyclopedia of Electrical and Electronics Engineering*; Webster, J. G., Ed.; Wiley-Interscience: New York, NY, USA, 1999; pp 24-37.

(6) Marcy, D. L.; Vought, B. W.; Birge, R. R. Bioelectronics and Protein-Based Optical Memories and Processors. In *Molecular Computing*; Sienko, T., Adamatzky, A., Rambidi, N. G., Conrad, M., Eds.; The MIT Press, Cambridge, MA, USA, 2003; pp 191-220.

(7) Khajetoorians, A. A.; Wiebe, J.; Chilian, B.; and Wiesendanger, R. Realizing All-Spin-Based Logic Operations Atom by Atom. *Science* **2011**, *332*, 1062-1064.

(8) Loss, D.; DiVencenzo, D. P. Quantum Computation with Quantum Dots. *Phys. Rev. A: At., Mol., Opt. Phys.* **1998**, *57*, 120-126.

(9) Keyes, R. W. Electronic Devices in Large Systems. AIP Conference Proceedings, 1992.

(10) Bandic, Z. Z. Advances in Magnetic Data Storage Technologies. *Proc. IEEE* **2008**, *96*, 1748-1753.

(11) Eleftheriou, E.; Haas, R.; Jelitto, J.; Lantz, M.; Pozidis, H. Trends in Storage Technology, Bulletin of the IEEE Computer Society Technical Committee on Data Engineering, 2008, pp 1–10.

(12) Kandel, E. R.; Schwartz, J. H.; Jessell, T. *Principles of Neural Science*; Appleton & Lange: Norwalk, CT, USA, 1991.

(13) Birge, R. R.; Lawrence, A. F.; Tallent, J. A. Quantum Effects, Thermal Statistics, and Reliability of Nanoscale Molecular and Semiconductor Devices. *Nanotechnology.* **1991**, *2*, 73-87.

(14) Hampp, N. Bacteriorhodopsin as a Photochromic Retinal Protein for Optical Memories. *Chem. Rev.* **2000**, *100*, 1755-1776.

(15) Birge, R. R.; Gillespie, N. B.; Izaguirre, E. W.; Kusnetzow, A.; Lawrence, A. F.; Singh, D.; Song, Q. W.; Schmidt, E.; Stuart, J. A.; Seetharaman, S.; Wise, K. J. Biomolecular Electronics: Protein-Based Associative Processors and Volumetric Memories. *J. Phys. Chem. B.* **1999**, *103*, 10746-10766.

(16) Qian, L.; Winfree, E.; Bruck, J. Neural Network Computation with DNA Strand Displacement Cascades. *Nature* **2011**, *475*, 368-372.

(17) Baum, E. B. Building an Associative Memory Vastly Larger Than the Brain. *Science* **1995**, *268*, 583.

(18) Laplante, J.; Pemberton, M. Experiments on Pattern Recognition by Chemical Kinetics. *J. Phys. Chem.* **1995**, *99*, 10063-10065.

(19) Hjelmfelt, A.; Weinberger, E. D.; Ross, J. Chemical Implementation of Neural Networks and Turing Machines. *Proc. Natl. Acad. Sci. U.S.A.* **1991**, *88*, 10983-10987.

(20) Stamm, U. Extreme Ultraviolet Light Sources for Use in Semiconductor Lithography - State of the Art and Future Development. *J. Phys. D: Appl. Phys.* **2004**, *37*, 3244.

(21) Wu, B.; Kumar, A. Extreme Ultraviolet Lithography: A Review. *J. Vac. Sci. Technol. B: Microelectron. Nanomet. Struct.--Process., Meas., Phenom.* **2007**, *25*, 1743.

(22) Wu, B.; Kumar, A. *Extreme Ultraviolet Lithography*; McGraw-Hill Professional, 2009.

(23) Birge, R. R. Molecular and Biomolecular Electronics. *Adv. Chem.* **1994**, *240*, 596.

(24) Ratner, M. A.; Jortner, J. *Molecular Electronics*; Blackwell Science: Oxford, England, 1997.

(25) Kuhn, H.; Forsterling, H.; Waldeck, D. H. *Principles of Physical Chemistry*; Wiley-Interscience: Hoboken, NJ, USA, 2009.

(26) Takimoto, K.; Kuroda, R.; Shido, S.; Yasuda, S.; Matsuda, H.; Eguchi, K.; Nakagiri, T. Writing and Reading Bit Arrays for Information Storage Using Conductance Change of a Langmuir-Blodgett Film Induced by Scanning Tunneling Microscopy. *J. Vac. Sci. Technol. B: Microelectron. Nanomet. Struct.--Process., Meas., Phenom.* **1997**, *15*, 1429-1431.

(27) Choi, J.; Nam, Y. S.; Fujihira, M. Nanoscale Fabrication of Biomolecular Layer and Its Application to Biodevices. *Biotechnol. Bioprocess Eng.* **2004**, *9*, 76-85.

(28) Ye, J.; Cui, H.; Ottova, A.; Tien, H. T. Interfaces, Bifaces, and Nanotechnology. *Adv. Planar Lipid Bilayers Liposomes* **2006**, *3*, 251-267.

(29) Sponsler, M. B. Hologram Switching and Erasing Strategies with Liquid Crystals. *Mol. Supramol. Photochem.* **2001**, *7*, 363-386.

(30) Qian, L.; Winfree, E. Scaling up Digital Circuit Computation with DNA Strand Displacement Cascades. *Science* **2011**, *332*, 1196-1201.

(31) Maley, C. C. DNA Computing and Its Frontiers. In *Molecular Computing*; Sienko, T., Adamatzky, A., Rambidi, N. G., Conrad, M., Eds.; The MIT Press: Cambridge, MA, USA, 2003; pp153-189.

(32) Adleman, L. M. Molecular Computation of Solutions to Combinatorial Problems. *Science* **1994**, *266*, 1021-1024.

(33) Jackson, M. B.; Sturtevant, J. M. Phase Transitions of the Purple Membranes of *Halobacterium halobium*. *Biochemistry* **1978**, *17*, 911-915.

(34) Ranaghan, M. J.; Shima, S.; Ramos, L.; Poulin, D. S.; Whited, G.; Rajasekaran, S.; Stuart, J. A.; Albert, A. D.; Birge, R. R. Photochemical and Thermal Stability of Green and Blue Proteorhodopsins: Implications for Protein-Based Bioelectronic Devices. *J. Phys. Chem. B* **2010**, *114*, 14064-14070.

(35) Hillebrecht, J. R.; Koscielecki, J. F.; Wise, K. J.; Marcy, D. L.; Tetley, W.; Rangarajan, R.; Sullivan, J.; Brideau, M.; Krebs, M. P.; Stuart, J. A.; Birge, R. R. Optimization of Protein-Based Volumetric Optical Memories and Associative Processors by Using Directed Evolution. *Nanobiotechnology* **2005**, *1*, 141-151.

(36) Hampp, N.; Popp, A.; Bräuchle, C. Diffraction Efficiency of Bacteriorhodopsin Films for Holography Containing Bacteriorhodopsin Wildtype BR and Its Variants D85E and D96N. *J. Phys. Chem.* **1992**, *96*, 4679-4685.

(37) Oesterhelt, D.; Bräuchle, C.; Hampp, N. Bacteriorhodopsin: A Biological Material for Information Processing. *Q. Rev. Biophys.* **1991**, *24*, 425-278.

(38) Bräuchle, C.; Hampp, N.; Oesterhelt, D. Optical Applications of Bacteriorhodopsin and Its Mutated Variants. *Adv. Mater.* **1991**, *3*, 420-428.

(39) Hampp, N.; Bräuchle, C.; Oesterhelt, D. Bacteriorhodopsin Wildtype and Variant Aspartate-96 to Asparagine as Reversible Holographic Media. *Biophys. J.* **1990**, *58*, 83-93.

(40) Birge, R. R. Photophysics and Molecular Electronic Applications of the Rhodopsins. *Annu. Rev. Phys. Chem.* **1990**, *41*, 683-733.

(41) Vsevolodov, N. N. *Biomolecular Electronics. An Introduction Via Photosensitive Proteins*; Birkhauser: Boston, MA, USA, 1998.

(42) Luecke, H.; Schobert, B.; Richter, H. T.; Cartailler, J. P.; Lanyi, J. K. Structure of Bacteriorhodopsin at 1.55 Å Resolution. *J. Mol. Biol.* **1999**, *291*, 899-911.

(43) Lawrence, A. F.; Stuart, J. A.; Singh, D. L.; Birge, R. R. Bit-Error Sources in 3D Optical Memory: Experiments and Models. *Proc. SPIE* **1998**, *3468*, 258-268.

(44) Lawrence, A. F.; Birge, R. R. Fundamentals of Reliability Calculations for Molecular Devices and Photochromic Memories. *Adv. Chem.* **1994**, *240*, 131-160.

(45) Oesterhelt, D.; Stoeckenius, W. Rhodopsin-Like Protein from the Purple Membrane of Halobacterium halobium. *Nature* **1971**, *233*, 149-152.

(46) Birge, R. R. Nature of the Primary Photochemical Events in Rhodopsin and Bacteriorhodopsin. *Biochim. Biophys. Acta* **1990**, *1016*, 293-327.

(47) Lanyi, J. K. Bacteriorhodopsin. *Annu. Rev. Physiol.* **2004**, *66*, 665-688.

(48) Oesterhelt, D.; Stoeckenius, W. Functions of a New Photoreceptor Membrane. *Proc. Natl. Acad. Sci. U.S.A.* **1973**, *70*, 2853-2857.

(49) Stuart, J. A.; Birge, R. R. Characterization of the Primary Photochemical Events in Bacteriorhodopsin and Rhodopsin. In *Biomembranes*; Lee, A. G., Ed.; JAI Press: London, England, 1996; Vol. 2A, pp 33-140.

(50) Zimányi, L.; Váró, G.; Chang, B.; Needleman, R.; Lanyi, J. Pathways of Proton Release in the Bacteriorhodopsin Photocycle. *Biochemistry* **1992**, *31*, 8535-8543.

(51) Balashov, S. P. Protonation Reactions and Their Coupling in Bacteriorhodopsin. *Biochim. Biophys. Acta, Bioenerg.* **2000**, *1460*, 75-94.

(52) Shen, Y.; Safinya, C. R.; Liang, K. S.; Ruppert, A. F.; Rothschild, K. J. Stabilization of the Membrane Protein Bacteriorhodopsin to 140°C in Two-Dimensional Films. *Nature* **1993**, *366*, 48-50.

(53) Lukashev, E. P.; Robertson, B. Bacteriorhodopsin Retains Its Light-Induced Proton-Pumping Function after Being Heated to 140°C. *Bioelectrochem. Bioenerg.* **1995**, *37*, 157-160.

(54) Nuss, M. C.; Zinth, W.; Kaiser, W.; Kölling, E.; Oesterhelt, D. Femtosecond Spectroscopy of the First Events of the Photochemical Cycle in Bacteriorhodopsin. *Chem. Phys. Lett.* **1985**, *117*, 1-7.

(55) Mathies, R. A.; Brito Cruz, C. H.; Pollard, W. T.; Shank, C. V. Direct Observation of the Femtosecond Excited-State Cis-Trans Isomerization in Bacteriorhodopsin. *Science* **1988**, *240*, 777-779.

(56) Subramaniam, S.; Greenhalgh, D. A.; Khorana, H. G. Aspartic Acid 85 in Bacteriorhodopsin Functions Both as Proton Acceptor and Negative Counterion to the Schiff Base. *J. Biol. Chem.* **1992**, *267*, 25730-25733.

(57) Hampp, N.; Popp, A.; Bräuchle, C.; Oesterhelt, D. Diffraction Efficiency of Bacteriorhodopsin Films for Holography Containing Bacteriorhodopsin Wildtype Br_{WT} and Its Variants BR_{D85E} and BR_{D96N}. *J. Phys. Chem.* **1992**, *96*, 4679-4685.

(58) Hampp, N.; Thoma, R.; Zeisel, D.; Bräuchle, C.; Oesterhelt, D. Bacteriorhodopsin Variants for Holographic Pattern Recognition. *Adv. Chem.* **1994**, *240*, 511-526.

(59) Hampp, N. Bacteriorhodopsin: Mutating a Biomaterial into an Optoelectronic Material. *Appl. Microbiol. Biotechnol.* **2000**, *53*, 633-639.

(60) Popp, A.; Wolperdinger, M.; Hampp, N.; Bräuchle, C.; Oesterhelt, D. Photochemical Conversion of the O-Intermediate to 9-Cis-Retinal-Containing Products in Bacteriorhodopsin Films. *Biophys. J.* **1993**, *65*, 1449-1459.

(61) Gillespie, N. B.; Wise, K. J.; Ren, L.; Stuart, J. A.; Marcy, D. L.; Hillebrecht, J.; Li, Q.; Ramos, L.; Jordan, K.; Fyvie, S.; Birge, R. R. Characterization of the Branched-Photocycle Intermediates P and Q of Bacteriorhodopsin. *J. Phys. Chem. B* **2002**, *106*, 13352-13361.

(62) Chang, C.-H.; Jonas, R.; Melchiore, S.; Govindjee, R.; Ebrey, T. G. Mechanism and Role of Divalent Cation Binding of Bacteriorhodopsin. *Biophys. J.* **1986**, *49*, 731-739.

(63) Zhang, Y. N.; Sweetman, L. L.; Awad, E. S.; El-Sayed, M. A. Nature of the Ca^{2+} Binding Sites in Ca^{2+}-Regenerated Bacteriorhodopsin. *Biophys. J.* **1992**, *61*, 1201-1206.

(64) Chang, C.-H.; Jonas, R.; Govindjee, R.; Ebrey, T. G. Regeneration of Blue and Purple Membranes from Deionized Bleached Membranes. *Photochem. Photobiol.* **1988**, *47*, 261-265.

(65) Kimura, Y.; Ikegami, A.; Stoeckenius, W. Salt and pH-Dependent Changes of the Purple Membrane Absorption Spectrum. . *Photochem. Photobiol.* **1984**, *40*, 641-646.

(66) Duñach, M.; Pardós, E.; Seigneuret, M.; Rigaud, J. On the Molecular Mechanism of the Blue to Purple Transition of Bacteriorhodopsin. UV-Difference Spectroscopy and Electron Spin Resonance Studies. *J. Biol. Chem.* **1988**, *263*, 7555-7559.

(67) Jonas, R.; Ebrey, T. G. Binding of a Single Divalent Cation Directly Correlates with the Blue-to-Purple Transition in Bacteriorhodopsin. *Proc. Natl. Acad. Sci. U.S.A.* **1991**, *88*, 149-153.

(68) Maeda, A.; Tatsuo, I.; Yoshizawa, T. Photoreaction of the Acidified Form of Bacteriorhodopsin and Its 9-cis Derivative in Purple Membrane at Low Temperatures. *Photochem. Photobiol.* **1981**, *33*, 559-565.

(69) Chang, C.-H.; Liu, S. Y.; Jonas, R.; Govindjee, R. The Pink Membrane: The Stable Photoproduct of Deionized Purple Membrane. *Biophys. J.* **1987**, *52*, 617-623.

(70) Tallent, J.; Song, Q. W.; Li, Z.; Stuart, J.; Birge, R. R. Effective Photochromic Nonlinearity of Dried Blue-Membrane Bacteriorhodopsin Films. *Opt. Lett.* **1996**, *21*, 1339-1341.

(71) Tallent, J. R.; Stuart, J. A.; Song, Q. W.; Schmidt, E. J.; Martin, C. H.; Birge, R. R. Photochemistry in Dried Polymer Films Incorporating the Deionized Blue Membrane Form of Bacteriorhodopsin. *Biophys. J.* **1998**, *75*, 1619-1634.

(72) Cladera, J.; Galisteo, M. L.; Duñach, M.; Mateo, P. L.; Padrós, E. Thermal Denaturation of Deionized and Native Purple Membranes. *Biochim. Biophys. Acta* **1988**, *943*, 148-156.

(73) Kresheck, G. C.; Lin, C. T.; Williamson, L. N.; Mason, W. R.; Jang, D.-J.; El-Sayed, M. A. The Thermal Stability of Native, Delipidated, Deionized and Regenerated Bacteriorhodopsin. *J. Photochem. Photobiol., B* **1990**, *7*, 289-302.

(74) Mogi, T.; Stern, L. J.; Marti, T.; Chao, B. H.; Khorana, H. G. Aspartic Acid Substitutions Affect Proton Translocation by Bacteriorhodopsin. *Proc. Natl. Acad. Sci. U.S.A.* **1988**, *85*, 4148-4152.

(75) Millerd, J. E.; Rohrbacher, A.; Brock, N. J.; Chau, C.-K.; Smith, P.; Needleman, R. Improved Sensitivity in Blue-Membrane Bacteriorhodopsin Films. *Opt. Lett.* **1999**, *24*, 1355-1357.

(76) Turner, G. J.; Miercke, L. J. W.; Thorgeirsson, T. E.; Kliger, D. S.; Betlach, M. C.; Stroud, R. M. Bacteriorhodopsin D85N: Three Spectroscopic Species in Equilibrium. *Biochemistry* **1993**, *32*, 1332-1337.

(77) Tittor, J.; Schweiger, U.; Oesterhelt, D.; Bamberg, E. Inversion of Proton Translocation in Bacteriorhodopsin Mutants D85N, D85T, and D85,96N. *Biophys. J.* **1994**, *67*, 1682-1690.

(78) Liu, S. Y.; Ebrey, T. G. The Quantum Efficiency for the Interphotoconversion of the Blue and Pink Forms of Purple Membrane. *Photochem. Photobiol.* **1987**, *46*, 263-267.

(79) Ohtani, H.; Kobayashi, T.; Iwai, J.; Ikegami, A. Picosecond and Nanosecond Spectroscopies of the Photochemical Cycles of Acidified Bacteriorhodopsin. *Biochemistry* **1986**, *25*, 3356-3363.

(80) Fischer, U. C.; Towner, P.; Oesterhelt, D. Light Induced Isomerization, at Acidic Ph, Initiates Hydrolysis of Bacteriorhodopsin to Bacterio-Opsin and 9-cis-Retinal. *Photochem. Photobiol.* **1981**, *33*, 529-537.

(81) Downie, J. D.; Timuçin, D. A.; Smithey, D. T.; Crew, M. Long Holographic Lifetimes in Bacteriorhodopsin Films. *Opt. Lett.* **1998**, *23*, 730-732.

(82) Paek, E. G.; Jung, E. C. Simplified Holographic Associative Memory Using Enhanced Nonlinear Processing with a Thermoplastic Plate. *Opt. Lett.* **1991**, *16*, 1034-1036.

(83) Birge, R. R.; Parsons, B.; Song, Q. W.; Tallent, J. R. Protein-Based Three-Dimensional Memories and Associative Processors. In *Molecular Electronics*; Ratner, M. A., Jortner, J., Eds.; Blackwell Science Ltd.; Oxford, England, 1997; pp 439-471.

(84) Paek, E. G.; Psaltis, D. Optical Associative Memory Using Fourier Transform Holograms. *Opt. Eng.* **1987**, *26*, 428-433.

(85) Stuart, J. A.; Marcy, D. L.; Wise, K. J.; Birge, R. R. Biomolecular Electronic Device Applications of Bacteriorhodopsin. In *Molecular Electrtonics: Bio-Sensors and Bio-Computers*; Barsanti, L., Ed.; Kluwer Academic Publishers: The Netherlands, 2003; pp 265-299.

(86) Psaltis, D.; Park, C. H.; Jong, J. Higher Order Associative Memories and Their Optical Implementations. *Neural Networks* **1988**, *1*, 149-163.

(87) Soffer, B. H.; Dunning, G.; Owechko, Y.; Marom, E. Associative Holographic Memory with Feedback Using Phase-Conjugate Mirrors. *Opt. Lett.* **1986**, *11*, 118-120.

(88) Gross, R. B.; Izgi, K. C.; Birge, R. R. Holographic Thin Films, Spatial Light Modulators, and Optical Associative Memories Based on Bacteriorhodopsin. *Proc. SPIE* **1992**, *1662*, 186-196.

(89) Birge, R. R.; Fleitz, P. A.; Gross, R. B.; Izgi, J. C.; Lawrence, A. F.; Stuart, J. A.; Tallent, J. R. Spatial Light Modulators and Optical Associative Memories Based on Bacteriorhodopsin. *Proc. IEEE EMBS* **1990**, *12*, 1788-1789.

(90) Haxby, J. V.; Hoffman, E. A.; Gobbini, M. I. Human Neural Systems for Face Recognition and Social Communication. *Biol. Psychiatry* **2002**, *51*, 59-67.

(91) Zhao, W.; Chellappa, R.; Phillips, P. J.; Rosenfeld, A. Face Recognition: A Literature Survey. *Acm Computing Surveys (CSUR)* **2003**, *35*, 399-458.

(92) Turk, M. A.; Pentland, A. P. Face recognition Using Eigenfaces. Proceedings of the Conference on Computer Vision and Pattern Recognition; 1991, pp 586-591.

(93) Gross, R. B.; Izgi, K. C.; Birge, R. R. Holographic Thin Films, Spacial Light Modulators, and Optical Associative Memories Based on Bacteriorhodopsin. *Proc. SPIE* **1992**, *1662*, 186-196.

(94) Psaltis, D.; Brady, D.; Wagner, K. Adaptive Optical Networks Using Photorefractive Crystals. *Appl. Opt.* **1988**, *27*, 1752-1759.

(95) Psaltis, D.; Neifeld, M. A.; Yamamura, A. Image Correlators Using Optical Memory Disks. *Opt. Lett.* **1989**, *14*, 429-431.

(96) Psaltis, D.; Brady, D.; Guang, X.; Lin, S. Holography in Artificial Neural Networks. *Science* **1990**, *343*, 325-330.

(97) Psaltis, D.; Neifeld, M. A.; Yamamura, A.; Kobayashi, S. Optical Memory Disks in Optical Information Processing. *Appl. Opt.* **1990**, *29*, 2038-2057.

(98) Wise, K. J.; Gillespie, N. B.; Stuart, J. A.; Krebs, M. P.; Birge, R. R. Optimization of Bacteriorhodopsin for Bioelectronic Devices. *Trends Biotechnol.* **2002**, *20*, 387-394.

(99) Bunkin, F. V.; Vsevolodov, N. N.; Druzhko, A. B.; Mitsner, B. I.; Prokhorov, A. M.; Savranskii, V. V.; Tkachenko, N. W.; Shevchenko, T. B. Diffraction Efficiency of Bacteriorhodopsin and Its Analogs. *Sov. Tech. Phys. Lett.* **1981**, *7*, 630-631.

(100) Bazhenov, V. Y.; Soskin, M. S.; Taranenko, V. B. Holographic Recording by Continuous Illumination in a Suspension of Purple Membranes of Halobacteria. *Sov. Tech. Phys. Lett.* **1987**, *13*, 382-384.

(101) Thoma, R.; Hampp, N.; Bräuchle, C.; Oesterhelt, D. Bacteriorhodopsin Films as Spatial Light Modulators for Nonlinear Optical Filtering. *Opt. Lett.* **1991**, *16*, 651-653.

(102) Renner, T.; Hampp, N. Bacteriorhodopsin-Films for Dynamic Time Average Interferometry. *Opt. Commun.* **1992**, *96*, 142-149.

(103) Loudon, R. *The Quantum Theory of Light*; Clarendon: Oxford, England, 1973.

(104) Ranaghan, M. J.; Greco, J. A.; Wagner, N. L.; Grewal, R.; Rangarajan, R.; Koscielecki, J. F.; Wise, K. J.; Birge, R. R. Photochromic Bacteriorhodopsin Mutant with High Holographic Efficiency and Enhanced Stability via a Putative Self-Repair Mechanism. *ACS Appl. Mater. Interfaces* **2014**, *6*, 2799-2808.

(105) Kogelnik, H. Coupled Wave Theory for Thick Hologram Gratings. *Bell Syst. Tech. J.* **1969**, *48*, 2909-2947.

(106) d'Auria, L.; Huignard, J. P.; Slezak, C.; Spitz, C. Experimental Holographic Read-Write Memory Using 3-D Storage. *Appl. Opt.* **1994**, *13*, 808-818.

(107) Heanue, J. F.; Bashaw, M. C.; Hesselink, L. Volume Holographic Storage and Retrieval of Digital Data. *Science* **1994**, *265*, 749-752.

(108) Psaltis, D.; Pu, A. Holographic 3-D Disks. *IEEE Nonvol. Mem. Tech. (INVMTC)* **1996**, *6*, 34-39.

(109) Parthenopoulos, D. A.; Rentzepis, P. M. Three-Dimensional Optical Storage Memory. *Science* **1989**, *245*, 428-433.

(110) Chen, Z.; Govender, D.; Gross, R.; Birge, R. R. Advances in Protein-Based Three-Dimensional Memories and Associative Processors. *BioSystems* **1995**, *35*, 145-151.

(111) Dvornikov, A. S.; Rentzepis, P. M. 3D Optical Memory Devices. System and Materials Characteristics. *IEEE Nonvol. Mem. Tech. (INVMTC)* **1996**, *6*, 40-44.

(112) Stuart, J. A.; Marcy, D. L.; Wise, K. J.; Birge, R. R. Volumetric Optical Memory Based on Bacteriorhodopsin. *Syth. Met.* **2002**, *127*, 3.

(113) Rajasekaran, S.; Kundeti, V.; Birge, R. R.; Kumar, V.; Sahni, S. Efficient Algorithms for Computing with Protein-Based Volumetric Memory Processors. *IEEE Trans. Nanotechnol.* **2011**, *10*, 881-890.

(114) Trinca, D.; Rajasekaran, S. Specialized Compression for Coping with Diffraction Effects in Protein-Based Volumetric Memories: Solving Some Challenging Instances. *J. Nanoelectron. Optoelectron.* **2010**, *5*, 290-294.

(115) Trinca, D.; Rajasekaran, S. Coping with Diffraction Effects in Protein-Based Computing through a Specialized Approximation Algorithm with Constant Overhead. Proceedings IEEE NANO, Seoul, Korea, August 17-20, 2010.

(116) Trinca, D.; Rajasekaran, S. Using a Specialized Compression Scheme Based on Antidictionaries for Coping with Diffraction Effects in Protein-Based Computing. Proceedings of the 14th International Biotechnology Symposium and Exhibition, Rimini, Italy, September 14-18, 2010.

(117) Trinca, D.; Rajasekaran, S. Optimized Bzip2 Compression for Reducing Diffraction Effects in Protein-Based Computing: A Study of Feasibility. Proceedings of the 31st Annual International IEEE EMBS COnference, Minneapolis, MN, USA, September 2-6, 2009.

(118) Kundeti, V.; Rajasekaran, S. Generalized Algorithms for Generating Balanced Modulation Codes in Protein-Based Volumetric Memories. Proceedings of the 10th Annual IEEE Congress on Evolutionary Computation (IEEE CEC), Norway, May 18-21, 2009.

(119) Brizzolara, R. A.; Boyd, J. L.; Tate, A. E. Evidence for Covalent Attachment of Purple Membrane to a Gold Surface via Genetic Modification of Bacteriorhodopsin. *J. Vac. Sci. Technol. A* **1997**, *15*, 773-778.

(120) Schranz, M.; Noll, F.; Hampp, N. Oriented Purple Membrance Monolayers Covalently Attached to Gold by Multiple Thiole Linkages Analyzed by Single Molecule Force Spectroscopy. *Langmuir* **2007**, *23*, 11134-11138.

(121) Hsu, K. C.; Rayfield, G. W.; Needleman, R. Reversal of the Surface Charge Asymmetry in Purple Membrane Due to Single Amino Acid Substitutions. *Biophys. J.* **1996**, *70*, 2358-2365.

(122) Arnold, F. H. Design by Directed Evolution. *Accts. Chem. Res.* **1998**, *31*, 125-131.

(123) Arnold, F. H.; Volkov, A. A. Directed Evolution of Biocatalysts. *Curr. Opin. Chem. Biol.* **1999**, *3*, 54-59.

(124) Schmidt-Dannert, C.; Arnold, F. H. Directed Evolution of Industrial Enzymes. *Trends Biotechnol.* **1999**, *17*, 135-136.

(125) Jackel, C.; Kast, P.; Hilvert, D. Protein Design by Directed Evolution. *Annu. Rev. Biophys.* **2008**, *37*, 153-173.

(126) Jackel, C.; Bloom, J. D.; Kast, P.; Arnold, F. H. Consensus Protein Design without Phylogenetic Bias. *J. Mol. Biol.* **2010**, *399*, 541-546.

(127) Yano, T.; Oue, S.; Kagamiyama, H. Directed Evolution of an Aspartate Aminotransferase with New Substrate Specificities. *Proc. Natl. Acad. Sci. U.S.A.* **1998**, *95*, 5511-5515.

(128) Miyazaki, K.; Wintrode, P. L.; Grayling, R. A.; Rubingh, D. N.; Arnold, F. H. Directed Evolution Study of Temperature Adaptation in a Psychrophilic Enzyme. *J. Mol. Biol.* **2000**, *297*, 1015-1026.

(129) Moore, J. C.; Arnold, F. H. Directed Evolution of a Para-Nitrobenzyl Esterase for Aqueous-Organic Solvents. *Nat. Biotechnol.* **1996**, *14*, 458-467.

(130) Spiller, B.; Gershenson, A.; Arnold, F. H.; Stevens, R. C. A Structural View of Evolutionary Divergence. *Proc. Natl. Acad. Sci. U.S.A.* **1999**, *96*, 12305-12310.

Chapter 2

Enhancing the Sequential Two-Photon Branching Reaction in Bacteriorhodopsin by Using the V49A Mutation: Characterization and Application in a Protein-Based Retinal Implant

2.0. Abstract

Retinal degenerative diseases are characterized by the loss of photoreceptor cells within the retina and affect 30-50 million people worldwide. Despite the availability of treatments that slow the progression of degeneration, affected patients will go blind. Thus, there is a significant need for a prosthetic that is capable of restoring functional vision for these patients. The protein-based retinal implant offers a high-resolution option for replacing the function of diseased photoreceptor cells by interfacing with the underlying retinal tissue, stimulating the remaining neural network, and transmitting this signal to the brain. The retinal implant uses the photoactive protein, bacteriorhodopsin, to generate an ion gradient in the subretinal space that is capable of activating the remaining bipolar and ganglion cells within the retina. Bacteriorhodopsin can also be photochemically driven to an active (**bR**) or inactive (**Q**) state, and we aim to exploit this photochemistry to mediate the activity of pixels within the retinal implant. Formation of the **Q** state is achieved by using a sequential two-photon process. These **bR** and **Q** states are shown to operate as a binary medium for data storage and manipulation when designated as bit 0 and bit 1, respectively, and we now aim to implement this photochemistry into the retinal prosthetic. However, the native protein only allows minimal access to the branched photocycle, which precludes the successful implementation of the protein in such technologies. In a recent study, directed evolution is used to optimize the formation and reversion efficiencies of the **Q** state by using an automated screening procedure. As a result, over 10,000 mutants are analyzed after six generations of optimization, and more than ten new protein mutants are discovered with superior **Q** state photochemistry, including the best mutant, V49A/I119T/T121S/A126T. The single mutation, V49A, is also revealed as a comparable **Q** state mutant, and in this investigation, we employ a photochemical and photophysical analysis to elucidate the key properties that enhance

the ability to form and revert the branched photocycle. V49A is capable of complete conversion to the **Q** state at alkaline pH, while also maintaining equivalent thermal and photochemical stability to native BR. The pH environment of V49A plays significant role in the efficiency of the desired photochemistry. Absolute and time-resolved absorption spectroscopy are used to describe the pH dependence, which results from the alteration of the pK_as of three amino acids that are important to the proton translocation pathway. Furthermore, the chromophore binding site is analyzed using chromophore extractions and Fourier transform infrared spectroscopy, and the role of V49A in the quadruple mutant is discussed. In this study, we also use a novel retinomorphic foveated image sensor to characterize the formation of active and inactive pixels within a protein-based retinal implant, and measure a significant difference between the output frequencies associated with the **bR** and **Q** states.

2.1 Introduction

2.1.1. Protein-Based Retinal Implants

Retinal degenerative diseases, including retinitis pigmentosa (RP) and age-related macular degeneration (AMD), involve the irreversible degeneration of the retinal photoreceptor cells.[1,2] These diseases cause the layer of light sensing cells in the eye to degenerate over time, however, a significant portion of the underlying retinal tissue that transmits visual information to the brain remains largely intact.[2-4] The resulting loss of vision causes a significant decline in the quality of life for those affected. Retinitis pigmentosa, the most common of the inherited retinal degenerative disorders, affects approximately 1.5 million people worldwide and can affect people of all ages.[5,6] Age-related macular degeneration is the leading cause of irreversible blindness among the elderly and is estimated to affect approximately 30 million people globally.[7,8] There are currently no cures for patients with RP or AMD, and all available treatments only slow progression, are limited in effectiveness, and ultimately fail to prevent permanent loss of vision. Thus, there is a significant need for a therapy or prosthetic capable of restoring functional vision to RP and AMD patients.

Many new biotechnologies and treatments for blindness resulting from retinal degeneration have been developed during the past decade. While these treatments are still in their infancy and are limited by inherent drawbacks, a number of diverse approaches are currently under investigation in order to achieve a cure for diseases like RP and AMD. Novel and emerging approaches to treat retinal degeneration include stem cell tissue transplants,[9-14] gene therapies,[15-17] and optogenetic technologies.[18-24] Despite the promise of these treatments in design and preliminary efficacy, these biotechnologies are still under development and are now undergoing early animal trials. Currently, intraocular and periocular injections and nutritional drug

supplements are treatment that show success in slowing the progression of degeneration, however, limited efficacy is observed and the treated patient will eventually go blind.[8,25,26] Electrode-based retinal prostheses, which currently represents the most common type of replacement of lost photoreceptor cells, are being designed, developed, and commercialized in an effort to replace the function of the damaged photoreceptor cell layer within the retina. These retinal implants generally utilize an external apparatus to capture an image, convert that image into electrical signals, and stimulate the remaining neural circuitry within the degenerated retina. It has long been demonstrated that electrical stimuli can initiate the visual cascade when delivered in the extracellular domain of a retinal neuron.[27] Retinal implant architectures that exploit this electrical stimulation have seen some promise, and a number of companies and academic groups have demonstrated efficacy in the clinical setting, including efforts by Second Sight,[28-30] Retinal Implant AG,[31-35] and the Epi-Ret 3 team.[36-38]

Of particular significance is the prosthetic developed by Second Sight, which continues to be at the forefront of retinal prosthetic development and commercialization. The Argus II, developed by Second Sight,[28-30] is the first approved retinal prosthetic for clinical trials in both the US and Europe, and is currently the only approved implant on the market. The design of the electrode-based implant consists of a 60-electrode array placed in an epiretinal position. The Argus II has been implanted into ~80 patients with RP, and the patients are capable of detecting some motion and performing simple mobility tasks.[30] However, these retinal prosthetics have intrinsic shortcomings.[39] First, replicating the spatiotemporal patterns of the neurosensory network with electrode arrays is a challenge.[40] This problem is exacerbated by the low resolution associated with the electrode arrays, resulting in limited ability to detect simple direction of motion through high contrast, black and white gradients.[28,41] Secondly, because the implant

contains transscleral cables that penetrate the eye, the risk of infection is high and a number of serious adverse effects were observed in as many as 9 out of 30 patients, including conjunctival erosion, endophthalmitis, and hypotony.[29,42] Furthermore, implantation requires laborious, complex surgery, and thereby limits adoption by the vitreoretinal surgeon community.[39,43] According to lead researchers in the field, there is still a significant need for a device of higher resolution that also mitigates the risk of surgical complications.

The protein-based retinal implant offers unique solutions to the inherent shortcomings demonstrated in current electrode-based retinal prosthetics.[44] The retinal implant architecture is manufactured via a bottom-up approach and is comprised of multiple layers of the light-activated proton pump, bacteriorhodopsin (BR), oriented on a flexible, ion-permeable membrane *via* layer-by-layer (LBL) electrostatic adsorption.[45] The high-resolution, subretinal implant converts light energy into an ion gradient that is capable of stimulating the remaining neural circuitry of the degenerated retina (Figure 2.1).[44] Like the electrode-based technologies, the protein-based prosthetic relies on the presence of the inner retinal tissue (i.e., intact bipolar and ganglion cells) in order to convert absorbed light energy into an electrochemical gradient that is interpreted by the brain as meaningful visual perception. The small and flexible protein-based retinal implant is a standalone prosthetic, which is capable of responding only to incident light without the influence of external devices that penetrate or communicate through the ocular tissue.

The optical resolution of the implant is comparable to that of native photoreceptors due to the nanometer-scale features of the protein and the molecular packing of the biomaterials within the implant structure. Moreover, the unique photochemistry of the protein can be used to calibrate the retinal implant by modulating the active pixel area relative to the extent of retinal degeneration.[46] Every patient that suffers from these diseases demonstrates a unique rate and

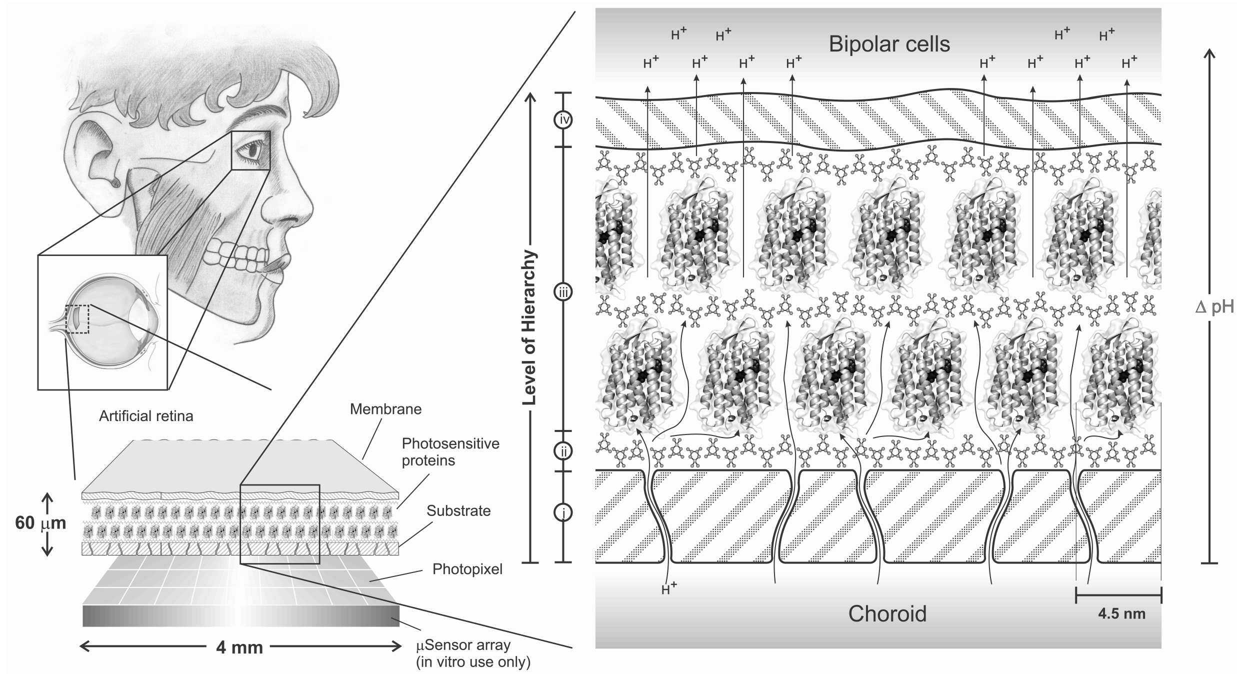

Figure 2.1. Architecture and application of the proposed protein-based retinal implant (or artificial retina). The implant acts as a subretinal implant located below the retinal tissue in place of degenerated photoreceptor cells. The implant consists of two ion-permeable membranes, depicted as (i) and (iv) in the RHS close up, with multilayers of the photosensitive protein, bacteriorhodopsin, contained between them. A polycation (ii) permits the deposition of alternating layers of the protein and polycation (iii) through a layer-by-layer electrostatic adsorption process. The orientation of the implant permits the generation of an H^+ gradient towards the remaining neural network of the retina. This novel approach of stimulating the intact bipolar cells mimics the native phototransduction cascade initiated by healthy photoreceptor cells. A photopixel microsensor array (bottom LHS image) was used in this study to examine the photoactive state of the bacteriorhodopsin *in vitro*, but is not a part of the prosthetic.

pattern of degeneration. As we will see below, BR is capable of forming a photoproduct (the **Q** state) that prevents the native proton pumping mechanism (the **bR** state). Areas of the retina with high retinal degeneration are targeted with active pixels in the **bR** state, which facilitates ion-mediated stimulation. Deactivation of pixels through the formation of **Q** prevents interference with functional clusters of photoreceptor cells. We envision that pixels could be selectively driven to the **Q** state following implantation and, subsequently, driven back to the **bR** state when degeneration has progressed in that region.

2.1.2. Bacteriorhodopsin

The protein-based retinal implant architecture harnesses the inherent pumping capability of BR, a feature necessary for the survival of the native organism, to generate a macroscopic ion gradient for retinal stimulation. Bacteriorhodopsin is a 26-kDa photoactive protein found in the outer membrane of the halophilic *archaeon*, *Halobacterium salinarum*.[47,48] When the concentration of oxygen is insufficient to sustain growth *via* respiration (i.e., ATP generation by oxidative phosphorylation),[47,48] BR is expressed within a two-dimensional crystalline lattice of trimers, known as the purple membrane.[49,50] Upon the absorption of a photon by the protein-bound chromophore, all-*trans* retinal, BR transports a proton from the intracellular domain to the extracellular milieu *via* a series of transient photochemical intermediates, known as the photocycle (Figure 2.2).[51] The net translocation of a proton generates a proton gradient, thereby driving cellular ATPase to synthesize ATP under anaerobic conditions.[47]

The proton pumping mechanism initiated by the absorption of a photon by the retinal chromophore of BR is one of the most efficient and well-understood photochemical reactions found in nature. The high quantum efficiency (Φ) of this reaction (~65%) is identical to that of the visual pigment, rhodopsin, which is found in the photoreceptor cells of the human retina.[52,53]

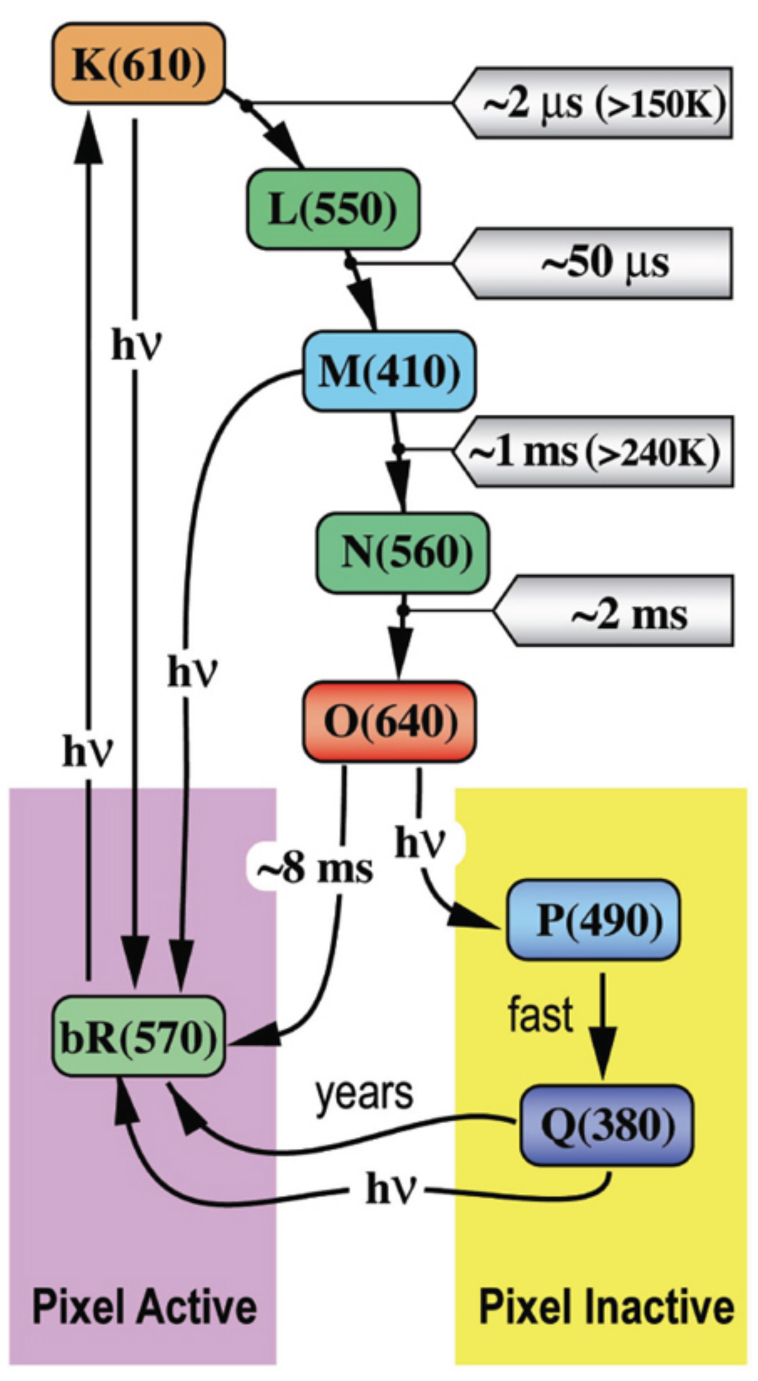

Figure 2.2. The main and branched photocycles of light adapted BR (**bR**). Upon the absorption of a single photon, the protein cycles through a series of transient intermediates (**K**, **L**, **M**, **N**, and **O**) and subsequently returns to the **bR** resting state. In order to access the branched photocycle (the **P** and **Q** states), a second photon must be absorbed to photochemically convert the **O** state to **P**. The resulting **Q** state is stable for several years at physiological temperature. The purple and yellow boxes also highlight the states in which the pixels within a retinal implant would be active or inactive, respectively. This figure is based on Figure 1 from reference 52.

Moreover, BR is a natural candidate for biophotonic devices due to a remarkable thermal stability and photochemical efficiency. Bacteriorhodopsin has a melting temperature in excess of 80 °C,[54] and has an observed photochemical cyclicity that exceeds 10^6 photocycles before a 37% loss of the irradiated ensemble.[55-57] Because BR is capable of withstanding high fluctuations in temperature, light flux, and chemical stress from a self-induced pH gradient, the biomaterial has been implemented as the photoactive medium in a number of devices for several decades.[58,59]

2.1.3. Bacteriorhodopsin Photocycle and Proton Translocation

The BR photocycle consists of a series of stepwise reactions that are concomitant with the thermal pathway towards reisomerization of 13-*cis* retinal to the initial all-*trans* conformation. The main photocycle is initiated by the absorption of a photon during the **bR** (resting) state and the resulting reaction sequence can be described as $\mathbf{bR} \rightarrow \mathbf{K} \leftrightarrow \mathbf{L} \leftrightarrow \mathbf{M_1} \leftrightarrow \mathbf{M_2} \leftrightarrow \mathbf{N} \leftrightarrow \mathbf{O} \rightarrow \mathbf{bR}$. Each of the well-characterized photointermediates, which have been described by numerous spectroscopic and crystallographic investigations, reflects a specific retinal and protein conformation that is necessary for the movement of a proton from the intracellular to the extracellular domain.

The primary photochemical event of BR, or the $\mathbf{bR} \rightarrow \mathbf{K}$ transition, is a 500-fs process that results in a shift of electron density down the polyene chain of the chromophore and a subsequent isomerization of all-*trans* retinal to 13-*cis* retinal.[60] Other studies report that there are distinguishable photointermediates with submicrosecond lifetimes that precede the **K** state (i.e., the **I** and **J** states),[61-63] however, these states remain to be speculative and are not observed despite efforts using low-temperature trapping.

The excited state represented by **K** is then followed by a cascade of thermally driven photointermediates that participate in proton translocation. The first proton transfer occurs during

the **L**$\rightarrow$**M** transition, in which a proton is transferred from the protonated Schiff base (PSB) to the primary counterion, Asp-85.[64,65] The **M** state is characterized by a distorted 13-*cis*, 15-*anti* retinal chromophore,[66] and is historically split into the M_1 and M_2 substates that are defined by the access of the Schiff base to the extracellular and cytoplasmic half-channels, respectively.[67-69] The second proton transfer event occurs during the transition from the **M**$\rightarrow$**N** states, and involves the release of a proton to the extracellular surface from the proton release complex (PRC). The residues involved with the PRC have been debated throughout numerous studies, however, Glu-194 and Glu-204 are known to be participants and likely share in stabilizing the transferred proton surrounded by water.[70-74] The third step also occurs during the **M**$\rightarrow$**N** transition, in which the Schiff base nitrogen is reprotonated *via* Asp-96 through a network of water molecules.[75,76] Asp-96 is then reprotonated by proton uptake from the cytoplasmic surface, which occurs during the transition to the **O** state and is coincident with the isomerization of 13-*cis* retinal to the all-*trans* conformation.[77-79] The initial **bR** resting state is restored during the final proton transfer event, where the PRC is reprotonated from Asp-85.[80]

2.1.4. Branched Photocycle

A branching reaction from the main photocycle of BR is observed to produce a stable photoproduct, the **Q** state.[81] The branched photocycle is accessed *via* a sequential two-photon event, wherein the photoactivation of the **O** state using red light induces all-*trans* to 9-*cis* photochemistry.[82] Popp *et al.*[82] were the first to describe the nature of this branching reaction and the ability to revert back to **bR** using blue light. Subsequent studies by Dancsházy *et al.*[83,84] further characterize the long-lived nature of the **Q** state. Because the 9-*cis* retinal is unstable within the binding site, hydrolysis of the Schiff base occurs and the chromophore remains in this kinked conformation, unable to rebind to Lys-216 or exit the binding site. The **Q** state has an

absorption maximum (λ_{max}) of 390 nm and has a barrier of ~190 kJ/mol to reform **bR**.[58] The **P** photointermediate was first defined as having a λ_{max} of 490 nm, however, a subsequent study reports that it can be split into two 9-*cis*-containing photointermediates, $\mathbf{P_1}$ (λ_{max} = 525 nm) and $\mathbf{P_2}$ (λ_{max} = 445 nm), that are in dynamic equilibrium with each other.[81]

While the discovery of the branched photocycle has been advantageous for the development of BR-based devices,[58] the biological role of a 9-*cis* chromophore is uncertain. The **P** and **Q** states render the protein incapable of pumping protons, which would be a biological disadvantage for *H. salinarum* while within an anaerobic environment. However, despite the fact that the native protein does not efficiently form the branched photocycle, access to the **P** state is conserved. Gillespie *et al*.[81] hypothesize that organisms at the surface of a salt marsh environment could be exposed to intense sunlight, and if these organisms were driven to the **Q** state, they would provide protection to the underlying layers by absorbing damaging UV radiation. This trait would benefit the whole of the population and is a potential example of bacterial altruism.

2.1.5. Directed Evolution

Although nature has yielded a robust photoactive protein capable of being harnessed in non-native environments, protein engineering of native BR is a necessary step for use as a photochromic material in devices. Manipulation of the kinetics, absorption profiles, and quantum efficiencies of the photointermediates of the BR photocycle are the primary focus of optimization, and mutagenesis of the **M** and **Q** states are particularly critical for biophotonic devices based on BR. Because the **M** state is transient, dynamic holography utilizing the **bR**/**M** photochromic pair is limited to the time constant of this transition, and in order to modulate the lifetime of the **M** state, amino acids involved in proton transfer to the Schiff base are targeted for

mutagenesis.[85-88] Devices based on the **Q** state remove the factor of time sensitivity due to the isolation of a stable photoproduct.[81] Because the **Q** state does not exist in nature, the genetic enhancement of the formation and reversion efficiencies are of interest for long-term data storage and application of the protein into the protein-based retinal implant.[88]

Directed evolution provides a cost and time efficient method of optimizing biological macromolecules such as BR to serve in non-native environments where enhanced photophysical properties are required.[85,88,89] This high-throughput process enhances a protein toward a specific characteristic *via* repeated iterations of genetic mutation, screening, and differential selection. Protein redesign of BR by directed evolution is accomplished through an iterative combination of site-directed site-specific saturation, semi-random, and random mutagenesis. In a recent study, directed evolution is used to enhance the ability of BR to form the **Q** photoproduct, which is otherwise minimized in the native organism.[46] Mutants of BR are generated *via* region-specific semi-random mutagenesis and were screened with respect to **Q** state formation and reversion. Subsequently, the most efficient **Q** state mutants discovered are employed as the parent to the next generation of genetic progeny. This process is repeated through six stages and a total of approximately 10,000 mutants are screened during this study. A number of mutants present significantly enhanced **Q** state performance, with the quadruple mutant, V49A/I119T/T121S/A126T, being the optimal **Q** state mutant identified to date. Importantly, the single mutation of V49A shows remarkable **Q** state enhancement that is almost as efficient as the quadruple mutant, particularly when pH is included as a factor during the fourth stage of the directed evolution experiment.[46] One goal of this study is to characterize the photochemical and photophysical attributes of V49A that allow this single, seemingly non-divisive, mutation to have such a dramatic effect on accessing the branched photocycle of BR. While past studies of Val-49

by Lanyi and coworkers (*vide infra*) suggest that the residue plays an important role in mediating the proton-translocation pathway, we reveal the unique properties of V49A that can be efficiently used in applications that exploit the **Q** state photochemistry, including the protein-based retinal implant.

2.1.6. Role of Valine-49 in Bacteriorhodopsin

Val-49 is located in helix B within the cytoplasmic half-channel and neighbors the side chain of Lys-216, in addition to other key groups within the proton translocation pathway. Photophysical analyses of BR mutants, including targeted substitutions at the Val-49 position, have been previously conducted in order to understand the role of surrounding residues that govern the dynamics of the proton translocation of BR. Brown *et al*.[90] suggests that Val-49 plays an important role in the alignment of the protonated Schiff base (PSB) and the primary counterion, Asp-85. Song *et al*.[91] conclude that when valine is replaced with alanine at this position (V49A), there is a disruption in the electrostatic environment of the binding pocket that disturbs the alignment of Asp-85 and the PSB and shifts the equilibrium towards protonation of the PSB. This effect leads to a shift in chromophore alignment within the binding pocket when compared to *wild-type* BR (WT-BR), which likely impacts the photochemistry of the mutant protein (Figure 2.3B). Fourier transform infrared (FTIR) spectroscopic studies suggest that there are water molecules present between the PSB and the carbonyl group of Val-49,[92] and that there is a direct interaction between the side chains of Val-49 and Lys-216.[93] It is also thought that a water molecule is coordinated to Asp-85 and the carbonyl bond of Val-49, therefore implicating a direct stabilization between the two residues.[94,95] Moreover, Taino *et al.*[94] suggest that there is an intrahelical stabilization through the hydrogen bonding of the hydroxyl group of Thr-46 with the backbone carbonyl or amide group of Val-49, leading to a long range backbone

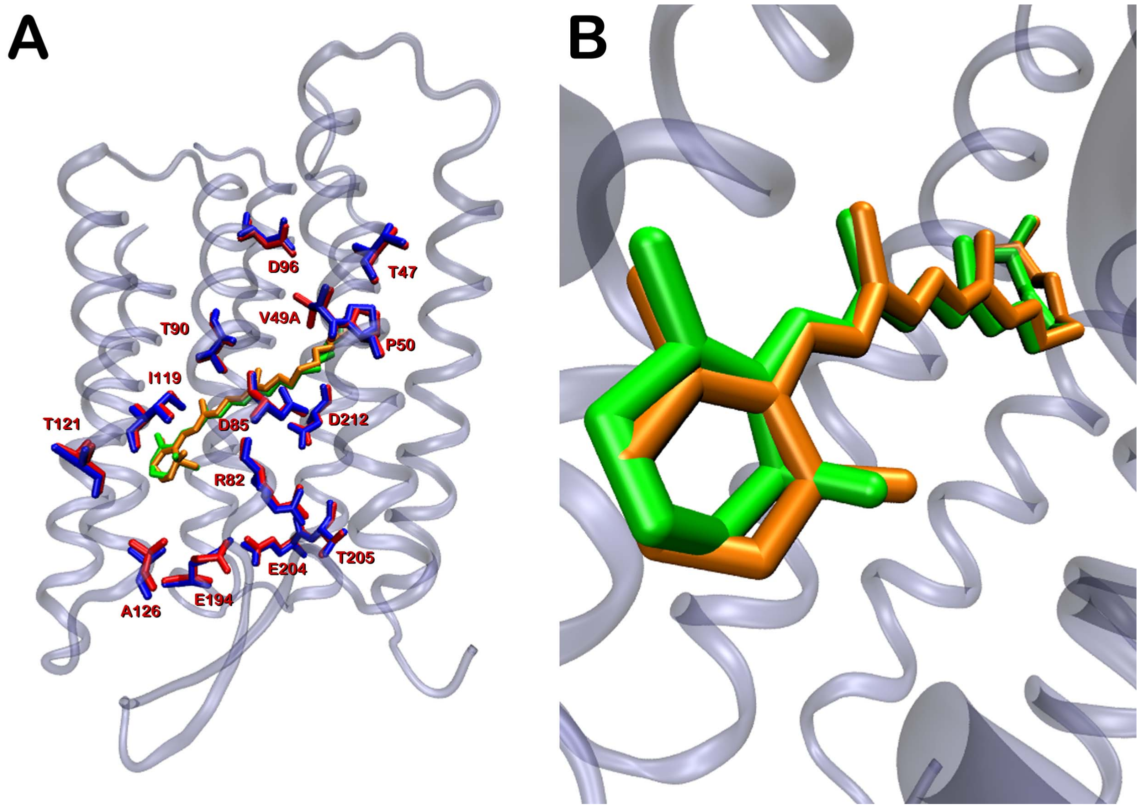

Figure 2.3. Overlay of the key residues (A) and the chromophores (B) of V49A (residues are blue, chromophore is orange) and native BR (residues are red, chromophore is green). The backbone atoms of the crystal structures of native BR (PDB code: 1C3W)[49] and V49A (PDB code: 3HAN)[96] were aligned in SWISS-PBD viewer (872 atoms, RMS = 0.7 Å). The coordinates were then imported to and overlaid in the Visual Molecular Dynamics software package for image construction.

conformational interaction between Val-49, Thr-46, Asp-85, and Glu-204. The crystal structure of the V49A mutant was solved in 2009,[96] and the study suggests that Val-49 plays an important role in the van der Waals packing of hydrophobic residues that stabilize the α-helical domains of the protein. The N-H group of Val-49 hydrogen bonds with the O-H group of Thr-46 through a mediating water molecule, which, in turn, hydrogen bonds with the carbonyl group of Asp-96.[92,97] Val-49 plays an important role in the long-range interaction between Asp-96 and the PSB region, and thus, largely influences the entirety of the proton-translocation pathway. Figure 2.3A highlights the altered orientation of the side chains of key residues when comparing the crystal structures of WT-BR and V49A (1C3W[49] and 3HAN[96], respectively), which infers the impact that this mutation will have on the proton transfer reactions during the photocycle.

Upon the V49A substitution, the BR mutant demonstrates some *wild-type*-like attributes, however, some perturbations do exist that change the structure and function of the protein. The λ_{max} of V49A has been measured at 551 nm and the extinction coefficient is calculated to be 54,000 $M^{-1}cm^{-1}$.[98] Logunov and El-Sayed[99] determined that the quantum yield of the V49A mutant (0.6 ± 0.1) is similar to that of native BR (0.65 ± 0.1), and also demonstrated that the energy content of the **K** intermediate is of a similar magnitude between the mutant and the native protein (50 ± 20 kJ/mol and 41 ± 15, respectively). The **L** → **M** transition of the V49A photocycle is shifted in equilibrium towards the **L** state, indicating a higher proton affinity for the PSB donor versus the Asp-85 acceptor.[90,100] The **M** state has a decay time constant that is 10 times slower than native BR[95] and an accumulation that is decreased by a factor of 6.[90,101] The **N** state also shows a 10-fold decrease in the decay time constant and is significantly more stable than native BR.[102] Maeda *et al*.[100,103] predict that the loss of the two methyl groups upon the V49A substitution creates a large water cavity that stabilizes the both the **L** and **N** states, and

makes these two photointermediates quite similar in structure. Proton uptake by Asp-96 is retarded significantly during the **N**$\rightarrow$**O** transition due to the perturbation of the hydrogen bonding network by Ala-49,[95,97] and Greenhalgh *et al.*[98] suggest that the **O** state formation and decay kinetics are elongated by ~10-fold compared to WT-BR. Overall, the proton pumping mechanism of BR is maintained despite the unfavorability of some of the equilibrium shifts and the significant increase in the photocycle lifetime.

2.1.7. Summary of our Investigation of V49A

We will first summarize the methodologies and results examined in the Type I directed evolution study that optimizes the photochemistry necessary to enhance the branched photocycle of BR.[46] Directed evolution has a short but distinguished history of optimizing proteins generated by native organisms,[104-106] however, this approach is extremely difficult to implement when a complex photochemical reaction is to be optimized, particularly if variables like pH govern this enhancement.[107,108] In this study, we use Type I directed evolution[85,89] to optimize both the formation and reversion efficiency of the **Q** state by implementing automated screening and microgram protein characterization. This process is iterative and builds upon successive improvements to the protein.[109] After six generations of development, involving the screening of over 10,000 mutants, more than ten new proteins are discovered with excellent **Q** state formation efficiencies, cyclicities, and thermal stabilities. Of the screened mutants, the quadruple mutant, V49A/I119T/T121S/A126T, is found to have the highest efficiency for **Q** state formation. Importantly, the single mutation, V49A, is found to have a comparable efficiency to this quadruple mutant at the end of the directed evolution stages. In this characterization study of V49A, we evaluate the remarkable enhancement of the **Q** state photochemistry and describe the

mechanistic forces that drive and stabilize this photoproduct within a seemingly inconsequential BR mutation.

The efficiency of **Q** state formation and reversion of V49A in buffered solutions are investigated, emphasizing the importance of the pH environment on these photochemical processes. Absolute and time-resolved absorption spectroscopy is used to define a model that explains this pH dependence, which is reliant on the modulation of the pK_as of three entities that are critical in the proton translocation pathway of the native protein, including Asp-85, Asp-96, and the PRC. An analysis of the binding site also provides insight into the accommodation of 9-*cis* retinal at alkaline pH. Chromophore extractions using high performance liquid chromatography (HPLC) and FTIR spectroscopy indicate the complete conversion to and from the **Q** photoproduct, and also suggests that V49A is unique in that it preferentially forms the 9-*cis* chromophore when it thermally relaxes in a dark-adapted state. Finally, we examine the role of the V49A mutation in the quadruple mutant, V49A/I119T/T121S/A126T, and hypothesize the combined mechanisms that yield this optimized BR mutant.

The enhanced BR biomaterial, V49A, is capable of forming two stable and spectrally discrete photoproducts (**bR** and **Q**), which have been exploited as differentiable bits (bit 0 and bit 1) in protein-based volumetric memories and processors.[58,110-112] Similarly, this photochemistry can provide a means to mediate pixels on the active surface area of a protein-based retinal implant. Because the **Q** state would prevent the protein from pumping protons, it has the potential to deactivate specific areas of the implant to prevent interference with functional photoreceptor cells following surgical implantation.

In this study, we also seek to characterize the ability to mediate pixels within a protein-based retinal implant comprised of the high **Q**-forming mutant, V49A. Our approach makes use

of a foveated complementary metal-oxide semiconductor (CMOS) imager, which is based on neural-inspired camera technologies that detect and process light similarly to the human eye. A foveated imager is a sensor that combines different pixel properties, which are dependent on their measured distance or computational delay relative to the center.[113] In using higher resolution in the center of the chip, one can simulate the fovea (higher concentration of cone photoreceptors) while keeping larger pixels towards the periphery of the chip working as large dynamic motion detectors (equivalent to the rods in the retina). Because we are not measuring the response to movement, we focus on the properties of the static pixels only, leaving the use of the larger dynamic peripheral pixels for future studies. The high resolution, sensitivity, and low noise properties of CMOS image sensors make them very good candidates for test platforms that can simulate the human retina and test the photosensitive properties of novel BR-based retinal implants.

Protein-based retinal implants are generated using the V49A BR mutant, and the implants are driven to the **Q** state by using LED-induced photochemistry. The hydrated retinal implants are then placed onto the foveated image sensor for relative light intensity measurements by the photodiodes, which is translated into an output frequency consisting of a series of action potentials (APs). At the conclusion of this study, we show that the image pixel properties can be extracted by attributing a light intensity to each of the pixels, which will allow for the differentiation between the **bR** or **Q** states and provide a basis for quantifying the extent to which the **Q** state has formed through a pixel light intensity map. The results of these proof-of-concept experiments show preliminary characterization of pixel mediation within a protein-based retinal implant, and ongoing experiments aim to quantify the limits of spatial resolution and generate the ability to drive local pixels between the two photoproducts.

2.2. Methods and Materials

2.2.1. Diversification of the Mutant Library

The mutants mentioned in this study are first identified from the type I directed evolution investigation performed to screen and characterize microgram quantities of BR mutants to enhance **Q** state formation and reversion.[46] As described above, a library of BR mutants is generated using a combination of region-specific semi-random mutagenesis, site-saturation mutagenesis, and site-directed mutagenesis. The methods used for this study are briefly described below, however, we refer the reader to Wagner *et al.*[46] for a more detailed description of the techniques and procedures used.

The mutant library is first produced by dividing the bacterio-opsin (*bop*) sequence into 17 regions. The amino acids of each region are color-coded and are presented in Figure 2.10A. Region-specific semi-random mutagenesis is then used, targeting each defined region and using the sequence overlap extension method with doped oligonucleotides that span the 17 regions.[85] The resulting mixture is transformed into XL-10 gold ultracompetent *Escherichia coli* (Stratagene) to isolate the genetically distinct colonies and amplify the mutant *bop* gene so that they could be harvested using alkaline lysis DNA extraction. The mutant DNA are then transformed into the MPK409 cell line of the native organism, *H. salinarum,*[114] and transformants are selected *via* mevinolin resistance, while recombinants are selected by using 5-fluoroorotic acid (5-FOA). Colonies are grown on 5-FOA plates and are picked when pigmented, which indicates the presence of properly folded BR. Each selected colony is allowed to grow in a 25 Erlenmeyer flask under conditions initially established by Oesterhelt and Stoeckenius[115,116] and were isolated and purified using standard procedures.

Once isolated, purified mutant protein samples then undergo a high-throughput screening method to test for the ability to form the **Q** photoproduct. Each sample is concentrated to an optical density of ~0.5 – 2.0 and distributed throughout a 96-well plate with other BR mutants. The resting (**bR**) state spectra (pre-illumination for **Q** formation) are collected from 350 – 750 nm using a μQuant microplate reader (BioTek Instruments, Winooski, VT). Next, the 96-well plate is irradiated with red light (100 mW/cm^2; >640 nm) at 35 °C for 3 hours using 12 Luxeon III Lambertian LEDs. The absorption spectra are collected to measure the extent to which the **Q** state has been formed for each mutant. Subsequently, the 96-well plate is exposed to blue light (0.03 mW/cm^2; 395 nm) at 35 °C for 2 hours using 28 510 mcd LEDs, and the absorption spectra are then collected to measure reversion back to the **bR** state. In total, each mutant had a set of three absorption spectra taken: the initial **bR** state spectrum, the spectrum following red-light illumination to measure **Q** formation, and the spectrum following UV-light illumination to measure **Q** reversion.

The three spectra were analyzed using computer algorithms to calculate the formation and reversion efficiencies with respect to the **Q** photoproduct. Q_{total} is the variable that represents the proficiency of the BR mutant as a **Q** state mutant, and is defined as the product of $Q_{formation}$ and $Q_{reversion}$. $Q_{formation}$ and $Q_{reversion}$ represent $\mathbf{bR} \rightarrow \mathbf{O} \rightarrow \mathbf{Q}$ and the $\mathbf{Q} \rightarrow \mathbf{bR}$ photochemistries, respectively. Equations 2.1 – 2.3 represent these relationships mathematically:

$$Q_{formation} = \xi_{\mathrm{experimental}} \times Q_{\mathrm{bR} \xrightarrow{h\nu} \mathrm{O}} \times Q_{\mathrm{O} \xrightarrow{h\nu} \mathrm{P}} \times Q_{\mathrm{P} \xrightarrow{\tau} \mathrm{Q}}$$
$$Q_{reversion} = \xi_{\mathrm{experimental}} \times Q_{\mathrm{Q} \xrightarrow{h\nu} \mathrm{bR}}$$
$$Q_{total} = Q_{formation} \times Q_{reversion} \qquad (2.1 – 2.3)$$

where $\xi_{\mathrm{experimental}}$ is an experimentally determined multiplier that is defined by the data. The $\xi_{\mathrm{experimental}}$ value is adjusted so that $Q_{formation}$ = 6.7 an $Q_{reversion}$ = 1.5 for the native protein at pH = 7, so that Q_{total} = 10 for the native protein. For the first three stages, two internal standards with

known Q_{total} were included in each 96-well plate, and three internal standards were used for stages 4 – 6. The calculated Q_{total} values were then compared to that of WT-BR, and the top 10 – 20 **Q**-forming mutants were sequenced and used as the parents for the next generation of genetic progeny.

2.2.2. Strain Generation, Protein Isolation, and Purification

In order to express V49A for studies beyond the directed evolution methods outlined above, mutant DNA is transformed into the MPK409 cell line of *H. salinarum* using methods outlined by Peck *et al*.[114] Purple membrane fractions are then prepared and isolated according to standard procedures.[115,116]

2.2.3. pH studies

In order to determine the response of the mutant proteins to different pH environments, each protein is solvent exchanged in various buffers. Buffers that are used for the pH analysis in the directed evolution study include 100 mM phostphate for pH 2.0, 2.5, 6.0, 6.5, 7.0, 7.5, 11.5, and 12.0, 100 mM glycine buffer for pH 3.0, 3.5, and 9.5, 100 mM citrate buffer for pH 4.0, 4.5, 5.0, and 5.5, 100 mM 2-amino-2-(hydroxymethyl)-1,3-propanediol (Tris base) for pH 8.0, 8.5, and 9.0, and 100 mM 3-(cyclohexylamino)-1-propanesulfonic acid (CAPS) for pH 10.0, 10.5, and 11.0. The protein samples are pelleted at 50,000 rpm at 4°C for 30 minutes in a 1.5 mL polyallomer microfuge tube using a Beckman Coulter ultra tabletop centrifuge (TLA-55 rotor). Each protein is resuspended in the appropriate buffer and allowed to equilibrate for 30 minutes before centrifugation. The process is repeated 3 times. Analysis of the **Q** state is carried out in a 96-well plate using the automated irradiation system.

Subsequent pH studies are performed to obtain absolute and time-resolved absorption spectra, FTIR spectra, HPLC chromatograms, and differential scanning calorimetry (DSC)

thermograms of V49A and WT-BR. Buffers used for the pH studies within this work included 50 mM phosphate for pH 6.0 and 6.5, 50 mM 4-(2-hydroxyethyl)-1-piperazineethanesulfonic acid (HEPES) for pH 7.0 and 7.5, 50 mM tris(hydroxymethyl)methyl-2-aminopropanesulfonic acid (TAPS) for pH 8.0 and 8.5, 50 mM glycine for pH 9.0 and 9.5, and 50 mM 3-(cyclohexylamino)propanesulfonic acid (CAPS) for pH 10.0 and 10.5. All chemicals were purchased from Fisher Scientific, Inc. (Pittsburg, PA) or Sigma Aldrich (St. Louis, MO). The solvent exchange methodology is used as described above.

2.2.4. Preparation of the Q State

The BR mutant used in this study (V49A) was selected due to the identification of this protein as a high **Q**-forming mutant.[46] The **Q** photoproduct is formed and reverted using the irradiation system that is described above in Section 2.2.1, which includes a red LED light bank (100 mW/cm^2; >640 nm; 35 °C) and a UV LED light bank (0.03 mW/cm^2; 395 nm; 35 °C) for **Q** formation and **Q** reversion, respectively. The illumination times are modulated based on the nature of the experiment.

The **Q** photoproduct is also formed while the protein is contained within the multilayered thin film that comprises the retinal implant. The thin films were placed in a petri dish filled with enough glycine buffer (50mM; pH 9.5) to completely hydrate the film for the duration of the illumination period. The film is placed under the red LED light bank for 8 hours at ambient temperature. Prior to further experiments, the **Q** state thin film is hydrated within the buffered solution and the petri dish is wrapped in aluminum foil to prevent exposure to ambient light.

2.2.5. Absorption Spectroscopy

All absorption spectra were collected at ambient temperature using a Varian Cary 50 or Varian Cary 5000 UV-visible spectrophotometer (Palo Alta, CA). The samples that are used in

the absolute absorption spectroscopic analysis of the **Q** state photochemistry are at an optical density of 0.5 and were placed in 70 μL, 1 cm path length methacrylate microcuvettes (Plastibrand Cuvettes, Fisher Scientific, Inc.). The retinal implants are inserted into a 1 mm quartz spectrophotometer cell (Starna Cells, Inc.; Atascadero, CA) and the films were suspended in 50 mM glycine buffer (pH 9.5). A bare PET mesh film in buffer is used as the blank for these measurements.

2.2.6. Time-Resolved Absorption Spectroscopy

Each protein sample is prepared at an optical density of 1.0 at the λ_{max} and transferred to 1-cm path length, 1.5 mL methacrylate cuvettes (Plastibrand Cuvettes, Fisher Scientific, Inc.). Prior to the time-resolved measurements, the protein samples are light adapted (LA) using 400 W white light source for one hour. A Neodymium:YAG laser system (Continuum Minilite II) is used as the actinic pump pulse directly preceding the time-resolved absorption measurements. A rapid-scanning monochromator (RSM) system (OLIS Instruments Inc., RSM-1000 stopped flow) is used to collect the absorption spectrum from 350 nm to 750 nm (*via* 50 L/mm, 500 nm blaze wavelength gratings) at a 1 ms time resolution. The initial absorption spectrum of LA BR is used as a baseline and the RSM system then monitors the difference spectra by using 1,000 scans averaged per second. Single-wavelength kinetic measurements following light activation were also measured by averaging 10 traces per protein sample. Equation 2.4 is used for the multiexponential fitting of the kinetic data, as implemented in FitDynamics 3.2.2U:

$$y(t) = A_0\left(1 - e^{[-(t-t_0)/\tau_{form}]}\right) - \left(e^{[-(t-t_0)/\tau_{decay}]}\right) \tag{2.4}$$

where A_0 is the absorption at the time of laser excitation, t_0 is the excitation time, τ_{form} is the time constant for formation of the state, and τ_{decay} is the time constant for the decay of the state. A

schematic of the time-resolved apparatus can be found in Figure 2.4. All measurements were collected at 25 °C.

2.2.7. FTIR Difference Spectroscopy

A ~100 μg sample of protein is centrifuged using a Beckman Coulter Optima™ MAX-E ultracentrifuge (50,000 rpm, 20 min, 4 °C) and the protein pellet is resuspended in minimal buffer (50 mM TAPS, pH 8.5) volume. A gentle stream of nitrogen is used to dry the sample on a cool BaF_2 window so that the protein thin film is minimally hydrated. A second BaF_2 window is placed on top of the first and vacuum grease is used to seal the pair of windows. A custom sample holder is used to place the protein thin film within the sample chamber of the IFS 66v/S step-scan Fourier Transform spectrometer (Bruker, Billerica, MA). A total of 100 spectral scans are taken and averaged at 2-cm^{-1} resolution using a nitrogen-cooled infrared mercury cadmium telluride (MCT) detector (Kolmar Technologies, IPV11-1-LJ2/239). All measurements are collected at room temperature.

2.2.8. Retinal Extraction and HPLC Analysis

For all chromophore extractions, light-adapted (LA) samples are illuminated under white light (400 W) at ambient temperature (~25°C) for one hour prior to the extraction. Dark-adapted (DA) samples are wrapped in foil and incubated at ambient temperature (~25°C) overnight. Preparation of the **Q** state is accomplished by illuminating solvent exchanged protein with the red LED light system (640 nm) for 16 hours. Samples are then wrapped in foil to prevent reversion from stray light, and are stored at ambient temperature (~25°C) until use.

Chromophore extraction and HPLC analysis are carried out in dim red light as described by Scherrer.[117] Approximately 100 μL of purple membrane suspension (OD = 1.0) is mixed with 250 μL of ice-cold ethanol. The sample is rapidly mixed using a vortex mixer for about 3

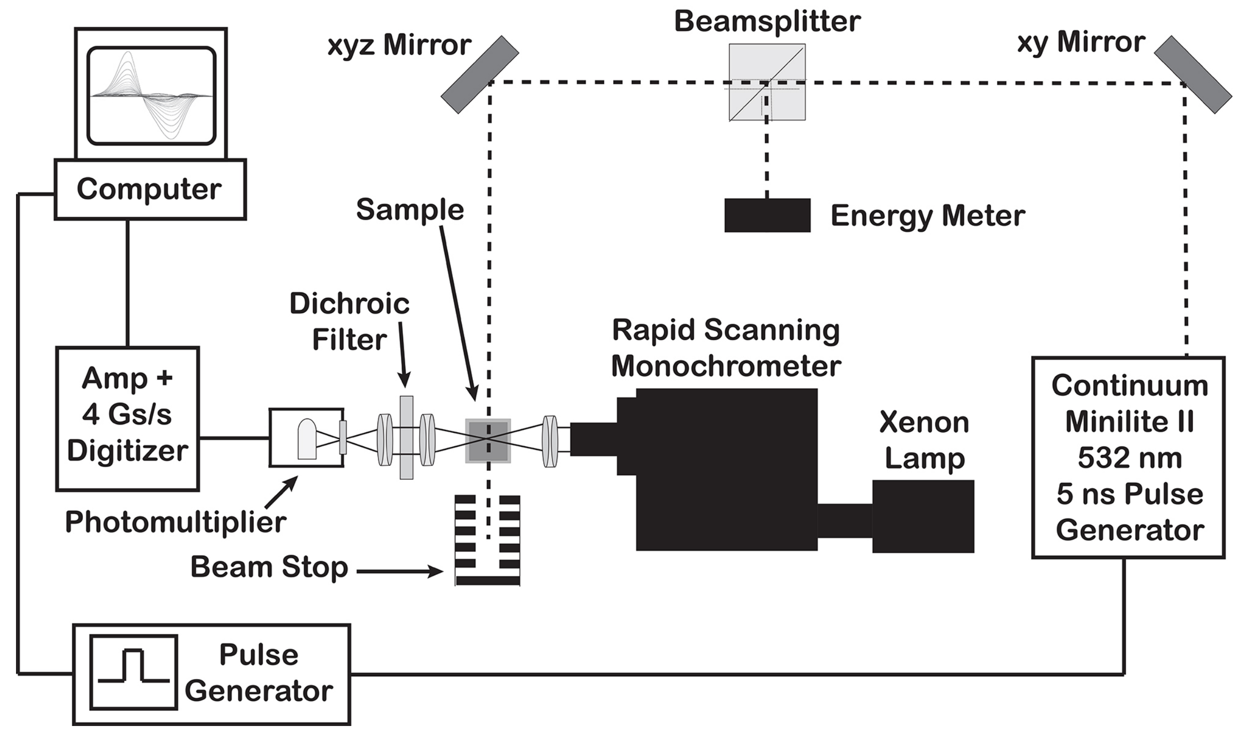

Figure 2.4. Schematic of the time-resolved absorption spectrophotometer used to collect the light-induced difference spectra and temporal kinetics of key photointermediates in the photocycles of WT-BR and V49A. All spectra were collected at a ms timescale at 25 °C.

seconds and is then incubated on ice for 2 minutes. The solution is subsequently treated with 250 μL of ice-cold hexane and is vortexed continuously for another 2 minutes. The resulting mixture is centrifuged for 1 minute using a microcentrifuge (CLAY ADAMS Brand Compact II). The non-polar hexane layer is transferred to a glass tube and the retinal isomers contained within this layer are separated and analyzed using an HPLC (Waters Corp, Milford, MA, USA). Two prep silica columns are used in series to separate the isomers (3.9 x 300 mm^2 Nova-Pak HR, Waters, WAT038501). A non-polar mobile solvent, comprised of 8% tert-butyl methyl ether and 0.8% isopropanol in *n*-hexane, is passed through the column at a rate of 1.0 mL/min. The unknown peaks in the resulting chromatogram are identified and quantified by comparing their elution times with that of the isomer standards for all-*trans*, 13-*cis* and 9-*cis* retinal.

2.2.9. Differential Scanning Calorimetry

All calorimetric experiments are performed with 1 mg mL^{-1} protein using a Microcal VP-DSC (Amherst, MA). Dialysis of all samples versus three one-liter volumes of the appropriate buffer is determined to generate the most reproducible data. The **Q** photoproduct is produced as described above and, because it is light sensitive, all manipulation was conducted under dim red light.

2.2.10. Manufacturing of the Protein-Based Retinal Implants

The protein-based retinal implants are comprised of a multilayered, BR-based thin film generated *via* sequential electrostatic adsorption, which is achieved through a LBL manufacturing technique.[45,118,119] Figure 2.5 describes the general architecture of the retinal prosthetic. The multilayered thin films are capable of harnessing and amplifying the proton pumping action of BR if the protein is uniformly oriented in the film at an optimal optical density. There must be enough layers of BR to adequately absorb incident light while also

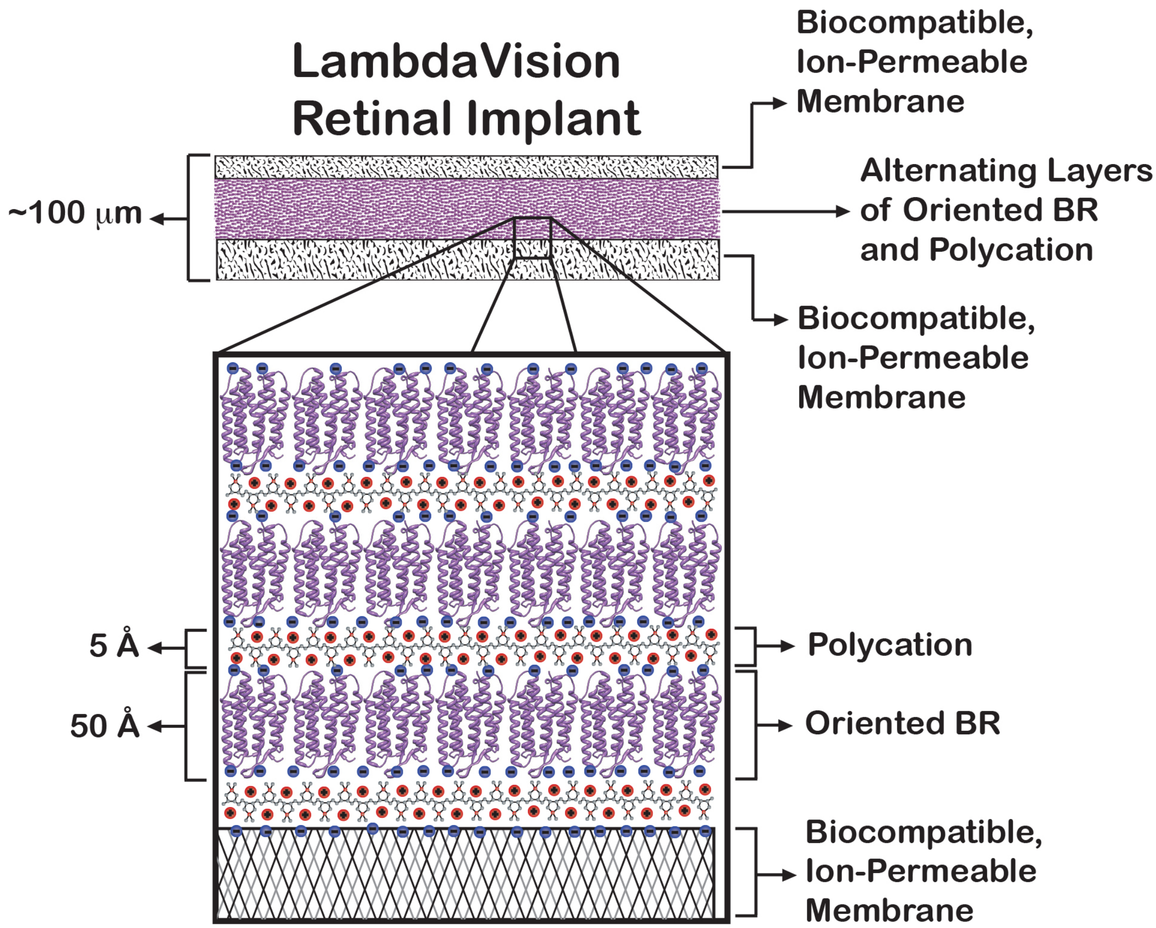

Figure 2.5. Schematic of the retinal implant and a diagram showing the arrangement of alternating layers of BR and polycation. The current implant design uses 200 layers of oriented BR, which provides an optical density of 0.6 and a thickness of 100 µm with two ion-permeable membranes incorporated into the design.

generating an appreciable unidirectional ion gradient for retinal stimulation. The solid support surface of the thin film is a bioinert, ion-permeable mesh comprised of polyethylene terephthalate (PET) microfibers. This material has previously found success in retinal prosthetics[120,121] and is amenable to surface modification in order to serve as a scaffolding for multilayers of BR within our protein-based retinal implant. Because the LBL process requires a charged surface for subsequent electrostatic adsorption, the PET film is first exposed to conditions that facilitate the reduction of surface carbonyl functional groups that renders the surface negatively charged.[122-124] The PET film is first washed in a scouring solution (10 g Na_2CO_3, 10 mL Tween 20, 1 L ddH_2O) for 30 minutes at 60°C. Next, the film is washed in ddH_2O for 30 minutes at 60°C before placement in a boiling solution of 0.5% (w/v) NaOH for 30 minutes. Finally, the film is rinsed with ddH_2O at ambient temperature.

Following preparation of the PET scaffolding, the LBL manufacturing technique is implemented as first described by He *et al*.[45,118,119] A schematic of an automated dipping system built *in-house* is shown in Figure 2.6. In brief, the PET film is first dipped in a solution of poly(diallyldimethyl ammonium chloride) (PDAC; 2 mg/mL, pH 6.8) for 5 min, followed by two 90 sec rinse periods in ddH_2O (Millipore, Billerica, MA) and a 5 min drying interval. The thin film is next transferred to a 0.5 mg/mL BR solution (in 50 mM glycine, pH 9.5) for 5 minutes, rinsed twice with 50 mM glycine buffer (pH 9.5), and dried for 5 min. It is important to note that this technique was carried out so that only one surface of the film was coated during the LBL methods outlined above. Following the completion of manufacturing, the protein-based thin films are then stored in 50 mM glycine buffer (pH 9.5).

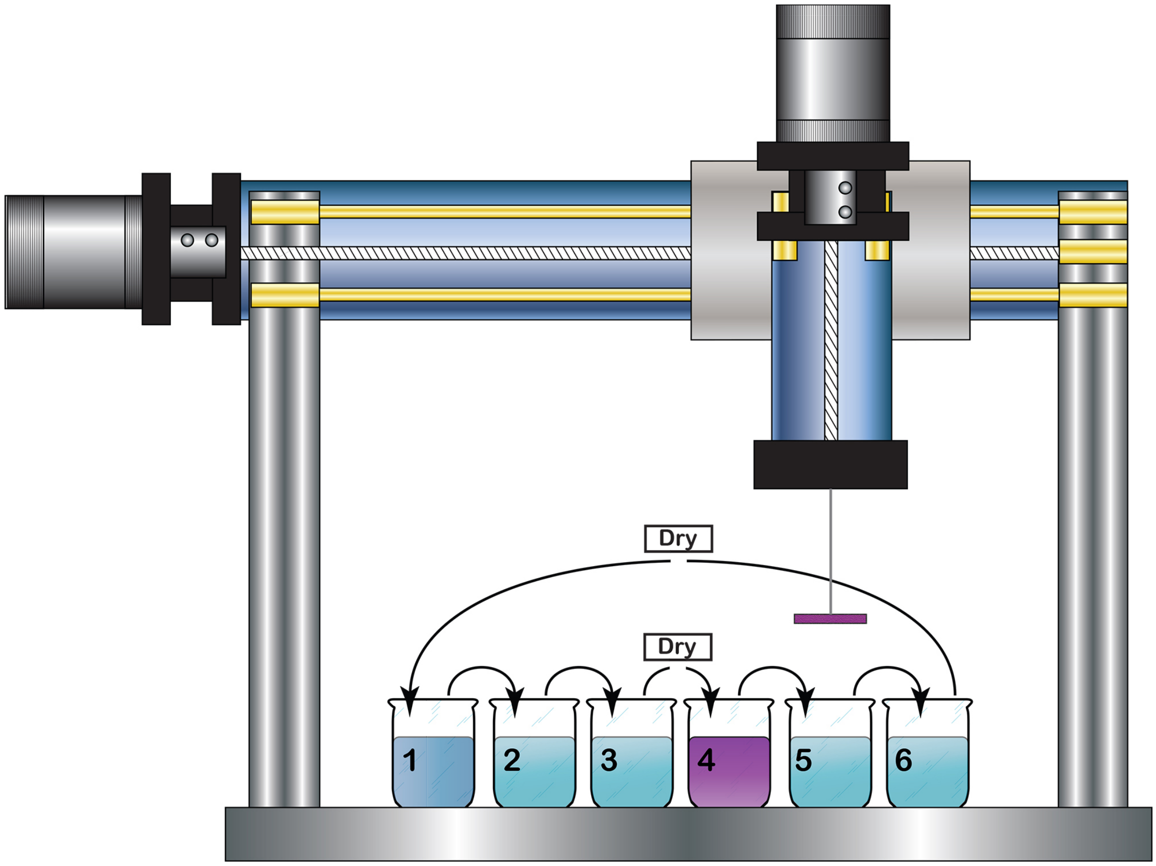

Figure 2.6. Schematic of the autodipper used to generate precision layers of protein on the Dacron substrate. A series of six solutions are implemented in sequence to accommodate the layer-by-layer electrostatic adsorption of the polycation (PDAC) and BR. The following lists the contents of each of the beakers labeled 1 – 6: (1) 2.0 mg/mL PDAC, pH 6.8; (2) ddH_2O; (3) ddH_2O; (4) 0.5 mg/mL BR, pH 9.5; (5) 50 mM glycine, pH 9.5; (6) 50 mM glycine, pH 9.5. Beakers 2 and 3 serve as wash solutions to rinse excess PDAC on the implant, while beakers 5 and 6 are wash solutions to remove excess BR. There are two dry periods; one between 3 and 4 and the other between 6 and 1. The current implant design uses 200 layers of oriented BR, which provides an optical density of 0.6.

2.2.11. Foveated Image Sensors

Modern CMOS sensor-based cameras offer an excellent optical resolution.[125] The CMOS image sensors that form the core of these cameras benefit from technology scaling that has provided them with a resolution increase (pixel size reduction) combined with the possibility to include more on-chip image processing circuitry. However, size scaling beyond sub-micron (< 0.25 μm) processing technologies is limited by dark current noises, tunneling effects through thin gate oxides, and a low photoresponsivity due to a combination of shallow junctions and high doping.[126] However, continuous effort is seeking to negotiate these limiting parameters through a gradual improvement of the fabrication technologies used, which together with the low cost of manufacture have continued to secure the commercial success of CMOS image sensors. This has in turn paved the way for new application possibilities such as neural-inspired, or retinomorphic, cameras[127,128] that mimic the way human eye detects and processes light and images.

The foveated image sensor used in this project is created using the commercial 0.35 μm CMOS processing technology, which measures 3.15 x 3.15 mm^2 in extent.[113] Like most neural-inspired circuits, this camera communicates with voltage pulses that resemble APs. Each pixel consists of a photodiode and the associated processing circuitry. The circuitry of the static photopixel cells (located in the center of the image sensor) consists mainly of an integrator. It integrates a current linearly proportional to the light level over a short period of time, and when a threshold is reached, an AP is fired. The AP is conveyed off chip by peripheral logic and the pixel is reset (Figure 2.7). Thus, the firing frequency reflects the light intensity collected by this pixel.

In more detail, the photo current *i* conveyed by the current mirror charges a capacitor C_m and, when the voltage across it reaches the threshold of the inverter, the output from the inverter

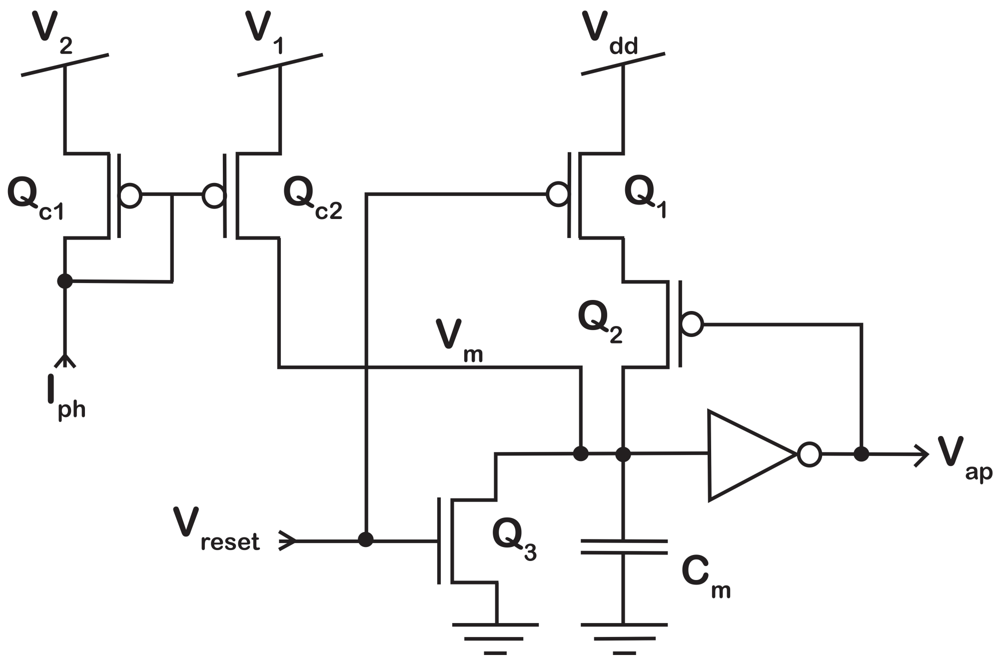

Figure 2.7. Foveated imager pixel logic. The photodiode is connected to I_{ph} and the current is mirrored in Q_{c1}-Q_{c2}, which can also act as an amplifier (tilted current mirror), charging C_m. Once V_m has reached the inverter threshold, it spikes an AP (V_{ap}) and initiates the communication circuit. Q_2 opens, and since V_{reset} is active high, Q_1 is already open and V_m is pulled to V_{dd}. When the communication circuit sends a reset signal to the pixel, V_m is set to ground and the reset signal goes low again, charging C_m once more.

changes from state 1 to 0 (digital representation). Through a feedback loop, the transistor Q_2 is activated and capacitor C_m is stabilized at the potential V_{dd} when the reset signal is low. When the reset signal is asserted, the transistor Q_1 will deactivate, and C_m will empty its charge to ground through Q_3, reaching the initial state. The size of C_m is essential to determine how fast the threshold voltage of the inverter will be reached. The voltage at C_m (V_m) is given by Eq. 2.5:

$$V(t)_m = \frac{1}{C}\int_0^t i d\tau + V(0). \quad (2.5)$$

For $V(0) = 0$:

$$V(t)_m = \frac{1}{C}\int_0^t i d\tau. \quad (2.6)$$

From Eq. 2.6, it is clear that the use of a small capacitor (capacitance, C) will reach the threshold potential ($V(t)_m$) faster. This also comes at the cost of a noisier circuit in which the leakage current (dark current at zero light intensity) charges a smaller capacitor faster, resulting in the generation of APs. In contrast, a larger capacitor will take a longer time to charge under these conditions, thus deceasing the rate of APs (and, consequently, the noise). This makes it less dependent on the dark current, but is at the cost of operating as a slower circuit. The area of the capacitor used in the static pixels of the foveated image sensor, C_m = 2.48 X10^{-4} μm^2, corresponds to a capacitance of 221.58 fF. The dark current will charge this capacitor at a rate that corresponds to the generation of 1 AP/s at zero lux. Increasing the light level to 3 lux (comparable to the test conditions described below) increases the firing rate to 8 AP/s. Hence, a change in the photocycle state of BR will reflect a change in light intensity and, consequently, a shift in the AP frequency.

The dynamic photopixel cells that are located in the periphery of the chip fire an AP if changes in light are detected according to the photoreceptor circuit described by Delbrück & Mead, where an electronic photoreceptor outputs a voltage that is logarithmic to the light

intensity.[129] The dynamic pixels are adaptive to various light levels and the APs are fired as the speed of that adaptation exceeds a certain threshold.[113] The photodiodes in all of the pixels are made from substrate diodes (n-well regions defined by, e.g., boron doping) in the bulk p-substrate of the chip.

While still large as compared to commercial CMOS image sensor pixels due to the in-pixel logic, the static photopixels are smaller than the dynamic pixels in order to produce high resolution pictures, measuring 26.8 × 25.2 μm^2 with a fill factor (photodiode area) of 11.3 %. The dynamic pixels are larger, measuring 53.6 × 50.4 μm^2, with a fill factor of 50.4 %. The photodiodes for the dynamic pixels are larger in order to achieve a higher sensitivity to light intensity variations. The pixel array is made up of 76 × 67 static cells in the center surrounded by 616 dynamic pixels according to (Figure 2.8).

The schematic in Figure 2.7 (except for the current mirror) is called an Integrate and Fire circuit and is a good example of a mixed-mode circuit. It is based on the "self-reset neuron".[130] A real biological neural network, which consists of point-to-point connections, is difficult to implement on an artificial neural CMOS chip due to a limiting amount of metal layers that are available for routing combined with a limited amount of contact pads that are available for interconnecting the generated signals to an external circuitry. A solution for asynchronous neuromorphic communication is the Address Event Representation (AER) protocol.[131] Most neurons communicate by way of nerve pulses or APs *via* dedicated point-to-point connections (axons). This is in contrast to the communication channels between computers, or inside computers, (such as busses) that transmit more complex signals at higher rates than an axon. The physical channels are mostly shared and time multiplexed by several components keeping a lower density. As neuromorphic engineers try to implement systems that are organized more like

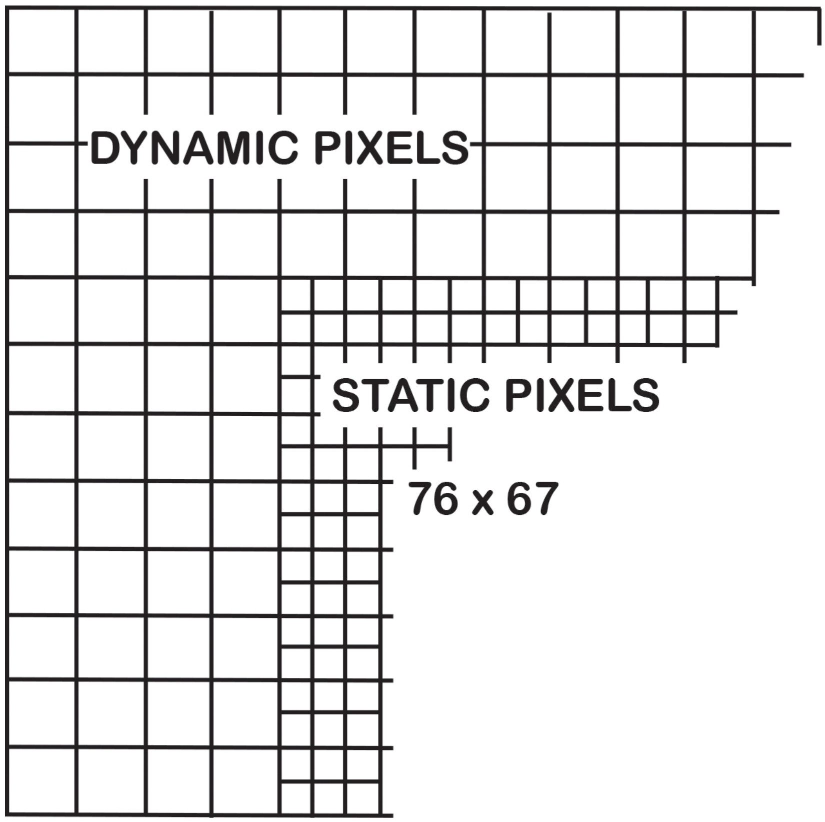

Figure 2.8. Layout of the pixels within the foveated image sensor.

the nervous system, communicating internal signals like the brain can become a major obstacle to electronics. The human brain contains about 10^{11} neurons, each of which has 1,000 to 10,000 synapses. All of those synapses receive input via a dedicated output line of the sending neuron, making the brain densely packed with connections between cortical areas and other parts.

Since neurons/pixels use APs to communicate, the AER bus is used to send the address of the neuron/pixel off-chip, either to a receiving neuromorphic circuit or a computer where the activity can be visualized, e.g., as a gray scale image of average pixel activity. This communication protocol takes advantage of the speed in integrated circuits, compensating for the lack of connections. The functioning principle can be explained as follows. When a neuron wishes to send an AP, it places its address on a digital bus via an encoder. Synapses that are supposed to receive that AP are connected to the same bus via a decoder and get stimulated when their address occurs (Figure 2.9). The bus can only transmit APs serially but does it much faster than an axon. It can transmit APs so tightly spaced in time that, for a network of neurons that operate on a natural time scale, these pulses are virtually instantaneous. Since multiple point-to-point connections share the same bus, it is necessary to have a bus control mechanism for handling collisions. The AER communication protocol is described in detail in reference 113.

2.2.12. Q State Detection Using a Foveated Image Sensor

In order to characterize the pixel content contained within the protein-based retinal implant, each film is placed directly on top of the foveated image sensor with a particular emphasis on the static pixels within the photodiode array. The retinal implants are either in the **bR** resting state or are driven to the **Q** state using the photonic criteria described above.[46] Each film is placed in a consistent orientation on the chip so that the pixel intensity measurements were under identical conditions. The sensor array was embedded in a sensor housing that

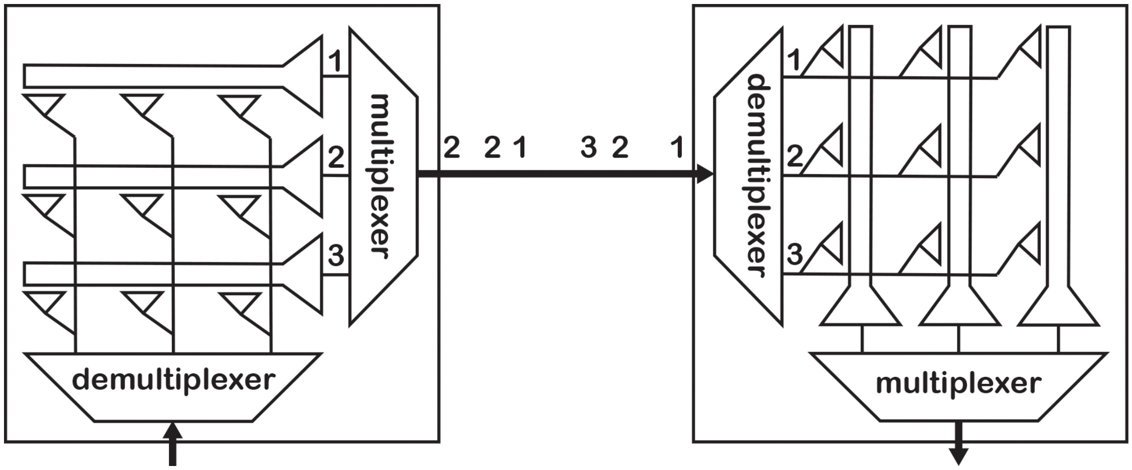

Figure 2.9. Schematic of the Address Event Representation (AER) principle.

protected the electrical interconnections from the hydrated films. Silicone purchased from Dow Corning (3140 RTV coating, Midland MI) is used to encapsulate the wire bonded contact pads on the sensor array. Once the BR-based retinal implant film is placed directly on the foveated imager (Figure 2.1, bottom LHS), the number of spikes generated by each pixel is measured under a controlled illumination environment (approximately 3 lux) for a 1-minute duration. The foveated image sensor does not provide colorimetric images, and therefore, a gray scale analysis of the pixels is used to measure the contrast between the two photoproducts of interest. The measured output is equivalent to the pulse frequencies that are proportional to the light intensities monitored by each pixel within the foveated imager.

2.3. Results and Discussion

2.3.1. Optimizing Q_{total} by Using Directed Evolution

Six stages of directed evolution were performed to enhance the access to and stability of the **Q** photoproduct of BR.[46] At the conclusion of each stage, the 10 – 20 best mutants are identified by calculating Q_{total}, and it is these mutants that are sequenced and used as starting materials to generate multiple mutants *via* site-directed, site-specific, or semi-random mutagenesis. Site-directed methods are used to produce mutants that incorporate the combinations of the best mutations of the previous round, in hopes that there would be an additive affect for the resulting BR mutant. Next, site-specific saturation mutagenesis is used to introduce all 20 amino acids at specific sites that were observed to likely enhance **Q** state formation.[132] If multiple mutations are found to yield a higher Q_{total}, site-directed mutagenesis is then used to prepare each of the participants for further examination. The goal is to only pass on useful mutations and to avoid the propagation of silent or diminutive mutations forward to the

next stages of evolution. Thus, the directed evolution process is optimized at each stage to reduce random branching from the native protein, which mitigates the risk of introducing destabilizing mutations[133] and reduces the time and cost to the process.

The notion that combining the two best mutations from each round of mutagenesis to generate progeny with improved and additive properties of the parent mutations, (a mutant with a higher Q_{total} than both of the parents) does not hold true for BR, and is unlikely to be observed for any biomaterial that is the subject of targeted genetic optimization. Only 12% of site combinations yield proteins that have a higher Q_{total} value than both of the parents. However, if the combination spans multiple regions (the regions are shown in color in Figure 2.10A), the success rate more than doubles (~28%). Figure 2.10B represents the total mutant library that was investigated in this study. The histograms are comprised of colored rectangles that represent the location of the mutation of the parent BR mutant relative to the colorimetric scheme of regions in Figure 2.10A. The boxes within each stage point out the top **Q**-forming mutants that are used as parent mutations for the subsequent BR mutants. It is interesting to note that more than 38% of the combinations generate a protein that had a lower Q_{total} than both of the parents. As can be seen from examination of Figure 2.10, the average of the next stage is well below the average of the best mutants that form the parents of the next generation. Nevertheless, our methodology yields systematic improvement in the average Q_{total} of the ensemble of new mutants compared to the previous stage. Table 2.1 summarizes a statistical analysis of Q_{total} for the library of mutants that are characterized during this study. The mean and median increased for each stage of directed evolution, with a notable increase in the geometric mean between stages 3 and 4 due to the introduction of pH as a variable (see below).

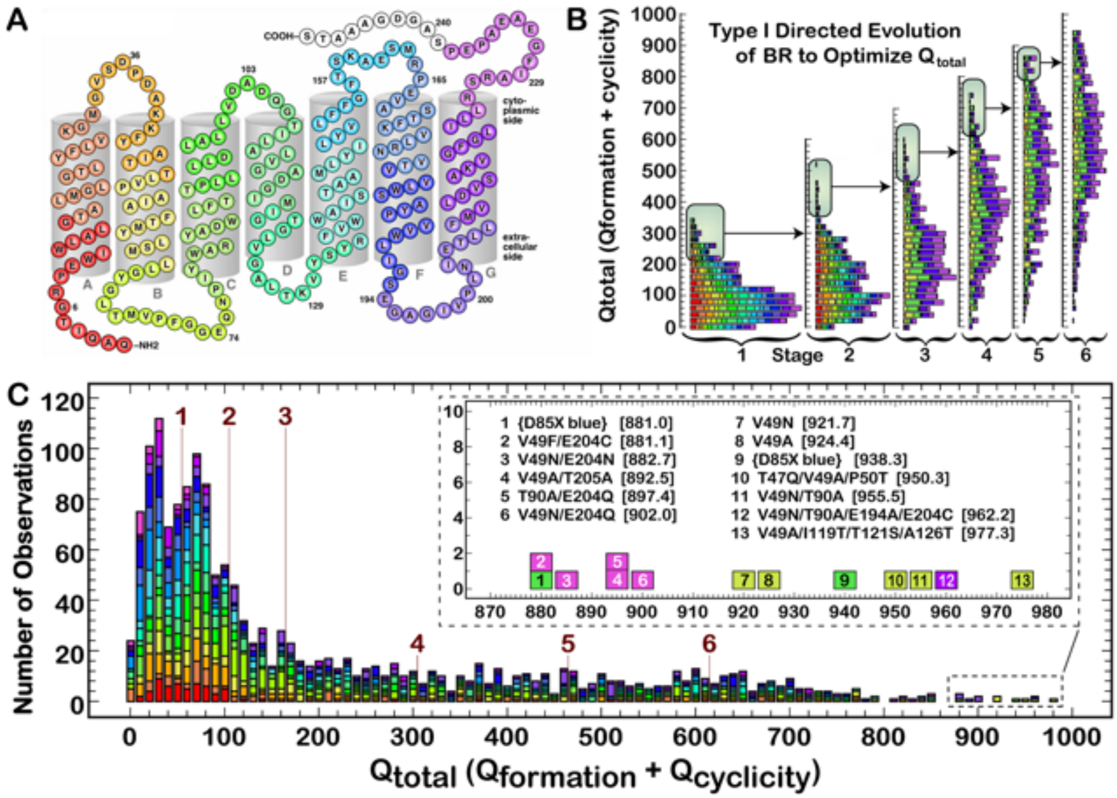

Figure 2.10. (A) The colorimetric two-dimensional map of native BR that was used to divide the protein into 17 target regions for mutagenesis during the directed evolution experiments. These regions span the following sets of residues (in numerical order): 1–16; 17–32; 33–47; 48–61; 62–76; 77–90; 91–104; 105–118; 119–133; 134–148; 149–163; 164–178; 179–193; 194–208; 209–223; 224–238. (B) The progression of Q_{total} is shown through six stages of Type I directed evolution, in which the color corresponds to the parent mutation indicated by the region in (A). (C) A histogram summary of the BR mutants that were created during the six stages of directed evolution, with the top 13 **Q**-forming mutants labeled with the corresponding Q_{total} in brackets.

Table 2.1. Statistical Analysis of the Q_{total} Data for Mutants Created at Each Stage of Directed Evolution[a]

property	stage 1	stage 2	stage 3	stage 4	stage 5	stage 6
number of new mutants (n)	941.0	802.0	748.0	804.0	804.0	761.0
maximum Q_{total}	334.1	404.3	573.9	694.9	854.2	977.4
minimum Q_{total}	1.6	1.6	2.4	3.9	16.8	2.2
mean (μ)[b]	105.8	144.1	226.3	356.7	487.0	566.2
geometric mean (μ_G)[c]	75.0	108.3	182.4	313.1	445.0	517.2
median	93.9	135.0	214.7	359.5	492.9	584.9
standard deviation (ϑ)[d]	72.8	88.3	119.4	152.3	174.7	199.4

[a] The statistical analysis of the Q_{total} data was carried out in order to track the mean or median evolution of the mutant population for each experimental stage.

[b] The arithmetic mean is calculated by

$$\mu = \frac{1}{n}\sum_{i=1}^{n} x_i$$

where n is the number of mutants for each data set.

[c] The geometric mean, which is often used to describe proportional growth, is calculated by

$$\mu_G = \left(\prod_{i=1}^{n} x_i\right)^{\frac{1}{n}}$$

[d] The standard deviation of each data set is calculated by

$$\vartheta = \sqrt{\frac{1}{n-1}\sum_{i=1}^{n}(x_i - \mu)}$$

2.3.2. pH Optimization of the Q State

The pH of the solvent environment impacts Q_{total} because the protonation states of the binding site residues and second shell residues are important to the proton translocation pathway and influence BR photochemistry.[134] Because of this significance, pH is included as a variable to characterize BR mutants and identify those that have an improved Q_{total}. During stages 4 – 6, the best mutants measured at pH = 7 were grown at larger volumes and were then scanned from pH = 6 to pH = 10.5 in increments of 0.5. The Q_{total} value for each mutant is registered at the pH value yielding the best result. Solvent environments below pH = 6 are not included in this study because we seek to avoid the formation of the acid-blue membrane.[134-136] The acid-blue membrane can form the **P** state *via* a direct single photon process, which would circumvent the branched photocycle route and would detract from the intended device architectures that are based on the sequential multiphoton process.[81] Moreover, the thermal and photochemical stability of most BR mutants decreases at pH values below 6, although the native protein is remarkably stable even at pH = 4.[137]

The results of six stages of Type I directed evolution are shown in Figure 2.10B. Table 2.2 also presents selected high **Q**-forming mutants and the relevant parent mutants. Note that most of the mutants with a Q_{total} greater than ~600 formed the **Q** state better at alkaline pH values. These findings are significant because most mutants are more photochemically and thermally stable at neutral to slightly alkaline pH, which is consistent with WT-BR and the native environment.[137,138] The highest **Q**-forming mutant that is from a single mutation is V49A, which is the primary subject of this study. Throughout Table 2.2, it is apparent that Val-49 is an important residue for enhancing the photochemistry necessary to form and revert **Q**. The V49A mutation is also a part of the BR quadruple mutant with the most efficient **Q** state

Table 2.2. Photophysical Properties of Selected Bacteriorhodopsin Mutants[a]

#	mutant[b]	λ_{max} (nm)[c]	Δt_{cycle} (ms)[d]	pH[e]	$Q_{formation}$	Q_{total}
1	Native BR	567.3	12	7.0	6.7	10.0
2	T90C	558.7	107	7.0	20.7	17.5
3	P200A/E204V	564.4	56	7.0	53.7	80.0
4	V199M/N202K/E204Y/T205A/L206M	562.5	64	7.0	83.5	124.3
5	E204A/T205Q/F208V	556.6	98	7.0	101.7	149.8
6	I198L/L201R/N202H/E204D/T205A/F208I	555.0	28	7.0	114.2	170.0
7	A196S/I198L/P200T/E204A/T205Q/F208Y	558.7	32	7.0	114.2	170.1
8	E204R	573.5	92	7.0	262.7	427.2
9	I203F/E204A	566.2	81	7.0	294.3	438.4
10	T90A	564.7	955	7.0	351.4	444.9
11	I198L/N202K/E204D	566.6	43	7.0	306.2	456.0
12	A196S/I198L/P200T/E204A/T205Q/F208V	564.2	46	7.0	310.5	461.7
13	E204G/F208V	559.7	122	7.0	352.4	479.7
14	G197E/V199M/E204A/L206M	566.7	62	7.0	329.2	490.3
15	I119T/T121S/A126T	570.7	50	7.5	300.4	490.5
16	E204Q/F208V	558.9	333	7.0	330.0	491.5
17	G197A/I198F/E204G	562.2	72	7.0	343.7	511.9
18	E204C	564.8	92	7.0	404.4	573.9
19	E204G	565.6	82	7.0	402.8	614.6
20	T90A/E194A/E204C	550.4	242	7.5	470.4	626.4
21	E194C/E204C	571.1	487	7.5	466.6	644.8
22	E204N	558.9	112	7.5	407.2	647.8
23	V49N/E204A	568.1	88	8.5	584.3	854.1
24	V49F/E204C	554.8	106	7.5	577.3	881.1
25	V49N/E204N	560.1	122	8.5	548.5	882.7
26	V49A/T205A	557.1	84	9.5	631.0	892.5
27	T90A/E204Q	562.4	502	7.5	713.7	897.4
28	V49N/E204Q	561.8	219	8.0	597.2	902.0
29	V49N	562.6	120	10.0	589.2	921.7
30	V49A	566.4	217	9.5	641.3	924.4
31	T47Q/V49A/P50T	561.0	75	9.5	691.2	950.3
32	V49N/T90A	567.7	740	10.0	648.3	955.5
33	V49N/T90A/E194A/E204C	563.0	242	8.5	432.2	962.2
34	V49A/I119T/T121S/A126T	559.2	73	8.0	738.4	977.3

[a] All data measured at 35°C. Table S1 presents results for all the mutants with Q_{total}>10.
[b] The mutants are listed in order of increasing Q_{total} values.
[c] The observed absorption maximum in nanometers in the light-adapted (LA) state.
[d] Δt_{cycle} refers to the total photocycle time in milliseconds, and is defined by the total time required for the 66% recovery of the resting state.

[e] The pH column indicates the pH at which the experimental data were collected, not necessarily the pH for optimal Q_{total}.

photochemistry, V49A/I119T/T121S/A126T. Without introducing pH as a variable, V49A demonstrates a relatively modest Q_{total} value of 623.1 at pH = 7 and would have not been discovered as an important mutant for access to the branched photocycle. While V49A has been previously studied to learn more about the proton translocation pathway, it has largely fallen under the radar as a viable biomaterial for device applications. For the remainder of this paper, we will characterize the **Q** state photochemistry of V49A and will also discuss its role in the BR quadruple mutant with the highest Q_{total} value.

2.3.3. Influence of pH on V49A Q State Formation and Reversion

The single site mutation, V49A, displays a Q_{total} of 924 (Table 2.2), a value comparable to the best mutant discovered throughout the directed evolution study, V49A/I119T/T121S/A126T. V49A has a Q_{total} which is ~62 times larger than the native protein at pH = 7, and is the best single site mutation with respect to **Q** state formation discovered to date after pH optimization. This finding is significant because the performance of a protein in a paged volumetric memory scales approximately as $Q_{formation}$ x Q_{total}.[139]

First we will explore the mechanism of V49A with respect to $Q_{formation}$. This mutant has been examined by other investigators with respect to structure and function,[92] and in combination with D85N, as a potential candidate for blue membrane based devices.[90,140] Interestingly, it is only after pH scans that V49A is revealed to be an efficient **Q**-forming mutant at alkaline pH. Figure 2.11A shows the absorption spectra of V49A in select pH conditions following the illumination criteria described above (100 mW/cm^2; >640 nm; 35 °C; 3 hours), which was used to analyze $Q_{formation}$. At pH 6.5 and 7.5, a small absorption band is present at 390 nm, which suggests only modest formation of the **Q** state. Once V49A is exposed to more alkaline conditions, the protein is able to fully convert to the **Q** photoproduct. The V49A mutant has the

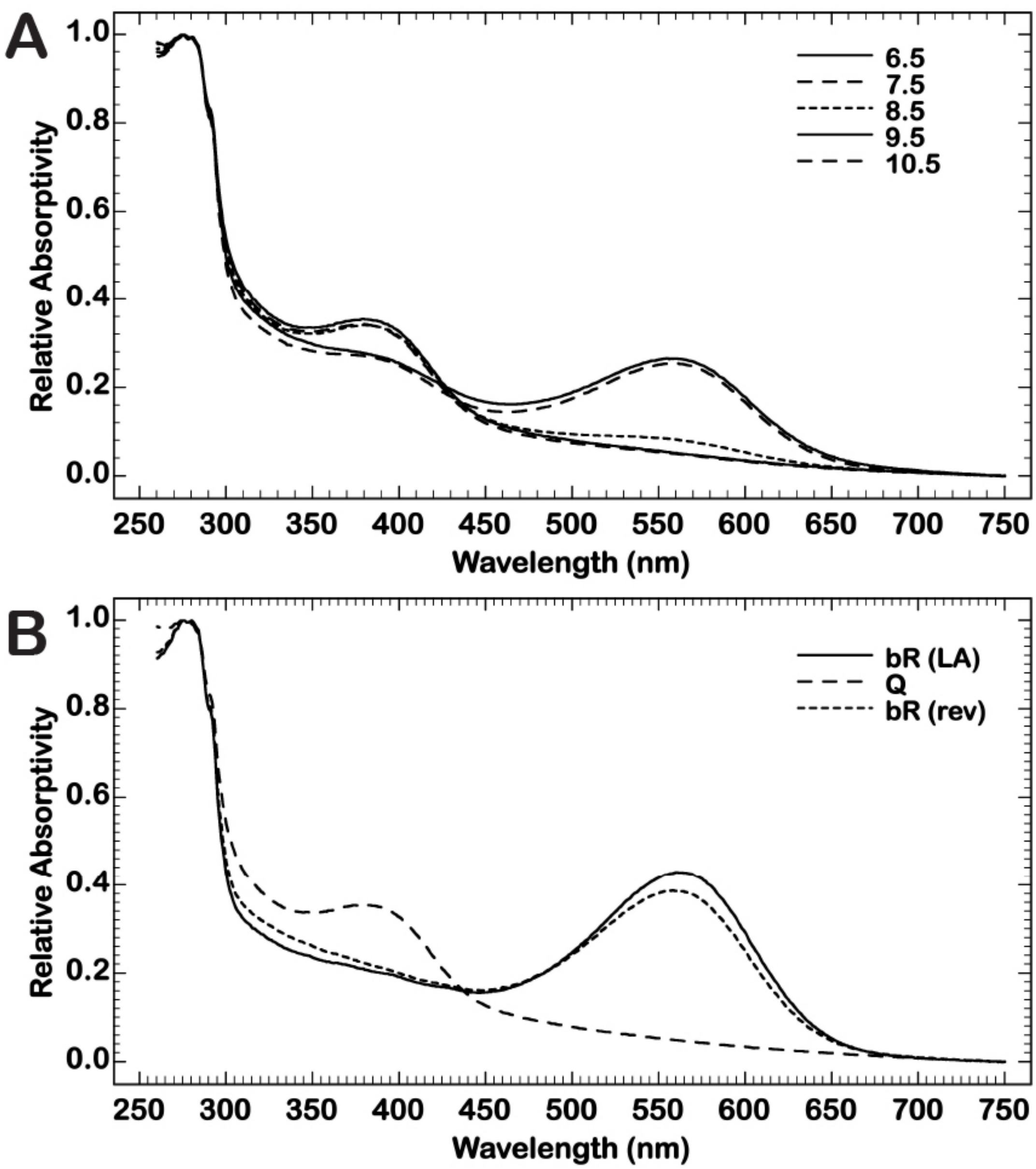

Figure 2.11. Absolute absorption spectra of the **Q** state of V49A in different buffers (A) and the formation and reversion of V49A at the optimal pH (B). The spectral set in panel (A) represents the absorption spectra following the exposure to the illumination conditions used in the directed evolution study (100 mW/cm^2; >640 nm; 35 °C; 3 hours) to determine $Q_{formation}$. The numbers used to label each spectrum refer to the pH of the solution. The spectra in panel (B) show the initial **bR** state (**bR(LA)**), the **Q** state, and the **bR** state after reversion from **Q** (**bR(rev)**). These three spectra were measured in pH 9.5 buffer, which is the optimal pH determined for the highest Q_{total} of V49A.

highest $Q_{formation}$ and Q_{total} at pH 9.5, and the absorption spectra of the LA **bR** state, the **Q** state, and the reverted **bR** state are shown in Figure 2.11B.

As shown in Figure 2.12, at pH = 7, V49A drops to a Q_{total} significantly lower than that at pH = 9.5. Additionally, $Q_{formation}$ behaves similarly (see below).[141] The value of Q_{total} between pH = 1 and pH = 12 fits well to three pK_a values of 3.689, 7.053, and 9.396, and this observation suggests that the protonation state of multiple residues or complexes is likely responsible for the enhancement of the **Q** state photochemistry. The interplay between these possible residues and the mechanism of **Q** state formation and reversion is examined further below in more detail. Recall that we are dealing with the branched photocycle, and if we assume a photochemical pathway that is similar to WT-BR, the formation of the **P** state and subsequently the **Q** state involves excitation of the **O** state (Figure 2.2). Residue Asp-85 is protonated in the **O** state, and this residue has an intrinsic pK_a that varies from 2.5 to 9 depending upon the localized environment during the photocycle of WT-BR.[142,143] In addition, the residue D96 has been assigned a pK_a of ~7.5 during the **N** intermediate, and therefore may also be responsible for the pH dependence of $Q_{formation}$.[144] Time-resolved absorption spectroscopy and an analysis of binding site of V49A allows us to explore the involvement of these residues and the mechanism in more detail below.

2.3.4. Photocycle of V49A

Because the **O** state is the access point from which the branched photocycle is reached, the quantum efficiency of the **O** to **P** state transition must be improved to make use of the **Q** photoproduct in BR-based technologies. Photochemical formation of the **P** state is measured for a deionized form of the native protein to be $\Phi \leq 1.2 \times 10^{-4}$,[134] which is significantly lower than Φ for the primary photochemical event (0.65). Improving access to the branched photocycle can be

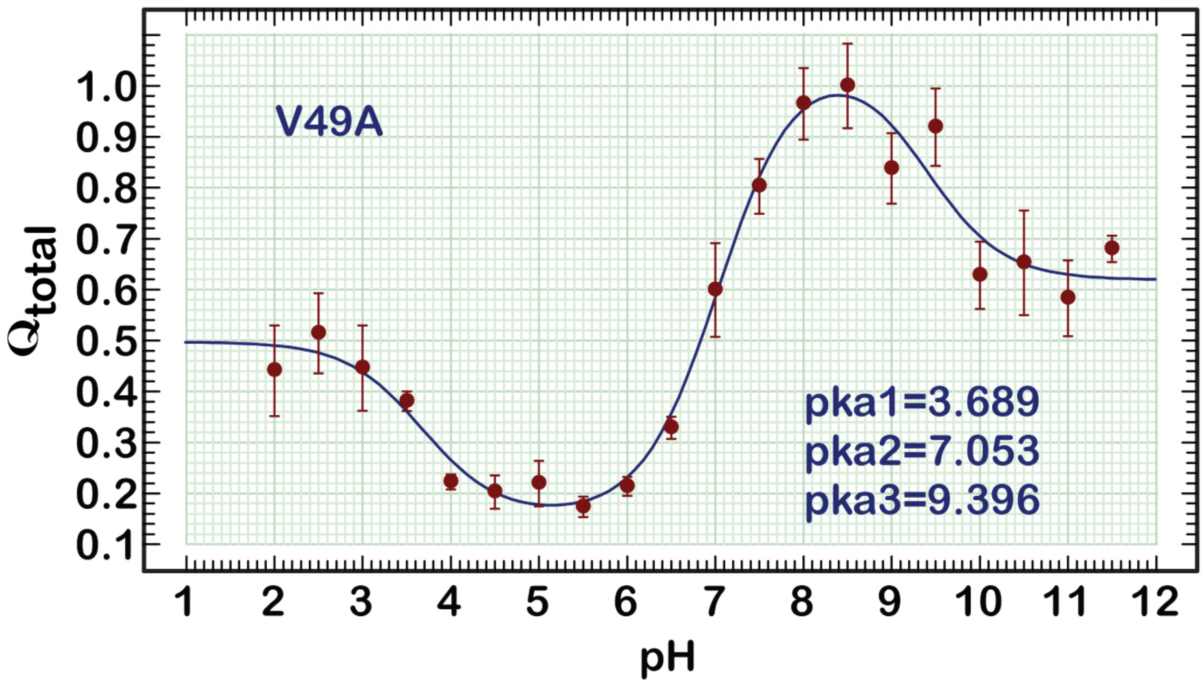

Figure 2.12. The effect of pH on the photochemical efficiency of **Q** state formation in V49A. The data was fit (blue trace) to a 3-term Henderson-Hasselbach equation and was used to extract the three pK_a values that are labeled on the plot. The fit indicates that there are three residues that are likely involved with the enhanced formation of the **Q** state at alkaline pH (see text).

achieved through three mechanisms: (1) increasing the **O** state yield, (2) increasing **O** state lifetime, and/or (3) perturbing the binding site to enhance all-*trans*$\rightarrow$9-*cis* photochemistry. At alkaline pH, V49A shows evidence of improvement through all three of these processes. In this section, we analyze the pH-dependent changes in the photocycle of WT-BR and V49A in order to understand the mechanism of the enhanced formation of the **Q** photoproduct observed through the V49A mutation.

The left-hand panels of Figure 2.13 depict the time-resolved absorption difference spectra for WT-BR in pH 6.5, 7.5, 8.5, 9.5, and 10.5 buffers. The nature of the spectra are similar to what has been previously observed for WT-BR at the ms time scale, in which the positive peak at 410 nm measures the formation and subsequent decay of the **M** state, the bleaching and recovery at 570 nm is due to the decrease in population of **bR** coincident with light absorption, and the small peak observed at 640 nm is presence of the **O** photointermediate. The lifetimes of each of the photointermediates remain consistent throughout the range of pH environments investigated here (Table 2.3), however, above pH 9.5, there is little to no **O** state formation and the **bR** and **M** states are elongated compared to neutral conditions.[145] The disappearance of the **O** state has been attributed to the slowing reprotonation of Asp-96 during the **N**$\rightarrow$**O** transition[144,146,147] and the prevention of proton transfer to the PRC.[148-151] Because this sequence is disrupted, the typical **O** state spectrum is undetected.

The V49A photocycle exhibits similar spectra linked to a preserved *wild-type*-like proton pumping mechanism, however, there are key differences that elucidate enhanced entry into the branched photocycle. The right-hand panels of Figure 2.13 show time-resolved absorption difference spectra for V49A at select pH values amongst the range studied. The **M** state absorption bands are red-shifted to 430 nm for each sample. Moreover, a red-shifted negative

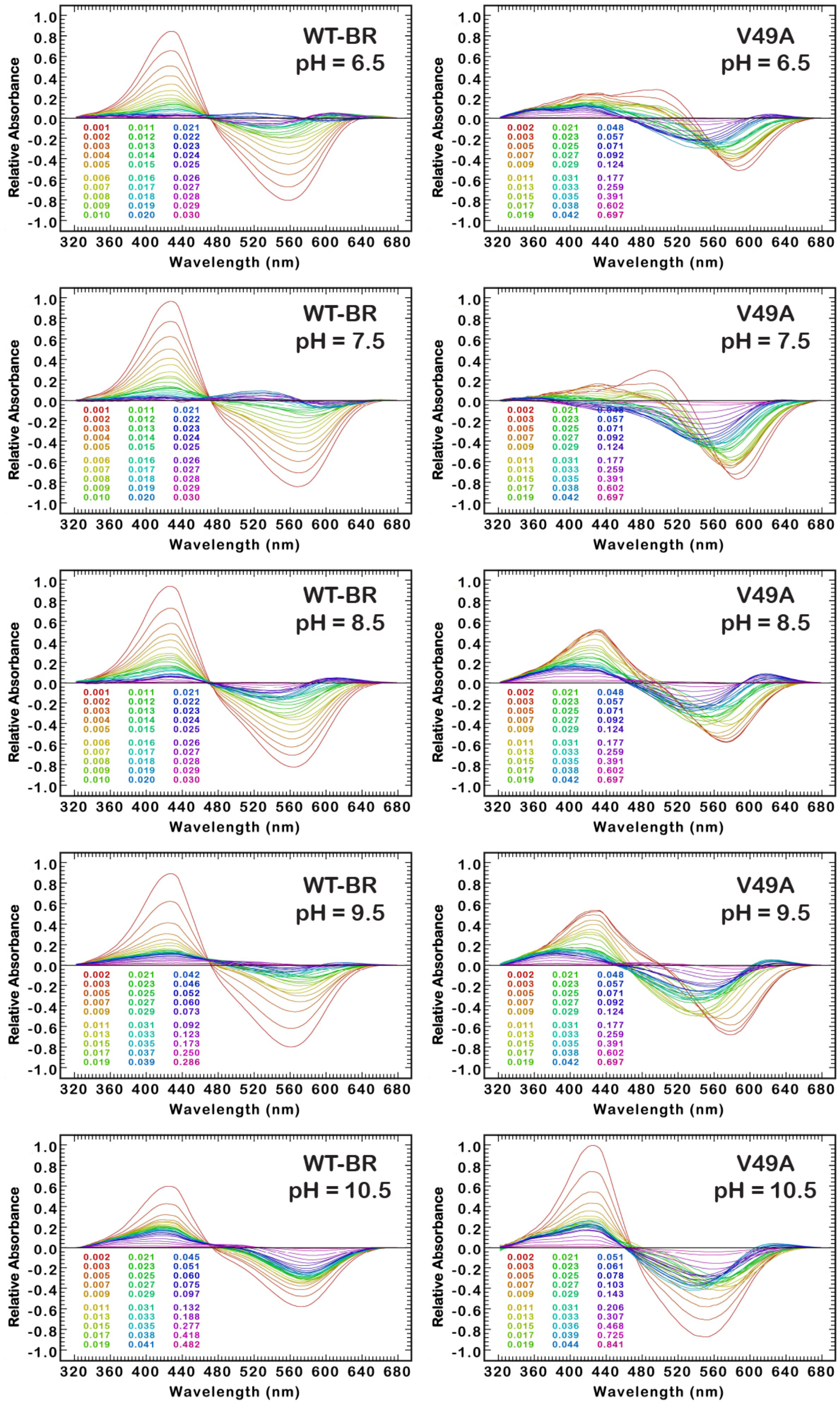

Figure 2.13. Time-resolved difference spectra of WT-BR (left panels) and V49A (right panels) in various buffered solutions at the pH values indicated. The list of numbers in each panel represent the time (in seconds) after light absorption by the sample, and the color of these numbers correspond to the color for each spectrum in the data sets.

Table 2.3. Lifetimes of Select Photointermediates of the Photocycles of WT-BR and V49A, Including the **M** state (τ_M, 410 nm), **bR** state (τ_{bR}, 570 nm), and **O** state (τ_O, 630 nm).

	WT-BR	V49A	WT-BR	V49A	WT-BR	V49A
pH	τ_M (ms)	τ_M (ms)	τ_{bR} (ms)	τ_{bR} (ms)	τ_O (ms)	τ_O (ms)
6.0	11.27	67.40	6.642	141.51	10.53	225.41
6.5	10.27	76.77	5.956	110.91	11.46	178.15
7.0	16.55	64.05	7.37	101.98	12.16	176.88
7.5	11.37	59.11	6.25	95.52	11.49	167.38
8.0	11.55	79.57	7.30	82.53	13.20	164.04
8.5	16.82	54.93	8.78	83.97	41.79	151.77
9.0	21.94	50.42	11.61	99.22	50.43	126.55
9.5	20.13	57.06	12.26	111.99	56.64	123.94
10.0	48.33	59.93	52.70	164.10	N/A	75.79
10.5	82.97	102.09	146.09	250.75	N/A	74.79

peak is observed in the difference spectra at 590 nm following light-absorption, which suggests the initial formation of a transient **O**-like species wherein both the PSB and Asp-85 are simultaneously protonated with an all-*trans* chromophore. This phenomenon has been previously observed and is described as a spontaneous protonation of Asp-85 that aids in lowering the barrier of photoisomerization by about 4.5 kcal/mol.[152] While it is not clear why this protonation would occur following light absorption by V49A, the increased distance between the PSB and Asp-85 destabilizes the positive charge on the nitrogen of Lys-216, provides greater flexibility of the carbon chain in the R group of Lys-216, and likely increases the pK_a of Asp-85 to facilitate this spontaneous protonation during the initial stages of the photocycle.

The increased flexibility of the Lys-216 side chain is also evident in the presence of an additional band appearing in the transient absorption spectra at ~490 nm. This species can be linked to a transient **P**-like photointermediate, which has a covalently linked 9-*cis* chromophore and has been shown to absorb at 490 nm when the $\mathbf{P_1}$ and $\mathbf{P_2}$ intermediates (λ_{max} = 525 and 445 nm, respectively) are observed simultaneously.[81] This effect demonstrates one of the key mechanisms for enhanced **Q** state photochemistry, in which the binding site electrostatics readily accommodates the 9-*cis* conformation of retinal. Further discussion of the nature of the V49A binding site will be provided in detail below.

Despite the presence of additional features not observed in WT-BR, the V49A time-resolved absorption spectra at pH ≤ 7.5 similarly exhibits a low **O** state yield, which leads to a modest Q_{total} for this BR mutant (see Table 2.2). For WT-BR, the $\mathbf{N} \rightarrow \mathbf{O}$ transition is characterized by proton uptake from the cytoplasm by Asp-96, followed by the isomerization of 13-*cis* to all-*trans* retinal.[77-79] The pK_a of Asp-96 is decreased from 11 in the unphotolyzed state to ~7.5 during the **N** photointermediate.[144] Below the pK_a of Asp-96 during **N**, the residue is

already protonated and the **N** state decays without accessing the **O** state;[144] however, when the pH environment is above the pK_a, the typical rise of the **O** state is observed and the photocycle is able to proceed to the final stages.[153] Dioumaev *et al.*[102] measure the pK_a of proton uptake by Asp-96 for V49A is ~7.0, which is lower than that of WT-BR by 0.5 pH units. This pK_a matches the measured pK_{a2} in Figure 2.12, illustrating that the proton affinity value of Asp-96 during the **N** state is important to improving Q_{total}. At higher pH, the more conventional **N** state is formed, and the protein is able to proceed to the **O** state unhindered.

The Q_{total} of V49A is particularly high between pH values of 8.0 and 9.5 (Figure 2.12). The photocycle of the BR mutant at this range is characterized by a number of important features. First, the **O** state yield is significantly higher than what is observed either below or above these pH values, as observed by the relative increase in the **O** state band in the time-resolved difference spectra of Figure 2.13. The presence of the **O** state is also notably higher than all WT-BR measurements in this study. Secondly, the **O** state demonstrates a ~10-fold increase in lifetime when compared to WT-BR (Figure 2.13; Table 2.3) and yields a significantly improved probability of absorbing a second photon to access the branched photocycle. A slow **O** state decay is linked to the prevention of proton transfer from Asp-85 to the PRC,[80] i.e., a change in the pK_a of Asp-85 and a shift in the **O** → **bR** equilibrium towards the **O** state. The pK_{a1} and pK_{a3} values calculated in Figure 2.12 can be connected to the pK_as of Asp-85 and the PRC, respectively, during this proton transfer reaction. For Asp-85, $pK_a = 9.396$ is significantly higher than what is observed for WT-BR during **O** state proton transfer, which suggests a higher proton affinity and slower rate of transfer from Asp-85 to the PRC (i.e., a slower **O** decay rate). Moreover, the pK_a of the PRC during the **O** state is shown to be 4.5 for WT-BR,[147,153] and a lowering to $pK_{a3} = 3.689$ adds to the decreased rate of proton transfer at this critical stage of the

photocycle. The combination of raising of the pK_a of Asp-85 and the lowering of the pK_a of the PRC is likely the key mechanism for the high **Q** state formation of V49A between a pH of 8.0 and 9.5. Val-49 directly stabilizes Asp-85 and has a long-range conformational interaction with Glu-204 of the PRC,[94,95] and the mutation of this residue with a smaller hydrophobic residue (alanine) alters the binding site electrostatics enough to have a profound impact on these protonation states during the **O** state.

Above a pH of 9.5, we notice that Q_{total} begins to decrease. Above pK_{a3} of Asp-85 during the **O** $\rightarrow$ **bR** transition, the rate of proton transfer from Asp-85 to the PRC increases significantly. This feature is reflected in the lowering of the **O** state lifetime at pH 10.0 and 10.5 when compared to the remaining photocycle data measured for V49A (Table 2.3), which is coincident with a less efficient access to the branching reaction of BR. Despite this decrease in efficiency, the **O** state is still present at pH > 9.5 for V49A, and WT-BR does not form **O** in this environment. The decrease of the pK_a of Asp-96 during the **N** $\rightarrow$ **O** transition and the increase and decrease of the pK_as of Asp-85 and the PRC, respectively, during the **O** $\rightarrow$ **bR** transition are all interrelating features that help to enhance the stability and lifetime of the **O** state and, consequently, improve Q_{total}.

2.3.5. Chromophore and Binding Site Analysis of V49A

Another key mechanism of **Q** state enhancement in V49A is associated with enhanced stability of the 9-*cis* chromophore in the binding site. In the native protein, the DA form selects a mixture of all-*trans* and 13-*cis* chromophores that is close to a 50:50 mixture (Figure 2.14).[154,155] Because the protein must readily accommodate the 13-*cis* conformation during the transient photointermediates, the protein thermally relaxes to equal populations of the chromophore. Upon exposure to light, the 13-*cis* chromophore is photoconverted to an all-*trans* conformation, which

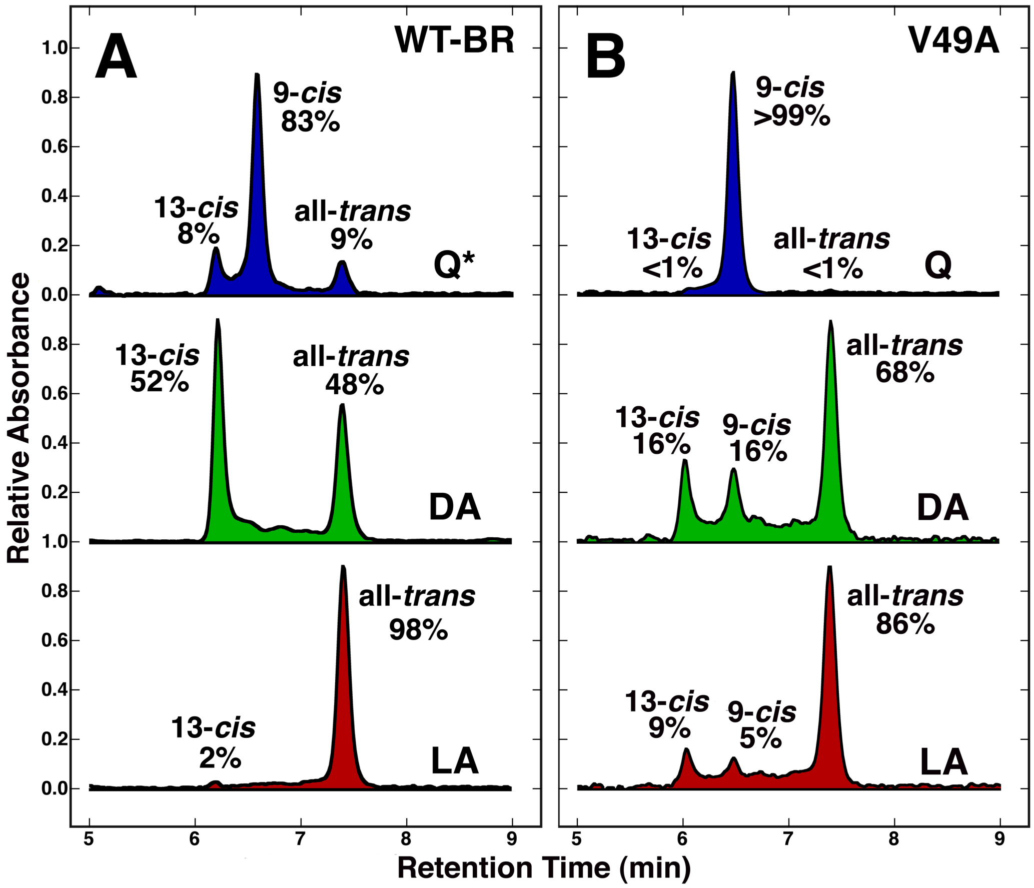

Figure 2.14. Analysis of chromophore configuration after cold extraction from dark-adapted (DA) and light-adapted (LA) native BR (WT-BR) (A) and V49A (B). The native protein contains a mixture of 13-*cis* and all-*trans* configurations in the DA state (Figure 1).[51] Upon exposure to light, the 13-*cis* configuration is photoconverted to an all-*trans* configuration, and it is the latter chromophore, which undergoes the photocycle shown in Figure 2.2. V49A, however, is unique in selecting a large amount of 9-*cis* chromophore in the DA state.

renders the protein available to initiate the light-induced photocycle shown in Figure 2.13. V49A, however, is unique in selecting a large amount of 9-*cis* chromophore in the DA state. The chromophore extraction data reveal that the binding site of V49A is just as capable of stabilizing 9-*cis* retinal as it is in forming 13-*cis* retinal. The LA form of V49A also shows some propensity to form 9-*cis* retinal in the chromatograms in Figure 2.14, even though this isomer is not directly involved in the proton-pumping mechanism. The presence of 9-*cis* during light adaptation is supported by the time-resolved absorption spectra shown in Figure 2.13, wherein a transient species absorbing at 490 nm (i.e., a **P**-like state) is accessed from pH 6.0 to pH 9.5. However, we cannot rule out the possibility that the **Q** state was formed during LA conditions for V49A. In fact, Greenhalgh *et al*.[98] reports that the LA retinal isomer composition of V49A is 71% all-*trans*, 18% 13-*cis*, and 11% other *cis* conformations. This observation was also linked to the formation of broad, blue-shifted bands, which can now likely be labeled as possible **Q** state formation.

The preferential formation of 9-*cis* in the DA state of V49A (Figure 2.14) provides insight into the comparative advantage that V49A exhibits in forming the **P** and **Q** states, both of which contain a 9-*cis* chromophore. Figure 2.14 demonstrates that the **Q** state of V49A is capable of forming > 99% 9-*cis* retinal. The difference in the 9-*cis* formation between the **Q** and **Q*** states is attributed to the fact that WT-BR can never form pure **Q** state, but instead forms a mixture of **P** and **Q** states, known as **Q***. Because the barrier for the **Q→bR** photoreaction is 190 kJ/mol in LA WT-BR,[81] a large amount of energy is needed for reversion to the resting state. The **P** state can decay to the **bR** resting state fairly easily, and it is likely that a small amount of **Q*** contains unstable **P** state that reverts rapidly.

Although several other V49X mutants select a 9-*cis* conformation (Table 2.4), we found no

Table 2.4. Retinal Composition of Dark-Adapted (DA) and Light-Adapted (LA) WT-BR and V49X[a]

	dark-adapted (DA)			light-adapted (LA)		
protein	13-*cis*	9-*cis*	all-*trans*	13-*cis*	9-*cis*	all-*trans*
WT-BR	52%	-	48%	2%	-	98%
V49A	16%	16%	68%	9%	5%	86%
V49F	17%	15%	68%	10%	8%	82%
V49N	21%	2%	77%	10%	3%	87%

other site replacement that yielded 9-*cis* selection. The selection of 9-*cis* is a key attribute in creating a high **Q**-forming mutant because the $O \xrightarrow{h\nu} P$ photochemical reaction involves an all-*trans* to 9-*cis* isomerization. By providing a binding site that preferentially accommodates 9-*cis*, V49A enhances the stability of the **P** state and appears to also lower the activation barrier to the formation of the **P** state. This observation means that **O** state photochemistry is directed preferentially towards the **P** state rather than a 13-*cis* photoproduct (a back reaction to form **N**).

The FTIR difference spectra of V49A in the **bR** and **Q** states are shown in Figure 2.15. While this is the first vibrational analysis of the **Q** photoproduct formed in BR, the peaks do agree with values from an investigation by Rüdiger *et al.*[156], which reports the characterization of unbound 9-*cis* retinal in the binding site to elucidate the pathway of reconstitution of WT-BR from the apoprotein. The green trace demonstrates the **Q**–$\mathbf{bR_{LA}}$ difference spectrum for V49A. The strongly absorbing positive peak at 1655 cm^{-1} are shown to be the C=O stretching mode of the hydrolyzed chromophore, while the measured absorption bands at 1574 cm^{-1} and 1150 cm^{-1} are used as markers for the C=C and C–C stretching modes of 9-*cis* retinal.[156] These modes are also observed for a **P** state investigation of 13-desmethyl BR, although the 9-*cis* chromophore was still covalently liked to protein *via* the PSB ($C{=}N^+$: 1680 cm^{-1}).[154] The negative peaks in this difference spectrum are from the LA form of V49A, in which 86% of the chromophore is in the all-*trans* conformation (see Figure 2.14). The **Q**–$\mathbf{bR_{rev}}$ spectrum (blue trace) is similar to the first trace, with $\mathbf{bR_{rev}}$ referring to the reversion of the **Q** state sample using UV LED irradiation. The similarity of the difference spectra between the **Q**–$\mathbf{bR_{LA}}$ and **Q**–$\mathbf{bR_{rev}}$ traces confirms the restoration of the chromophore and binding site to the **bR** resting state. The $\mathbf{bR_{DA}}$–$\mathbf{bR_{LA}}$ FTIR difference spectrum of V49A, which is analogous to a 13-*cis*–all-*trans* difference spectrum, is similar to what has previously been reported for WT-BR.[157] However, there are small changes in

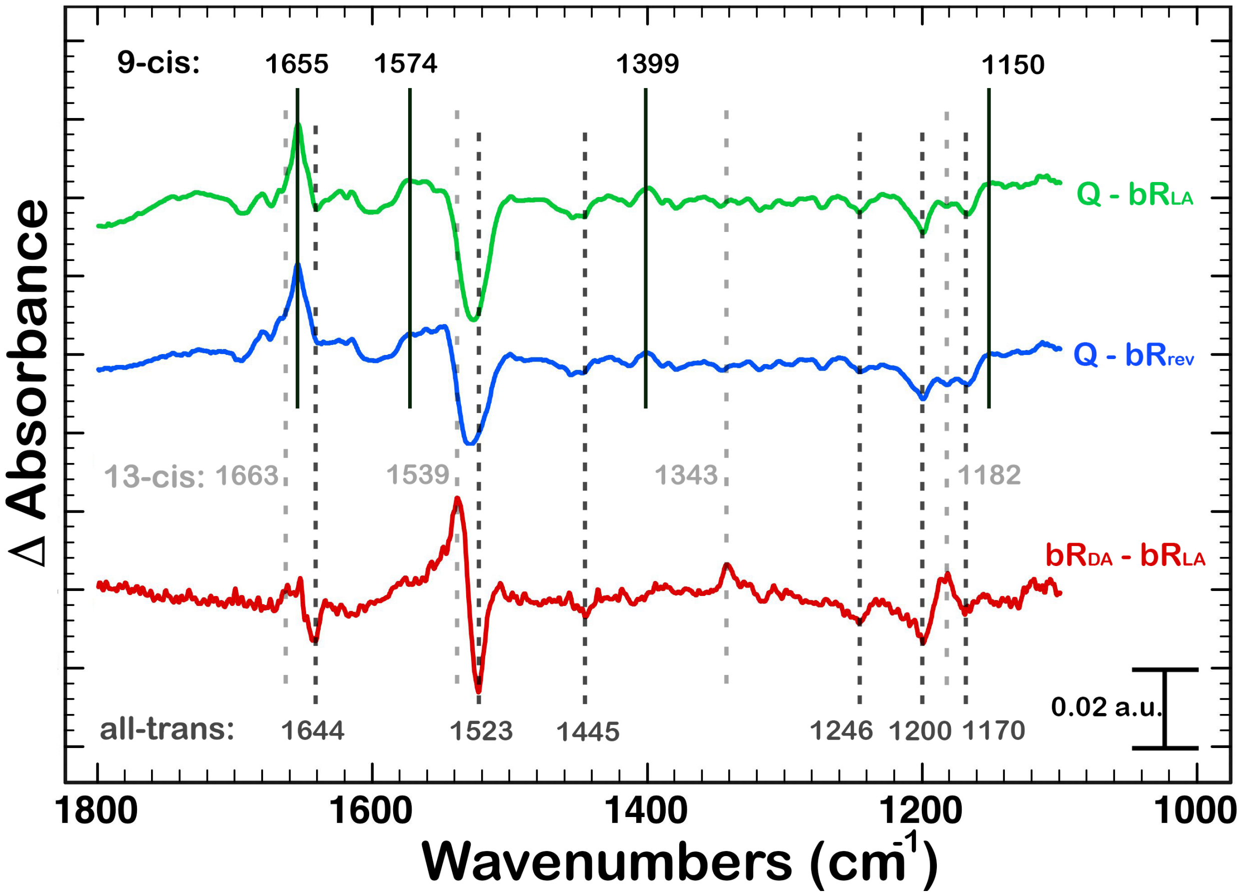

Figure 2.15. FTIR difference spectrum of V49A measured in the 1000 – 1800 cm^{-1} region at room temperature. The **Q** – $\mathbf{bR_{LA}}$ spectrum (green trace) highlights the difference between hydrolyzed 9-*cis* retinal and the all-*trans* chromophore that is covlanetly linked to the Lys-216. The **Q** – $\mathbf{bR_{rev}}$ spectrum (blue trace) is similar to the previous spectrum, however, the **bR** state was reverted after formation of the **Q** state. The bR_{DA} – bR_{LA} spectrum (red trace) shows the difference between the DA and LA chromophore compositions of V49A. Isomer-specific frequencies are pointed out using a solid black line, a dashed dark gray line, and a dashed light gray line for 9-*cis*, all-*trans*, and 13-*cis* retinal, respectively. All samples were in 50 mM TAPS buffer (pH = 8.5) to facilitate efficient **Q** state formation.

frequency due to the change in the binding site following the V49A mutation, and the frequencies are tabulated in Table 2.5. Small contributions of the 9-*cis* vibrational modes pointed out in the **Q** state difference spectra in Figure 2.15 are also present in the positive region of the **bR$_{DA}$–bR$_{LA}$**, which further indicates that the 9-*cis* chromophore is present in the DA form of V49A at alkaline pH.

A comparative analysis between the WT-BR and V49A crystal structures (1C3W[49] and 3HAN[96], respectively) provides key insights into the differences in electrostatics and cavity formation upon the substitution of alanine at the Val-49 position. Figure 2.16 demonstrates that the V49A mutation shifts electron density towards the β-ionone ring, thereby destabilizing the positive charge on the PSB nitrogen, increasing π-electron delocalization, and decreasing the order of double bonds. This electrostatic effect, although small in scale, results in a smaller barrier for isomerization and also allows for the formation of 9-*cis* retinal during the photocycle (Figure 2.12) and greater access to the branched photocycle during the **O** photointermediate. Moreover, the distance between the carboxyl group of Asp-85 and the protonated nitrogen of Lys-216 increases by ~0.2 Å, which further suggests a destabilization of the positively charged PSB and increases the pK_a of Asp-85 during the unphotolyzed state of V49A. Combined, these observations likely lead to the potential observation of a red-shifted negative peak following light-activation, which suggests an **O**-like state with protonated Asp-85 (Figure 2.13). The absence of the two methyl groups of Val-49 also leads to a ~2 Å increase in distance between the side chains of Ala-49 and Lys-216 and an increased flexibility of Lys-216. The higher degrees of freedom of the Lys-216 side chain makes the formation of 9-*cis* more favorable, and the cavity that is created provides a region that can accommodate unbound Lys-216 upon the cleavage of the Schiff base and formation of the aldehyde of unbound 9-*cis* retinal.

Table 2.5. Vibrational Frequencies Assigned to the all-*trans* and 13-*cis* Conformations of Retinal in the Binding Site of V49A[a]

	WT-BR frequency (cm^{-1})[a]		V49A frequency (cm^{-1})[b]	
vibrational mode	all-*trans*	13-*cis*	all-*trans*	13-*cis*
C=N stretch	1641	1663	1644	1663
C=C stretch	1525	1536	1523	1539
C–C–H bend	–	1343	–	1343
C–C stretch	1253, 1200	1181	1246, 1200, 1170	1182

[a]The all-*trans* retinal columns correspond to the negative peaks of a $\mathbf{bR_{DA}}$-$\mathbf{bR_{LA}}$ FTIR difference spectrum, and the 13-*cis* columns correspond to the positive peaks.
[b]All WT-BR data is from reference 157.
[c]All V49A data is from Figure 2.15.

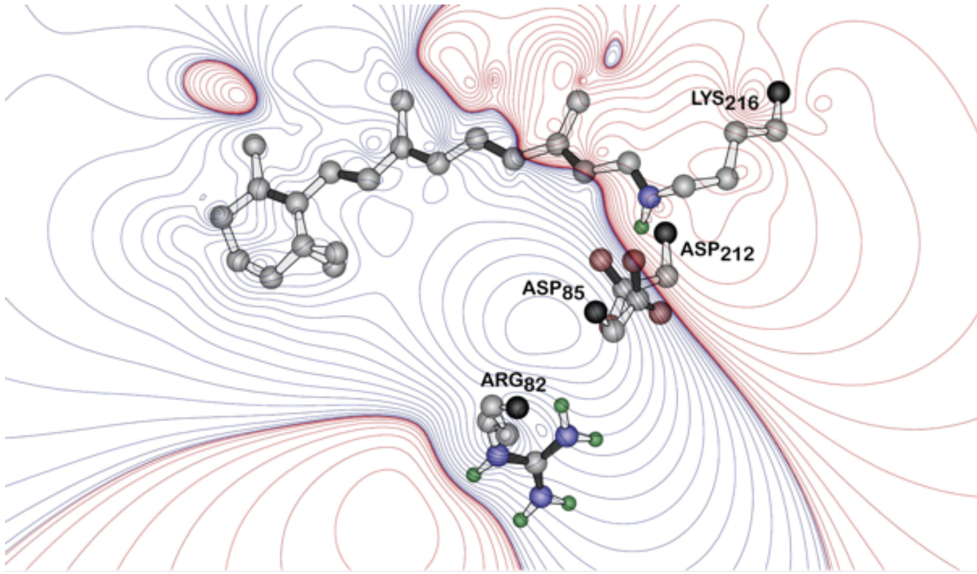

Figure 2.16. An electrostatic difference map associated with the V49A mutation. The red contours indicate an increase in positive charge and the blue contours indicate an increase in negative charge. The electrostatic changes are very small, however, and at maximum are equivalent to the shift of 0.1 electron by one Angstrom. We conclude that the very small electrostatic changes associated with the V49A mutation are of minor consequence to the photophysical properties of V49A.

2.3.6. Thermal Stability of V49A Photoproducts

The structural stability of BR is an important attribute when considering the incorporation of this biomaterial into devices that operate above ambient temperatures (e.g., human intraocular temperature) and within non-native environments. Differential scanning calorimetry is often used to evaluate the conformational changes of protein structure and measure the amount of heat that the material can absorb before denaturing. The point at which the protein is irreversibly denatured is often reported as the melting temperature (T_M) of the protein, which has been reported to be ~98 °C for BR in the purple membrane.[54] The thermal stability of BR has been shown to be sensitive to alkaline or acidic pH environments,[137,138] chemical modulation,[158,159] or altering the lipid environment.[160,161] Moreover, the introduction of point mutations can also have a potentially negative affect on structural stability, and are often exacerbated through multiple mutations of the protein. The V49A mutation is a relatively nominal substitution, in which two methyl groups of valine are replaced with hydrogens. While this small change impacts Q_{total} significantly, the mutant protein maintains *wild-type*-like thermal stability. Even at an alkaline pH of 9.5, which is the optimized pH environment for V49A, the mutant protein has T_M values of 93.7 °C and 84.7 °C for the **bR** and **Q** photoproducts, respectively. In Figure 2.17, the thermograms are relatively simple in nature with one main protein phase transition present for each state, which implies that the protein maintains structural integrity until the T_M is reached. The measured T_M values are more than sufficient to recommend the use of V49A as a stable **Q**-forming mutant in BR-based devices.

2.3.7. Role of V49A in the Quadruple Mutant

The best mutants found after six stages of directed evolution to optimize Q_{total} are listed in Table 2.2. In our analysis so far, we have focused on the single mutation, V49A, since it is the

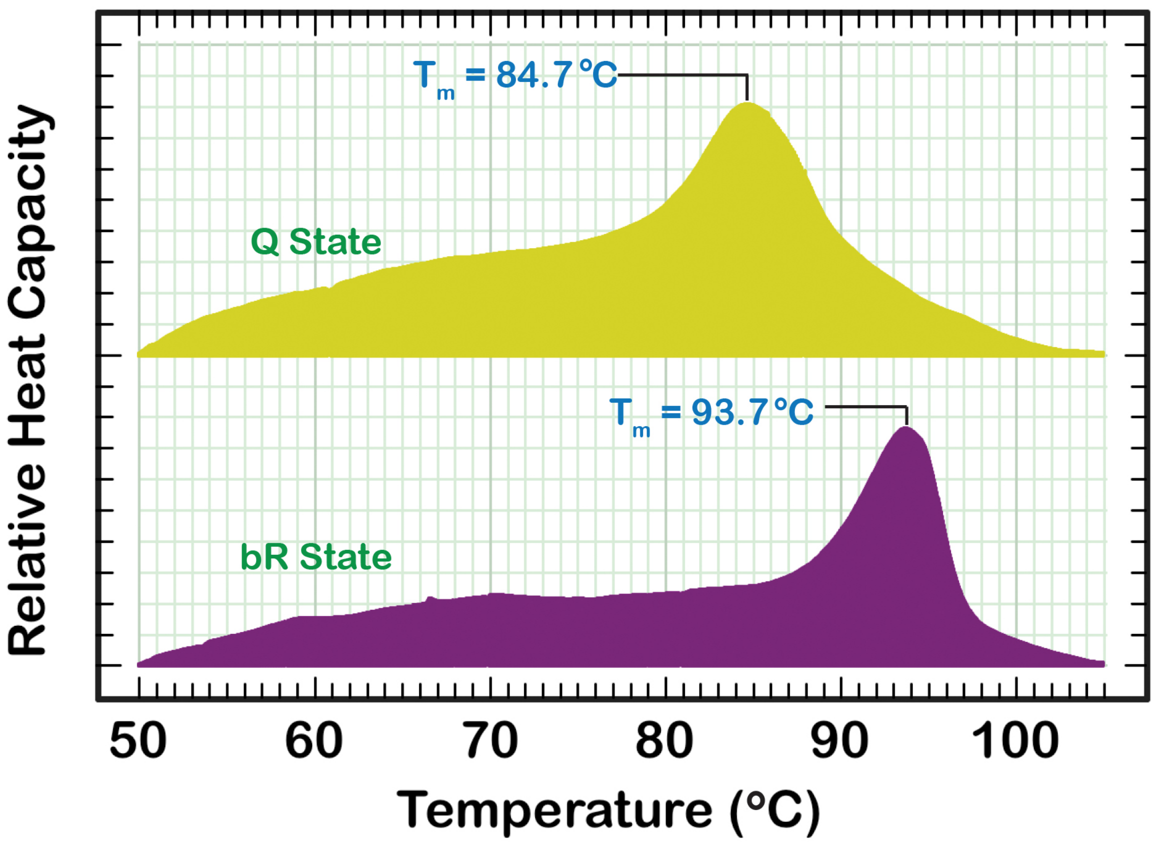

Figure 2.17. Differential scanning calorimetry traces of V49A in the **bR** state (purple) and the **Q** state (yellow). The plotted relative heat capacity is used to compare the melting temperature (T_M) between the two photoproducts of the high **Q**-forming mutant.

highest **Q**-forming mutant that is the result of a single mutation, and plays a key role in other enhanced BR mutants with optimized **Q** state photochemistry. In this section, we examine the best mutant, V49A/I119T/T121S/A126T, which forms the **Q** state *via* two complementary mechanisms: one involving the V49A substitution analyzed in detail above and the second involving the I119T/T121S/A126T triad.

The quadruple mutant, V49A/I119T/T121S/A126T, was generated by combining V49A and the triple mutant I119T/T121S/A126T discovered from semi-random mutagenesis. This triple mutant has two interesting properties. First, it enhances **O** state production. Second, it provides internal electrostatic buffering that shifts the optimal pH for performance towards neutrality. The lifetime of the **O** state in native BR is ~12 ms at 30°C. In the I119T/T121S/A126T mutant, the **O** state lifetime is increased to 42 ms at 30°C. The V49A mutation also has been shown to elongate the **O** photointermediate, however, the key observation is that the triple mutant optimizes the yield of the **O** state as expressed by the dimensionless integral:

$$\text{O state yield} = \frac{1}{\tau_O}\int_0^{\infty}[O]\,dt \tag{2.7}$$

where [**O**] is proportional to the concentration of **O** state (as measured by absorbance at 650 nm divided by the absorbance of the **bR** sample at λ_{max}) and τ_O is the apparent lifetime of the **O** state, as represented by the sum of the formation and decay times of the **O** state. The I119T/T121S/A126T mutant is one of the best mutants found based on **O** state yield as represented by this integral. Based on the titration curves in Figure 2.18, the pK_a values of $Q_{formation}$ are modified slightly for the quadruple mutant when compared to that of V49A. The quadruple mutant forms the **Q** state more efficiently at a lower pH (pH = 8.0), and it is likely no coincidence that pK_{a2} is also decreased significantly relative to V49A (6.004 vs. 6.777,

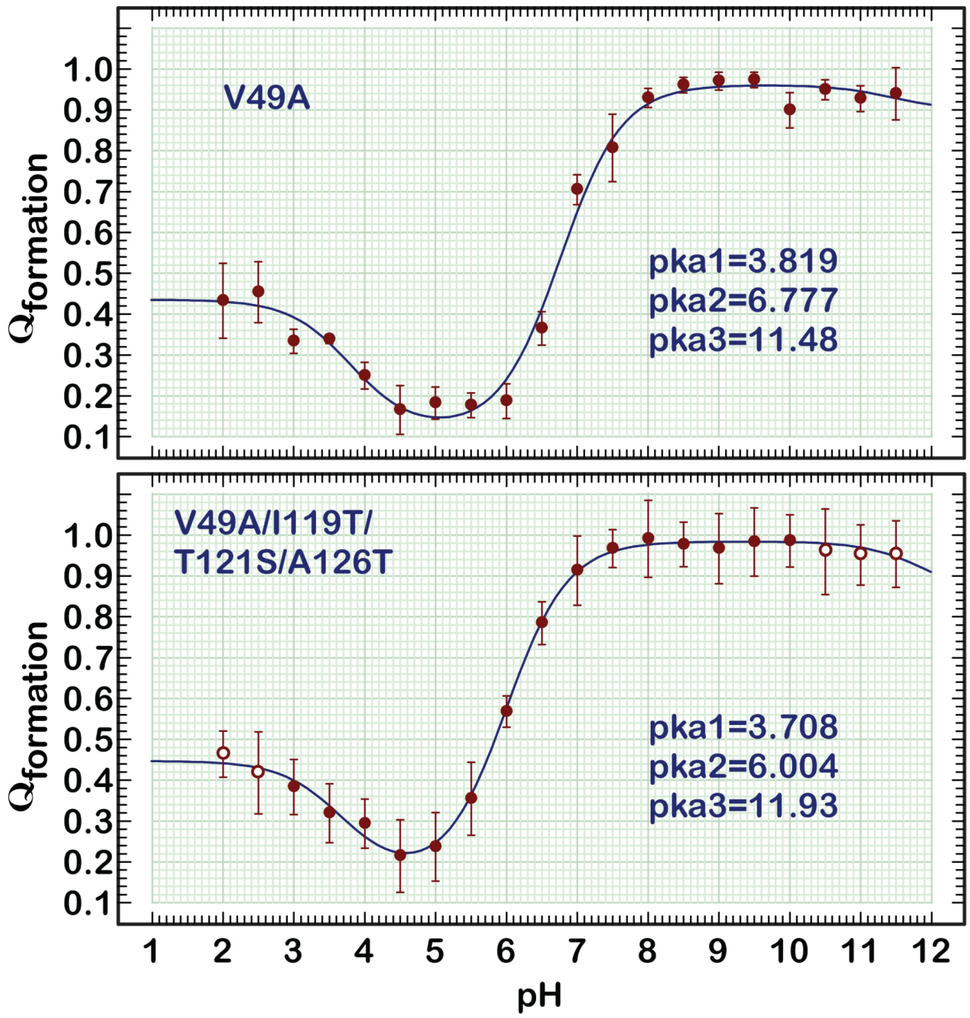

Figure 2.18. The effect of pH on the photochemical efficiency of $Q_{formation}$ in V49A and V49A/I119T/T121S/A126T. The data sets were fit to 3-term Henderson-Hasselbach equations (blue traces) and were used to extract the three pK_a values that are labeled each of the plots.

respectively). This pK_a was linked to that of Asp-96 during the **NO** transition, and the lowering of proton affinity during this stage of the photocycle plays a key role in increasing the **O** state yield and enhancing **Q** state photochemistry.

The mechanism of how I119T/T121S/A126T enhances **O** state production is not fully understood. These three residues are localized near the chromophore ring (Figure 2.19), and the composite impact of this mutant is to increase the number of hydroxyl groups and, thus, the polarity around the chromophore ring. These residues will align with the local dipole moment. MOZYME calculations predict a preferential 17 kJ/mol stabilization of the **O** state, which is due primarily to electrostatics.

The best mutant, V49A/I119T/T121S/A126T, has several advantages over V49A worth noting. First, V49A/I119T/T121S/A126T forms the **Q** state most efficiently at pH = 8.0 (rather than pH = 9.5), due to the role played by hydroxyl groups near the chromophore ring, and what we believe is a self-buffering effect associated with the resulting electrostatic field (Figure 2.19). The small pH difference can be important for the use of the protein to mediate pixels within a protein-based retinal implant (see below), because the pH environment of the intraocular space is closer to neutral. Moreover, in terms of the preparation of memory cuvettes for our three-dimensional optical memory, the ability to make stable polymeric matrices becomes increasingly difficult at alkaline pH.[162,163] Finally, V49A/I119T/T121S/A126T has an excellent $Q_{formation}$ value that allows for the use of very low laser write intensities. When coupled with the relatively fast photocycle time (73 ms), the protein can be driven to **Q** more and efficiently.[139] The key advantage of V49A is the ease of preparing this mutant and the excellent stability of this protein. It is roughly twice as stable as V49A/I119T/T121S/A126T.

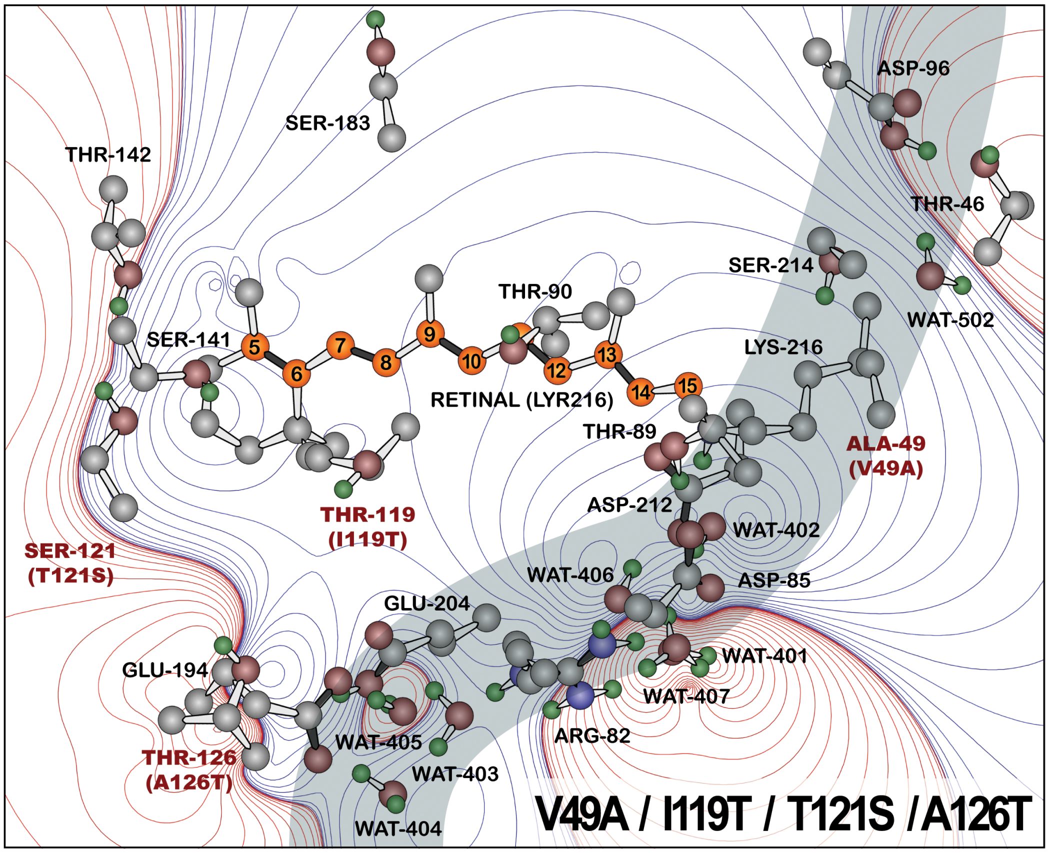

Figure 2.19. Location of the residues modified to form the high Q mutant V49A/I119T/T121S/A126T, with the relevant residues marked with red lettering. Other residues that are important to the photochemical properties or proton translocation process are also shown. The proton channel is marked in light blue. The contours of the electrostatic difference map associated with the quadruple mutation are shown in the background, where red contours indicate an increase is positive charge and the blue contours indicate an increase in negative charge. The key electrostatic impact of the mutation is to increase negative charge in the Asp-85 (D85) and Asp-212 (D212) region which stabilizes the protonation of D85 and prolongs the yield and lifetime of the **O** state. The V49A component of this mutation also preferentially stabilizes the 9-*cis* conformation. Contour lines are drawn at the following energies (J/mol): ±1, ±6, ±21, ±49, ±96, ±170, ±260, ±390, ±560, ±760, ±1000, ±1300, ±1700, ±2100, ±2600, ±3100, ±3800, ±4500, ±5200, ±6100. This figure is based on Figure 7 from reference 46.

2.3.8. Q State Formation within a Retinal Implant

Up to this point, we have characterized the branching reaction of the V49A photocycle and have measured the efficiency of this photochemistry in various aqueous buffer solutions. One application of the V49A mutant is for mediating the active surface area of a protein-based retinal implant in order to deactivate the proton pumping mechanism while implanted into the subretinal space. This study is the first to use a mutant form of BR to fabricate a protein-based retinal implant, and serves as a proof of concept for the pixel mediation capability that can be beneficial for the targeted patient or end-user.

The absorption spectra of the implant are first measured to demonstrate the ability to convert the V49A layers between the two photoproducts (**bR** and **Q** states, Figure 2.20). The solid line (1) shows the absorption spectra of the implant in the **bR** state, whereas the dashed line (2) shows the absorption spectra of the implant in the **Q** state. A photograph of the films with the V49A protein in each photostate is shown in the insert. The **Q** state has a transparent/yellow color with an absorption maximum on the periphery of the visible spectrum (~380 nm). This state is reversible, but a high intensity UV light is required to drive the protein back to the photoactive **bR** state, which is characterized by the vibrant, purple color shown in Figure 2.20. Spectral analysis indicates that the film has completely converted from the **bR** resting state to the **Q** state using the red LED light bank (100 mW/cm^2) for 8 hours. There is no spectroscopic evidence of protein denaturation following the immobilization of the protein within the retinal implant architecture, and following the intense red light exposure, the device retained a high optical clarity as suggested by minimal absorption in a wavelength range of > 700 nm.

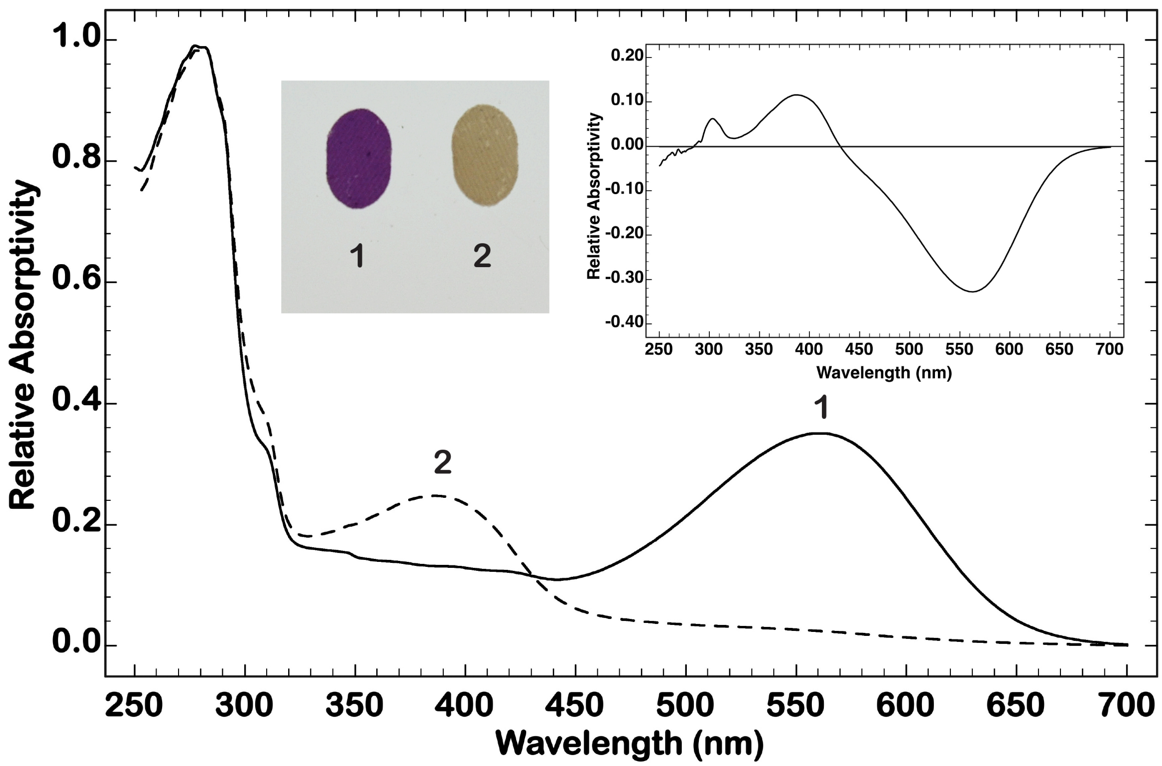

Figure 2.20. Absorption spectra of the protein-based retinal implants in the **bR** state (solid line) and the **Q** state (dashed line). The left inset image is a photograph of the retinal implants in the **bR** state (1) and **Q** state (2) after red LED illumination. The right inset figure shows the difference spectra, in which the **bR** state spectrum is subtracted from the **Q** state spectrum.

2.3.9. Pixel Characterization using a Foveated Image Sensor

The foveated image sensor is used as a proof-of-concept experiment to demonstrate the capability of monitoring **Q** state formation within a retinal implant architecture. Following a demonstration that the retinal implant could be completely converted to the **Q** photoproduct under intense LED illumination (Figure 2.20), the image sensor is subsequently used to quantify differences in pixel intensities through a contrast comparison between the **bR** and **Q** states. Because the foveated imager does not provide a color image, a gray scale is used to measure the difference between the purple pixels of **bR** and the transparent/yellow pixels of the **Q** state. A histogram of the image acquired by the foveated image sensor (Figures 2.21A and 2.21B), shows a shift in the pixel intensity to the right, reflecting an increase in the number of AP firing events recorded by the pixels (x-axis). The number of active pixels corresponding to the image area that is illuminated is depicted on the y-axis. The observed shift corresponds to the formation of the **Q** state, where a brighter image will result in a higher number of APs. In contrast, a "zero" events situation would correspond to the reference background (black color) where no image is detectable, and where only the dark current noise would prevail. This is an expected result, since a brighter shade of gray results in a higher light intensity which in turn triggers the photodiodes to generate more APs over a given time domain. Because the **bR** state results in a darker shade of gray, the light intensity falls and the photodiodes would reduce the number of APs generated over the same period. However, a comparable amount of active photodiodes should be present in both the **bR** and **Q** state recording.

Throughout this study, we first record the maximum frequency corresponding to complete **Q** state formation, and the lowest frequency, corresponding to the film resting in the **bR** state. Considering Figure 2.21, there is an output frequency increase of 2 AP/s (or 120

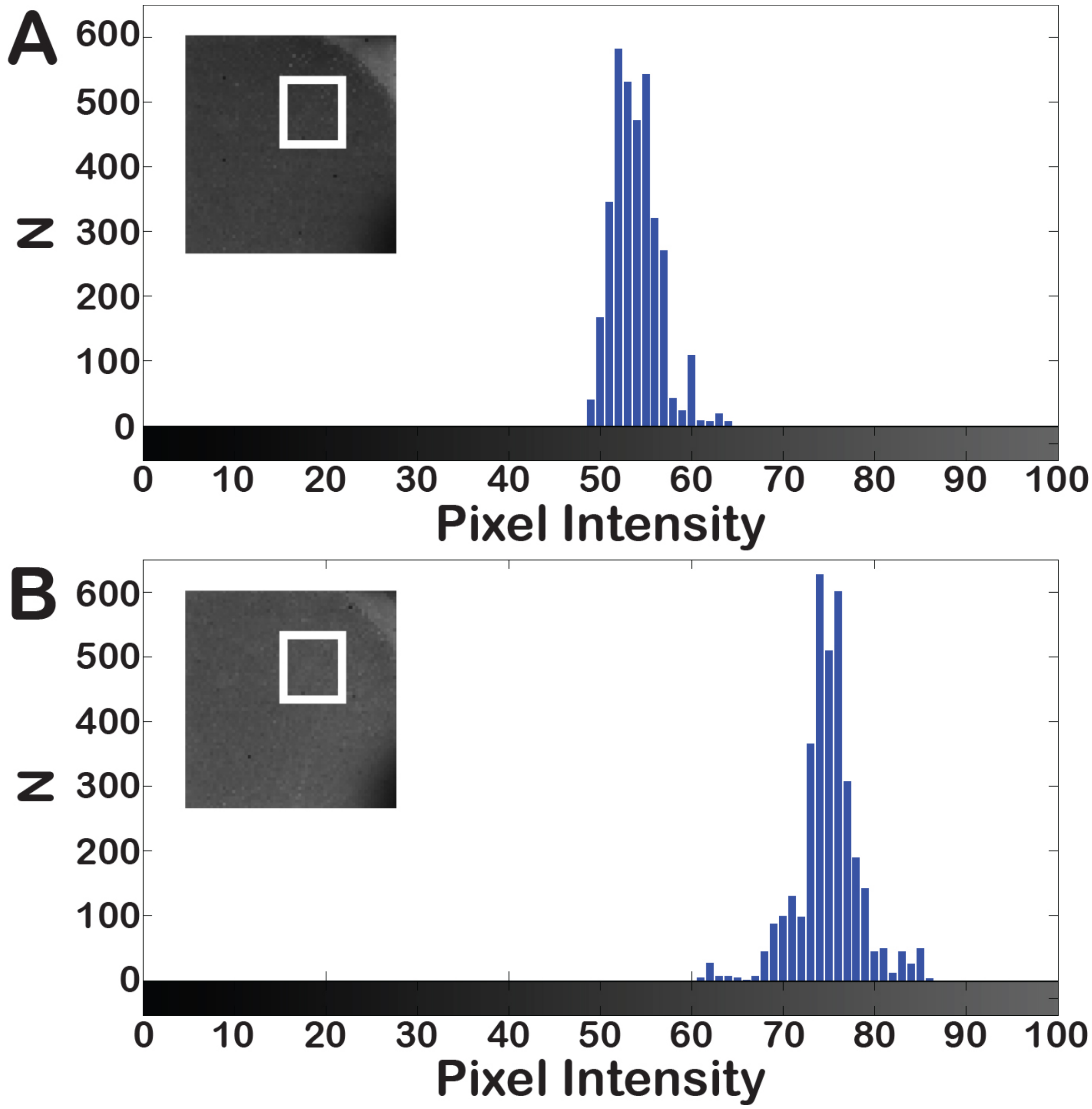

Figure 2.21. Quantification of pixel intensity of BR in the **bR** state (A) and the **Q** state (B). The value, N, on the y-axis was measured by the static pixels on the foveated image sensor as the number of events recorded during a 1 minute.

AP/min) in forming the **Q** state. The inset images for Figures 2.21A and 2.21B shows the measured pixel intensity distribution map for the retinal implant in both the **bR** and **Q** states, respectively (as the film is placed onto the static pixels of the foveated imager). Note that the curved edges of the retinal implant can be observed in the top right hand corner of each of the inset images, and that the implant was placed in an identical location on the foveated imager between measurements of the **bR** and **Q** states. This placement was performed to ensure that the ambient light conditions and relative pixel measurements were consistent throughout the study. The measured pixel intensities were taken from the same location on the imager for both states, which is shown by the white boxes of the insert images in Figure 2.21.

The pixel intensity analysis demonstrates that there is a significant frequency separation observed between the two accessible photoproducts of the retinal implant based on the V49A BR mutant, and that the protein was uniformly present in each respective photostate within the sensitivity of the imager. This result also mirrors the spectral analysis shown in Figure 2.20, in which the protein contained within the retinal implant is completely converted from the **bR** resting state to the **Q** state. While this study does not approach the measurability limits of the foveated image sensor in terms of resolution, sensitivity, and function (i.e., dynamic vs. static pixels), the first steps have been taken towards monitoring two spectrally distinct photoproducts within a multilayered thin film architecture, and have laid the groundwork for future experiments that will further characterize the pixel mediation properties of BR-based retinal implants.

Following these initial proof-of-concept experiments, there are a number of conditions that remain to be optimized for further pixel characterization of the retinal prosthetic. First, the ambient light conditions that are used for measurement should be modulated to promote the greatest output frequency separation between the **bR** and **Q** states. We so far use ambient

laboratory lighting for these measurements, but efforts in optimization will lead to enhanced performance of the sensor. Moreover, the use of a focusing lens could improve the function of the foveated imager. Once the data collection conditions are optimized and are reproducible, intermediate frequencies should be measured during the **Q** state formation process in order to monitor incomplete conversion and, perhaps, the kinetics of formation within the retinal implant architecture. Finally, we would like to develop a more sensitive irradiation technique based on fiber optics to locally drive individual pixels or pixel clusters within the retinal implant to the **Q** state. Our global analysis so far predicts that the foveated imager is capable of differentiating between **bR** and **Q**, however, we hope to further exploit the sensitivity of the CMOS sensor to quantify the limits of pixel mediation within our retinal implant.

2.4. Comments and Conclusions

The directed evolution study has revealed several new mutants (Table 2.2) with properties optimal for device applications that rely on the formation of two stable photoproducts, including three-dimensional optical memories and protein-based retinal implants. When all photophysical characteristics are considered, the two best mutants are V49A (λ_{max} = 563 nm, $Q_{formation}$ = 641, Q_{total} = 924, photocycle time = 112 ms, pH = 9.5) and V49A/I119T/T121S/A126T (λ_{max} = 559 nm, $Q_{formation}$ = 738, Q_{total} = 977, photocycle time = 73 ms, pH = 8.0), where the pH values represent the value closest to neutral pH yielding optimal photochemical behavior. Both of these mutants have excellent Q_{total} values that allow for the use of low energy lasers (3-6 mW) to write data, which is a significant improvement over the 100 mW lasers that were necessary for the initial three-dimensional memory prototypes absed on WT-BR.[139]

The V49A mutation represents a relatively small exchange of two hydrophobic residues, in which two methyl groups are removed and replaced with two hydrogen atoms. While this change is superficially trivial, the amino acid substitution engenders BR with the key structural properties that facilitate the desired photochemical optimization. The pH environment is shown to have a profound impact on the identification of several of the BR mutants listed in Table 2.2, and is a vital parameter used to reveal V49A as a mutant with superior **Q** state photochemistry. Photochemical and photophysical analyses of V49A in various buffers also help to reveal the fundamental mechanisms which make this mutant an important biomaterial for device applications that exploit the branched photocycle of BR. The Q_{total} of V49A as a function of pH suggests that the pK_as of three amino acids are involved in enhancing access to the **P** state. Upon the V49A substitution, the pK_a of Asp-96 is lowered to 7.053 during the transition from the **N** state to the **O** state, and the pK_as of Asp-85 and the PRC are raised and lowered to 9.396 and 3.689, respectively, during the **O** to **bR** transition. These alterations lead to a greater yield and a longer lifetime of the **O** state, which is the access point to the branched photocycle. Furthermore, an analysis of the chromophore and the binding site of V49A using chromophore extractions and FTIR spectroscopy suggests that the BR mutant preferentially relaxes to 9-*cis* retinal at an alkaline pH. Computational studies are ongoing to reveal the relative energetics of the hydrolyzed 9-*cis* chromophore in the binding pocket, which will further characterize the mechanism of **Q** state enhancement at an atomistic level.

Additionally, this work demonstrates the feasibility of using CMOS image sensors, in this case a foveated image sensor, as a lab-on-chip (LOC) platform for testing the light sensitivity of the two stable photoproducts within a novel photosensitive protein-based retinal implant. The foveated imager measures a significant difference of output frequencies between the **bR** and **Q**

states using gray scale analysis. This result also mirrors the spectral properties of the two isolatable photoproducts of V49A. Moreover, this investigation represents a first example that demonstrates the possibility of not only fabricating a protein-based retinal implant using a BR mutant, but also to characterize the photoactive behavior of BR that will be responsible for restoring vision at a resolution that is only limited by the density of the protein layers. The **bR** and **Q** states of V49A provide a photochemical pathway towards pixel mediation within the retinal implant, which will help RP or AMD patients manage the gradual progression of retinal degeneration. Areas of the retina with high retinal degeneration will be targeted with active pixels in the **bR** state, where light-activated proton pumping can be harnessed for retinal stimulation. Deactivation of pixels *via* the accession of **Q** will prevent interference with functional patches of photoreceptor cells. We envision that pixels could be selectively driven to the **Q** state following implantation of the retinal prosthetic using a targeted, multiphoton optical apparatus.

The experiments performed here are the first step in a series of ongoing work to explore the ability to mediate pixels of the BR-based retinal implant, quantify the spatial resolution, and develop the optics necessary for localized **Q** state formation within the retinal implant. In addition to optimizing the experimental conditions for the studies outlined above, we are assembling an optical system for irradiation of areas identical to the size of one pixel of the foveated image sensor to validate the ability of modulating the surface area on a scale relevant to *in vivo* pixel mediation. Finally, we are currently developing a similar LOC platform using ion-sensitive field-effect transistors (ISFETs) for the on-chip measurement of the proton-pumping action of BR as a means to quantify spatial sensitivity of the protein-based retinal implant.

2.5. References

(1) Hartong, D. T.; Berson, E. L.; Dryja, T. P. Retinitis Pigmentosa. *Lancet* **2006**, *368*, 18-24.

(2) Gehrs, K. M.; Jackson, J. R.; Brown, E. N.; Allikmets, R.; Hageman, G. S. Complement, Age-Related Macular Degeneration and a Vision of the Future. *Arch. Ophthalmol.* **2010**, *128*, 349-358.

(3) Santos, A.; Humayun, M. S.; de Juan, E.; Greenburg, R. J.; Marsh, M. J.; Klock, I. B.; Milam, A. H. Preservation of the Inner Retina in Retinitis Pigmentosa. A Morphometric Analysis. *Arch. Ophthalmol.* **1997**, *115*, 511-515.

(4) Stone, J. L.; Barlow, W. E.; Humayun, M. S.; de Juan, E. J.; Milam, A. H. Morphometric Analysis of Macular Photoreceptors and Ganglion Cells in Retinas with Retinitis Pigmentosa. *Arch. Ophthalmol.* **1992**, *110*, 1634-1639.

(5) Berson, E. L. Retinitis Pigmentosa: Unfolding Its Mystery. *Proc. Natl. Acad. Sci. U.S.A.* **1996**, *93*, 4526-4528.

(6) Weleber, R. G. Clinical Progress in Inherited Orphan Retinal Diseases: Phenotypes, Genotypes, and Probable Treatment Groups. *Retina* **2005**, *25*, S4-S7.

(7) Friedman, D. S.; O'Colmain, B. J.; Munoz, B.; Tomany, S. C.; McCarty, C.; de Jong, P. T.; Nemesure, B.; Mitchell, P.; Kempen, J. Prevalence of Age-Related Macular Degneration in the United States. *Arch. Ophthalmol.* **2004**, *122*, 564-572.

(8) Hubschman, J. P.; Reddy, S.; Schwartz, S. D. Age-Related Macular Degeneration: Current Treatments. *Clin. Ophthalmol.* **2009**, *3*, 155-166.

(9) Wiley, L. A.; Burnight, E. R.; Songstad, A. E.; Drack, A. V.; Mullins, R. F.; Stone, E. M.; Tucker, B. A. Patient-Specific Induced Pluripotent Stem Cells (iPSCs) for the Study and Treatment of Retinal Degenerative Diseases. *Prog. Retinal Eye Res.* **2015**, *44*, 15-35.

(10) Baranov, P. Y.; Tucker, B. A.; Young, M. J. Low-Oxygen Culture Conditions Extend the Multipotent Properties of Human Retinal Prorgenitor Cells. *Tissue Eng. Part A* **2014**, *20*, 1465-1475.

(11) Chatoo, W.; Abdouh, M.; Duparc, R.-H.; Bernier, G. Bmi1 Distinguishes Immature Retinal Progenitor/Stem Cells from the Main Progenitor Cell Population and Is Required for Normal Retinal Development. *Stem Cells* **2010**, *28*, 1412-1423.

(12) Hafler, B. P.; Surzenko, N.; Beier, K. T.; Punzo, C.; Trimarchi, J. M.; Kong, J. H.; Cepko, C. L. Transcription Factor *Olig2* Defines Subpopulations of Retinal Progenitor Cells Biased Towards Specific Cell Fates. *Proc. Natl. Acad. Sci. U. S. A.* **2012**, *109*, 7882-7887.

(13) Luo, J.; Baranov, P. Y.; Patel, S.; Ouyang, H.; Quach, J.; Wu, F.; Qiu, A.; Luo, H.; Hicks, C.; Zeng, J.; Zhu, J.; Lu, J.; Sfeir, N.; Wen, C.; Zhang, M.; Reade, V.; Patel, S.; Sinden, J.; Sun, X.; Shaw, P.; Young, M. J.; Zhang, K. Human Retinal Progenitor Cell Transplantation Preserves Vision. *J. Biol. Chem.* **2014**, *289*, 6362-6371.

(14) Schmitt, S.; Aftab, U.; Jiang, C.; Redenti, S.; Klassen, H.; Miljan, E.; Sinden, J.; Young, M. Molecular Characterization of Human Retinal Progenitor Cells. *Invest. Ophthalmol. Vis. Sci.* **2009**, *50*, 5901-5908.

(15) Gonzalez-Cordero, A.; West, E. L.; Pearson, R. A.; Duran, Y.; Carvalho, L. S.; Chu, C. J.; Naeem, A.; Blackford, S. J.; Georgiadis, A.; Lakowski, J.; Hubank, M.; Smith, A. J.; Bainbridge, J. W.; Sowden, J. C.; Ali, R. R. Photoreceptor Precursors Derived from Three-

Dimensional Embryonic Stem Cell Cultures Integrate and Mature within an Adult Degenerate Retina. *Nat. Biotechnol.* **2013**, *31*, 741-747.

(16) Schwartz, S. D.; Hubschman, J. P.; Heilwell, G.; Franco-Cardenas, V.; Pan, C. K.; Ostrick, R. M.; Mickunas, E.; Gay, R.; Klimanskaya, I.; Lanza, R. Embryonic Stem Cell Trials for Macular Degeneration: A Preliminary Report. *Lancet* **2012**, *379*, 713-720.

(17) Cramer, A. O.; MacLaren, R. E. Clinical Trials Using Induced Pluripotent Stem Cells from Bench to Bedside: Application to Retinal Diseases. *Curr. Gene Ther.* **2013**, *13*, 139-151.

(18) Buchen, L. Neuroscience: Illuminating the Brain. *Nature* **2010**, *465*, 26-28.

(19) Boyden, E. S.; Zhang, F.; Bamberg, E.; Nagel, G.; Deisseroth, K. Millisecond-Timescale, Genetically Targeted Optical Control of Neural Activity. *Nat. Neurosci.* **2005**, *8*, 1263-1268.

(20) Han, X.; Boyden, E. S. Multiple-Color Optical Activation, Silencing, and Desynchronization of Neural Activity, with Single-Spike Temporal Resolution. *PLoS One* **2007**, *2*, e299.

(21) Busskamp, V.; Roska, B. Optogenetic Approaches to Restoring Visual Function in Retinitis Pigmentosa. *Curr. Opin. Neurobiol.* **2011**, *21*, 942-946.

(22) Busskamp, V.; Picaud, S.; Sahel, J. A.; Roska, B. Optogenetic Therapy for Retinitis Pigmentosa. *Gene Ther.* **2011**, 1-7.

(23) Degenaar, P.; Grossman, N.; Memon, M. A.; Burrone, J.; Dawson, M.; Drakakis, E.; Neil, M.; Nikolic, K. Optobionic Vision - A New Genetically Enhanced Light on Retinal Prosthesis. *J. Neural Eng.* **2009**, *6*.

(24) Cehajic-Kapetanovic, J.; Eleftheriou, C.; Allen, A. E.; Milosavljevic, N.; Pienaar, A.; Bedford, R.; Davis, K. E.; Bishop, P. N.; Lucas, R. J. Restoration of Vision with Ectopic Expression of Human Rod Opsin. *Curr. Biol.* **2015**, *25*, 2111-2122.

(25) Shintani, K.; Shechtman, D. L.; Gurwood, A. S. Review and Update: Current Treatment Trends for Patients with Retinitis Pigmentosa. *J. Am. Optom. Assoc.* **2009**, *80*, 384-401.

(26) Kovach, J. L.; Schwartz, S. G.; Flynn Jr., H. W.; Scott, I. U. Anti-VEGF Treatment Strategies for Wet AMD. *J. Opthalmol.* **2012**, *2012*.

(27) Grill, W. M.; Mortimer, J. T. Stimulus Waveforms for Selective Neural Stimulation. *IEEE Eng. Med. Biol. Mag.* **1995**, *14*, 375-385.

(28) Weiland, J. D.; Cho, A. K.; Humayun, M. S. Retinal Prostheses: Current Clinical Results and Future Needs. *Ophthalmology* **2011**, *118*, 2227-2237.

(29) Humayun, M. S.; Dorn, J. D.; da Cruz, L.; Dagnelie, G.; Sahel, J.-A.; Stanga, P. E.; Cideciyan, A. V.; Duncan, J. L.; Eliott, D.; Filley, E.; Ho, A. C.; Santos, A.; Safran, A. B.; Arditi, A.; Del Priore, L. B.; Greenberg, R. J. Interim Results from the International Trial of Second Sight's Visual Prosthesis. *Ophthalmology* **2012**, *119*, 779-788.

(30) Barry, M. P.; Dagnelie, G. Use of the Argus II Retinal Prosthesis to Improve Visual Guidance of Fine Hand Movements. *Invest. Ophthalmol. Vis. Sci.* **2012**, *53*, 5095-5101.

(31) Wilke, R.; Gabel, V. P.; Sachs, H.; Bartz Schmidt, K. U.; Gekeler, F.; Besch, D.; Szurman, P.; Stett, A.; Wilhelm, B.; Peters, T.; Harscher, A.; Greppmaier, U.; Kibbel, S.; Benhav, H.; Bruckmann, A.; Stingl, K.; Kusnyerik, A.; Zrenner, E. Spatial Resolution and Perception of Patterns Mediated by a Subretinal 16-Electrode Array in Patients Blinded by Hereditary Retinal Dystrophies. *Invest. Ophthalmol. Vis. Sci.* **2011**, *52*, 5995-6003.

(32) Benav, H.; Bartz Schmidt, K. U.; Besch, D.; Bruckmann, A.; Gekeler, F.; Greppmaier, U.; Harscher, A.; Kibbel, S.; Kusnyerik, A.; Peters, T.; Sachs, H.; Stett, A.; Stingl, K.; Wilhelm, B.; Wilke, R.; Wrobel, W.; Zrenner, E. Restoration of Useful Vision up to Letter Recognition Capabilities Using Subretinal Microphotodiodes. *Conf. Proc. IEEE Eng. Med. Biol. Soc.* **2010**, *2010*, 5919-5922.

(33) Kusnyerik, A.; Greppmaier, U.; Wilke, R.; Gekeler, F.; Wilhelm, B.; Sachs, H.; Bartz Schmidt, K. U.; Klose, U.; Stingl, K.; Resch, M. D.; Hekmat, A.; Bruckmann, A.; Karacs, K.; Nemeth, J.; Suveges, I.; Zrenner, E. Positioning of Electronic Subretinal Implants in Blind Retinitis Pigmentosa Patients through Multimodal Assessment of Retinal Structures. *Invest. Ophthalmol. Vis. Sci.* **2012**, *53*, 3748-3755.

(34) Stingl, K.; Bartz-Schmidt, K. U.; Besch, D.; Braun, A.; Bruckmann, A.; Gekeler, F.; Greppmaier, U.; Hipp, S.; Hortdorfer, G.; Kernstock, C.; Koitschev, A.; Kusnyerik, A.; Sachs, H. G.; Schatz, A.; Stingl, K. T.; Peters, T.; Wilhelm, B.; Zrenner, E. Artificial Vision with Wirelessly Powered Subretinal Electronic Implant Alpha-IMS. *Proc. R. Soc. B* **2013**, *280*, 20130077.

(35) Zrenner, E. Fighting Blindness with Microelectronics. *Sci. Transl. Med.* **2013**, *5*, 210-216.

(36) Klauke, S.; Goertz, M.; Rein, S.; Hoehl, D.; Thomas, U.; Eckhorn, R.; Bremmer, F.; Wachtler, T. Stimulation with a Wireless Intraocular Epiretinal Implant Elicits Visual Percepts in Blind Humans. *Invest. Ophthalmol. Vis. Sci.* **2011**, *52*, 449-455.

(37) Roessler, G.; Laube, T.; Brockmann, C.; Kirschkamp, T.; Mazinani, B.; Goertz, M.; Koch, C.; Krisch, I.; Sellhaus, B.; Khiem Trieu, H.; Weis, J.; Bornfeld, N.; Rothgen, H.; Messner, A.; Mokwa, W.; Walter, P. Implantation and Explanation of a Wireless Epiretinal Retina Implant Device: Observations During the EPIRET3 Prospective Clinical Trial. *Invest. Ophthalmol. Vis. Sci.* **2009**, *50*, 3003-3008.

(38) Menzel-Severing, J.; Laube, T.; Brockmann, C.; Bornfield, N.; Mokwa, W.; Mazinani, B.; Walter, P.; Roessler, G. Implantation and Explantation of an Active Epiretinal Visual Prosthesis: 2-Year Follow-Up Data from the EPIRET3 Prospective Clinical Trial. *Eye* **2012**, *26*, 501-509.

(39) Javaheri, M.; Hahn, D. S.; Lakhanpal, R. R.; Weiland, J. D.; Humayun, M. S. Retinal Prostheses for the Blind. *Ann. Acad. Med. Singapore* **2006**, *35*, 137-144.

(40) Palanker, D.; Vankov, A.; Huie, P.; Baccus, S. Design of a High-Resolution Optoelectronic Retinal Prosthesis. *J. Neural Eng.* **2005**, *2*, S105-S120.

(41) Zrenner, E. Neuroprosthetics: Fighting Blindness with Microelectronics. *Sci. Transl. Med.* **2013**, *5*, 1-7.

(42) Dorn, J. D.; Ahuja, A. K.; Caspi, A.; da Cruz, L.; Dagnelie, G.; Sahel, J. A.; Greenberg, R. J.; McMahon, M. J. The Detection of Motion by Blind Subjects with the Epiretinal 60-Electrode (Argus II) Retinal Prosthesis. *JAMA Ophthalmol.* **2013**, *131*, 183-189.

(43) Kien, T. T.; Maul, T.; Bargiela, A. A Review of Retinal Prosthesis Approaches. *Int. J. Mod. Phys.: Conf. Ser.* **2012**, *9*, 209-231.

(44) Wagner, N. L.; Greco, J. A.; Birge, R. R. Visual Restoration Using Microbial Rhodopsins. In *Bionanotechnology: Biological Self-Assembly and Its Applications*; Rehm, B. H. A., Ed.; Caister Academic Press: Norfolk, UK, 2013, pp 205-240.

(45) He, J.-A.; Samuelson, L.; Li, L.; Kumar, J.; Tripathy, S. K. Oriented Bacteriorhodopsin/Polycation Multilayers by Electrostatic Layer-by-Layer Assembly. *Langmuir* **1998**, *14*, 1674-1679.

(46) Wagner, N. L.; Greco, J. A.; Ranaghan, M. J.; Birge, R. R. Directed Evolution of Bacteriorhodopsin for Applications in Bioelectronics. *J. R. Soc., Interface* **2013**, *10*, 20130197.

(47) Oesterhelt, D.; Stoeckenius, W. Functions of a New Photoreceptor Membrane. *Proc. Natl. Acad. Sci. U.S.A.* **1973**, *70*, 2853-2857.

(48) Oesterhelt, D.; Stoeckenius, W. Rhodopsin-Like Protein from the Purple Membrane of Halobacterium halobium. *Nature (London), New Biol.* **1971**, *233*, 149-152.

(49) Luecke, H.; Schobert, B.; Richter, H. T.; Cartailler, J. P.; Lanyi, J. K. Structure of Bacteriorhodopsin at 1.55 Å Resolution. *J. Mol. Biol.* **1999**, *291*, 899-911.

(50) Heyes, C. D.; El-Sayed, M. A. The Role of the Native Lipids and Lattice Structure in Bacteriorhodopsin Protein Conformation and Stability as Studied by Temperature-Dependent Fourier Transform-Infrared Spectroscopy. *J. Biol. Chem.* **2002**, *277*, 29437-29443.

(51) Bogomolni, R.; Baker, R.; Lozier, R.; Stoeckenius, W. Light-Driven Proton Translocations in *Halobacterium halobium*. *Biochim. Biophys. Acta, Bioenerg.* **1976**, *440*, 68-88.

(52) Tittor, J.; Oesterhelt, D. The Quantum Yield of Bacteriorhodopsin. *FEBS Lett.* **1990**, *263*, 269-273.

(53) Birge, R. R.; Cooper, T. M.; Lawrence, A. F.; Masthay, M. B.; Vasilakis, C.; Zhang, C. F.; Zidovetzki, R. A Spectroscopic, Photocalorimetric and Theoretical Investigation of the Quantum Efficiency of the Primary Event in Bacteriorhodopsin. *J. Am. Chem. Soc.* **1989**, *111*, 4063-4074.

(54) Jackson, M. B.; Sturtevant, J. M. Phase Transitions of the Purple Membranes of *Halobacterium halobium*. *Biochemistry* **1978**, *17*, 911-915.

(55) Birge, R. R. Photophysics and Molecular Electronic Applications of the Rhodopsins. *Annu. Rev. Phys. Chem.* **1990**, *41*, 683-733.

(56) Bräuchle, C.; Hampp, N.; Oesterhelt, D. Optical Applications of Bacteriorhodopsin and Its Mutated Variants. *Adv. Mater.* **1991**, *3*, 420-428.

(57) Ranaghan, M. J.; Shima, S.; Ramos, L.; Poulin, D. S.; Whited, G.; Rajasekaran, S.; Stuart, J. A.; Albert, A. D.; Birge, R. R. Photochemical and Thermal Stability of Green and Blue Proteorhodopsins: Implications for Protein-Based Bioelectronic Devices. *J. Phys. Chem. B* **2010**, *114*, 14064-14070.

(58) Birge, R. R.; Gillespie, N. B.; Izaguirre, E. W.; Kusnetzow, A.; Lawrence, A. F.; Singh, D.; Song, Q. W.; Schmidt, E.; Stuart, J. A.; Seetharaman, S.; Wise, K. J. Biomolecular Electronics: Protein-Based Associative Processors and Volumetric Memories. *J. Phys. Chem. B* **1999**, *103*, 10746-10766.

(59) Hampp, N. Bacteriorhodopsin as a Photochromic Retinal Protein for Optical Memories. *Chem. Rev.* **2000**, *100*, 1755-1776.

(60) Birge, R. R. Nature of the Primary Photochemical Events in Rhodopsin and Bacteriorhodopsin. *Biochim. Biophys. Acta* **1990**, *1016*, 293-327.

(61) Kobayashi, T.; Ohtani, H.; Iwai, J.; Ikegami, A.; Uchiki, H. Effect of pH on the Photoreaction Cycles of Bacteriorhodopsin. *FEBS Lett.* **1983**, *162*, 197-200.

(62) Doig, S. J.; Reid, P. J.; Mathies, R. A. Picosecond Time-Resolved Resonance Raman Spectroscopy of Bacteriorhodopsin's J, K, and KL Intermediates. *J. Phys. Chem.* **1991**, *95*, 6372-6379.

(63) Shim, S.; Dasgupta, J.; Mathies, R. A. Femtosecond Time-Resolved Stimulated Raman Reveals the Birth of Bacteriorhodopsin's J and K Intermediates. *J. Am. Chem. Soc.* **2008**, *131*, 7592-7597.

(64) Zimányi, L.; Váró, G.; Chang, B.; Needleman, R.; Lanyi, J. Pathways of Proton Release in the Bacteriorhodopsin Photocycle. *Biochemistry* **1992**, *31*, 8535-8543.

(65) Dickopf, S.; Heyn, M. P. Evidence for the First Phase of the Reprotonation Switch of Bacteriorhodopsin from Time-Resolved Photovoltage and Flash Photolysis Experiments on the Photoreversal of the M-Intermediate. *Biophys. J.* **1997**, *73*, 3171-3181.

(66) Schobert, B.; Brown, L. S.; Lanyi, J. K. Crystallographic Structures of the M and N Intermediates of Bacteriorhodopsin: Assembly of a Hydrogen-Bonded Chain of Water Molecules between Asp-96 and the Retinal Schiff Base. *J. Mol. Biol.* **2003**, *330*, 553-570.

(67) Lanyi, J.; Váró, G. The Photocycles of Bacteriorhodopsin. *Isr. Jour. Chem.* **1995**, *35*, 365-385.

(68) Haupts, U.; Tittor, J.; Oesterhelt, D. Closing in on Bacteriorhodopsin: Progress in Understanding the Molecule. *Annu. Rev. Biophys. Biomol. Struct.* **1999**, *28*, 367-399.

(69) Brown, L. S.; Dioumaev, A. K.; Needleman, R.; Lanyi, J. K. Local-Access Model for Proton Transfer in Bacteriorhodopsin. *Biochemistry* **1998**, *37*, 3982-3993.

(70) Morgan, J. E.; Vakkasoglu, A. S.; Lanyi, J. K.; Gennis, R. B.; Maeda, A. Coordinating the Structural Rearrangements Associated with Unidirectional Proton Transfer in the Bacteriorhodopsin Photocycle Induced by Deportonation of the Proton-Release Group: A Time-Resolved Difference FTIR Spectroscopic Study. *Biochemistry* **2010**, *49*, 3273-3281.

(71) Balashov, S. P.; Govindjee, R.; Imasheva, E. S.; Misra, S.; Ebrey, T. G.; Feng, Y.; Crouch, R. K.; Menick, D. R. Complex Titration of Asp-85 in the Unphotolyzed Protein Reflects Dependence of Another Group. *Biochemistry* **1995**, *35*, 4054-4062.

(72) Balashov, S.; Imasheva, E.; Ebrey, T.; Chen, N.; Menick, D.; Crouch, R. Glutamate 194 to Cysteine Mutation Inhibits Fast Light-Induced Proton Release in Bacteriorhodopsin. *Biochemistry* **1997**, *36*, 8671-8676.

(73) Dioumaev, A. K.; Richter, H.-T.; Brown, L. S.; Michikazu, T.; Tuzi, S.; Saito, H.; Kimura, Y.; Needleman, R.; Lanyi, J. K. Existence of a Proton Transfer Chain in Bacteriorhodopsin: Participation of Glu-194 in the Release of Protons to the Extracellular Surface. *Biochemistry* **1998**, *37*, 2496-2506.

(74) Luecke, H.; Schobert, B.; Richter, H. T.; Cartailler, J. P.; Lanyi, J. K. Structural Changes in Bacteriorhodopsin During Ion Transport at 2 Angstrom Resolution. *Science* **1999**, *286*, 255-261.

(75) Cao, Y.; Váró, G.; Chang, M.; Ni, B. F.; Needleman, R.; Lanyi, J. K. Water Is Required for Proton Transfer from Aspartate-96 to the Bacteriorhodopsin Schiff Base. *Biochemistry* **1991**, *30*, 10972-10979.

(76) Cao, Y.; Váró, G.; Klinger, A. L.; Czajkowsky, D. M.; Braiman, M. S.; Needleman, R.; Lanyi, J. K. Proton Transfer from Asp-96 to the Bacteriorhodospin Schiff Base Is Caused by a Decrease of the Pka of Asp-96 Which Follows a Protein Backbone Conformational Change. *Biochemistry* **1993**, *32*, 1981-1990.

(77) Holz, M.; Drachev, L. A.; Mogi, T.; Otto, H.; Kaulen, A. D.; Heyn, M. P.; Skulachev, V. P.; Khorana, H. G. Replacement of Aspartic Acid-96 by Asparagine in Bacteriorhodopsin Slows Both the Decay of the M Intermediate and the Associated Proton Movement. *Proc. Natl. Acad. Sci. U.S.A.* **1989**, *86*, 2167-2171.

(78) Otto, H.; Marti, T.; Holz, M.; Lindau, M.; Khorana, H. G.; Heyn, M. P. Aspartic Acid-96 Is the Internal Proton Donor in the Repronation of the Schiff Base of Bacteriorhodopsin. *Proc. Natl. Acad. Sci. U.S.A.* **1989**, *86*, 9228-9232.

(79) Brown, L.; Needleman, R.; Lanyi, J. Functional Roles of Aspartic Acid Residues at the Cytoplasmic Surface of Bacteriorhodopsin. *Biochemistry* **1999**, *38*, 6855-6861.

(80) Richter, H.-T.; Needleman, R.; Kandori, H.; Maeda, A.; Lanyi, J. K. Relationship of Retinal Configuration and Internal Proton Transfer at the End of the Bacteriorhodopsin Photocycle. *Biochemistry* **1996**, *35*, 15461-15466.

(81) Gillespie, N. B.; Wise, K. J.; Ren, L.; Stuart, J. A.; Marcy, D. L.; Hillebrecht, J.; Li, Q.; Ramos, L.; Jordan, K.; Fyvie, S.; Birge, R. R. Characterization of the Branched-Photocycle Intermediates P and Q of Bacteriorhodopsin. *J. Phys. Chem. B* **2002**, *106*, 13352-13361.

(82) Popp, A.; Wolperdinger, M.; Hampp, N.; Bräuchle, C.; Oesterhelt, D. Photochemical Conversion of the O-Intermediate to 9-cis-Retinal-Containing Products in Bacteriorhodopsin Films. *Biophys. J.* **1993**, *65*, 1449-1459.

(83) Dancsházy, Z.; Tokaji, Z.; Dér, A. Bleaching of Bacteriorhodopsin by Continuous Light. *FEBS Lett.* **1999**, *450*, 154-157.

(84) Dancsházy, Z.; Tokaji, Z. Blue Light Regeneration of Bacteriorhodopsin Bleached by Continuous Light. *FEBS Lett.* **2000**, *476*, 171-173.

(85) Wise, K. J.; Gillespie, N. B.; Stuart, J. A.; Krebs, M. P.; Birge, R. R. Optimization of Bacteriorhodopsin for Bioelectronic Devices. *Trends Biotechnol.* **2002**, *20*, 387-394.

(86) Hampp, N.; Bräuchle, C.; Oesterhelt, D. Bacteriorhodopsin Wildtype and Variant Aspartate-96 to Asparagine as Reversible Holographic Media. *Biophys. J.* **1990**, *58*, 83-93.

(87) Hampp, N.; Thoma, R.; Zeisel, D.; Bräuchle, C.; Oesterhelt, D. Bacteriorhodopsin Variants for Holographic Pattern Recognition. *Adv. Chem.* **1994**, *240*, 511-526.

(88) Hillebrecht, J. R.; Koscielecki, J. F.; Wise, K. J.; Marcy, D. L.; Tetley, W.; Rangarajan, R.; Sullivan, J.; Brideau, M.; Krebs, M. P.; Stuart, J. A.; Birge, R. R. Optimization of Protein-Based Volumetric Optical Memories and Associative Processors by Using Directed Evolution. *Nanobiotechnology* **2005**, *1*, 141-152.

(89) Hillebrecht, J. R.; Wise, K. J.; Birge, R. R. Directed Evolution of Bacteriorhodopsin for Device Applications. *Methods Enzymol.* **2004**, *388*, 333-347.

(90) Brown, L.; Y., G.; Sheves, M.; Yamazaki, Y.; Maeda, A.; Needleman, R.; Lanyi, J. The Retinal Schiff Base-Counterion Complex of Bacteriorhodopsin: Changed Geometry During the Photocycle Is a Cause of Proton Transfer to Aspartate 85. *Biochemistry* **1994**, *33*, 12001-12011.

(91) Song, L.; El-Sayed, M. A.; Lanyi, J. K. Effect of Changing the Position and Orientation of Asp85 Relative to the Protonated Schiff Base within the Retinal Cavity on the Rate of Photoisomerization in Bacteriorhodopsin. *J. Phys. Chem.* **1996**, *100*, 10479-10481.

(92) Yamazaki, Y.; Tuzi, S.; Saitô, H.; Kandori, H.; Needleman, R.; Lanyi, J.; Maeda, A. Hydrogen Bonds of Water and C=O Groups Coordinate Long-Range Structural Changes in the L Photointermediate of Bacteriorhodopsin. *Biochemistry* **1996**, *35*, 4063-4068.

(93) Yamazaki, Y.; Kandori, H.; Needleman, R.; Lanyi, J.; Maeda, A. Interaction of the Protonated Schiff Base with the Peptide Backbone of Valine 49 and the Intervening Water Molecule in the N Photointermediated of Bacteriorhodopsin. *Biochemistry* **1998**, *37*, 1559-1564.

(94) Taino, M.; Inoue, S.; Yokota, K.; Seki, T.; Tuzi, S.; Needleman, R.; Laynyi, J. K.; Naito, A.; Saito, H. Long-Distance Effects of Site-Directed Mutations on Backbone Conformation in Bacteriorhodopsin from Solid State NMR of [1-^{13}C]Val-Labeled Proteins. *Biophys. J.* **1999**, *77*, 431-442.

(95) Koyama, K.; Miyasaka, T. The Proton Uptake Channel of Bacteriorhodopsin as Studied by a Photoectrochemical Method. *Bioelectrochemistry* **2000**, *53*, 111-118.

(96) Joh, N. H.; Oberai, A.; Yang, D.; Whitelegge, J. P.; Bowie, J. U. Similar Energy Contributions of Packing in the Core of Membrane and Water-Soluble Proteins. *J. Am. Chem. Soc.* **2009**, *131*, 10846-10847.

(97) Maeda, A.; Kandori, H.; Yamazaki, Y.; Nishimura, S.; Hatanaka, M.; Chon, Y.; Sasaki, J.; Needleman, R.; Lanyi, J. Intramembrane Signaling Mediated by Hydrogen Bonding of Water and Carboxyl Groups in Bacteriorhodopsin and Rhodopsin. *J. Biochem.* **1997**, *121*, 399-406.

(98) Greenhalgh, D. A.; Farrens, D. L.; Subramaniam, S.; Khorana, H. G. Hydrophobic Amino Acids in the Retinal-Binding Pocket of Bacteriorhodopsin. *J. Biol. Chem.* **1993**, *268*, 20305-20311.

(99) Logunov, S. L.; El-Sayed, M. A. Redetermination of the Quantum Yield of Photoisomerization and Energy Content in the K-Intermediate of Bacteriorhodopsin Photocycle and Its Mutants by the Photoacoustic Technique. *J. Phys. Chem. B* **1997**, *101*, 6629-6633.

(100) Maeda, A.; Morgan, J. E.; Gennis, R. B.; Ebrey, T. G. Water as a Cofactor in the Unidirectional Light-Driven Proton Transfer Steps in Bacteriorhodopsin. *Photochem. Photobiol.* **2006**, *82*, 1398-1405.

(101) Chen, D.; Lanyi, J. K. Structural Changes in the N and N' States of the Bacteriorhodopsin Photocycle. *Biophys. J.* **2009**, *96*, 2779-2788.

(102) Dioumaev, A. K.; Brown, L. S.; Needleman, R.; Lanyi, J. K. Coupling of the Reisomerization of the Retinal, Proton Uptake, and Reprotonation of Asp-96 in the N Photointermediate of Bacteriorhodopsin. *Biochemistry* **2001**, *40*, 11308-11317.

(103) Maeda, A.; Gennis, R. B.; Balashov, S. P.; Ebrey, T. G. Relocation of Water Molecules between the Schiff Base and the Thr46-Asp96 Region During Light-Driven Unidirectional Proton Transport by Bacteriorhodopsin: An FTIR Study of the N Intermediate. *Biochemistry* **2005**, *44*, 5960-5968.

(104) Arnold, F. H. Design by Directed Evolution. *Acc. Chem. Res.* **1998**, *31*, 125-131.

(105) Jäckel, C.; Kast, P.; Hilvert, D. Protein Design by Directed Evolution. *Annu. Rev. Biophys.* **2008**, *37*, 153-173.

(106) Bloom, J. D.; Meyer, M. M.; Meinhold, P.; Otey, C. R.; MacMillan, D.; Arnold, F. H. Evolving Strategies for Enzyme Engineering *Curr. Opin. Struct. Biol.* **2005**, *15*, 447-452.

(107) Jäckel, C.; Bloom, J. D.; Kast, P.; Arnold, F. H.; Hilvert, D. Consensus Protein Design without Phylogenetic Bias. *J. Mol. Biol.* **2010**, *399*, 541-546.

(108) Boxer, S. G.; Stocker, J.; Franzen, S.; Salafsky, J. Re-Engineering Photosynthetic Reaction Centers. In *Molecular Electronics- Science and Technology*; Aviram, A., Ed.; American Institute of Physics: New York, NY, USA, 1992; Vol. 262, pp 226-241.

(109) Bloom, J. D.; Arnold, F. H. *Proc. Natl. Acad. Sci. USA* **2009**, *106*.

(110) Stuart, J. A.; Marcy, D. L.; Wise, K. J.; Birge, R. R. Volumetric Optical Memory Based on Bacteriorhodopsin. *Synth. Met.* **2002**, *127*, 3-15.

(111) Stuart, J. A.; Tallent, J. R.; Tan, E. H. L.; Birge, R. R. Protein-Based Volumetric Memories. *Proc. IEEE Nonvol. Mem. Tech. (INVMTC)* **1996**, *6*, 45-51.

(112) Greco, J. A.; Wagner, N. L.; Ranaghan, M. J.; Rajasekaran, S.; Birge, R. R. Biomolecular Electronics and Protein-Based Optical Computing. In *Biomolecular Information Processing: From Logic Systems to Smart Sensors and Actuators*; Katz, E., Ed.; Wiley-VCH: Weinheim, Germany, 2012, pp 33-59.

(113) Azadmehr, M.; Abrahamsen, J. P.; Häfliger, P. A Foveated AER Imager Chip, IEEE International Symposium on Circuits and Systems (ISCAS). Kobe, Japan, 2005; Vol. 3, p 2751-2754.

(114) Peck, R. F.; DasSarma, S.; Krebs, M. P. Homologous Gene Knockout in the Archaeon *Halobacterium salinarum* with *ura3* as a Counterselectable Marker. *Mol. Microbiol.* **2000**, *35*, 667-676.

(115) Becher, B. M.; Cassim, J. Y. Improved Isolation Procedures for the Purple Membrane of Halobacterium Halobium. *Prep. Biochem.* **1975**, *5*, 161-178.

(116) Oesterhelt, D.; Stoeckenius, W. Isolation of the Cell Membrane of *Halobacterium Halobium* and Its Fractionation into Red and Purple Membrane. *Methods Enzymol.* **1974**, *31*, 667-678.

(117) Scherrer, P.; Mathew, M. K.; Sperling, W.; Stoeckenius, W. Retinal Isomer Ratio in Dark-Adapted Purple Membrane and Bacteriorhodopsin Monomers. *Biochemistry* **1989**, *28*, 829-834.

(118) He, J.-A.; Samuelson, L.; Li, L.; Kumar, J.; Tripathy, S. K. Photoelectric Properties of Oriented Bacteriorhodopsin / Polycation Multilayers by Electrostatic Layer-by-Layer Assembly. *J. Phys. Chem. B* **1998**, *102*, 7067-7072.

(119) He, J.-A.; Samuelson, L.; Li, L.; Kumar, J.; Tripathy, S. K. Bacteriorhodopsin Thin Film Assemblies - Immobilization, Properties, and Applications. *Adv. Mater.* **1999**, *11*, 435-446.

(120) Scholz, C. Perspectives On: Materials Aspects for Retinal Prostheses. *J. Bioact. Compat. Pol.* **2007**, *22*, 539-568.

(121) Roll, S.; Müller-Nordhorn, J.; Keil, T.; Scholz, H.; Eidt, D.; Greiner, W.; Willich, S. N. Dacron® vs. PTFE as Bypass Materials in Peripheral Vascular Surgery - Systematic Review and Meta-Analysis. *BMC Surg.* **2008**, *8*, 1-8.

(122) Liu, Y.; He, T.; Song, H.; Gao, C. Layer-by-Layer Assembly of Biomacromolecules on Poly(Ethylene Terephthalate) Films and Fiber Fabrics to Promote Endothelial Cell Growth. *J. Biomed. Mater. Res., Part A* **2007**, *81A*, 692-704.

(123) Liu, Y.; He, T.; Gao, C. Surface Modification of Poly(Ethylene Terephthalate) Via Hydroysis and Layer-by-Layer Assembly of Chitosan and Chondroitin Sulfate to Construct Cytocompatible Layer for Human Endothelial Cells. *Colloids Surf., B* **2005**, *46*, 117-126.

(124) Wyers, M. C.; Phaneuf, M. D.; Rzucidlo, E. M.; Contreras, M. A.; LoGerfo, F. W.; Quist, W. C. *In Vivo* Assessment of a Novel Dacron Surface with Covalently Bound Recombinant Hirudin. *Cardiovasc. Pathol.* **1999**, *8*, 153-159.

(125) Matsuzawa, A. Nano-Scale CMOS and Low Voltage Analog to Digital Converter Design Challenges, 8th International Conference on Solid-State and Integrated Circuit Technology, October 23-26, 2006, pp 1676-1679.

(126) El Gamal, A. Trends in CMOS Image Sensor Technology and Design, International Electron Devices Meeting, December 8-11, 2002. pp 805-808.

(127) Chiang, C. T.; Wu, C. Y. Implantable Neuromorphic Vision Chips. *Electron. Lett.* **2004**, *40*, 361-363.

(128) Wentai, L.; Vichienchom, K.; Clements, M.; DeMarco, S. C.; Hughes, C.; McGucken, E.; Humayun, M. S.; De Juan, E.; Weiland, J. D.; Greenberg, R. J. A Neuro-Stimulus Chip with Telemetry Unit for Retinal Prosthetic Device. *IEEE J. Solid-State Circuits* **2000**, *35*, 1487-1497.

(129) Delbrück, T.; Mead, C. A. An Electronic Photoreceptor Sensitive to Small Changes in Intensity. In *Advances in Neural Information Processing Systems 1*; David, S. T., Ed.; Morgan Kaufmann Publishers Inc.: 1989, pp 720-727.

(130) Mead; Carver. *Analog VLSI and Neural Systems,* Addison-Wesley: 1989, pp 371-379.

(131) Mortara, A.; Vittoz, E. A. A Communication Architecture Tailored for Analog VLSI Artificial Neural Networks: Intrinsic Performance and Limitations. *IEEE Trans. Neural Networks* **1994**, *5*, 459-466.

(132) Miyazaki, K.; Arnold, F. H. Exploring Nonnatural Evolutionary Pathways by Saturation Mutagenesis: Rapid Improvement of Protein Function. *J. Mol. Evol.* **1999**, *49*, 716-720.

(133) Wells, J. A. Additivity of Mutational Effects in Proteins. *Biochemistry* **1990**, *29*, 8509-8517.

(134) Tallent, J. R.; Stuart, J. A.; Song, Q. W.; Schmidt, E. J.; Martin, C. H.; Birge, R. R. Photochemistry in Dried Polymer Films Incorporating the Deionized Blue Membrane Form of Bacteriorhodopsin. *Biophys. J.* **1998**, *75*, 1619-1634.

(135) Fischer, U. C.; Towner, P.; Oesterhelt, D. Light Induced Isomerization, at Acidic pH, Initiates Hydrolysis of Bacteriorhodopsin to Bacterio-Opsin and 9-CIS-Retinal. *Photochem. Photobiol.* **1981**, *33*, 529-537.

(136) Turner, G. J.; Miercke, L. J. W.; Thorgeirsson, T. E.; Kliger, D. S.; Betlach, M. C.; Stroud, R. M. Bacteriorhodopsin D85n: Three Spectroscopic Species in Equilibrium. *Biochemistry* **1993**, *32*, 1332-1337.

(137) Kresheck, G. C.; Lin, C. T.; Williamson, L. N.; Mason, W. R.; Jang, D.-J.; El-Sayed, M. A. The Thermal Stability of Native, Delipidated, Deionized and Regenerated Bacteriorhodopsin. *J. Photochem. Photobiol., B* **1990**, *7*, 289-302.

(138) Brouillette, C. G.; Muccio, D. D.; Finney, T. K. pH Dependence of Bacteriorhodpsin Thermal Unfolding. *Biochemistry* **1987**, *26*.

(139) Birge, R. R.; Gillespie, N. B.; Izaguirre, E. W.; Kusnetzow, A.; Lawrence, A. F.; Singh, D.; Song, Q. W.; Schmidt, E.; Stuart, J. A.; Seetharaman, S.; Wise, K. J. Biomolecular Electronics: Protein-Based Associative Processors and Volumetric Memories. *J. Phys. Chem. B.* **1999**, *103*, 10746-10766.

(140) Millerd, J. E.; Rohrbacher, A.; Brock, N. J.; Chau, C.-K.; Smith, P.; Needleman, R. Improved Sensitivity in Blue-Membrane Bacteriorhodopsin Films. *Opt. Lett.* **1999**, *24*, 1355-1357.

(141) Matsumoto, H.; Yoshizawa, T. Rhodopsin Regeneration is Accelerated *Via* Noncovalent 11-*cis* Retinal-Opsin Complex – A Role of Retinal Binding Pocket of Opsin. *Photochem. Photobiol.* **2008**, *84*, 985-989.

(142) Hatcher, M. E.; Hu, J. G.; Belenky, M.; Verdegem, P.; Lugtenburg, J.; Griffin, R. G.; Hertzfeld, J. Control of the Pump Cycle in Bacteriorhodopsin: Mechanisms Elucidated by Solid-State Nmr of the D85n Mutant. *Biophys. J.* **2002**, *82*, 1017-1029.

(143) Sampogna, R. V.; Honig, B. Environmental Effects on the Protonation States of Active Site Residues in Bacteriorhodopsin. *Biophys. J.* **1994**, *66*, 1341-1352.

(144) Zscherp, C.; Schlesinger, R.; Tittor, J.; Oesterhelt, D.; Heberle, J. *In Situ* Determination of Transient pKa Changes of Internal Amino Acids of Bacteriorhodopsin by Using Time-Resolved Attenuated Total Reflection Fourier-Transform Infrared Spectroscopy. *Proc. Natl. Acad. Sci. U.S.A.* **1999**, *96*, 5498-5503.

(145) Kono, M.; Misra, S.; Ebrey, T. G. pH Dependence of Light-Induced Proton Release by Bacteriorhodopsin. *FEBS Lett.* **1993**, *331*, 31-34.

(146) Ames, J. B.; Mathies, R. A. The Role of Back-Reactions and Proton Uptake During the N --> O Transition in Bacteriorhodopsin's Photocycle: A Kintetic Resonance Raman Study. *Biochemistry* **1990**, *29*, 7181-7190.

(147) Balashov, S. P.; Lu, M.; Imasheva, E. S.; Govindjee, R.; Ebrey, T. G.; Otherson III, B.; Chen, Y.; Crouch, R. K.; Menick, D. R. The Proton Release Group of Bacteriorhodopsin Controls the Rate of the Final Step of Its Photocycle at Low pH. *Biochemistry* **1999**, *38*, 2026-2039.

(148) Richter, H.-T.; Brown, L. S.; Needleman, R.; Lanyi, J. K. A Linkage of the pKa's of Asp-85 and Glu-204 Forms Part of the Reprotonation Switch of Bacteriorhodopsin. *Biochemistry* **1996**, *35*, 4054-4062.

(149) Chizov, I.; Englehard, M.; Chernavskii, D. S.; Zubov, B.; Hess, B. Temperature and pH Sensitivity of the O_{640} Intermediate of the Bacteriorhodopsin Photocycle. *Biophys. J.* **1992**, *61*, 1001-1006.

(150) Govindjee, R.; Misra, S.; Balashov, S. P.; Ebrey, T. G.; Crouch, R. K.; Menick, D. R. Arginine-82 Regulates the pKa of the Group Responsible for the Light-Driven Proton Release in Bacteriorhodopsin. *Biophys. J.* **1996**, *71*, 1011-1023.

(151) Váró, G.; Lanyi, J. K. Protonation and Deprotonation of the M, N, and O Intermediates During the Bacteriorhodopsin Photocycle. *Biochemistry* **1990**, *29*, 6858-6865.

(152) Balashov, S.; Govindjee, R.; Kono, M.; Imasheva, E.; Lukashev, E.; Ebrey, T. G.; Crouch, R. K.; Menick, D. R.; Feng, Y. Effect of the Arginine-82 to Alanine Mutation in Bacteriorhodopsin on Dark Adaptation, Proton Release, and the Photochemical Cycle. *Biochemistry* **1993**, *32*, 10331-10343.

(153) Li, Q.; Bressler, S.; Ovrutsky, D.; Ottolenghi, M.; Friedman, N.; Sheves, M. On the Protein Residues That Control the Yield and Kinetics of O_{630} in the Photocycle of Bacteriorhodopsin. *Biophys. J.* **2000**, *78*, 354-362.

(154) Gillespie, N. B.; Ren, L.; Ramos, L.; Daniell, H.; Dews, D.; Utzat, K. A.; Stuart, J. A.; Buck, C. H.; Birge, R. R. Characterization and Photochemistry of 13-Desmethyl Bacteriorhodopsin. *J. Phys. Chem. B* **2005**, *109*, 16142-16152. (155) Ulrich, A. S.; Wallat, I.; Heyn, M. P.; Watts, A. Re-Orientation of Retinal in the M-Photointermediate of Bacteriorhodopsin. *Nat. Struct. Biol.* **1995**, *2*, 190-192.

(156) Rüdiger, M.; Tittor, J.; Gerwert, K.; Oesterhelt, D. Reconstitution of Bacteriorhodopsin from the Apoprotein and Retinal Studied by Fourier Transform Infrared Spectroscopy. *Biochemistry* **1997**, *36*, 4867- 4874.

(157) Bagley, K.; Dollinger, G.; Eisenstein, L.; Singh, A. K.; Zimanyi, L. Fourier-Transform Infrared Difference Spectroscopy of Bacteriorhodopsin and Its Photoproducts. *Proc. Natl. Acad. Sci. U.S.A.* **1982**, *79*, 4972-4976.

(158) Gao, M. M.; Boucher, F. The Uncoupling of Bacteriorhodopsin by High Temperature and Anaesthetics. *Toxicol. Lett.* **1998**, *100-101*, 393-396.

(159) Cladera, J.; Galisteo, M. L.; Duñach, M.; Mateo, P. L.; Padrós, E. Thermal Denaturation of Deionized and Native Purple Membranes. *Biochim. Biophys. Acta, Biomembr.* **1988**, *943*, 148-156.

(160) Alonso, A.; Restall, C. J.; Turner, M.; Gomez-Fernandez, J. C.; Goñi, F. M.; Chapman, D. Protein-Lipid Interactions and Differential Scanning Calorimetric Studies of

Bacteriorhodopsin Reconstituted Lipid-Water Systems. *Biochim. Biophys. Acta, Biomembr.* **1982**, *689*, 283-289.

(161) Brouillette, C. G.; McMichens, R. B.; Stern, L. J.; Khorana, H. G. Structure and Thermal Stability of Monomeric Bacteriorhodopsin in Mixed Pospholipid/Detergent Micelles. *Proteins: Struct., Funct., Genet.* **1989**, *5*, 38-46.

(162) Martínez-Ruvalcaba, A.; Becerra-Bracamontes, F.; Sánchez-Díaz, J. C.; González-Álvarez, A. Polyacrylamide-Gelatin Polymeric Networks: Effect of pH and Gelatin Concentration on the Swelling Kinetics and Mechanical Properties. *Polym. Bull.* **2009**, *62*, 539-548.

(163) Zhou, X.; Weng, L.; Chen, Q.; Zhang, J.; Shen, D.; Li, Z.; Shao, M.; Xu, J. Investigation of pH Sensitivity of Poly(Acrylic Acid-Co-Acrylamide) Hydrogel. *Polym. Int.* **2003**, *52*, 1153-1157.

Chapter 3

Two-Photon Spectroscopy of the Q-Bands of *meso*-Tetraphenyl-Porphyrin and -Chlorin Framework Derivatives

Selected portions of the material presented in this chapter are published in: Greco, J. A., Shima, S., Wagner, N. L., McCarthy, J. R., Atticks, K., Bruckner, C., and Birge, R. R. Two-Photon Spectroscopy of the Q-Bands of *meso*-Tetraphenyl-Porphyrin and –Chlorin Framework Derivatives. *J. Phys. Chem. C* **2015**, *119*, 3711-3724.

3.0. Abstract

The two-photon absorption and excitation spectra in the Q-band region (900 – 1360 nm) were measured for a number of porphyrinoids, including simple porphyrins (porphin, *meso*-tetraphenyl-porphyrin), chlorins (*meso*-tetraphenyl-2,3-dimethoxychlorin), and porphyrin- (*meso*-tetraphenyl-porpholactone) and chlorin-analogues (*meso*-tetraphenyl-porpholactol). These molecules were chosen to provide a series of compounds that differed structurally only in 'single points'. Vibronic structure is observed in the two-photon spectra for all porphyrinoids investigated, but their relative intensities show distinct differences from the vibronic development observed in the corresponding one-photon spectra. A Franck-Condon analysis provides insight into the observed differences. The calculations also indicate that the two-photon absorptivities are associated primarily with Type I processes involving multiple intermediate states, and that accurate assignment requires a summation over at least 30 intermediate states. The Q-bands of the *meso*-tetraphenyl-2,3-dimethoxychlorin exhibit anomalously high two-photon absorptivities, which we have traced to facile conformational distortion of the chlorin chromophore. Calculations indicated that the relative Q-band absorptivities are sensitive to the phase and magnitude of the chlorin ring distortions.

3.1. Introduction

The nonlinear optical properties of porphyrins and related oligopyrrolic compounds have been widely investigated due to their potential utility in medical and optical sensing technologies.[1-9] For instance, the ability of porphyrins and chlorins to generate the highly cytotoxic singlet oxygen ($^1O_2$) upon irradiation with visible light recommends them for use in the photodynamic therapy (PDT) of tumors.[1,10-12] However, a major limitation of one-photon-mediated PDT is associated with the visible wavelengths needed to activate a porphyrin. Blue and green light, the wavelengths absorbed best by regular porphyrins, do not penetrate tissue to any appreciable depths and possess low spatial selectivity due to scatter.[13,14]

Two-photon absorption is a nonlinear optical process that involves the simultaneous absorption of two photons.[15,16] This optical process provides an advantageous alternative for activating porphyrin photosensitizers because it promotes the chromophore into an excited state using the combined energy of two near-infrared (NIR) photons ($\lambda \approx 700 - 1400$ nm), which typically fall in a region where no one-photon absorption exists for the molecule. Importantly, the NIR region also falls within the optical window of biological tissue.[17] While significant effort has been directed towards the design of porphyrins, chlorins, and bacteriochlorins to enhance one-photon absorption in the NIR domain,[18-24] we focus here on enhancing the two-photon absorptivities of the two lowest-lying singlet states of porphyrin and chlorin analogues. The quadratic dependence of two-photon absorption on laser intensity allows for high spatial resolution of the PDT event and three-dimensional selectivity to target tumors at greater depths.

Porphyrins are comprised of four pyrrole subunits linked by methine bridges, which yields a closed-conjugated aromatic 18 π-electron system that is cross-conjugated with two β,β'-double bonds (Figure 3.1). The fully unsaturated aromatic structure is highly planarized and

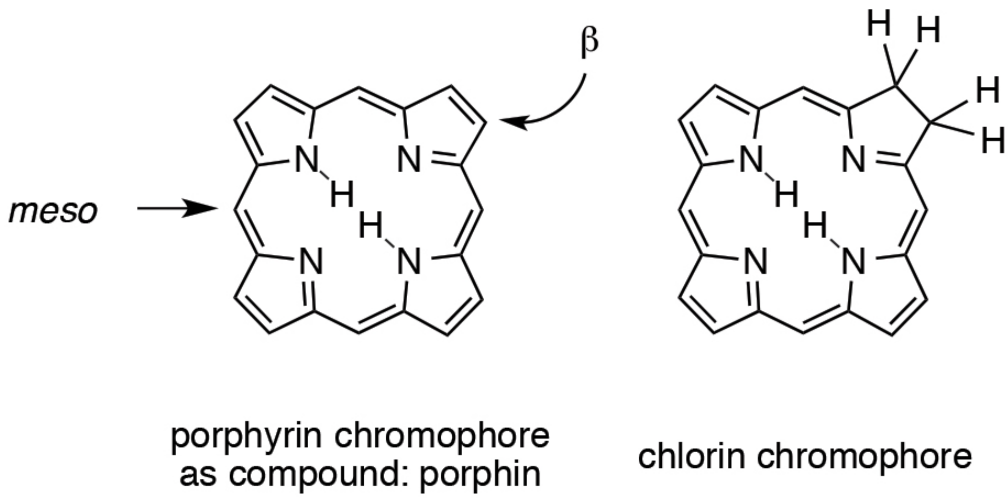

Figure 3.1. The chromophore structure of porphyrins and chlorins and the naming convention of the *meso*- and β-positions.

dominates the chemical and physical properties of porphyrins. Electronic properties are highly sensitive to modifications of one (or both) of the β,β'-double bonds.[25,26] Reduction of a β,β'-double bond results in the formation of a chlorin. The addition of *meso*-aryl substituents generally leads to little cross-talk with the porphyrinoid chromophore because *o*-aryl-to-β-hydrogen steric interactions hold the aryl groups in idealized orthogonal orientation with respect to the chromophore,[27] however, distortion to the macrocycle core often permits interaction with *meso*-substituents and leads to modulation of the optical properties of these systems.[28]

The entirely unsubstituted porphyrin macrocycle is referred to as porphin (Figure 3.1). Gouterman's four-orbital model of porphyrins describes the origin of the linear absorption of porphyrins and chlorins by transitions within the two highest occupied molecular orbitals (HOMOs) and the two lowest unoccupied molecular orbitals (LUMOs).[29] The one-photon absorption spectrum of porphin is composed of a Soret band (also called B-band), an intense band found at ~400 nm, and a set of Q-bands between 500 and 650 nm that decrease in intensity with increasing wavelength. Figure 3.2 demonstrates that the Q_x (570 nm) and Q_y (500 nm) transitions correspond to the *x*- and *y*-polarized transitions.[30] As defined by Gouterman,[29] the x-axis runs through the sp^2-hybridized nitrogen atoms, whereas the y-axis runs through the sp^3-hybridized nitrogen atoms. The symmetry of the four molecular orbitals (MOs) are also shown in Figure 3.2.[19,21,22] The electron density of the b_1 and c_2 orbitals are dominated by β,β'-double bonds, and are therefore destabilized upon saturation of the double bond.[31,32] Substitution and/or oxidation of the β,β'-double bond of porphin also reduces the symmetry, which broadens the Soret band due to an increased separation of two degenerate energy levels.[29]

Reduction of the free-base porphyrin to chlorin decreases the symmetry of the chromophore to C_{2v}, generating characteristic chlorin optical spectra.[33-35] The B-band to Q-band

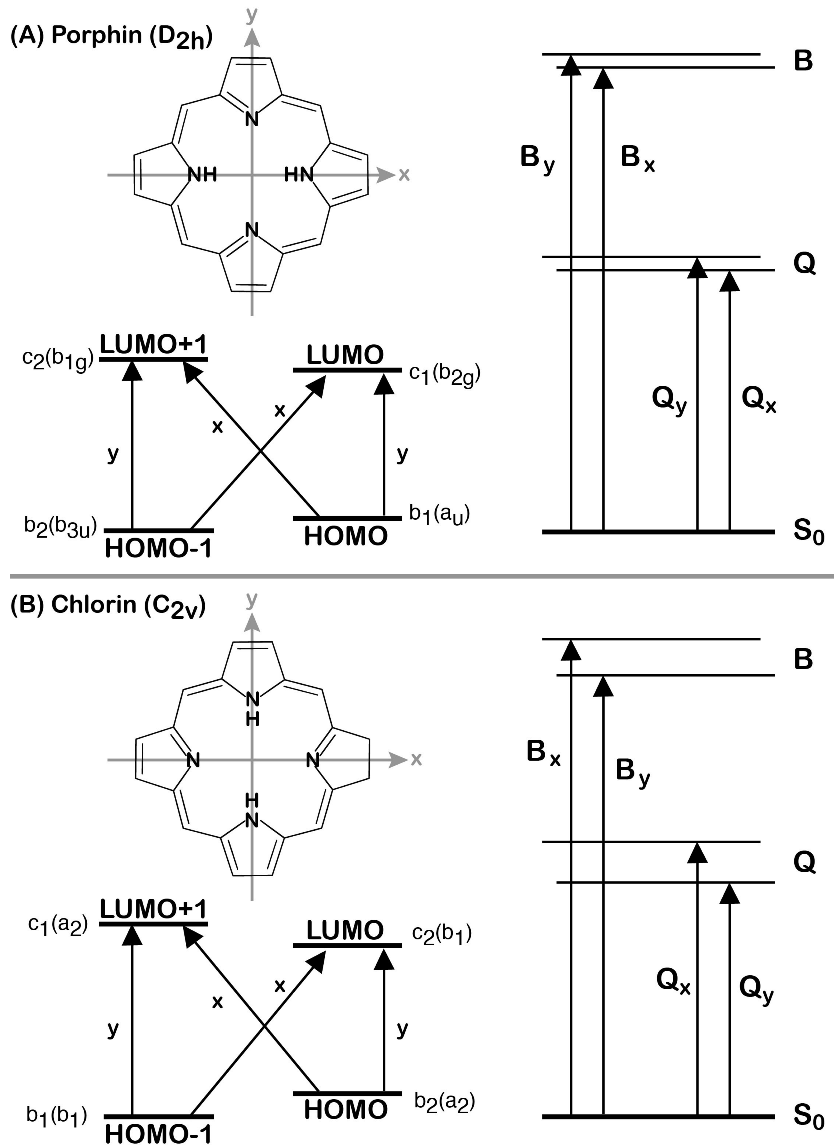

Figure 3.2. The coordinate systems used to assign the low-lying weakly allowed (Q) bands and the higher energy, strongly allowed Soret (B) bands in porphin (A) and chlorin (B) systems. Note that, unfortunately, the historical assignments create a situation where the lowest Q-band in porphyrins is designated Q_x whereas the lowest Q-band in chlorins is designated Q_y.

ratio and the Q_x to Q_y band ratio are modulated relative to porphin. The intensity of the Q-bands depends on mixing with the B-bands, which is proportional to the square of the energy gap between these orbitals.[36] Moreover, the increased conformational flexibility of the chlorin chromophore leads to a broadening of the spectral features, and any non-planar conformations lead to a general red-shift of the spectra.[25,26] We will adhere to the historical axis labeling convention shown in Figure 3.2, in which the lowest energy singlet state in porphyrins is labeled Q_x, whereas the lowest energy singlet state in chlorins is labeled Q_y..

The classic porphyrin sensitizers used in PDT, such as protoporphyrin IX and Photofrin®, are characterized by low two-photon cross-sections.[37,38] This led to the development of porphyrinoids with enhanced nonlinear optical properties. These structures include, *inter alia*, diporphyrins,[39,40] asymmetric *meso*-substituted molecules[41-44] and π-expanded macrocycles,[45-47] polymer-templated *J*-aggregates,[48] and self-assembled supramolecular porphyrin chains.[49-52] The modified structures are still capable of generating $^1O_2$ via energy transfer processes, the mechanism of which is referred to as Type II PDT. Note that the Type I (electron transfer) and Type II (energy transfer) nomenclature associated with PDT are separate from the Type I and Type II two-photon processes described in detail below.

In this study, we examine the two-photon properties of the low-lying Q-bands of porphyrin and chlorin derivatives. The majority of previous studies have been directed at the Soret bands, which have intrinsically large oscillator strengths. When substituents are added that induce charge transfer character into the Soret band, the Soret bands have been shown to gain high two-photon absorptivities.[40,45,47,53,54]

We prepared a series of strongly fluorescing porphyrinoids that allow a systematic study of the effects of 'single-point' modulations of the chromophore itself, also varying symmetry and

dipole moments (Scheme 3.1). The parent compound, *meso*-tetraphenyl-porphyrin (**TPP**), was converted, in three steps, to the stable symmetric chlorin, *meso*-tetraphenyl-2,3-dimethoxychlorin [**(OMe)$_2$TPC**].[55] A two-step oxidation of **TPP** replaced a porphyrin double-bond with a lactone moiety, generating *meso*-tetraphenyl-porpholactone (**TPL**).[56] From previous studies, we knew that this compound showed some spectral characteristics of a porphyrin and a chlorin.[56] Lastly, a reduction of the lactone generated *meso*-tetraphenyl-porpholactol **[(OH)TPO**], a typical chlorin but with an asymmetric chromophore.[56] We have shown previously that the replacement of an sp^3-carbon by an oxygen led to enhanced single-photon absorptivities.[56] In addition, a comparison of porphyrin with **TPP** allows the study of the influence of the presence of *meso*-phenyl groups.

The primary goal of this study is to understand both the vibronic and electronic characteristics responsible for the nonlinear optical properties of the Q-bands in porphyrins and chlorins. The principal value of this series of molecules is the opportunity to more fully characterize the mechanism of two-photon absorption into excited states in cases where absorptivity was not gained through resonance with lower-lying states. We will also demonstrate that despite the low one-photon oscillator strengths of the Q-bands, large two-photon absorptivities are possible when the chromophore is derivatized in a way that introduces some degree of chromophore non-planarity.

3.2. Experimental Section

3.2.1 Materials

Porphin was purchased from Frontier Scientific (Logan, UT) and rhodamine 6G and rhodamine B were purchased from Eastman Kodak Company (Rochester, NY). All other

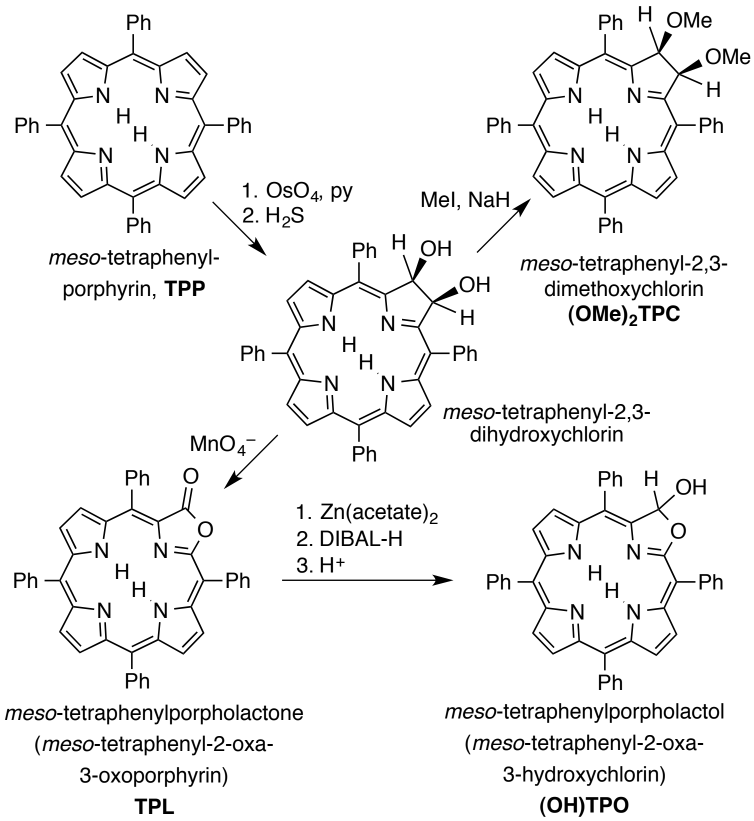

Scheme 3.1. Structures and synthetic pathways of the β, β'-modified chromophores investigated.

chromophores were prepared as described in the literature: **TPP** was synthesized according to the method of Adler;[57] **$(OMe)_2$TPC** was prepared by dihydroxylation of **TPP** and subsequent alkylation of the intermediate dihydroxychlorin;[55] oxidation of the intermediate dihydroxychlorin generated **TPL**;[56] reduction of the lactone generated the oxazolochlorin, **(OH)TPO**.[56] Solvents were spectroscopic grade (Aldrich) and were used as received.

3.2.2. Sample Preparation

For both one-photon and two-photon spectroscopy, the porphyrinoids were dissolved in carbon disulfide (CS_2). Carbon disulfide was chosen as a solvent environment for four reasons: (1) it has a high refractive index (η = 1.628), (2) it is a reasonable solvent for the compounds investigated in terms of solubility, (3) there is no major solvent absorption band in the visible and NIR regions of interest, and (4) the lack of absorbing vibrational modes also avoids the thermal shock events that limit the repetition rate of two-photon excitation studies and that add an additional source of noise to the experiments. The sample solutions were placed in a 1 × 1 cm glass cuvette to minimize secondary harmonic generation, which is known to reduce two-photon induced events. The sample optical density (OD) was adjusted to be 1 – 1.5 for linear measurements and 6 – 10 for nonlinear measurements.

Rhodamine 6G and rhodamine B, dissolved in ethanol, methanol, and 95:5 CS_2:methanol (v/v), were used as standards for the fluorescence quantum efficiency and two-photon absorptivity measurements. Because rhodamine 6G and rhodamine B are insoluble in CS_2, 5% methanol was added to solvate the compounds, and a minimal volume of hexafluoroisopropanol (HFIP) was added as a deaggregating agent.

3.2.3. Two-Photon Absorption Spectroscopy

The two-photon excitation spectra were collected by using the tunable pulsed-laser spectrometer shown in Figure 3.3. The spectroscopic methods were identical to those used by us previously.[58] The two-photon spectrum was scanned for each molecule from 800 – 1400 nm and the two-photon character of the process was verified by fitting the magnitude of the fluorescence signal versus the intensity of the excitation beam. Sample results are shown in Figure 3.4, and the details are explored below.

We now examine the extent to which the spectra we report here can be verified as pure two-photon in origin. Data were collected for four molecules at various wavelengths, and we examine here the results for an analysis of **TPP** at 1200 nm. This study showed the highest multi-photon contamination, due primarily to the fact that **TPP** is not one of the stronger two-photon absorbers, and the wavelength of excitation intercepted a relatively weak two-photon vibronic feature (see Figure 3.5).

We used singular value decomposition (SVD) based regression to fit the signal versus laser intensity to equations of the form,

$$Signal = a \times E^{i}_{pulse} + b \times E^{j}_{pulse} + ... + d \times E^{l}_{pulse} \tag{3.1}$$

where *a,b,..,d* are parameters fit by the SVD analysis for fixed values of the integers *i,j,…,l*. The best fit equation was assigned by minimizing the product of the RMS error and the number of fit parameters. The best fit was found for i=2 and j=3 (see Figure 3.6):

$$Signal = 24.864 \times E(mJ)^{2} + 0.83575 \times E(mJ)^{3} \tag{3.2}$$

We use energy as the independent variable in these analyses because the energy is directly measured (Figure 3.3) and is linearly proportional to the intensity because the pulse

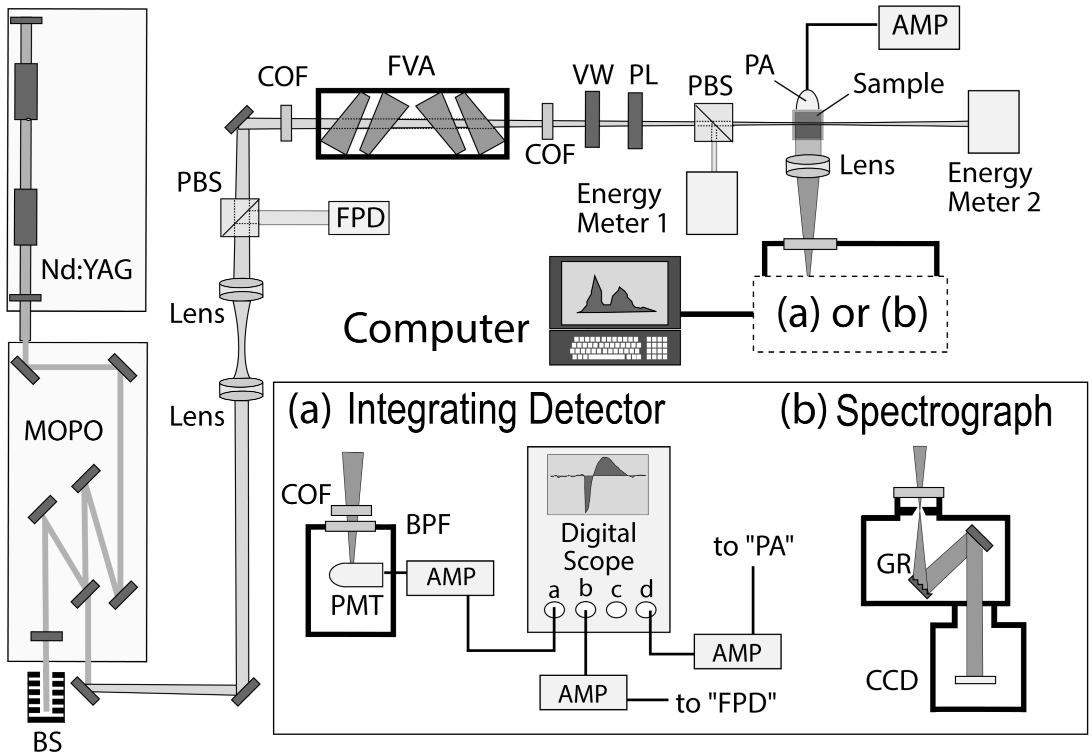

Figure 3.3. A schematic of the two-photon spectroscopy system used to obtain the nonlinear optical spectra reported here.[58] The system can simultaneously observe two-photon induced fluorescence and photoacoustic signals, but all the data reported here are based on fluorescence excitation, which provided a better signal-to-noise ratio. Abbreviations: AMP (amplifier), BPF (band-pass filter), BS (beam stop), COF (cut-off filter), FPD (fast photodiode), FVA (Fresnel variable attenuator), GR (grating), PA (photoacoustic detector), PBS (pellicle beam splitter), PL (polarizer), PMT (photomultiplier tube), VW (variable waveplate).

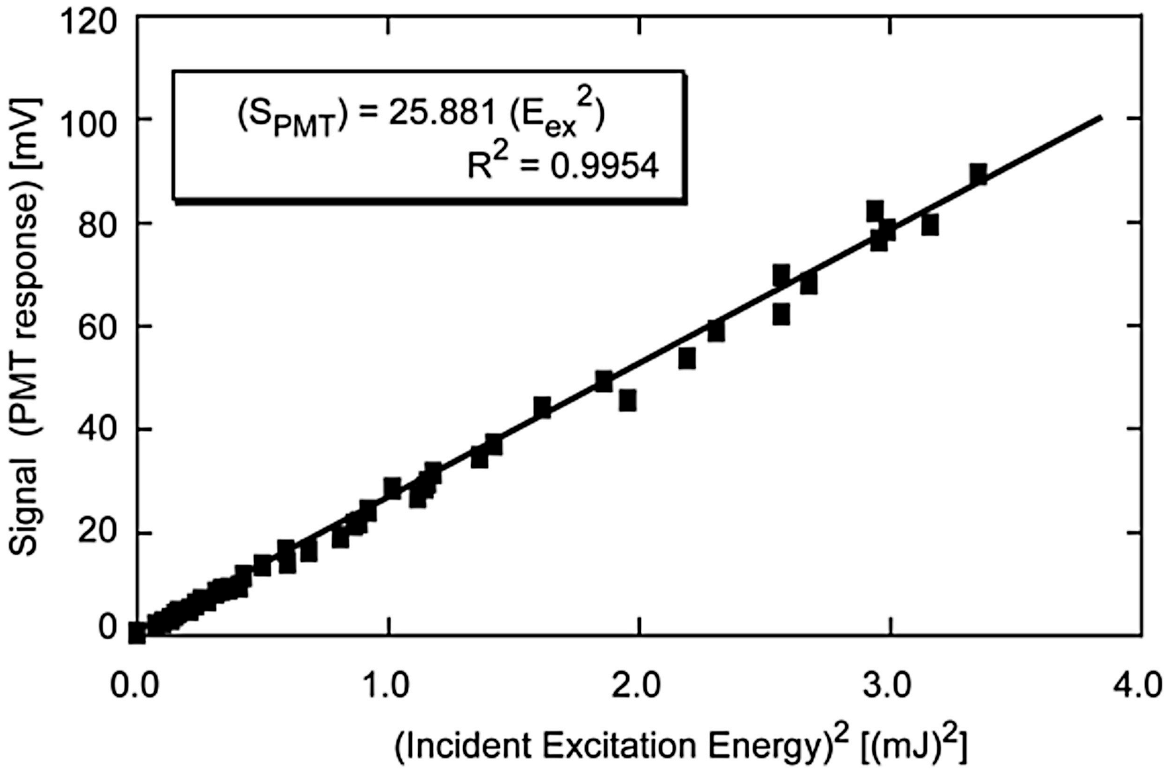

Figure 3.4. An alternative approach to the graphical validation of the two-photon character of the signals observed from two-photon excitation of **TPP** at 1200 nm observed by plotting the signal intensity versus the square of the laser excitation energy.

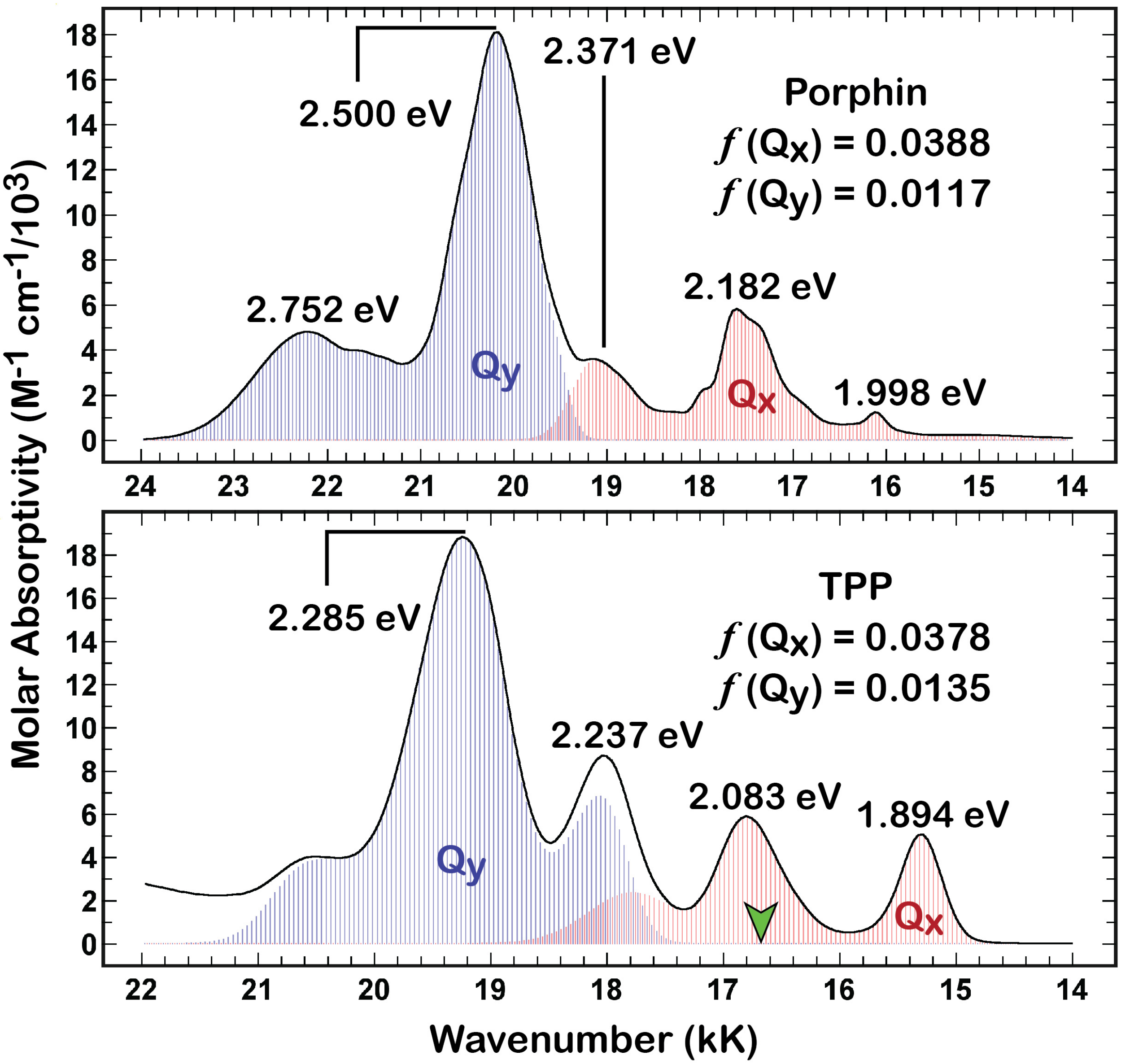

Figure 3.5. Decomposition of the oscillator strength of the Q_x and Q_y bands of porphin (top) and **TPP** (bottom) in CS_2. The experimental spectra were fit to multiple Gaussian bands and the bands were partitioned into the Q_x and Q_y bands by inspection. The oscillator strength was calculated by summing the oscillator strengths associated with the component Gaussians (see text). The first and maximum vibronic band maxima are assigned in electron volts (eV). The green arrow indicates the final excitation wavenumber, which was determined *via* the analysis shown in Figure 3.6.

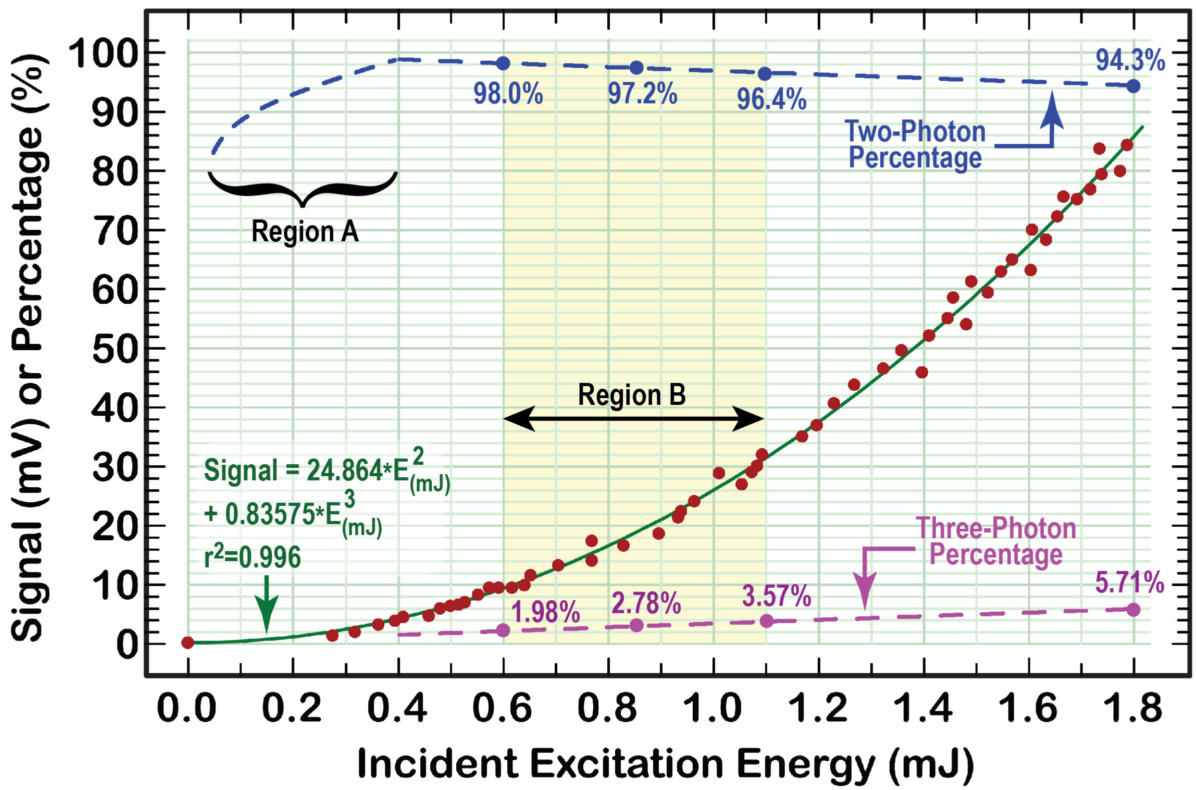

Figure 3.6. Regression analysis of the laser induced fluorescence of **TPP** at 1200 nm excitation. The equation Signal = a*E^m + b*E^n, where m and n are constrained to be unique integers, was fit to the data by using singular value decomposition and yielded the equation and fit shown in green. Fits to higher order equations such as a*E^l + b*E^m + c*E^n generated worse fits based on minimization of RMS error times parameters. We are thus confident that within experimental error, our data show evidence of only two-photon and three-photon excitation processes. Our spectra were collected using energies in **Region B** to maximize the percentage of two-photon signal while avoiding **Region A**, in which one-photon events have a significant impact on the signal. Although multi-photon processes should be fit with respect to intensity rather than energy, we used the incident energy because it was a directly measured quantity (see Figure 3.3). The pulse width is invariant to energy in these experiments, and thus the incident intensity is linearly proportional to the energy. The 1200 nm excitation wavelength excites near the maximum of the second vibronic band of **TPP**, assuming a two-photon process. The final state excitation wavenumber is indicated by using a green arrow in Figure 3.5.

width is constant. Equation 3.2 indicates that the observed signal has increasing three-photon character as the excitation energy increases, and reaches 5.7% at pulse energies of 1.8 mJ. We recognized this potential source of error early on in our studies, and limited the excitation energies used in all of our experiments to the range 0.6 mJ $\leq E_{pulse} \leq$ 1.1 mJ to make sure that the two-photon component of the signal would be 96% or greater (see Figure 3.6). A potential outlier in this regard is porphin, which has Q_x and Q_y two-photon absorptivities even smaller than **TPP** (see below). However, a regression analysis at the two-photon maximum indicated no higher order components of the signal above that associated with noise.

Absolute two-photon absorptivities were measured by using rhodamine B in methanol or methanol/CS_2 as an external standard.[59] The excitation measurements followed the methods described in the literature.[15] The photoacoustic measurements used bacteriorhodopsin as an external standard.[60] The results agreed to within 12%, but the final results are reported based on the excitation measurements due to a larger signal-to-noise ratio. The absolute two-photon absorptivities are plotted in Figure 3.7 and tabulated in Table 3.1.

3.2.4. One-Photon Absorption Spectroscopy

All one-photon absorption spectra were measured using a Cary 50 UV-visible spectrophotometer. Oscillator strengths of the bands were determined by assigning the vibronic features to the Q_x or Q_y states as shown in Figures 3.5 and 3.8, and integrating the respective regions.

3.2.5. Fluorescence Quantum Yields

Rhodamine 6G and rhodamine B were used as standards, in which the fluorescence quantum yield (Φ_F) in ethanol is known to be 0.95 and 0.65, respectively.[59] The Φ_F values of the porphyrinoid samples were measured by using the following formula,

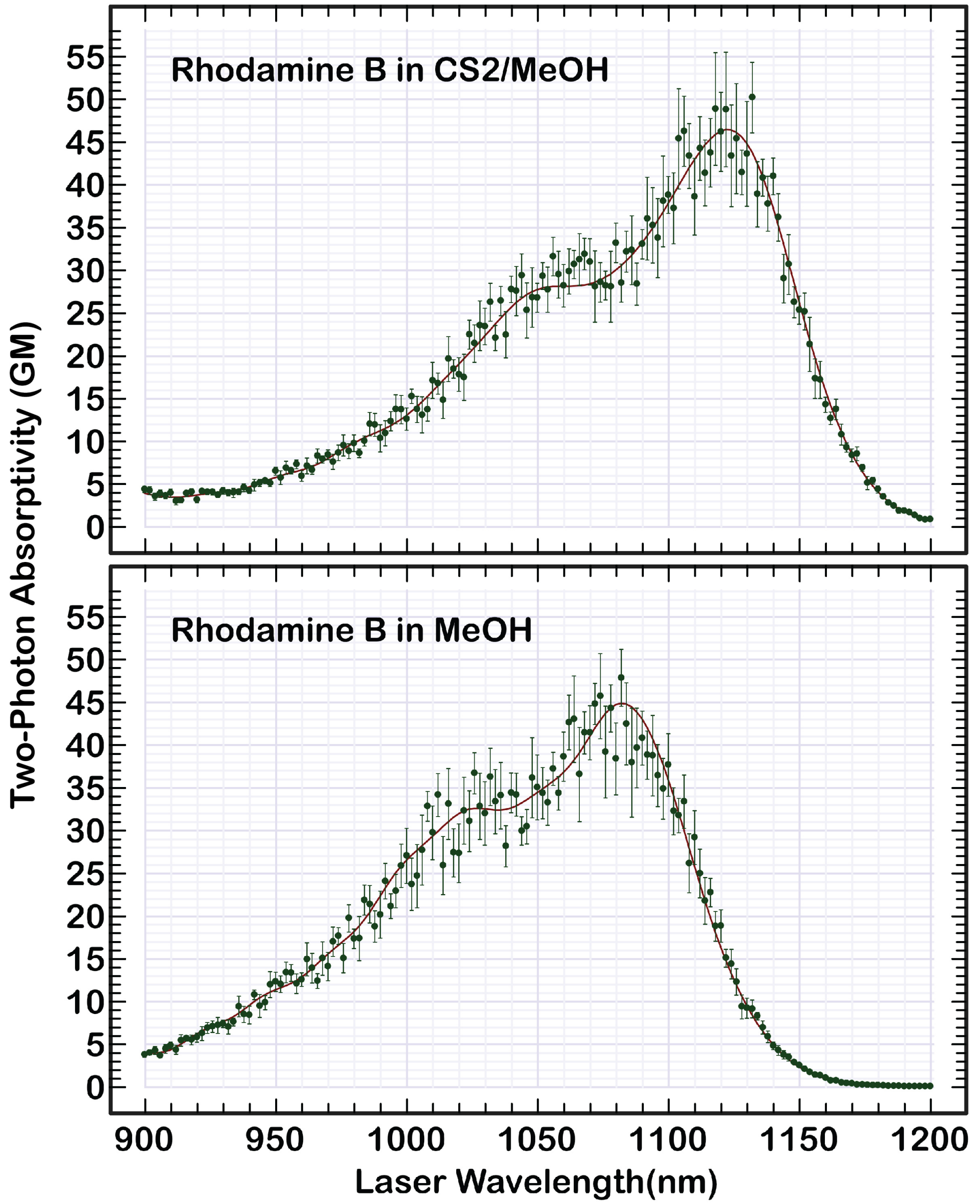

Figure 3.7. Two-photon excitation spectra of rhodamine B in CS_2 with 5% methanol (v/v) (top) and pure methanol (bottom). The vertical axis is in units of Göppert-Mayers (1 GM = 10^{-50} cm^4 s). The observed absorptivities, averaged in increments of 10 nm, are listed in Table 3.1.

Table 3.1. Two-Photon Absorptivities[a] (TPA) of Rhodamine B in MeOH and 95:5 CS_2:MeOH (v/v) in the 900 – 1200 nm Region

wavelength (nm)	TPA(GM) (MeOH)	TPA(GM) (CS_2/MeOH)
900	3.85 ± 0.59	3.86 ± 0.66
910	4.28 ± 0.78	3.39 ± 0.64
920	6.13 ± 0.96	3.64 ± 0.54
930	7.53 ± 1.09	4.03 ± 0.63
940	9.44 ± 1.70	4.59 ± 0.73
950	11.30 ± 1.88	5.69 ± 0.93
960	12.75 ± 2.20	6.55 ± 0.97
970	15.44 ± 2.39	7.90 ± 1.21
980	18.06 ± 2.94	9.73 ± 1.39
990	22.20 ± 3.43	11.15 ± 2.29
1000	26.41 ± 4.82	12.92 ± 2.35
1010	29.21 ± 4.96	15.76 ± 2.98
1020	31.87 ± 5.96	18.93 ± 3.37
1030	32.45 ± 5.70	22.23 ± 3.64
1040	32.55 ± 4.27	25.56 ± 3.78
1050	34.34 ± 5.39	27.66 ± 4.21
1060	36.71 ± 5.01	28.07 ± 3.91
1070	40.87 ± 6.18	28.33 ± 4.68
1080	44.63 ± 6.84	29.93 ± 4.23
1090	43.00 ± 7.24	33.11 ± 5.82
1100	35.98 ± 5.19	37.70 ± 7.37
1110	25.86 ± 5.09	42.82 ± 6.64
1120	16.35 ± 2.70	46.18 ± 9.29
1130	9.47 ± 1.86	44.79 ± 7.70
1140	4.93 ± 0.97	37.34 ± 4.38
1150	2.28 ± 0.40	26.31 ± 4.08
1160	0.93 ± 0.15	15.95 ± 2.43
1170	0.34 ± 0.08	8.53 ± 1.24
1180	0.13 ± 0.02	4.06 ± 0.66
1190	0.05 ± 0.01	1.73 ± 0.34
1200	0.02 ± 0.01	0.71 ± 0.22

[a]Two-photon absorptivities for two parallel propagating photons of identical energy and polarization. Values in units of Göppert-Mayers (1 GM = 10^{-50} cm^4 s).

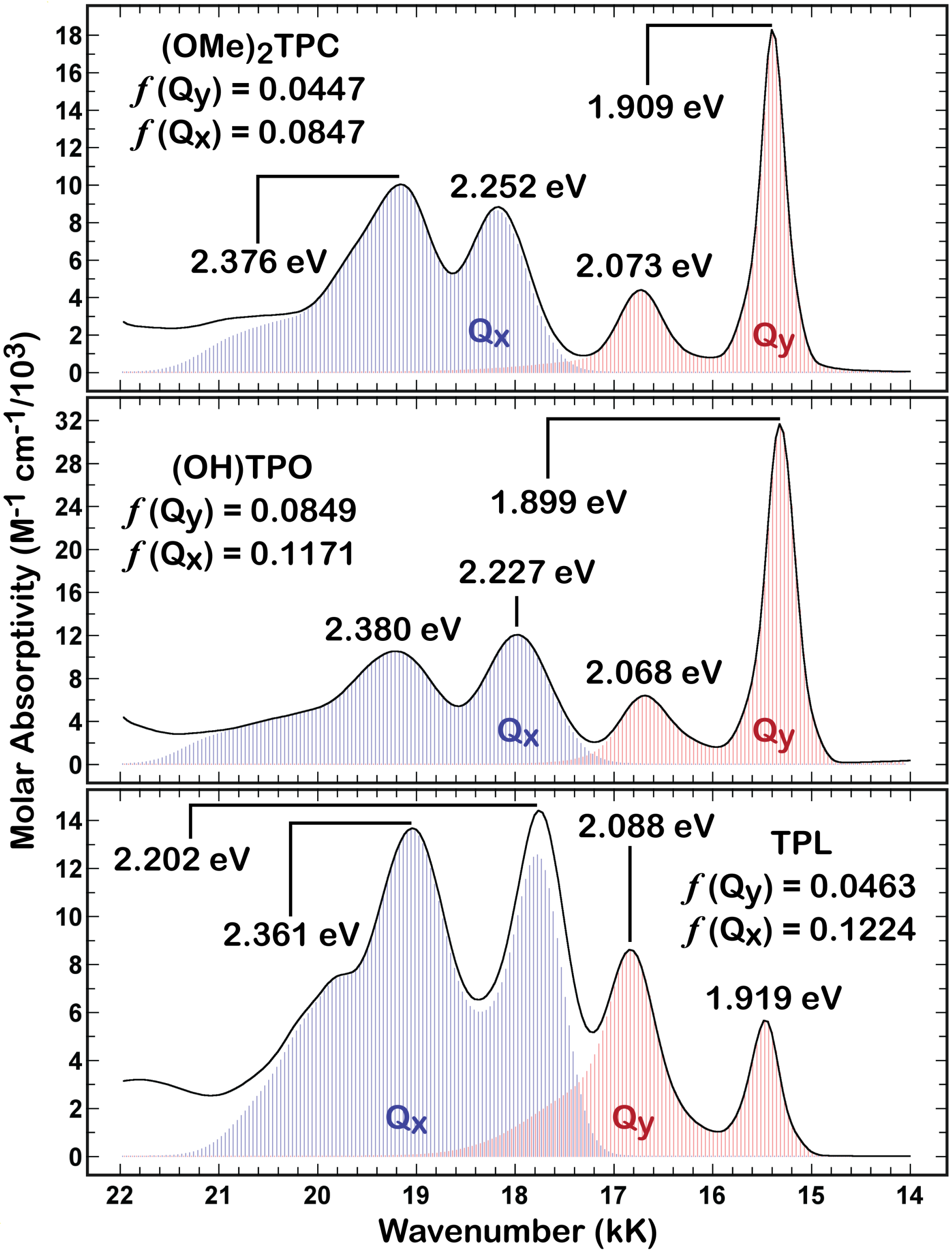

Figure 3.8. Decomposition of the oscillator strength of the Q_y and Q_x bands of three chlorin-like porphyrinoids in CS_2. See the caption for Figure 3.5 for further details.

$$\frac{\int I_{F,X}}{\int I_{F,ST}} = \frac{\Phi_{F,X}}{\Phi_{F,ST}}\left(\frac{\eta_X^2}{\eta_{ST}^2}\right) \tag{3.3}$$

where $\int I_{F,X}$ and $\int I_{F,ST}$ are the integrated fluorescence spectra, $\Phi_{F,X}$ and $\Phi_{F,ST}$ are the fluorescence quantum yields, and η_X and η_{ST} are the refractive indices of the solvents used for measurement, all with respect to unknown (*X*) and standard (*ST*) samples for the measurements, respectively.

3.2.6. Determination of Two-Photon Properties

The two-photon properties of the porphyrinoids investigated were calculated by using a variety of theoretical methods for comparison. All calculations were based on the orientationally averaged procedures originally proposed by Monson and McClain,[61] and as implemented by Masthay *et al*.[62] The equations can be simplified if both photons have the same energy, as is the case in the present study, in which a single laser is used to induce the two-photon event. The two-photon absorptivity at the two-photon absorption maximum ($d_{f\,0}$) is given by,

$$\delta_{f0} = \frac{(2\pi e)^4}{(4\pi\varepsilon_0 ch)^2}\left[E_\lambda^2\, g_{\max}(2E_\lambda)\right]\left|S_{f0}(\lambda,\lambda)\right|^2 \tag{3.4}$$

where E_λ is the energy of the photon, $g_{\max}(2E_\lambda)$ is the maximum value of the normalized line shape function described below, and S_{f0} is given by,

$$\left|S_{f0}(\lambda,\lambda)\right|^2 = \frac{1}{30}\sum_i^N\sum_j^N S_{ij}^{(f)} \tag{3.5}$$

and

$$S_{ij}^{(f)} = \left\{ \begin{array}{l} \dfrac{a\left(\langle i|\mathbf{r}|0\rangle \cdot \langle f|\mathbf{r}|i\rangle\right)\left(\langle j|\mathbf{r}|0\rangle \cdot \langle f|\mathbf{r}|j\rangle\right)}{\left[\left(E_i - E_\lambda\right)\left(E_j - E_\lambda\right) + \Gamma^2\right]} + \\ \dfrac{b\left(\langle i|\mathbf{r}|0\rangle \cdot \langle j|\mathbf{r}|0\rangle\right)\left(\langle f|\mathbf{r}|i\rangle \cdot \langle f|\mathbf{r}|j\rangle\right)}{\left[\left(E_i - E_\lambda\right)\left(E_j - E_\lambda\right) + \Gamma^2\right]} + \\ \dfrac{b\left(\langle i|\mathbf{r}|0\rangle \cdot \langle f|\mathbf{r}|j\rangle\right)\left(\langle f|\mathbf{r}|i\rangle \cdot \langle j|\mathbf{r}|0\rangle\right)}{\left[\left(E_i - E_\lambda\right)\left(E_j - E_\lambda\right) + \Gamma^2\right]} \end{array} \right\} \tag{3.6}$$

Note that the sum over states in Equation 3.5 includes the initial and final states.[62-64] The variables a and b in Equation 3.6 specify the polarization of the two photons. For two photons propagating along the same path with identical polarization, a and b both equal 8. Other polarization and propagation situations are given in Table I of reference 62. A damping constant of Γ = 2 eV was used to prevent fortuitous resonances from "blowing up". The function $g_{\max}(2E_\lambda)$ has units of seconds and is normally approximated by using a Gaussian distribution.[62] That approach, however, is not adequate for the present investigation. The Q-bands of porphyrins and chlorins display discrete vibronic structure with two or more separate vibronic bands. In such cases, the line shape function must be assigned for each final state by integrating under the normalized two-photon spectrum in frequency space and setting $g_{\max}$ equal to the inverse of the integral,

$$g_{\max} = \left[\int_0^\infty \hat{\delta}(\nu)\, d\nu\right]^{-1} \tag{3.7}$$

where $\hat{\delta}(\nu)$ is the normalized and dimensionless function that represents the two-photon spectrum in frequency space. There is some confusion in the literature regarding this function.[15] It is not the integral that is normalized, but rather the function, so that $\hat{\delta}(\nu_{\max}) = 1$, where $\nu_{\max}$ is the frequency of maximum two-photon absorption.

The key difficulty in calculating the two-photon absorptivity is the necessity to generate the many transition energies, transition lengths, and dipole moments that appear in the summation of states (SOS) in Equation 3.6. We used both semi-empirical MNDO-PSDCI procedures[58,65,66] and a hybrid *ab initio* approach using both the symmetry-adapted cluster-configuration interaction (SAC-CI)[67-70] and full single configuration interaction (CIS)[71] methods. The semi-empirical MNDO-PSDCI method used calculates excited state properties by implementing full single and double configuration interaction within the π system.[58,65,66] The code is available upon request from RRB. All MNDO-PSDCI calculations reported here used the standard parameterization, which assigns the σ and π mobility constants an identical value of 1.7, the Nishimoto-Mataga approximation for electron-repulsion integrals,[72] and the AM1[73] Hamiltonian.[58,65,66] The SOS calculations included the lowest 60 excited singlet states. The hybrid approach used the SAC-CI method to calculate the dipole moments in the ground and first two excited singlet states and the oscillator strengths into these states. The CIS method was used to assign the transition energies and transition lengths between the lowest 40 excited singlet states.

Ground state geometries were calculated by using density functional theory (DFT) methods, the B3LYP functional, and the 6-31G(d) basis set.[74] The effect of solvent environment on both the ground state geometries and transition energies was calculated by using the polarizable continuum model (PCM) method.[75-78] We observed that the calculated two-photon absorptivities were very sensitive to the ground state geometry, and that the chlorin ring system was remarkably flexible. This resulted in much reduced rotational barriers for *meso*-phenyl groups. We also observed that ground state geometries based on well-studied semi-empirical Hamiltonians, such as MOPAC/PM3 and MOPAC/PM6, generated equilibrium geometries that

included significant distortion from planarity in the ring system. Surprisingly, these geometries often generated two-photon absorptivities that were in much better agreement with the experiment than those generated by using the B3LYP/6-31G(d) DFT methods. Thus, we explored both DFT and semi-empirical ground state geometries.

3.3. Results and Discussion

3.3.1. Experimental One-Photon and Two-Photon Spectra

The one-photon and two-photon spectra of the porphyrinoids studied in the Q-band region are shown in Figure 3.9. The vibronic features are assigned based on the over-simplified notion that there is a single promoting mode. This approach works reasonably well for the *meso*-tetraphenyl-substituted compounds, but is not adequate for unsubstituted porphin, which exhibits a much more complex vibronic development (Figure 3.9). A comparison of the one-photon and two-photon spectra indicates that the vibronic distributions of the linear and nonlinear spectra are different. For example, the 1,0 vibronic component of the lowest singlet state is the most intense feature in all of the two-photon spectra. In contrast, the one-photon spectra do not display a dominant vibronic mode, nor do the Q-bands display consistent relative intensities. One of the key goals of this paper is to provide an explanation for these vibronic anomalies.

3.3.2. One-Photon and Two-Photon Vibronic Distributions

We can calculate the vibronic distribution of a two-photon transition by replacing the $S_{f0}(\lambda\lambda)$ in Equation 3.4 with a Taylor's series with respect to the normal coordinate, Q_a.[79] The resulting expansion provides the two-photon absorptivity in terms of the individual vibrational modes, $v_k^{'}$, within the final excited state manifold:

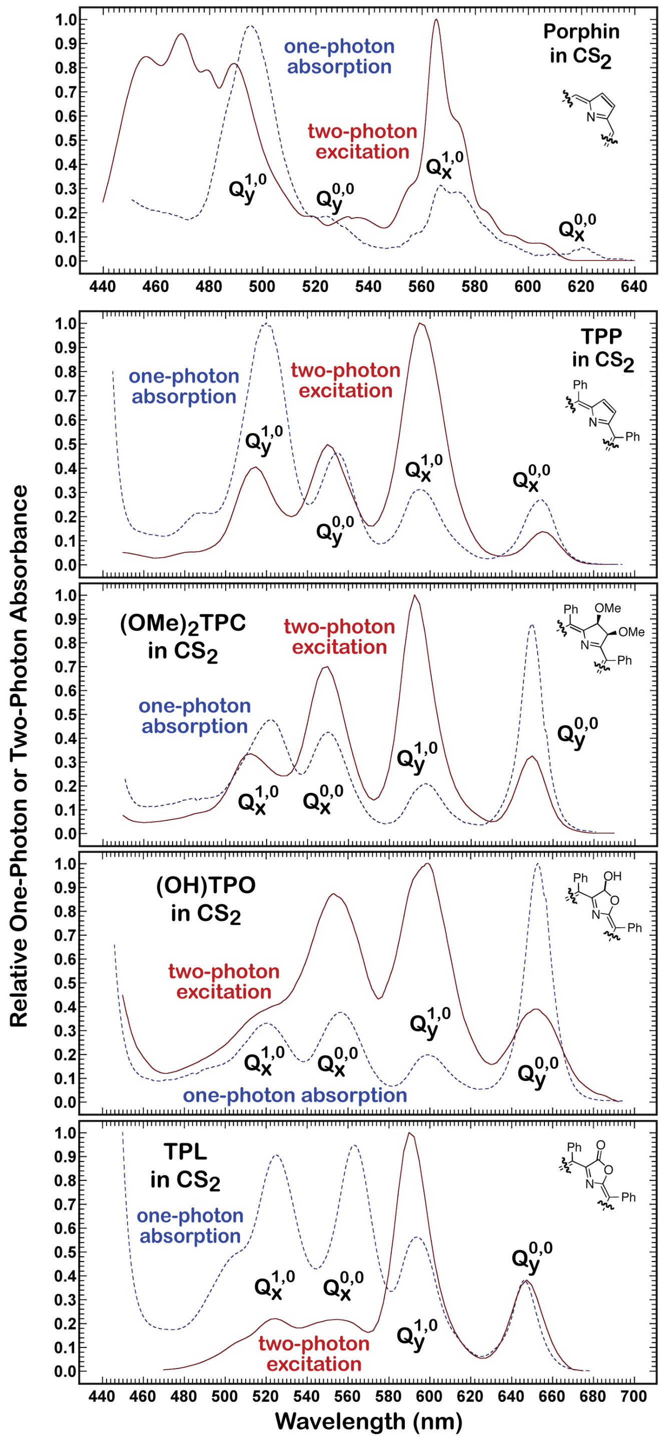

Figure 3.9. Ambient temperature one-photon absorption (dashed, blue trace) and two-photon excitation (red, solid trace) spectra of the porphyrinoids indicated in CS_2. The two-photon data are plotted relative to the wavelength of the final state transition associated with the simultaneous absorption of the two photons. The vibronic bands are marked using a simple notion that each electronic state contributes a system origin (0,0) and a higher energy vibronic component (1,0).

$$S_{f0}^{k} = S_{f0}^{e}(Q_{eq})\left\langle v_{k}^{'} \,|\, 0^{"} \right\rangle + \sum_{a} \frac{\partial S_{f0}^{e}}{\partial Q_{a}} \left\langle f \middle| Q_{a} \middle| 0 \right\rangle + \ldots \tag{3.8}$$

The first term on the right-hand side of Equation 3.8 assumes that the transition occurs from the zero vibrational level in the ground state and represents the first term of the Taylor expansion, where $S_{f0}^{e}(Q_{eq})$ is the pure electronic contribution evaluated at the ground state equilibrium geometry (Q_{eq}) and is the Franck-Condon overlap integral between the vibrational mode in the final excited state and the zero point level in the ground state ($0^{"}$). The second term on the right-hand side represents the contribution from second order effects, in which vibrational modes mediate the electronic transition probability, and will be ignored in our simulations. Substituting for $S_{f0}(\lambda\lambda)$ in Equation 3.4 and including the energy term, the vibronic distribution in the final state takes the form,

$$\delta_{f0}^{k} \propto \mathrm{P}\left[\Gamma[\psi_{vib}^{k}] \otimes \Gamma[\psi_{elec}^{f}] \in \left\{ \begin{matrix} \xi^{2} \\ xy \\ xz \\ yz \end{matrix} \right\} \right] \frac{E_{k0}^{f}}{E_{00}^{f}} \left| \left\langle v_{k}^{'} \,|\, 0^{"} \right\rangle \right|^{2} \tag{3.9}$$

where the symmetry function, P[…], returns unity when the product of the electronic and vibrational symmetries are two-photon allowed (and zero otherwise), and E_{k0}^{f} is the energy of the transition from the ground state to the k^{th} mode in the final state. The Franck-Condon overlap integral, $\left\langle v_{k}^{'} \,|\, 0^{"} \right\rangle$, is calculated by generating the vibrational modes in the ground state and in the final excited state and matching up the modes. Thus, each mode, *k*, has a potentially different frequency in the ground and excited state, and will likely be associated with a different effective reduced mass. Provided the polyatomic molecule has high symmetry so that the vibrational

modes are divided up into symmetry groups, matching the modes is a straightforward process. The principal variable in assigning the Franck-Condon distribution for a given mode is the displacement upon excitation, or simply Δ_k. We used Gaussian 09 and the method proposed by Niedzwiedzki *et al.*[80] to calculate this dimensionless displacement for the k^{th} mode,

$$\Delta Q_k^{f0} = \Delta_k = 95.76 \left| \left[\frac{1}{\left(\mu_j\right)^{1/3}\left(\sigma_j\right)^{2/3}} - \frac{1}{\left(\mu_i\right)^{1/3}\left(\sigma_i\right)^{2/3}} \right]_k \right| \tag{3.10}$$

where σ_i is the frequency and μ_i is the reduced mass of the k^{th} mode in the ground state, and σ_j and μ_j are the corresponding values for the k^{th} mode in the excited state. The prefactor assumes that the frequencies are in wavenumbers (cm^{-1}) and the reduced masses are in amu. The key advantage of Equation 3.10 is the partial compensation for the Duschinsky effect, which is reflected in a change in the reduced mass of the mode upon excitation.

What remains is to calculate the Franck-Condon vibrational overlap integrals. The calculation is facilitated by using the very efficient, closed form expansions proposed by Chang for displaced and distorted harmonic oscillators.[81] We carried out the calculations for porphin and the corresponding chlorin (2,3-dihydroporphin) molecule for which the vibrational mode assignments are unambiguous. The Franck-Condon active vibrational modes are listed in Tables 3.2 and 3.3, and the resulting vibronic distributions are shown in Figure 3.10. Note, however, that some of these modes are active in the one-photon spectra, whereas others are active only in the two-photon spectra, as determined by evaluation of the function P[…] in Equation 3.9.

Despite the significant approximations inherent in the results shown in Figure 3.10, these simulations provide an excellent perspective on why the one-photon and two-photon vibronic distributions are different. First, the system origin is relatively weak in the two-photon spectra

Table 3.2. Vibronic Analysis of the $S_0 \rightarrow S_1(Q_x)$ Transition of Porphin[a]

#(0)	#(*)	freq(0)	freq(*)	sym	IR(0)	IR(*)	force(0)	force(*)	rmass(0)	rmass(*)	Δfreq	ΔQ
77	76	1508.773	1496.31	a_g	0	0	13.00	9.366	9.697	7.100	-12.456	0.0421
81	80	1559.936	1544.04	a_g	0	0	4.292	4.964	2.994	3.534	-15.891	0.0249
84	83	1608.509	1589.56	a_g	0	0	9.639	7.832	6.323	5.261	-18.942	0.0288
3	2	75.696	73.798	a_u	0	0	0.017	0.016	5.112	5.115	-1.898	0.0558
13	11	329.366	316.503	a_u	0	0	0.299	0.281	4.682	4.758	-12.863	0.0274
23	22	526.170	493.527	a_u	0	0	0.615	0.537	3.769	3.741	-32.643	0.0465
29	27	753.404	736.361	a_u	0	0	1.505	1.327	4.501	4.153	-17.043	0.0321
30	28	775.727	753.611	a_u	0	0	1.249	1.157	3.522	3.456	-22.116	0.0206
7	6	143.625	136.900	b_{1g}	0	0	0.064	0.058	5.221	5.243	-6.725	0.0666
10	10	226.437	219.952	b_{1g}	0	0	0.172	0.165	5.692	5.77	-6.485	0.023
22	21	484.817	451.525	b_{1g}	0	0	0.534	0.46	3.856	3.833	-33.292	0.0534
40	39	885.379	869.223	b_{1g}	0	0	0.777	0.686	1.683	1.541	-16.156	0.0396
6	5	138.804	130.417	b_{2g}	0	0	0.048	0.043	4.239	4.297	-8.387	0.0887
9	8	206.535	200.719	b_{2g}	0	0	0.129	0.123	5.123	5.192	-5.816	0.0249
21	19	469.239	437.042	b_{2g}	0	0	0.496	0.429	3.824	3.815	-32.197	0.0533
25	23	713.094	679.435	b_{2g}	0	0	0.381	0.353	1.272	1.298	-33.659	0.0305
27	25	733.969	722.831	b_{2g}	0	0	0.822	0.775	2.590	2.517	-11.138	0.0182
32	30	783.595	760.052	b_{2g}	0	0	1.249	1.152	3.452	3.385	-23.543	0.0216
44	41	890.565	870.425	b_{2g}	0	0	0.648	0.605	1.387	1.354	-20.140	0.0233
73	71	1400.042	1373.66	b_{3g}	0	0	1.753	2.048	1.518	1.842	-26.375	0.0358
76	74	1482.869	1480.83	b_{3g}	0	0	4.679	3.340	3.611	2.585	-2.039	0.0608
78	77	1522.234	1510.58	b_{3g}	0	0	2.706	3.154	1.982	2.346	-11.645	0.0306
79	78	1551.624	1524.81	b_{3g}	0	0	5.225	3.243	3.684	2.368	-26.809	0.0849
94	91	1772.172	1739.15	b_{3g}	0	0	8.419	7.033	4.55	3.946	-33.014	0.0260
85	84	1655.378	1618.26	b_{1u}	0	4	8.365	7.001	5.181	4.537	-37.109	0.0258
90	88	1706.592	1687.53	b_{1u}	7	12	7.970	7.152	4.644	4.263	-19.061	0.0157
24	36	650.805	808.15	b_{2u}	526	34	2.074	1.888	8.309	4.907	157.345	0.0213
38	37	830.403	847.279	b_{2u}	1	0	1.919	2.492	4.723	5.891	16.876	0.0574
45	49	893.362	1008.10	b_{2u}	103	148	2.153	4.134	4.579	6.905	114.743	0.1294
57	57	1075.839	1076.38	b_{2u}	11	3	2.469	1.804	3.621	2.643	0.544	0.0698
62	61	1145.778	1172.97	b_{2u}	14	26	1.633	0.965	2.111	1.19	27.198	0.1393
66	67	1217.36	1281.72	b_{2u}	1	2	1.319	1.780	1.511	1.839	64.368	0.0741
69	68	1295.702	1303.63	b_{2u}	1	2	1.545	2.495	1.562	2.492	7.935	0.1092
72	72	1387.969	1377.42	b_{2u}	40	30	3.080	3.255	2.713	2.911	-10.548	0.0107
75	75	1476.992	1487.57	b_{2u}	1	0	1.817	2.139	1.414	1.64	10.579	0.0370
83	82	1595.380	1579.90	b_{2u}	18	25	5.108	4.612	3.406	3.136	-15.476	0.0172
86	85	1666.160	1666.35	b_{2u}	2	1	4.893	5.253	2.992	3.211	0.196	0.0118
89	89	1694.563	1687.77	b_{2u}	0	4	10.47	8.571	6.192	5.107	-6.787	0.0270
2	1	61.018	58.058	b_{3u}	0	0	0.012	0.011	5.639	5.591	-2.960	0.1355
11	9	227.252	215.051	b_{3u}	3	2	0.214	0.198	7.021	7.282	-12.201	0.0357
16	15	368.649	343.601	b_{3u}	7	7	0.305	0.265	3.804	3.816	-25.048	0.0596
26	24	720.593	701.603	b_{3u}	1	4	1.015	0.942	3.318	3.247	-18.99	0.0216
42	40	888.514	869.307	b_{3u}	179	186	0.722	0.602	1.552	1.352	-19.207	0.0595

[a]Only vibronic modes involving ΔQ>0.02 are listed. The ground [freq(0)] and excited singlet [freq(*)] state vibrational frequencies are in wavenumbers (cm^{-1}), the IR intensities of the modes for the ground [IR(0)] and excited singlet [IR(*)] states are in KM/mol, the ground [force(0)] and excited singlet [force(*)] state force constants are listed in mDyne/Å, and the ground [rmass(0)] and excited singlet [rmass(*)] state force constants are listed in amu. The change in frequency, Δfreq, is in wavenumbers (cm^{-1}) and the dimensionless coordinate displacement, ΔQ, is listed in the last column.

Table 3.3. Vibronic Analysis of the $S_0 \rightarrow S_1(Q_y)$ Transition of Chlorin[a]

#(0)	#(*)	freq(0)	freq(*)	sym	IR(0)	IR(*)	force(0)	force(*)	rmass(0)	rmass(*)	$\Delta\sigma$/cm^{-1}	ΔQ
13	12	319.837	322.595	a_1	1	0	0.310	0.323	5.139	5.272	2.758	0.017
79	81	1498.695	1515.603	a_1	46	6	3.011	3.675	2.276	2.716	7.289	0.035
86	91	1580.632	1661.108	a_1	0	83	8.808	6.091	5.984	3.747	11.777	0.050
88	85	1623.596	1584.717	a_1	81	7	4.033	5.939	2.597	4.014	4.085	0.060
89	89	1642.092	1641.477	a_1	54	0	2.128	1.788	1.339	1.127	-0.615	0.037
90	84	1649.331	1541.277	a_1	187	1	3.998	4.996	2.495	3.570	-7.492	0.036
7	6	133.623	129.597	a_2	0	0	0.044	0.042	4.217	4.227	-4.026	0.044
17	16	359.221	348.927	a_2	0	0	0.344	0.324	4.518	4.522	-10.294	0.022
23	22	516.697	472.219	a_2	0	0	0.570	0.496	3.626	3.778	-44.478	0.045
24	27	623.071	715.501	a_2	0	0	0.778	0.942	3.401	3.122	10.560	0.053
27	25	698.960	669.565	a_2	0	0	0.505	0.325	1.753	1.232	-29.395	0.157
28	23	704.941	593.064	a_2	0	0	0.529	0.683	1.806	3.296	-30.007	0.080
46	47	917.505	946.128	a_2	0	0	0.808	0.729	1.629	1.382	-47.106	0.030
49	45	993.234	899.599	a_2	0	0	0.743	0.689	1.277	1.446	-17.906	0.022
53	52	1056.036	1032.688	a_2	0	0	0.919	0.864	1.399	1.375	-23.348	0.017
3	2	55.524	53.908	b_1	0	0	0.009	0.009	5.061	5.053	-1.616	0.078
5	4	100.512	99.641	b_1	10	10	0.025	0.024	4.167	4.166	-0.871	0.016
10	9	216.427	213.387	b_1	2	1	0.172	0.163	6.226	6.086	-3.040	0.025
16	13	340.770	322.804	b_1	5	4	0.266	0.242	3.888	3.949	-17.966	0.039
22	20	477.974	437.318	b_1	1	0	0.502	0.437	3.727	3.879	-40.656	0.047
26	29	696.999	751.135	b_1	1	0	1.168	1.065	4.082	3.202	-26.879	0.024
36	33	809.112	782.875	b_1	52	74	0.462	0.437	1.198	1.210	-26.237	0.019
41	40	864.978	856.203	b_1	4	42	0.545	0.520	1.236	1.204	-8.775	0.015
45	42	904.397	868.677	b_1	59	67	0.728	0.686	1.510	1.542	-0.466	0.018
47	49	931.727	955.185	b_1	191	142	0.822	0.774	1.606	1.441	-62.116	0.017
50	46	1017.301	919.647	b_1	34	78	0.805	0.743	1.320	1.491	-12.080	0.023
54	51	1056.449	1012.852	b_1	11	3	0.915	0.837	1.392	1.385	-43.597	0.025
15	15	337.412	332.275	b_2	0	0	0.451	0.429	6.719	6.595	-5.137	0.017
67	70	1279.701	1307.550	b_2	38	2	1.563	1.831	1.620	1.818	-12.789	0.035
70	71	1308.696	1330.855	b_2	67	130	2.089	2.484	2.070	2.381	-69.505	0.035
71	65	1320.339	1260.854	b_2	2	2	1.746	1.986	1.699	2.120	-18.847	0.028
75	68	1400.360	1290.719	b_2	157	138	1.759	2.324	1.522	2.368	-17.977	0.058
77	78	1419.289	1487.972	b_2	4	18	2.666	2.466	2.246	1.890	-23.450	0.015
78	77	1465.802	1420.643	b_2	602	8	3.658	2.662	2.889	2.239	-45.159	0.058
81	76	1511.422	1415.417	b_2	558	42	3.597	2.497	2.672	2.115	-3.872	0.067
82	80	1536.433	1509.640	b_2	3	0	4.378	3.473	3.147	2.586	-26.793	0.039
84	88	1552.389	1617.052	b_2	25	53	4.082	3.092	2.875	2.007	-33.033	0.048
85	82	1578.007	1530.389	b_2	23	35	5.002	3.731	3.409	2.704	-22.000	0.048
87	86	1612.806	1607.704	b_2	0	43	1.679	2.172	1.096	1.427	-5.102	0.055
93	90	1693.031	1644.822	b_2	36	31	6.578	5.302	3.895	3.326	-48.209	0.032
94	103	1741.194	3368.485	b_2	396	10	11.214	7.284	6.278	1.089	1.742	0.055
98	95	1796.583	1736.557	b_2	548	2	10.011	7.203	5.264	4.054	-60.026	0.043

[a]Only vibronic modes involving $\Delta Q>0.014$ are listed. Other details as in Table 3.2.

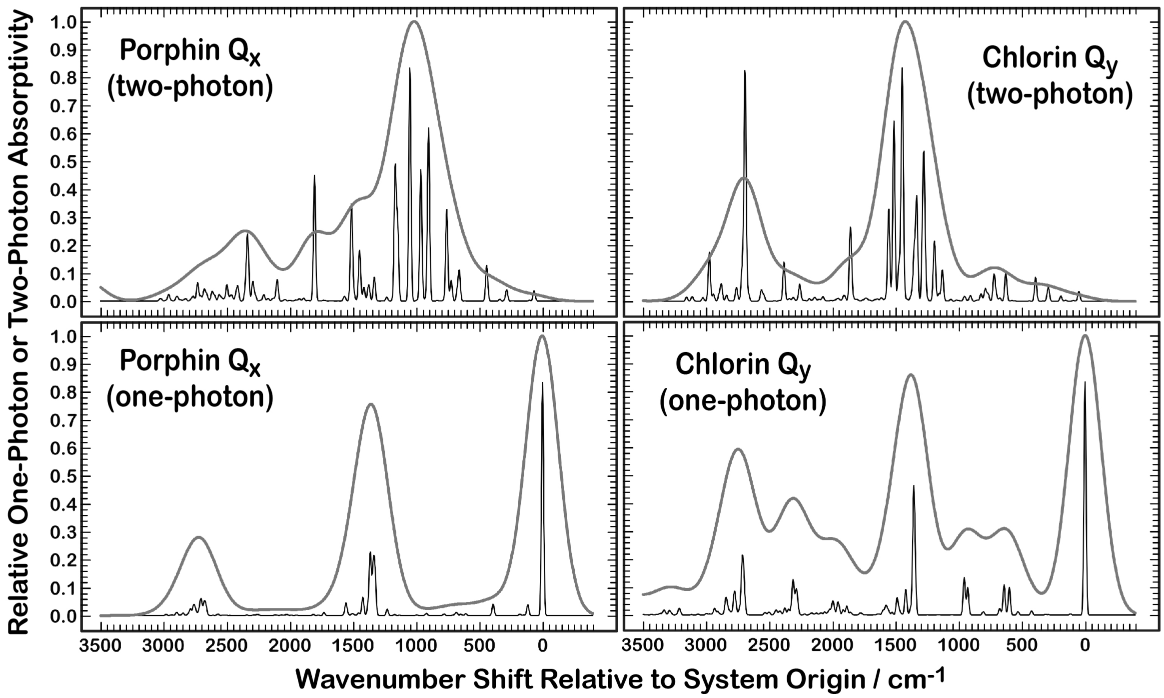

Figure 3.10. Simulations of the vibronic band development in the lowest lying Q-bands of the porphin Q_x band (left) and chlorin (2,3-dihydroporphin) Q_y band (right) under one-photon (lower) and two-photon (upper) selection rules.

because all of the electronic states studied here are two-photon forbidden. Two-photon bands appearing in the region of the system origin are due to low-frequency modes, or hot bands, which were not included in these simulations. Second, the most intense band in the two-photon spectra is the second vibronic band, which is made up of a significant number of vibronic bands that are unique to the two-photon vibrational manifold. In contrast, the one-photon spectra involve many fewer contributing promoting modes.

3.3.3. Two-Photon Absorptivities

Molecules absorb two photons via two possible mechanisms, as schematically shown in Figure 3.11 based on semi-classical single intermediate state two-photon theory.[16] Two-photon absorption events can be viewed as a two-step process, even though these two events typically happen within less than one fs. The first photon interacts with the molecule and prepares what is known as a virtual state (i). The virtual state is not a stationary state of the molecule, but is created momentarily during the forward scattering of the first photon.

In the Type I process, the stationary state is mediated by a nearby strongly allowed state, which exhibits large one-photon cross-sections between the final state (σ_{ba}) and the ground state (σ_{b0}). If we assume the allowed state is separated from the virtual state by 1.5 eV, then the lifetime of the virtual state, t_I, is ~0.22 fs. If we assume a strong one-photon cross section of $\sigma_{b0} = \sigma_{ba} = 10^{-16}$ cm^2, then the Type I process has a two-photon absorptivity of 26×10^{-50} cm^4 s (26 GM).

Calculation of the corresponding lifetime for a Type II process is more complicated, as this process depends on the photophysical properties of both the initial and final states. If the transition is strongly allowed and the dipole moment changes upon excitation, a Type II process can lead to very large two-photon absorptivities. Let us assume the transition occurs at ΔE_{b0} =

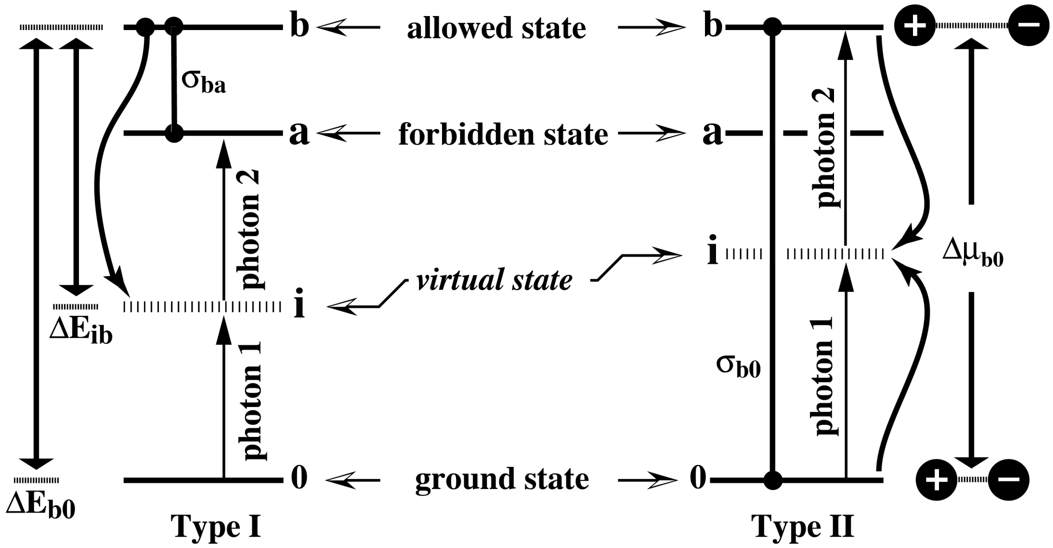

$$\delta \cong \frac{3}{25}\sigma_{b0}\,\sigma_{ba}\,t_I \qquad \delta \cong \frac{3}{25}\sigma_{b0}^2\,t_{II}$$

$$t_I \cong \frac{h}{4\pi\,\Delta E_{ib}} \qquad t_{II} \cong \frac{\pi\,\Delta\mu_{b0}^2}{c\,\varepsilon_0\,\sigma_{b0}\,\Delta E_{b0}}$$

Figure 3.11. The two principal mechanisms of two-photon absorption are compared based on semi-classical two-photon theory.[16,58] The Type I process (left) is important for excited states which are one-photon forbidden. A strongly allowed one-photon state can also be a two-photon allowed state via a Type II process (right) if it undergoes a change in dipole moment upon excitation ($\Delta\mu$). The equations shown are based on a single intermediate state approximation and assume further that both photons have parallel polarization and propagation, and equal energy. The σ_{ij} variables are one-photon cross sections and are in units of length squared. The t_I and t_{II} equations calculate the expectation value of the lifetime of the virtual state, i. These equations are for vacuum conditions, where ε_0 is the vacuum permittivity.

3 eV, has a strong one-photon cross-section of 10^{-16} cm^2 and exhibits a large change in dipole moment ($\Delta\mu$ = 10 D). The resulting virtual state lifetime is calculated to be 0.27 fs. Assuming σ_{b0} = 10^{-16} cm^2 (see above), the Type II process has a two-photon absorptivity of δ_{II} = 33 GM, slightly larger than the Type I process (δ_I = 26 GM). Thus, there are two key molecular properties that make a Type II process important: a large change in dipole moment upon excitation and a final state that is strongly one-photon allowed. We note that the change in dipole moment, $\Delta\mu_{b0}$, is not the difference of the magnitude of the ground (0) and excited (b) state dipole moments, but represents the vectorial change as given below:

$$|\Delta\mu_{b0}| = \left[\left(\mu_b^{(x)} - \mu_0^{(x)}\right)^2 + \left(\mu_b^{(y)} - \mu_0^{(y)}\right)^2 + \left(\mu_b^{(z)} - \mu_0^{(z)}\right)^2\right]^{\frac{1}{2}} \tag{3.11}$$

The low-lying Q-bands of the porphyrins or chlorins studied here are not corresponding to strongly one-photon allowed transitions and no large changes in dipole moment upon excitation occur. The largest change in dipole moment calculated for any of the Q-bands studied here is less than one Debye. We can thus conclude that Type I processes will dominate for the molecules studied here. This prediction is confirmed by the detailed calculations reported below.

The properties of the low lying excited singlet states under different solvent conditions based on SAC-CI molecular orbital theory are presented in Figures 3.12 and 3.13. The ground state equilibrium geometry was assumed for all calculations, and hence the results are appropriate for Franck-Condon vertical excitations. The calculated two-photon absorptivities that are presented in Table 3.4 are based on the B3LYP/6-31G(d) equilibrium geometries and, in the case of the hybrid *ab initio* calculations, PCM-based solvent effects.

Calculations based on the equilibrium geometries predict that the second excited Q-band is the more two-photon allowed. In contrast, the experimental results indicate that the two Q-

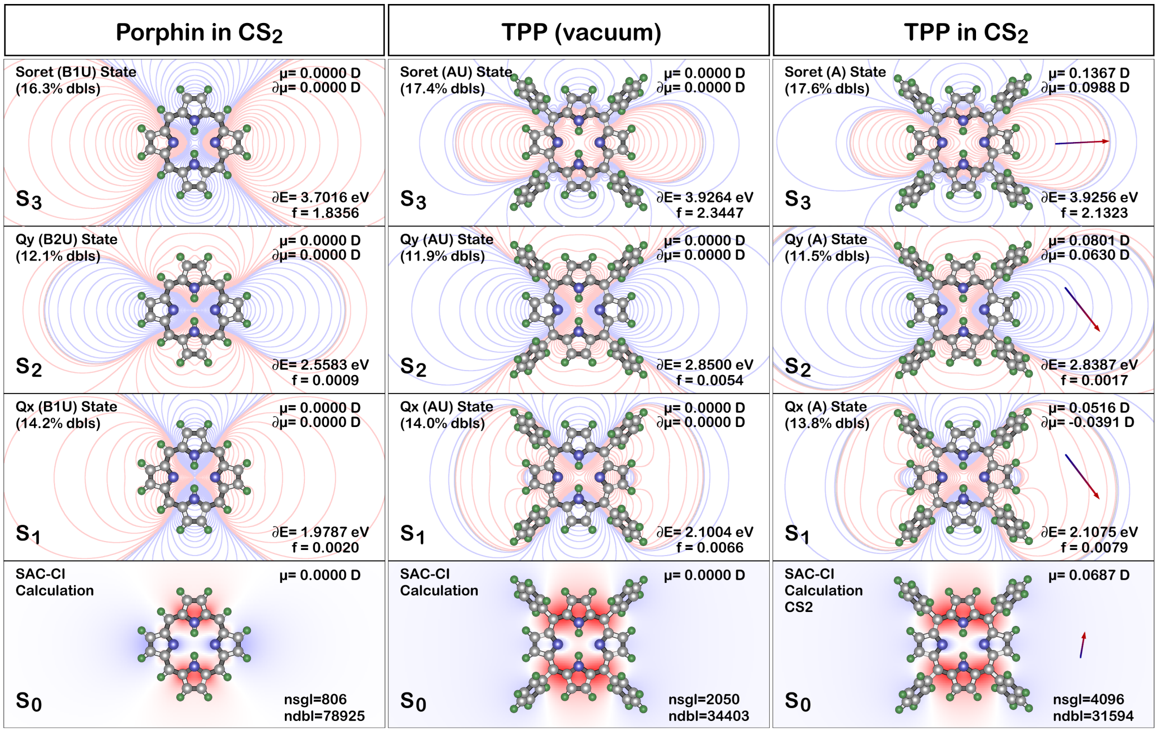

Figure 3.12. SAC-CI analyses of the ground and low-lying excited singlet states (in vacuum and CS_2) of the porphyrins indicated. All calculations were carried out using an active space of 64 filled and 64 virtual orbitals. Solvent effects were approximated by using PCM methods. The charge distribution in the ground state is visualized by using blue to indicate regions of excess negative charge and red to indicate regions of excess positive charge. The shift in charge upon excitation is shown using contour lines, with red lines indicating excess positive charge and blue lines indicating excess negative charge. The arrows show the direction of the dipole moments.

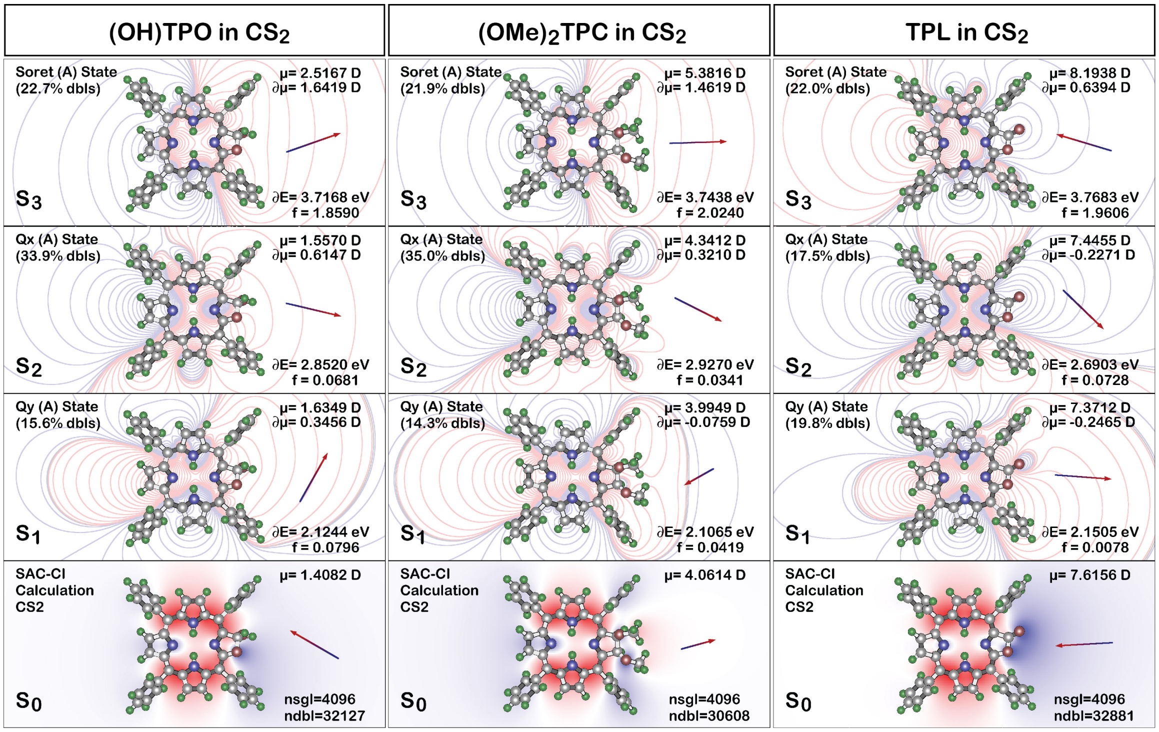

Figure 3.13. SAC-CI analyses of the ground and low-lying excited singlet states of the substituted chlorin-like porphyrinoids studied in this paper. Calculation details, contour plots, charge shifts upon excitation, and dipole moments are as described in Figure 3.12.

Table 3.4. One-Photon and Two-Photon Properties of the Lowest Two Excited Singlet States of Selected Porphyrins and Chlorins[a]

Property[b]	Porphin	TPP	(OH)TPO	$(OMe)_2$TPC	TPL
One-Photon (obsvd):					
ΔE (S_1 state, 0,0) /eV	1.998	1.894	1.899	1.909	1.919
ΔE (S_1 state, max) /eV	2.182	2.083	2.068	2.073	2.088
f (S_1 state)	0.0388	0.0378	0.0849	0.0447	0.0463
ΔE (S_2 state, 0,0) /eV	2.500	2.237	2.227	2.252	2.202
ΔE (S_2 state, max) /eV	2.500	2.385	2.380	2.376	2.361
f (S_2 state)	0.0177	0.0135	0.1171	0.0847	0.1224
Fluorescence Q Yield	0.05	0.09	0.39	0.26	0.07
Figures	3.5 & 3.9	3.5 & 3.9	3.5 & 3.8	3.5 & 3.8	3.5 & 3.8
One-Photon (calcd):					
ΔE (S_1 state) /eV	1.9787	2.1075	2.1244	2.1065	2.1505
f (S_1 state)	0.0020	0.0079	0.0796	0.0419	0.0078
ΔE (S_2 state) /eV	2.5583	2.8387	2.8520	2.9270	2.6903
f (S_2 state)	0.0009	0.0017	0.0681	0.0341	0.0728
Figures	3.12	3.12	3.13	3.13	3.13
Two-Photon (obsvd):					
ΔE (S_1 TPE max) /eV	2.192	2.080	2.078	2.078	2.098
g_{max} (S_1 state) /(s x 10^{-14})	4.543	3.867	3.161	3.892	3.949
δ (S_1 TPE max) /GM[b,c]	0.023	2.37	43.7	67.6	30.5
ΔE (S_2 TPE max) /eV	2.643	2.252	2.237	2.237	2.229
g_{max} (S_2 state) /(s x 10^{-14})	1.378	1.900	1.932	2.271	1.443
δ (S_2 TPE max) /GM[b,c]	0.022	1.15	37.6	54.9	6.8

Figures	3.9 & 3.14	3.9 & 3.14	3.9 & 3.15	3.9 & 3.15	3.9 & 3.15
Two-Photon (calcd):[d]					
½[$\delta(S_1)+\delta(S_2)$]/GM hybrid	0.0	0.14	83	54	23
½[$\delta(S_1)+\delta(S_2)$]/GM mndoci	0.0	0.86	25	22	18

[a]Ambient temperature in CS_2 unless noted otherwise.

[b]Two-photon absorptivities are in Göppert-Mayers (GM) where 1 GM = 10^{-50} cm^4 s.

[c]Observed absolute two-photon absorptivities are estimated to have an error of ±15% and use rhodamine as the internal standard (Table 3.1, Figure 3.7).

[d]Calculated by using the methods described in the text.

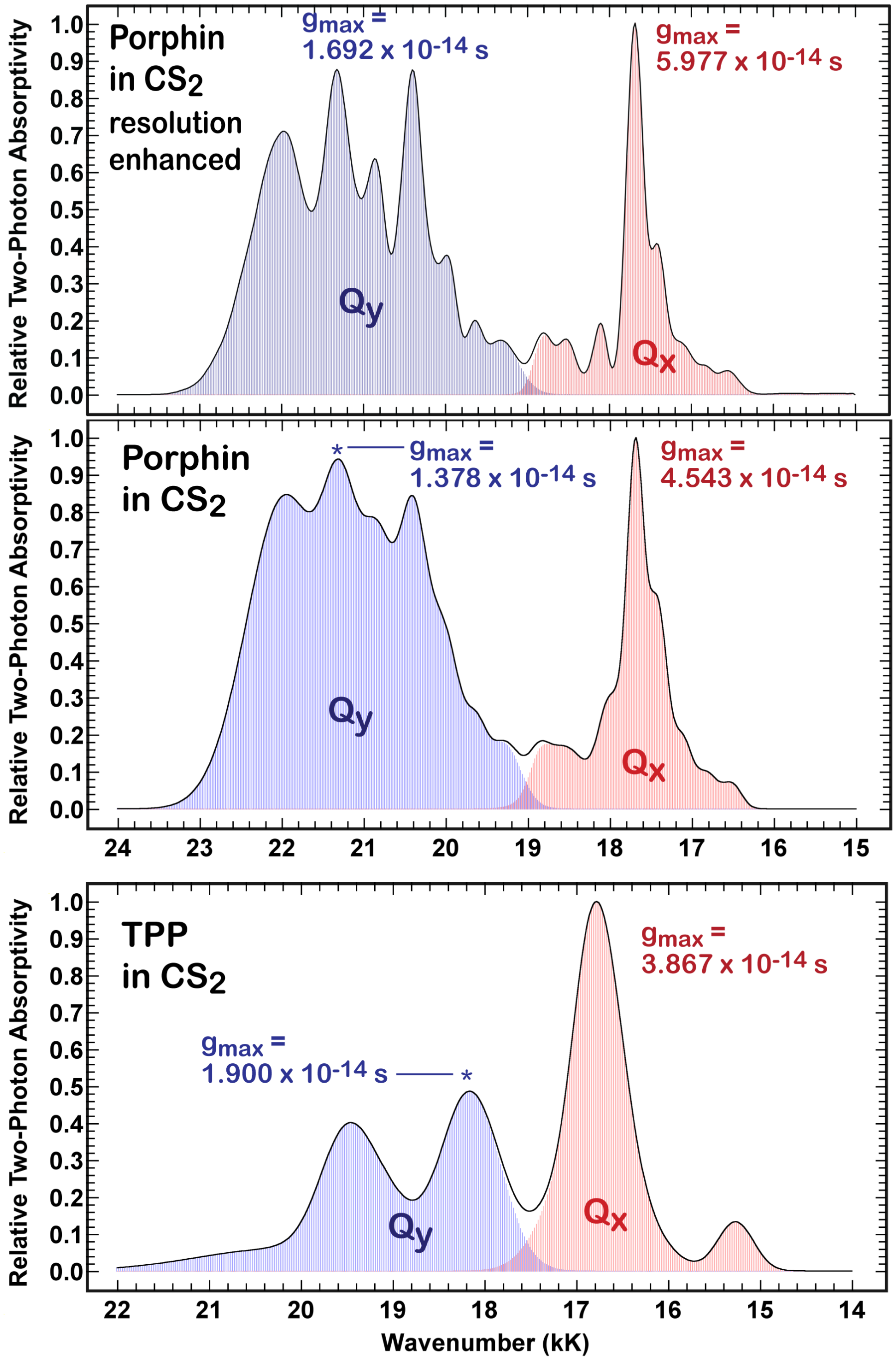

Figure 3.14. Analysis of the maximum in the line shape function, g_{max}, for porphin (top) and **TPP** (bottom). The observed two-photon spectra were fit using Gaussian bands and the component bands were assigned to the Q_x and Q_y bands via inspection. The normalized bands were integrated over frequency and the inverse of the integral yields g_{max}. The top spectrum used resolution enhancement to explore the impact of resolution on g_{max}. Note that as the vibronic features become sharper, the value of g_{max} increases accordingly.

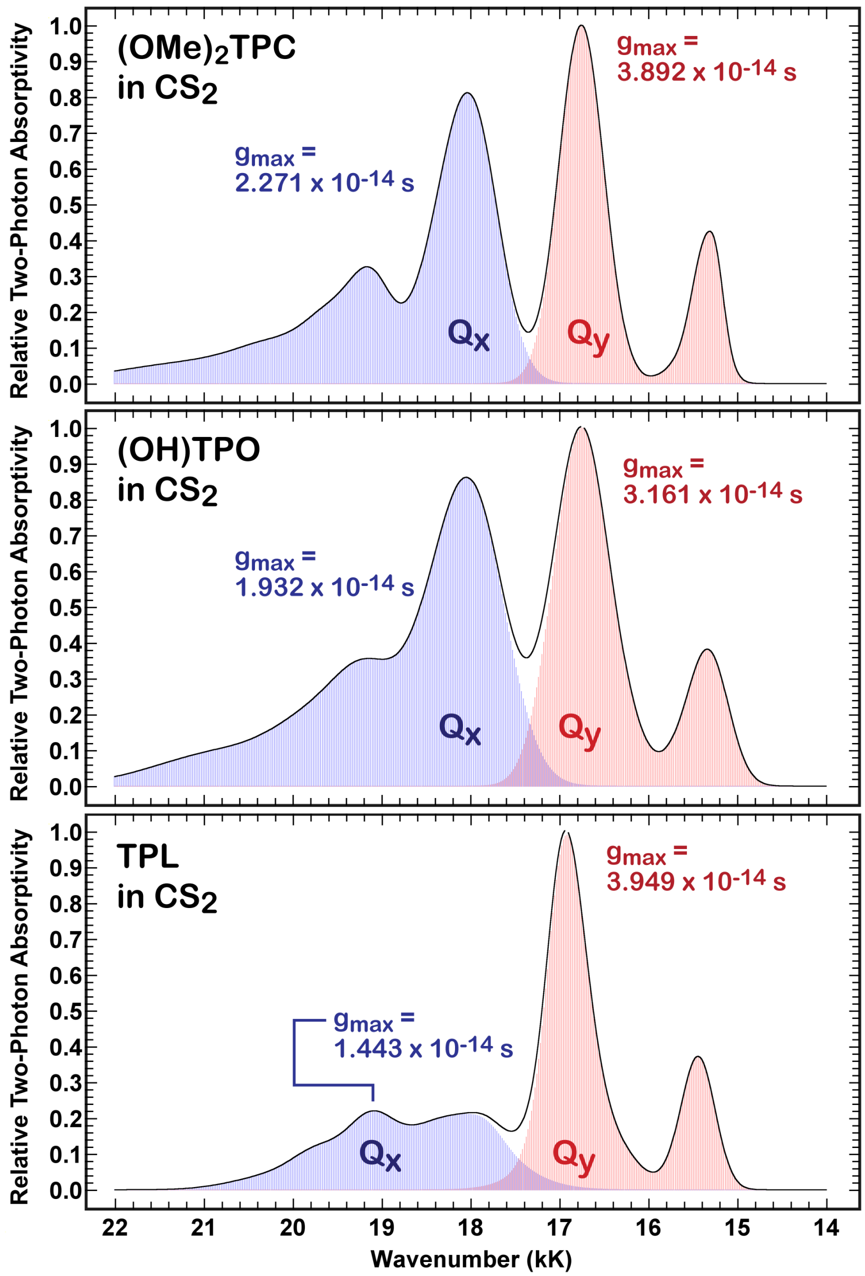

Figure 3.15. Analysis of the maximum in the line shape function, g_{max}, for **(OMe)$_2$TPC**, **(OH)TPO**, and **TPL**. Other details as in Figure 3.14.

bands have comparable two-photon absorptivity with the exception of **TPL**, which has a second excited Q_x absorptivity four times larger than that of the lower Q_y band. We observed that the calculated two-photon absorptivities are extremely sensitive to conformation, and that while the relative two-photon absorptivities vary dramatically with conformation, the average of the Q_x and Q_y two-photon absorptivities are not overly sensitive to conformation. Hence, we reported the calculated averages in Table 3.4, and explore the fundamental issue in more detail below.

The first molecular variable we explored was the extent to which the phenyl groups influence the two-photon absorptivities. Porphin is the only molecule we studied without phenyl groups, and it is predicted to have no two-photon absorptivity in the ground resting state. However, if we populate individual vibrations in the ground state, we do calculate observable absorptivities (shown in Table 3.2 for porphin and Table 3.3 for chlorin). Hot bands impact the two-photon absorptivity via two mechanisms. The most important effect is the changing of the symmetry of the initial vibronic state, which is crucial since in the absence of symmetry lowering, two-photon transitions into both Q_x and Q_y are symmetry forbidden. The second effect is to induce mixing of the singlet states by out-of-plane ring distortions. As the ring system forms a saddle-like conformation, the low-lying singlet states are mixed, and the Type I two-photon process is enhanced by increasing the magnitude of the transition lengths between the states. This process will be explored in more detail below as we examine why **$(OMe)_2$TPC** has an anomalously high two-photon absorptivity.

Introduction of the phenyl groups to porphyrin has a number of effects. Partial rotation of the phenyl groups allows cross-talk between the phenyl- and the porphyrin-π systems, inducing mixing via conjugative interactions. In addition, the smaller the dihedral angle between the two planar systems, the larger the sterically induced ring out-of-plane distortions. The phenyl groups

are observed to have a more important impact on the chlorins because the ring systems of the chlorins are more flexible,[82-84] allowing for a much reduced rotational barrier for phenyl group rotation at ambient temperature, thus allowing for a larger phenyl-chlorin interaction. The geometry of **TPP** in vacuum is C_i, but in solvent, the dispersive environment encourages the formation of a small dipole moment, which provides dipole-induced electrostatic stabilization.

The average experimental two-photon absorptivities of the two Q-bands increase in the following order: Porphin < **TPP** < **TPL** < **(OH)TPO** < **(OMe)$_2$TPC**. In contrast, the calculated ordering is: Porphin < **TPP** < **TPL** < **(OMe)$_2$TPC** < **(OH)TPO**. The semi-empirical and the *ab initio* (hybrid) theoretical methods agree with each other on the ordering, and **(OMe)$_2$TPC** is the outlier when the results are compared with experiment. This compound is observed to have roughly twice the two-photon absorptivity as predicted (Table 3.4). The origin of this difference should provide fundamental insight into the mechanism of two-photon absorption in these molecules.

In the course of studying **(OMe)$_2$TPC**, we observed significant differences in the results based on how we calculated the ground state geometry. Two different scenarios and their impact on the calculated two-photon properties are explored in Figure 3.16 and Table 3.5. When DFT methods (B3LYP/6-31G(d)) are used, **(OMe)$_2$TPC** is calculated to have a nearly planar ring structure (Figures 3.16A1 and 3.16A2) and the Q_x (S_2) state is calculated to have a majority of the two-photon absorptivity (Figure 3.16A, Table 3.5). In contrast, when semi-empirical methods are used (MNDO/PM3), the geometry optimization yields a saddled geometry as shown in Figures 3.16B1 and 9B2. Table 3.6 presents a normal-coordinate structure decomposition (NSD) of the **(OMe)$_2$TPC** structures depicted in Figure 3.16. The NSD procedure provides a numerical and qualitative description of the distortion of porphyrinoids in terms of displacement from a D_{4h}

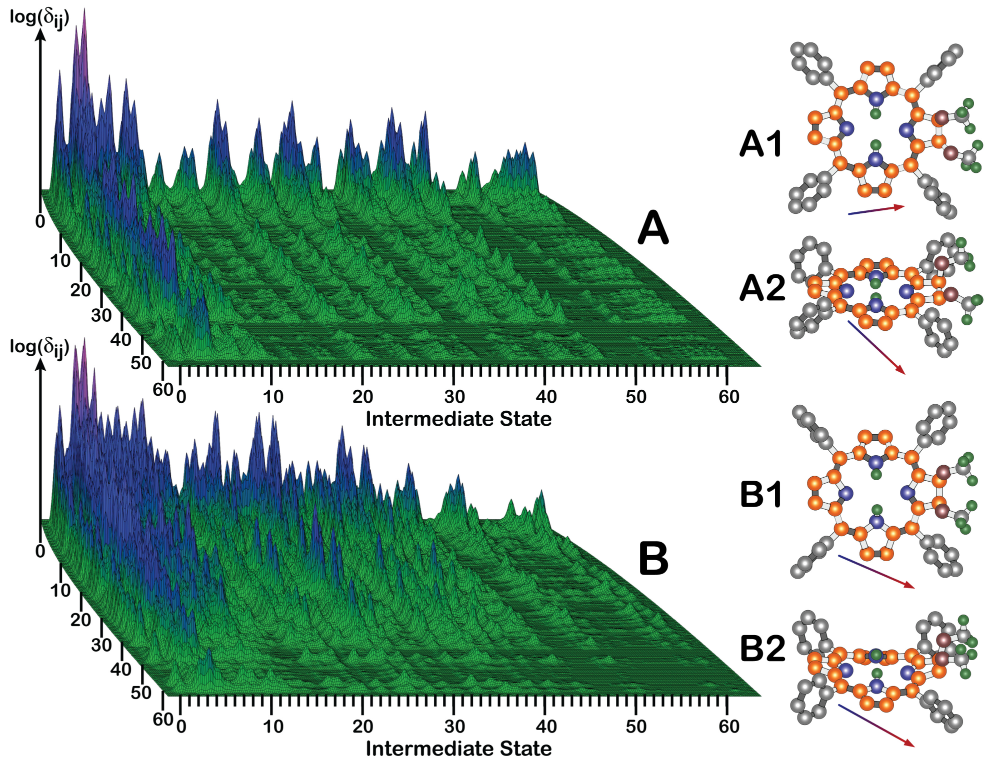

Figure 16. Analysis of intermediate state contributions to the calculated two-photon absorptivity of the Q_y band of **(OMe)$_2$TPC** based on MNDO-PSDCI theory and sixty intermediate states. The height of each element is proportional to the log of the contribution of the matrix element to the two-photon absorptivity. The matrix shown in A is for the equilibrium geometry (A1, A2) as determined by DFT (B3LYP/6-31G(d)) for the molecule in CS_2 (PCM methods). The matrix shown in B is for a saddled ring conformation (B1, B2) generated by using MNDO/PM3 semi-empirical methods.

Table 3.5. Calculated Two-Photon Absorptivities for Selected Systems[a,b]

molecule	geometry (method)	state	ΔE(eV)	<A>[b]	<B>[c]	<C>[d]	<D>[e]	<C>[d]/<A>[b]
porphin	S_0 equilibrium	Q_x (S_1)	2.5457	0.0	0.0	0.0	0.0	0.0
	S_0 equilibrium	Q_y (S_2)	2.6821	0.0	0.0	0.0	0.0	0.0
	60 cm^{-1} (b3u) mode	Q_x (S_1)	2.5316	0.1498	0.1124	0.2248	0.0375	1.5
	60 cm^{-1} (b3u) mode	Q_y (S_2)	2.6680	0.0348	0.0261	0.0521	0.0087	1.5
	76 cm^{-1} (au) mode	Q_x (S_1)	2.5200	0.1637	0.1228	0.2455	0.0419	1.5
	76 cm^{-1} (au) mode	Q_y (S_2)	2.6583	0.0349	0.0261	0.0523	0.0087	1.5
	100 cm^{-1} (b3u) mode	Q_x (S_1)	2.5355	0.0019	0.0015	0.0029	0.0005	1.5
	100 cm^{-1} (b3u) mode	Q_y (S_2)	2.6663	0.0034	0.0026	0.0052	0.0009	1.5
chlorin	S_0 equilibrium	Q_y (S_1)	2.4866	1.6164	1.2123	2.4246	0.4041	1.5
	S_0 equilibrium	Q_x (S_2)	3.1632	97.821	19.907	39.814	77.914	0.4070
	37 cm^{-1} (a2) mode	Q_y (S_1)	2.6518	3.4259	2.5694	5.1389	0.8565	1.5
	37 cm^{-1} (a2) mode	Q_x (S_2)	3.4797	155.55	27.15	54.29	123.40	0.3490
	56 cm^{-1} (b1) mode	Q_y (S_1)	2.6473	3.5149	2.6362	5.2723	0.8787	1.5
	56 cm^{-1} (b1) mode	Q_x (S_2)	3.4750	156.26	27.59	55.17	128.68	0.3531
	92 cm^{-1}	Q_y (S_1)	2.6397	3.3770	2.5328	5.0655	0.8443	1.5

	(a2) mode							
	92 cm^{-1} (a2) mode	Q_x (S_2)	3.4689	156.25	27.49	54.98	128.76	0.3519
rhodamine B	S_0 methanol (mndoci)	S_1	1.6255	168.07	56.59	113.18	111.48	0.6730
	S_0 methanol (hybrid)	S_1	1.8208	34.360	27.753	51.504	8.6067	1.4990
$(OMe)_2$TPC	S_0 (PM3) (mndoci)	Q_y(S_1)	2.3525	105.90	36.40	72.81	69.49	0.6875
	S_0 (PM3) (mndoci)	Q_x (S_2)	2.5083	69.972	22.83	45.56	92.80	0.6526
	S_0 CS_2 (hybrid)	Q_y(S_1)	2.4271	15.391	11.49	22.97	3.905	1.4925
	S_0 CS_2 (hybrid)	Q_x (S_2)	2.9810	106.97	26.13	52.26	80.84	0.4886

[a]All two-photon absorptivities in Göppert-Mayers (10^{-50} cm^4 s). Vibrational hot band geometries were generated by using GaussView 5 based on a B3LYP/6-31G(d) force field calculation and a displacement level of unity. These geometries overestimate the displacement, and thus the enhanced two-photon absorptivity is overestimated as well.

[b]Two-photon absorptivity calculated for both photons linearly polarized with parallel polarization.

[c]Two-photon absorptivity calculated for both photons linearly polarized with perpendicular polarization.

[d]Two-photon absorptivity calculated for both photons circularly polarized in the same sense with parallel propagation.

[e]Two-photon absorptivity calculated for both photons circularly polarized in the opposite sense with parallel propagation.

Table 3.6. Normal-Coordinate Structure Decomposition (NSD)[a] of the Out-of-Plane Distortions of **$(OMe)_2$TPC**[b]

molecule	B_{2u}	B_{1u}	A_{2u}	$E_g(x)$	$E_g(y)$	A_{1u}
$(OMe)_2$TPC (DFT)	-0.6194	-0.3918	0.0137	0.0193	0.0848	0.1209
$(OMe)_2$TPC (PM3)	-1.8062	-0.1599	-0.1199	0.1577	-0.511	-0.0023

[a]The NSD analysis is based on methods developed in references 85 and 86.

[b]The absolute value of each quantity is proportional to the out-of-plane distortion. The sign is only dependent on the orientation of the molecule and has no impact on the extent of distortion.

symmetric reference structure.[85,86] While the DFT structure of **(OMe)$_2$TPC** demonstrates modest saddling (B_{2u} mode) and ruffling (B_{1u} mode) distortions, the semi-empirical structure exhibits a significant saddling (B_{2u} mode) distortion that is necessary to replicate the observed two-photon absorptivity. This ring distortion mixes the states and inverts the absorptivities such that the first excited singlet state has the highest two-photon absorptivity (Figure 3.16B, Table 3.5). This was the only molecule for which PM3 geometries produced better agreement with experiment. The result does provide a perspective on the origin of the large two-photon absorptivity of **(OMe)$_2$TPC** compared to the other systems studied: an on-average saddled ground state conformation causes the Q_y and Q_x states to mix with higher excited states and thus lead to an enhanced two-photon absorptivity of both. This is visually expressed in Figure 3.16 (comparison of matrices A and B) by enhancement of the off-diagonal transition lengths creating additional contributions to the sum over states. In fact, the known solid state structures of porphin, **TPP**, **TPL**, **(OMe)$_2$TPC**, and (**OH)TPO** also indicate that all are approximately planar but that **(OMe)$_2$TPC** shows the largest distortions from ideality, in part due to the system trying to avoid an eclipsed conformation of the two methoxy groups on the pyrroline.

3.4. Conclusions

The simple planar porphyrins investigated here, including porphin and **TPP**, possess low-intensity Type I two-photon absorption processes in the Q-band region (0.02 and 2.37, respectively). The *meso*-phenyl groups do not contribute in a significant way to macrocycle distortion for **TPP**, which minimizes the enhancement of two-photon absorptivity. Porpholactone, **TPL**, also shows an anomalously small, porphyrin-like two-photon absorptivity maximum of 6.8 GM in the first excited (Q_y) singlet state. Both theory and experiment support a model of **TPL** with a nearly planar ground state geometry. The vibronic development in the two-

photon spectra of the chlorins **(OH)TPO** and **$(OMe)_2$TPC** is also significantly different from that observed in the one-photon spectra, with the $Q_y^{(1,0)}$ band exhibiting anomalous two-photon intensity. Frank-Condon analyses indicated that both vibrational symmetry, which makes the system origin band weak, and Duschinsky-mediated mode displacements combine to enhance the higher (1,0) mode. Moreover, it was found that Type II processes contribute to the two-photon cross section of **(OH)TPO** and **TPL**, but for no compound or geometry did we calculate a Type II contribution greater than 8% to the total absorptivity. Even though the single-photon absorption spectra of the chlorins **(OH)TPO** and **$(OMe)_2$TPC** are very similar, their two-photon absorptivities differ greatly. Chlorin **$(OMe)_2$TPC** exhibits an anomalously large two-photon absorptivity maxima of 67.6 GM (Q_y) and 54.9 GM (Q_x), whereas the corresponding values for **(OH)TPO** are 43.7 and 37.6. We attributed the high absorptivity of **$(OMe)_2$TPC** to state mixing associated with a saddle ring conformation. Calculations on the static structures of the chlorin invariably predict that one of the Q-bands has much higher two-photon absorptivity than the other, but the experimental observation indicates that both bands have similar two-photon absorptivities. Calculations of the two-photon spectra indicated that the relative Q-band absorptivities are sensitive to the phase and magnitude of the chlorin ring distortions. The observation of comparable two-photon absorptivities indicated that the non-planar conformations of **$(OMe)_2$TPC** are in dynamic fluctuation in response to rapid torsional rotation of the phenyl groups. The high two-photon absorptivity in the 1000 – 1400 nm region is particularly advantageous for the potential utility of **$(OMe)_2$TPC** in two-photon induced biomedical applications as the regime under ~1100 nm falls within the optical window of biological tissue[87] and allows the use of solid state Nd:YAG lasers (emission at 1064 nm). This work also points at saddled chlorin macrocycle conformations that should be incorporated into two-photon dyes

designed for high absorptivity. We believe that the results of this study will prompt subsequent investigations that lead to optimized photosensitizers for clinical evaluations as NIR PDT photosensitizers.

3.5. References

(1) Henderson, B. W.; Dougherty, T. J. How Does Photodynamic Therapy Work? *Photochem. Photobiol.* **1992**, *55*, 147-157.

(2) Drobizhev, M.; Sigel, C.; Rebane, A. Photo-Tautomer of Br-Porphyrin: A New Frequency-Selective Material for Ultrafast Time-Space Holographic Storage. *J. Lumin.* **2000**, *86*, 391-397.

(3) Rebane, A.; Kaarli, R.; Saari, P.; Anijalg, A.; Timpmann, K. Photochemical Time-Domain Holography of Weak Picosecond Pulses. *Opt. Commun.* **1983**, *47*, 173-176.

(4) Wood, G. L.; Miller, M. J.; Mott, A. G. Investigation of Tetrabenzoporphyrin by the Z-Scan Technique. *Opt. Lett.* **1995**, *20*, 973-975.

(5) Mathai, S.; Bird, D. K.; Stylli, S. S.; Smith, T. A.; Ghiggino, K. P. Two-Photon Absorption Cross-Sections and Time-Resolved Fluorescence Imaging Using Porphyrin Photosensitisers. *Photochem. Photobiol. Sci.* **2007**, *6*, 1019-1026.

(6) Finikova, O. S.; Lebedev, A. Y.; Aprelev, A.; Troxler, T.; Gao, F.; Garnacho, C.; Muro, S.; Hochstrasser, R. M.; Vinogradov, S. A. Oxygen Microscopy by Two-Photon-Excited Phosphorescence. *ChemPhysChem* **2008**, *9*, 1673-1679.

(7) Lecoq, J.; Parpaleix, A.; Roussakis, E.; Ducros, M.; Houssen, Y. G.; Vinogradov, S. A.; Charpak, S. Simultaneous Two-Photon Imaging of Oxygen and Blood Flow in Deep Cerebral Vessels. *Nat. Med.* **2011**, *17*, 893-898.

(8) Sakadžić, S.; Roussakis, E.; Yaseen, M. A.; Mandeville, E. T.; Srinivasan, V. J.; Arai, K.; Ruvinskaya, S.; Devor, A.; Lo, E. H.; Vinogradov, S. A.; Boas, D. A. Two-Photon High-Resolution Measurement of Partial Pressure of Oxygen in Cerebral Vasculature and Tissue. *Nat. Methods* **2010**, *7*, 755-759.

(9) Spencer, J. A.; Ferraro, F.; Roussakis, E.; Klein, A.; Wu, J.; Runnels, J. M.; Zaher, W.; Mortensen, L. J.; Alt, C.; Turcotte, R.; Yusuf, R.; Côté, D.; Vinogradov, S. A.; Scadden, D. T.; Lin, C. P. Direct Measurement of Local Oxygen Concentration in the Bone Marrow of Live Animals. *Nature* **2014**, *508*, 269-273.

(10) Collins, H.; Khurana, M.; Moriyama, E. H.; Mariapillai, A.; Dahlstedt, E.; Balaz, M.; Kuimova, M. K.; Drobizhev, M.; Yant, V. X. D.; Phillips, D.; Rebane, A.; Wilson, B. C.; Anderson, H. L. Blood-Vessel Closure Using Photosensitizers Engineered for Two-Photon Excitation. *Nat. Photonics* **2008**, *2*, 420-424.

(11) Wilson, B. C.; Patterson, M. S. The Physics of Photodynamic Therapy. *Phys. Med. Biol.* **1986**, *31*, 327-360.

(12) Sternberg, E. D.; Dolphin, D.; Brückner, C. Porphyrin-Based Photosensitizers for Use in Photodynamic Therapy. *Tetrahedron* **1998**, *54*, 4151-4202.

(13) Muller, P. J.; Wilson, B. C. Photodynamic Therapy for Recurrent Supratentorial Gliomas. *Semin. Surg. Oncol.* **1995**, *11*, 345-354.

(14) Vrouenraets, M. B.; Visser, G. W. M.; Snow, G. B.; van Dongen, G. A. M. S. Basic Principles, Applications in Oncology and Improved Selectivity of Photodynamic Therapy. *Anticancer Res.* **2003**, *23*, 505-522.

(15) Birge, R. R. One-Photon and Two-Photon Excitation Spectroscopy. In *Ultrasensitive Laser Spectroscopy*; Kliger, D. S., Ed.; Academic Press, Inc.: New York, 1983; pp 109-174.

(16) Birge, R. R.; Pierce, B. M. Semi-Classical Time Dependent Theory of Two-Photon Spectroscopy. The Effect of Dephasing in the Virtual Level on the Two-Photon Excitation Spectrum of Isotachysterol. *Int. J. Quantum Chem.* **1986**, *29*, 639-656.

(17) Wan, S.; Parrish, J. A.; Anderson, R. R.; Madden, M. Transmittance of Nonionizing Radiation in Human Tissues. *Photochem. Photobiol.* **1981**, *24*, 679-681.

(18) Mroz, P.; Huang, Y.-Y.; Janjua, S.; Zhiyentayev, T.; Ruzie, C.; Borbas, K. E.; Fan, D.; Krayer, M.; Balasubramanian, T.; Yang, E. K.; Kee, H. L; Holten, D.; Lindsey, J. S.; Hamblin, M. R. New Stable Synthetic Bacteriochlorins for Photodynamic Therapy of Melanoma. *Proc. SPIE* **2009**, *7380*, 73802S-1-73802S-14.

(19) Mroz, P.; Huang, Y.-Y.; Szokalska, A.; Zhiyentayev, T.; Janjua, S.; Nifli, A.-P.; Sherwood, M. E.; Ruzie, C.; Borbas, K. E.; Fan, D.; Krayer, M.; Balasubramanian, T.; Yang, E.; Kee, H. L.; Kirmaier, C.; Diers, J. R.; Bocian, D. F.; Holten, D.; Lindsey, J. S.; Hamblin, M. R. Stable Synthetic Bacteriochlorins Overcome the Resistance of Melanoma to Photodynamic Therapy. *FASEB J.* **2010**, *24*, 3160-3170.

(20) Krayer, M.; Yang, E.; Kim, H.-J.; Kee, H. L.; Deans, R. M.; Sluder, C. E.; Diers, J. R.; Kirmaier, C.; Bocian, D. F.; Holten, D.; Lindsey, J. S. Synthesis and Photophysical Characterization of Stable Indium Bacteriochlorins. *Inorg. Chem.* **2011**, *50*, 4607-4618.

(21) Krayer, M.; Yang, E.-K.; Diers, J. R.; Bocian, D. F.; Holten, D.; Lindsey, J. S. *De Novo* Synthesis and Photophysical Characterization of Annulated Bacteriochlorins: Mimicking and Extending the Properties of Bacteriochlorophylls. *New J. Chem.* **2011**, *35*, 587-601.

(22) Yang, E.; Diers, J. R.; Huang, Y.-Y.; Hamblin, M. R.; Lindsey, J. S.; Bocian, D. F.; Holten, D. Molecular Electronic Tuning of Photosensitizers to Enhance Photodynamic Therapy: Synthetic Dicyanobacteriochlorins as a Case Study. *Photochem. Photobiol.* **2012**, *89*, 605-618.

(23) Taniguchi, M.; Cramer, D. L.; Bhise, A. D.; Kee, H. L.; Bocian, D. F.; Holten, D.; Lindsey, J. S. Accessing the Near-Infrared Spectral Region with Stable, Synthetic, Wavelength-Tunable Bacteriochlorins. *New J. Chem.* **2008**, *32*, 947-958.

(24) Mroz, P.; Bhaumik, J.; Dogutan, D. K.; Aly, Z.; Kamal, Z.; Khalid, L.; Kee, H. L.; Bocian, D. F.; Holten, D.; Lindsey, J. S.; Hamblin, M. R. Imidazole Metalloporphyrins as Photosensitizers for Photodynamic Therapy: Role of Molecular Charge, Central Metal and Hydroxyl Radical Production. *Cancer Lett.* **2009**, *282*, 63-76.

(25) Parusel, A. B. J.; Wondimagegn, T.; Ghosh, A. Do Nonplanar Porphyrins Have Red-Shifted Electronic Spectra? A DFT/SCI Study and Reinvestigation of a Recent Proposal. *J. Am. Chem. Soc.* **2000**, *122*, 6371-6374.

(26) Ryeng, H.; Ghosh, A. Do Nonplanar Distortions of Porphyrins Bring about Strongly Red-Shifted Electronic Spectra? Controversy, Consensus, New Developments, and Relevance to Chelatates. *J. Am. Chem. Soc.* **2002**, *124*, 8099-8103.

(27) Senge, M. O. Database of Tetrapyrrole Crystal Structure Determinations. In *The Porphyrin Handbook*; Kadish, K. M., Smith, K. M., Guilard, R., Eds.; Academic Press: San Diego, 2000; Vol. *10*, pp 1-218.

(28) Senge, M. O. Highly Substituted Porphyrins. In *The Porphyrin Handbook*; Kadish, K. M., Smith, K. M., Guilard, R., Eds.; Academic Press: Boston, 2000, Vol. *1*, pp 239-347.

(29) Gouterman, M. Spectra of Porphyrins. *J. Mol. Spectrosc.* **1961**, *6*, 138-163.

(30) Platt, J. R. Classification and Assignments of Ultraviolet Spectra of Conjugated Organic Molecules. *J. Opt. Soc. Am.* **1953**, *43*, 252-257.

(31) Brückner, C.; McCarthy, J. R.; Daniell, H. W.; Pendon, Z. D.; Ilagan, R. P.; Francis, T. M.; Ren, L.; Birge, R. R.; Frank, H. A. A Spectroscopic and Computational Study of the Singlet and Triplet Excited States of Synthetic *β*-Functionalized Chlorins. *Chem. Phys.* **2003**, *294*, 285-303.

(32) Hasegawa, J.; Ozeki, Y.; Ohkawa, K.; Hada, M.; Nakatsuji, H. Theoretical Study of the Excited States of Chlorin, Bacteriochlorin, Pheophytin *a*, and Chlorophyll *a* by the SAC/SAC−CI Method. *J. Phys. Chem. B* **1998**, *102*, 1320-1326.

(33) Flitsch, W. Hydrogenated Porphyrin Derivaties: Hydroporphyrins. *Adv. Heterocyl. Chem.* **1988**, *43*, 73-126.

(34) Whitlock, H. W.; Hanauer, R.; Oester, M. Y.; Bower, B. K. Diimide Reduction of Porphyrins. *J. Am. Chem. Soc.* **1969**, *91*, 7485-7489.

(35) Bonnett, R.; White, R. D.; Winfield, U. J.; Berenbaum, M. C. Hydroporphyrins of the *meso*-Tetra(hydroxyphenyl) porphyrin Series as Tumour Photosensitizers. *Biochem. J.* **1989**, *261*, 277-280.

(36) Gouterman, M. Study of the Effects of Substitution on the Absorption Spectra of Porphin. *J. Chem. Phys.* **1959**, *30*, 1139-1161.

(37) Goyan, R. L.; Cramb, D. T. Near-Infrared Two-Photon Excitation of Protoporphyin IX: Photodynamics and Photoproduct Generation. *Photochem. Photobiol.* **2000**, *72*, 821-827.

(38) Karotki, A.; Khurana, M.; Lepock, J. R.; Wilson, B. C. Simultaneous Two-Photon Excitation of Photofrin in Relation to Photodynamic Therapy. *Photochem. Photobiol.* **2006**, *82*, 443-452.

(39) Kim, D.Y.; Ahn, T. K.; Kwon, J. H.; Kim, D.; Ikeue, T.; Aratani, N.; Osuka, A.; Shigeiwa, M.; Maeda, S. Large Two-Photon Absorption (TPA) Cross-Section of Directly Linked Fused Diporphyrins. *J. Phys. Chem. A* **2005**, *109*, 2996-2999.

(40) Drobizhev, M.; Stepanenko, Y.; Dzenis, Y.; Karotki, A.; Rebane, A.; Taylor, P. N.; Anderson, H. L. Extremely Strong Near-IR Two-Photon Absorption in Conjugated Porphyrin Dimers: Quantitative Description with Three-Essential-States Model. *J. Phys. Chem. B* **2005**, *109*, 7223-7236.

(41) Nowak-Król, A.; Wilson, C. J.; Drobizhev, M.; Kondratuk, D. V.; Rebane, A.; Anderson, H. L.; Gryko, D. T. Amplified Two-Photon Absorption in *Trans*-A_2B_2-Porphyrins Bearing Nitrophenylethynyl Substituents. *ChemPhysChem* **2012**, *13*, 3966-3972.

(42) Koszelewski, D.; Nowak-Król, A.; Drobizhev, M.; Wilson, C. J.; Haley, J. E.; Cooper, T. M.; Romiszewski, J.; Górecka, E.; Anderson, H. L.; Rebane, A.; Gryko, D. T. Synthesis and Linear and Nonlinear Optical Properties of Low-Melting π-Extended Porphyrins. *J. Mater. Chem. C* **2013**, *1*, 2044-2053.

(43) Karotki, A.; Kruk, M.; Drobizhev, M.; Rebane, A.; Nickel, E.; Spangler, C. W. Efficient Singlet Oxygen Generation Upon Two-Photon Excitation of New Porphyrin With Enhanced Nonlinear Absorption. *IEEE J. Sel. Top. Quantum Electron.* **2001**, *7*, 971-975.

(44) Drobizhev, M.; Meng, F.; Rebane, A.; Stepanenko, Y.; Nickel, E.; Spangler, C. W. Strong Two-Photon Absorption in New Asymmetrically Substituted Porphyrins: Interference between Charge-Transfer and Intermediate-Resonance Pathways. *J. Phys. Chem. B* **2006**, *110*, 9802-9814.

(45) Drobizhev, M.; Karotki, A.; Kruk, M.; Mamardashvili, N. Z.; Rebane, A. Drastic Enhancement of Two-Photon Absorption in Porphyrins Associated with Symmetrical Electron-Accepting Substitution. *Chem. Phys. Lett.* **2002**, *361*, 504-512.

(46) Esipova, T. V.; Vinogradov, S. A. Synthesis of Phosphorescent Asymmetrically π-Extended Porphyrins for Two-Photon Applications. *J. Org. Chem* **2014**, *79*, 8812-8825.

(47) Karotki, A.; Drobizhev, M.; Kruk, M.; Spangler, C.; Nickel, E.; Mamardashvili, N.; Rebane, A. Enhancement of Two-Photon Absorption in Tetrapyrrolic Compounds. *J. Opt. Soc. Am. B* **2003**, *20*, 321-332.

(48) Biswas, S.; Ahn, H.-Y.; Bondar, M. V.; Belfield, K. D. Two-Photon Absorption Enhancement of Polymer-Templated Porphyrin-Based J-Aggregates. *Langmuir* **2012**, *28*, 1515-1522.

(49) Ogawa, K.; Hasegawa, H.; Inaba, Y.; Kobuke, Y.; Inouye, H.; Kanemitsu, Y.; Kohno, E.; Hirano, T.; Ogura, S.-I.; Okura, I. Water-Soluble Bis(imidazolylporphyrin) Self-Assemblies with Large Two-Photon Absorption Cross Sections as Potential Agents for Photodynamic Therapy. *J. Med. Chem.* **2006**, *49*, 2276-2283.

(50) Ogawa, K.; Ohashi, A. K.; Kobuke, Y.; Kamada, K.; Ohta, K. Two-Photon Absorption Properties of Self-Assemblies of Butadiyne-Linked Bis(Imidazolylporphyrin). *J. Phys. Chem. B* **2005**, *109*, 22003-22012.

(51) Tanihara, J.; Ogawa, K.; Kobuke, Y. Two-photon Absorption Properties of Conjugated Supramolecular Porphyrins with Electron Donor and Acceptor. *J. Photochem. Photobiol., A* **2006**, *178*, 140-149.

(52) Mongin, O.; Sankar, M.; Charlot, M.; Mir, Y.; Blanchard-Desce, M. Strong Enhancement of Two-Photon Absorption Properties in Synergic 'Semi-Disconnected' Multiporphyrin Assemblies Designed for Combined Imaging and Photodynamic Therapy. *Tetrahedron Lett.* **2013**, *54*, 6474-6478.

(53) Drobizhev, M.; Karotki, A.; Kruk, M.; Rebane, A. Resonance Enhancement of Two-Photon Absorption in Porphyrins. *Chem. Phys. Lett.* **2002**, *355*, 175-182.

(54) Humphrey, J. L.; Kuciauskas, D. Charge Transfer Enhances Two-Photon Absorption in Transition Metal Porphyrins. *J. Am. Chem. Soc.* **2006**, *128*, 3902-3903.

(55) Samankumara, L. P.; Zeller, M.; Krause, J. A.; Brückner, C. Syntheses, Structures, Modification, and Optical Properties of *meso*-Tetraaryl-2,3-dimethoxychlorin, and Two Isomeric *meso*-Tetraaryl-2,3,12,13-tetrahydroxybacteriochlorins. *Org. Biomol. Chem.* **2010**, *8*, 1951-1965.

(56) Brückner, C.; Ogikubo, J.; McCarthy, J. R.; Akhigbe, J.; Hyland, M. A.; Daddario, P.; Worlinsky, J. L.; Zeller, M.; Engle, J. T.; Ziegler, C. J.; Ranaghan, M. J.; Sandberg, M. N.; Birge, R. R. *meso*-Arylporpholactones and their Reduction Products. *J. Org. Chem.* **2012**, *77*, 6480-6494.

(57) Adler, A. D.; Longo, F. R.; Finarelli, J. D.; Goldmacher, J.; Assour, J.; Korsakoff, L. A Simplified Synthesis for meso-Tetraphenylporphine. *J. Org. Chem.* **1967**, *32*, 476-476.

(58) Shima, S.; Ilagan, R. P.; Gillespie, N.; Sommer, B. J.; Hiller, R. G.; Sharples, F. P.; Frank, H. A.; Birge, R. R. Two-Photon and Fluorescence Spectroscopy and the Effect of

Environment on the Photochemical Properties of Peridinin in Solution and in the Peridinin-Chlorophyll-Protein from *Amphidinium carterae*. *J. Phys. Chem. A* **2003**, *107*, 8052 - 8066.

(59) Kubin, R. F.; Fletcher, A. N. Fluorescence Quantum Yields of Some Rhodamine Dyes. *J. Lumin.* **1983**, *27*, 455-462.

(60) Birge, R. R.; Zhang, C.-F. Two-Photon Double Resonance Spectroscopy of Bacteriorhodopsin. Assignment of the Electronic and Dipolar Properties of the Low-Lying $^1A_g{}^{*-}$ –like and $^1B_u{}^{*+}$-like π, π* states. *J. Chem. Phys.* **1990**, *92*, 7178-7195.

(61) Monson, P. R.; McClain, W. M. Polarization Dependence of the Two-Photon Absorption of Tumbling Molecules with Application to Liquid 1-Chloronaphthalene and Benzene. *J. Chem. Phys.* **1970**, *53*, 29-37.

(62) Masthay, M. B.; Findsen, L. A.; Pierce, B. M.; Bocian, D. F.; Lindsey, J. S.; Birge, R. R. A Theoretical Investigation of the One- and Two-Photon Properties of Porphyrins. *J. Chem. Phys.* **1986**, *84*, 3901-3915.

(63) Mortensen, O. S.; Svendsen, E. N. Initial and Final Molecular States as "Virtual States" in Two-Photon Processes. *J. Chem. Phys.* **1981**, *74*, 3185-3189.

(64) Dick, B.; Hohlneicher, G. Importance of Initial and Final States as Intermediate States in Two-Photon Spectroscopy of Polar Molecules. *J. Chem. Phys.* **1982**, *76*, 5755-5760.

(65) Ren, L.; Martin, C. H.; Wise, K. J.; Gillespie, N. B.; Luecke, H.; Lanyi, J. K.; Spudich, J. L.; Birge, R. R. Molecular Mechanism of Spectral Tuning in Sensory Rhodopsin II. *Biochemistry* **2001**, *40*, 13906-13914.

(66) Martin, C. H.; Birge, R. R. Reparameterizing MNDO for Excited State Calculations Using ab Initio Effective Hamiltonian Theory: Application to the 2,4-Pentadien-1-iminium Cation. *J. Phys. Chem. A* **1998**, *102*, 852-860.

(67) Miyahara, T.; Nakatsuji, H.; Hasegawa, J.; Osuka, A.; Aratani, N.; Tsuda, A. Ground and Excited States of Linked and Fused Zinc Porphyrin Dimers: Symmetry Adapted Cluster (SAC)-Configuration Interaction (CI) Study. *J. Chem. Phys.* **2002**, *117*, 11196-11207.

(68) Miyahara, T.; Tokita, Y.; Nakatsuji, H. SAC/SAC-CI Study of the Ground, Excited, and Ionized States of Cytochromes P450CO. *J. Phys. Chem. B* **2001**, *105*, 7341-7352.

(69) Nakajima, T.; Nakatsuji, H. Energy Gradient Method for the Ground, Excited, Ionized, and Electron-Attached States Calculated by the SAC (Symmetry-Adapted Cluster)/SAC-CI (Configuration Interaction) Method. *Chem. Phys.* **1999**, *242*, 177-193.

(70) Nakatsuji, H. Description of Two- and Many-Electron Processes by the SAC-CI Method. *Chem. Phys. Lett.* **1991**, *177*, 331-337.

(71) Foresman, J. B.; Head-Gordon, M.; Pople, J. A.; Frisch, M. J. Toward a Systematic Molecular Orbital Theory for Excited States. *J. Phys. Chem.* **1992**, *96*, 135-149.

(72) Nishimoto, K.; Mataga, N. Electronic Structure and Spectra of Some Nitrogen Heterocycles. *Z. Phys. Chem. (Muenchen, Ger.)* **1957**, *12*, 335-338.

(73) Dewar, M. J. S.; Zoebisch, E. G.; Healy, E. F.; Stewart, J. J. P. Development and Use of Quantum Mechanical Molecular Models. 76. AM1: A New General Purpose Quantum Mechanical Molecular Model. *J. Am. Chem. Soc.* **1985**, *107*, 3902-3909.

(74) Frisch, M. J.; Trucks, G. W.; Schlegel, H. B.; Scuseria, G. E.; Robb, M. A.; Cheeseman, J. R.; Scalmani, G.; Barone, V.; Mennucci, B.; Petersson, G. A.; Nakatsuji, H.; Caricato, M.; Li, X.; Hratchian, H. P.; Izmaylov, A. F.; Bloino, J.; Zheng, G.; Sonnenberg, J. L.; Hada, M.; Ehara, M.; Kitao, O.; Nakai, H.; Vreven, T.; Montgomery, J., J. A.; Peralta, J. E.; Ogliaro, F.; Bearpark, M.; Heyd, J. J.; Brothers, E.; Kudin, K. N.; Staroverov, V. N.; Kobayashi, R.; Normand, J.; Raghavachari, K.; Rendell, A.; Burant, J. C.; Iyengar, S. S.; Tomasi, J.; Cossi,

M.; Rega, N.; Millam, J. M.; Klene, M.; Knox, J. E.; Cross, J. B.; Bakken, V.; Adamo, C.; Jaramillo, J.; Gomperts, R.; Stratmann, R. E.; Yazyev, O.; Austin, A. J.; Cammi, R.; Pomelli, C.; Ochterski, J. W.; Martin, R. L.; Morokuma, K.; Zakrzewski, V. G.; Voth, G. A.; Salvador, P.; Dannenberg, J. J.; Dapprich, S.; Daniels, A. D.; Farkas, O.; Foresman, J. B.; Ortiz, J. V.; Cioslowski, J.; Fox, D. J.. *Gaussian 09*, revision D.01; Gaussian, Inc., Wallingford, CT, 2009.

(75) Barone, V.; Cossi, M.; Tomasi, J. Geometry Optimization of Molecular Structures in Solution by the Polarizable Continuum Model. *J. Comput. Chem.* **1998**, *19*, 404-417.

(76) Cossi, M.; Rega, N.; Scalmani, G.; Barone, V. Energies, Structures, and Electronic Properties of Molecules in Solution with the C-PCM Solvation Model. *J. Comput. Chem.* **2003**, *24,* 669-681.

(77) Tomasi, J.; Mennucci, B.; Cammi, R. Quantum Mechanical Continuum Solvation Models. *Chem. Rev.* **2005**, *105*, 2999-3093.

(78) York, D. M.; Karplus, M. Smooth Solvation Potential Based on the Conductor-Like Screening Model. *J. Phys. Chem. A* **1999**, *103*, 11060-11079.

(79) Macak, P.; Luo, Y.; Ågren, H. Simulations of Vibronic Profiles in Two-Photon Absorption. *Chem. Phys. Lett.* **2000**, *330*, 447-456.

(80) Niedzwiedzki, D. M.; Sandberg, D. J.; Cong, H.; Sandberg, M. N.; Gibson, G. N.; Birge, R. R.; Frank, H. A. Ultrafast Time-Resolved Absorption Spectroscopy of Geometric Isomers of Carotenoids. *Chem. Phys.* **2009**, *357*, 4-16.

(81) Chang, J. L. A New Formula to Calculate Franck–Condon Factors for Displaced and Distorted Harmonic Oscillators. *J. Mol. Spectrosc.* **2005**, *232*, 102-104.

(82) Barkigia, K. M.; Thompson, M. A.; Fajer, J.; Pandey, R. K.; Smith, K. M.; Vicente, M. G. H. Conformational Flexibility of Chlorin Macrocycles. Structural Determinations and Theoretical Calculations of a Benzochlorin, a *meso*-Dimethyl Chlorin and a Nickel Chlorin. *New J. Chem.* **1992**, *16*, 599-607.

(83) Senge, M. O.; Hope, H.; Smith, K. M. Structure and Conformation of Photosynthetic Pigments and Related Compounds. Part 6. The First Crystal Structure of a Covalently-Linked Chlorin Dimer: 20,20'-Ethylenebis(*trans*-2,3,7,8,12,13,17,18-octaethylchlorin). *J. Chem. Soc., Perkin Trans. 2* **1993**, 11-16.

(84) Senge, M. O.; Wiehe, A.; Ryppa, C. Synthesis, Reactivity and Structure of Chlorophylls. *Adv. Photosynth. Respir.* **2006**, *25*, 27-37.

(85) Jentzen, W.; Song, X.-Z.; Shelnutt, J. A. Structural Characterization of Synthetic and Protein-Bound Porphyrins in Terms of the Lowest-Frequency Normal Coordinates of the Macrocycle. *J. Phys. Chem. B* **1997**, *101*, 1684-1699.

(86) Normal-Coordinate Structural Decomposition Engine; http://jasheln.unm.edu/jasheln/content/nsd/NSDengine/start.htm (accessed 1/09/2015).

(87) Cerussi, A. E.; Berger, A. J.; Bevilacqua, F.; Shah, N.; Jakubowski, D.; Butler, J.; Holcombe, R. F.; Tromberg, B. J. Sources of Absorption and Scattering Contrast for Near-Infrared Optical Mammography. *Acad. Radiol.* **2001**, *8*, 211-218.

Chapter 4

A Spectroscopic and Theoretical Investigation of a Free-Base *meso*-Trithienylcorrole

Selected portions of the material presented in this chapter are published in: Greco, J. A., Rossi, A., Birge, R. R., and Bruckner, C. (2014) A Spectroscopic and Theoretical Investigation of a Free-Base *meso*-Trithienylcorrole. *Photochem. Photobiol.* **2014**, *90*, 402-414.

4.0 Abstract

The unique optical properties of free-base *meso*-trithienylcorrole were compared to those of the widely investigated *meso*-triphenyl-substituted analogue. A combination of spectroscopic and computational experiments were undertaken to elucidate the relationship between structural features of the neutral, mono-anionic, and mono-cationic forms of the corroles and their corresponding optical properties. A general bathochromic shift was measured for the thienyl-substituted corrole. The experimental spectra are supported by excited state calculations. A systematic series of ground state minimizations were performed to determine energy minima for the flexible and solvent-sensitive molecules. Trithienylcorrole was found to have a more non-planar macrocycle in conjunction with a high degree of π-overlap with the *meso*-substituents. Both structural features contribute to their bathochromically shifted optical spectra. The configurational character of the thienyl-substituted corrole is shown to have a larger degree of molecular orbital mixing and doubly excited character, which suggest a more complex electronic structure that does not fully adhere to the Gouterman four-orbital model. The reactivity of the thienyl groups, particularly with respect to their ability to be (electro)-polymerized, combined with the tight coupling of the *meso*-thienyl groups with the corrole chromophore elucidated in this work, recommends the *meso*-thienylcorroles as building blocks in, for instance, organic semiconductor devices.

4.1. Introduction

The fundamental understanding of the properties of tetrapyrrolic macrocycles, the 'pigments of life',[1] has long been of interest for their biological significance and potential for applications in a wide variety of biological and technical applications. In an upshot of these studies, novel synthetic pathways and the discovery of many tetrapyrrolic pigments and analogues without natural precedent provided the ability to modulate the electronic structure of the porphyrinoids,[2-9] an important prerequisite for the optimal utilization of these chromophores.

Corroles are tetrapyrrolic macrocycles that contain three methine bridges and one direct pyrrole-pyrrole bond.[10] Thus, they lack one *meso*-position compared to a regular porphyrin structure (Scheme 4.1). However, both porphyrins and corroles contain 18 π-electron systems (with two or one 'cross-conjugated' β,β'-double bonds, respectively). The 18 π-electron system in the contracted molecular framework of corroles is maintained by change of the hybridization state of one nitrogen. Thus, only a single imine-type nitrogen and three pyrrole-type nitrogens line the central cavity of corroles as compared to two nitrogens of each type in porphyrins.

meso-Triaryl-substituted corroles were firstly described by Gross and co-workers in 1999.[11,12] Their syntheses were improved since,[10,13-16] and numerous investigations illuminated the unique structural and electronic aspects of triarylcorroles (and their metal complexes).[17-34] As a consequence, the smaller trianionic corrolato ligand has a greater ability to stabilize higher central metal oxidation states than the larger dianionic porphyrinato ligand.[35-37] This property was utilized in applications of metallocorroles as catalysts for a range of transformations.[38-44] *meso*-Arylcorroles were also utilized,[10,45,46] *inter alia*, in light-harvesting devices,[47] as chemosensors,[48] and as chemotherapeutics.[49-54]

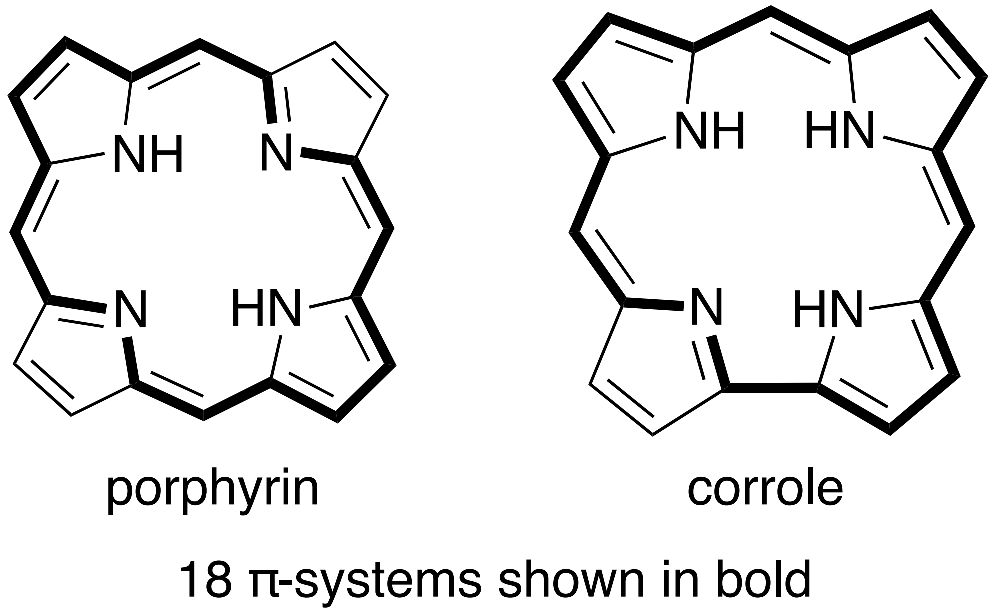

Scheme 4.1. Framework structures of corroles and porphyrins.

With notable exceptions,[55,56] substituents attached to the *meso*-phenyl groups on porphyrins have generally only minimal influence on the electronic structure of a porphyrin[57] because the phenyl moieties are, due to an unfavorable β-H to *o*-H steric interaction, positioned essentially orthogonal to the porphyrinic chromophore.[58] However, we have demonstrated that the smaller *meso*-thienyl groups lacking an *o*-H group have a pronounced influence on the conformation and electronic spectra of the porphyrinic chromophore, particularly when protonation induces a non-planar conformation of the macrocycle.[59] As a result, a significant bathochromic shift of the optical spectra is observed for *meso*-thienyl-substituted porphyrins when compared to the phenyl analogues.[59-64] *meso*-Thienyl-substituted porphyrins have been used in the study of rotational barriers in peripherally crowded porphyrins,[65] and have been incorporated in the design of organic semiconductor devices,[66] light harvesting and energy-transfer molecules,[64,67,68] and supramolecular architectures with extended electronic states.[69] *meso*-Thienyl-substituted porphyrin analogues were also reported.[70,71] Some *meso*-thienyl substituted core-modified porphyrins proved to be potent phototoxins.[71] Significantly, the thienyl substituents can be (electro)-polymerized to furnish, for instance, ultrathin films of quasi two-dimensional porphyrin polymers,[66,72,73] to produce electrodes possessing electrocatalytic properties for the four-electron reduction of oxygen[74] or to be part of electrochemical glucose[75] or novel TNT sensors[76].

Because of their larger degree of non-planarity and contracted frameworks, *meso*-aryl-substituted corroles exhibit a reduced β-H to *o*-H steric interaction with their *meso*-substituents.[11] Thus, the conformation of the aryl substituents can be more co-planar with the corrole chromophore than the same *meso*-substituents with the porphyrin chromophore. Consequently, this leads to a larger π-overlap with the *meso*-aryl substituents, and variation of these

substituents allows a much more prominent spectral tuning of the corrole chromophore (and its metal complexes) than is observed in comparable porphyrins.[12,26,28,77-81]

The group of Churchill pioneered the synthesis of *meso*-thienyl-substituted corroles and their building blocks, and studied their characteristics.[80-83] Through these investigations, it became clear that the presence of the *meso*-thienyl-substituents in corroles (and dipyrrin-based chromophores, such as boron-dipyrromethene (BODIPY))[84-89] have a significant effect on the electronic structure and photophysical properties of the chromophores. However, we are not aware of a detailed description of the nature of the electronic interactions between the thienyl moieties and the central corrole chromophore.

In this contribution, we will compare the UV-visible spectra of a *meso*-tris(5-methyl-thien-2-yl-substituted) corrole in a number of solvents and at varying protonation/deprotonation states with the corresponding spectra of its triphenyl-substituted analogue. This investigation assesses the degree to which the thienyl groups influence the optical spectra of free-base thienylcorroles. Moreover, a computational study will delineate structural implications of the electronic overlap of the two π-systems and will define the origins of the observed differences between a *meso*-phenyl- and *meso*-thienyl-substituted corrole. We thus provide complementary information to the existing studies that describe the surprising electronic properties of corroles.

4.2. Methods and Materials

4.2.1. Materials

All reagents and solvents were from commercial sources and used without prior purification, except that pyrrole was distilled over KOH before use. *meso*-Triphenylcorrole (**(Ph-Cor)H$_3$**) was prepared as described previously (Scheme 4.2).[90]

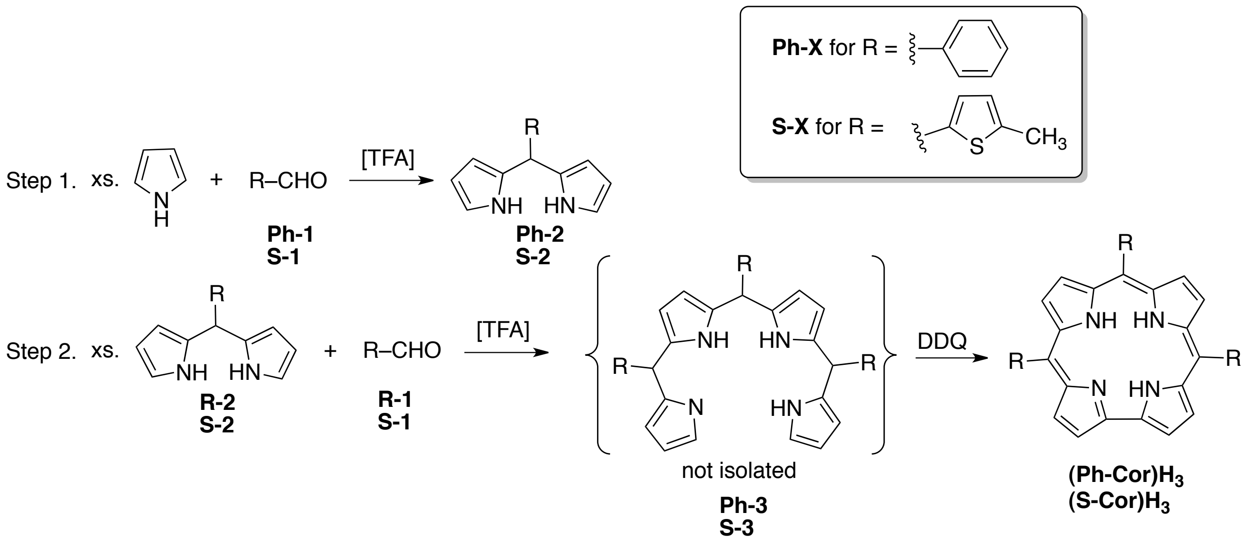

Scheme 4.2. Synthesis of the triarylcorroles investigated.

4.2.2. 5-(5-Methyl-2-thienyl)dipyrromethane

In a 100 mL round-bottom flask, 1 mL (9.3 mmol) of 5-methyl-2-thiophenecarboxaldehyde (**S-1**) and 4.5 mL (64.9 mmol) of freshly distilled pyrrole were combined and the mixture was degassed with N_2 for 5 min. To this solution, 84 µL (1.1 mmol) of trifluoroacetic acid (TFA) were added via a microsyringe and the mixture was magnetically stirred under an atmosphere of dry N_2 at ambient temperature for 30 min. After this time, thin layer chromatography indicated the formation of dipyrromethane (in a fume hood, fumigation of the dipyrromethane with Br_2 fumes from the headspace of a bromine bottle stains the dipyrromethane bright red). The solution is quenched with 1 mL (7.2 mmol) of Et_3N and diluted with ethyl acetate (50 mL). The organic phase was washed multiple times with water, dried over $MgSO_4$, and reduced to dryness by rotary evaporation. The crude mass was purified by column chromatography (silica–CH_2Cl_2) to provide **S-2** as an off-white solid in 65% yield (1.46 g). The reaction is readily scaled 5-fold. R_f = 0.79 (silica–CH_2Cl_2); ^1H NMR (300 MHz, $CDCl_3$): δ = 7.92 (br s, 2H), 6.74-6.68 (m, 4H), 6.25 (m, 2H), 6.13 (s, 2H), 5.65 (s, 1H), 2.53 (s, 3H) ppm; ^{13}C NMR (75 MHz, $CDCl_3$): δ = 143.4, 139.1, 132.2, 125.4, 124.8, 117.5, 108.5, 106.1, 39.4, 15.4 ppm; HR-MS (ESI+, 100% ACN, TOF detection) calculated for $C_{14}H_{15}N_2S$ (M+H): 243.0956, found: 243.0970.

4.2.3. *meso*-Tris(5-methyl-thien-2-yl)corrole

In a 100 mL round-bottom flask equipped with a stir bar and a gas inlet, 174 µL (1.6 mmol) of 5-methyl-2-thiophenecarboxaldehyde (**S-1**) were dissolved in acetonitrile (60 mL) and the mixture was degassed with N_2 for 5 min. Then, 2.56 g (10.6 mmol) of dipyrromethane **S-2** were added, followed by 120 µL (1.6 mmol) of TFA added via microsyringe, and the solution was stirred at ambient temperature under an N_2 atmosphere. After the consumption of the

aldehyde was judged to be complete using gas chromatography (after about 3 h), the reaction was quenched with 450 µL (3.2 mmol) of Et_3N. Next, 1.83 g (8.1 mmol) of 2,3-dichloro-5,6-dicyano-1,4-benzoquinone (DDQ) dissolved in warm toluene (~20 mL) was added to the reaction mixture that was stirred at ambient temperature for 12 h. Removal of the solvent by rotary evaporation and purification of the residue by flash column chromatography (silica–CH_2Cl_2:petroleum ether 2:1) provided the deep green non-polar product **(S-Cor)H$_3$** in 22% yield (205 mg) in the form of a powder. R_f = 0.85 (silica–CH_2Cl_2:pet ether 2:1); ^{1}H NMR (400 MHz, $CDCl_3$ + 1% TFA): δ = 8.53 (s, 1H), 7.87 (s, 2H), 7.42 (s, 2H), 7.25 (s, 1H) 7.19 (s, 1H), 7.09 (s, 1H), 6.67 (d, 3H) 2.94 (s, 2H), 2.74 (s, 6H), 2.41 (s, 3H), 2.34 (s, 3H); UV-visible (CH_2Cl_2) λ_{max} (log ε): 433 (5.16), 591 (4.18), 641 (4.23) nm; for this spectrum and the spectra in other solvents, see Figure 4.2; HR-MS (ESI+, 100% ACN, TOF detection) calculated for $C_{34}H_{27}N_4S_3$ (M+H): 587.1398, found: 587.1420.

4.2.4. UV-Visible Spectroscopic Methods

All spectra were recorded on a Cary 50 UV-visible spectrophotometer, Agilent Technologies, in 1 cm glass cuvettes in the solvents indicated.

4.2.5. Theoretical Methods

Potential energy surface (PES) scans were systematically performed for each of the three thienyl groups of trithienylcorrole using a Becke, 3-parameter, Lee-Yang-Parr (B3LYP) hybrid functional[91] and a 6-31G(d) basis set, as implemented in Gaussian 09.[92] The geometry of the molecule was optimized following 20° rotational increments around a predefined dihedral angle for each of the three substituents. As the probed group was varied through this rotation, the dihedral angle remained fixed while the rest of the molecule was optimized. The energetics and permanent dipole moment of the molecules throughout each scan were observed to be dependent

on the starting conformations of the other two groups of the trisubstituted molecule. Because of this interdependence, the starting orientations of the two freely rotating groups in a scan were modulated based on the position of the sulfur atoms with respect to the macrocycle core. A series of 12 starting conformations were used to accommodate relative differences in substituent orientation. Consequently, a library of 12 local minima was obtained, thereby establishing a reasonable global minimum from the set of PES scans. Tabulation of the resulting dihedral angles, energies, and dipole moments of the minimum from each scan are comprehensively shown in Table 4.1; a subset is shown in Table 4.2. Subsequently, solvent effects were introduced to the optimized local minima from the PES data set. For simulations involving a solvent environment, the Polarizable Continuum Model (PCM) was employed in Gaussian 09 by using the self-consistent reaction field (SCRF) method.[92-94] The local minima obtained from the PES scans in vacuum were optimized again in a PCM-derived solvent environment and a B3LYP/6-31G(d) method to pinpoint the global minimum in the solvent of interest. The 12 local minima were also used as starting geometries to determine reasonable global minima for the mono-anionic and mono-cationic molecules. All calculations involving anions included diffuse functions within the basis set (6-31+G(d)).[95]

Although we included diffuse orbitals in our calculations on the anions, we should point out that the simultaneous use of diffuse orbitals and PCM solvent methods remains to be fully substantiated as a viable combination. The problem derives from the fact that a solvent cavity is expected to compact diffuse orbitals significantly. This effect is observed because the energetic advantages of reducing coulombic repulsion are offset by the energetic costs of creating the enlarged solvent cavity necessary to accommodate the diffuse orbitals. At present, theory only partially compensates for these effects. Further work in this area is therefore important.

Table 4.1. Summary of the PES Scans of **(S-Cor)H$_3$**, Tautomer 2, in Vacuum, DCM, and ACN

	(a) vacuum					**(b)** DCM					**(c)** ACN				
	ϕ_1 (°)	ϕ_2 (°)	ϕ_3 (°)	μ (D)	HOF (kJ/mol)	ϕ_1 (°)	ϕ_2 (°)	ϕ_3 (°)	μ (D)	HOF (kJ/mol)	ϕ_1 (°)	ϕ_2 (°)	ϕ_3 (°)	μ (D)	HOF (kJ/mol)
1	36.88	119.57	133.21	1.60	963.26	36.24	119.87	133.85	2.66	937.94	36.08	119.97	134.05	2.88	933.51
2	-141.63	119.54	-133.21	2.50	962.62	-142.56	119.96	-48.20	3.95	936.84	-142.75	120.09	-47.98	4.27	932.27
3	36.93	-58.47	133.07	1.92	963.61	36.31	-58.08	133.74	3.20	938.37	36.21	-57.92	133.95	3.48	933.94
4	-141.37	-58.54	-49.10	2.99	963.26	-142.13	-58.21	-48.42	4.63	937.41	-142.32	-58.00	-48.27	5.02	932.77
5	37.19	124.47	50.83	1.98	964.90	36.52	124.90	50.33	3.18	939.38	36.33	125.03	50.13	3.43	934.89
6	-141.46	124.60	60.63	2.41	964.10	-142.35	124.84	50.11	3.85	938.55	-142.57	124.91	49.95	4.15	934.05
7	37.17	124.44	-127.46	1.71	964.98	36.51	124.77	-128.06	2.79	939.72	36.33	124.89	-128.27	3.01	935.29
8	-141.37	124.54	-127.56	2.20	964.22	-142.29	124.91	-128.22	3.47	938.89	-142.48	125.02	-128.38	3.74	934.46
9	-141.46	124.60	50.63	2.40	964.10	-142.35	124.84	50.11	3.85	938.55	-142.57	124.91	49.95	4.15	934.05
10	-141.24	-54.05	50.27	2.72	964.33	-142.02	-53.61	49.60	4.31	938.74	-142.23	-53.46	49.40	4.67	934.19
11	-141.37	124.54	-127.56	2.20	964.22	-142.29	124.91	-128.22	3.47	938.89	-142.48	125.02	-128.38	3.40	934.457
12	-141.14	-54.16	-127.84	2.69	964.61	-141.83	-53.60	-128.58	4.15	939.15	-142.02	-53.44	-128.75	4.49	934.611

Table 4.2. Heat of Formation (HOF, kJ/mol) for Ground State Geometry Optimizations of the Neutral, Mono-Anionic, and Mono-Cationic Forms of **(Ph-Cor)H$_3$** and **(S-Cor)H$_3$**

	Solvent		
Compound	**Vacuum**	**DCM**	**ACN**
(Ph-Cor)H$_3$	1043.09	910.53	906.40
(S-Cor)H$_3$	962.62	936.84	932.77
[(Ph-Cor)H$_2$]$^-$	614.32	459.92	492.56
[(S-Cor)H$_2$]$^-$	649.87	436.62	470.81
[(Ph-Cor)H$_4$]$^+$	1534.57	1403.20	Not determined[a]
[(S-Cor)H$_4$]$^+$	1427.81	1301.25	Not determined[a]

[a] The mono-cationic structures were not determined in ACN because the configurations were irrelevant to the experimental data.

The excited state properties were calculated using equation-of-motion coupled-cluster with singles and doubles (EOM-CCSD)[96-98] and symmetry-adapted-cluster configuration-interaction (SAC-CI)[99-103] methods. Excited state calculations were all performed using an active space consisting of the eight highest energy filled orbitals and the eight lowest energy virtual orbitals, and by using a Dunning/Huzinaga full double-ζ (D95) basis set.[104] Unless otherwise mentioned, the calculated spectroscopic properties were investigated in reference to the Hartree-Fock ground state energies.

Test calculations were initially undertaken to include polarization orbitals in the basis sets of the EOM-CCSD calculations (e.g., a D95(d) basis set instead of D95). In addition to a significant increase in computation time, the results demonstrate that there are negligible differences for the molecules of interest (Figure 4.1). We conclude that while including polarization orbitals is very important for the assignment of ground state geometries, the low occupation of these orbitals relegates the additional orbitals of modest importance to the calculation of transition energies and oscillator strengths for the Franck-Condon geometry. We further note that using a D95 basis set is a near optimal choice for EOM-CCSD calculations in terms of efficiency and relevant orbital degrees of freedom. Because there is some confusion in the literature on which basis orbitals are included in the D95 basis set, we include Table 4.3, which formally lists both the orbitals, basis functions and Gaussian primitives that are included for the various basis sets used in this study.

Both the EOM-CCSD and SAC-CI methods yielded reliable results compared to experiment when the PCM solvent environments were included in the simulation.[105] The EOM-CCSD methodology has proven to be a reliable method for calculating transition energies and oscillator strengths.[96-98,106,107] The SAC-CI methods were also used because they provide excited

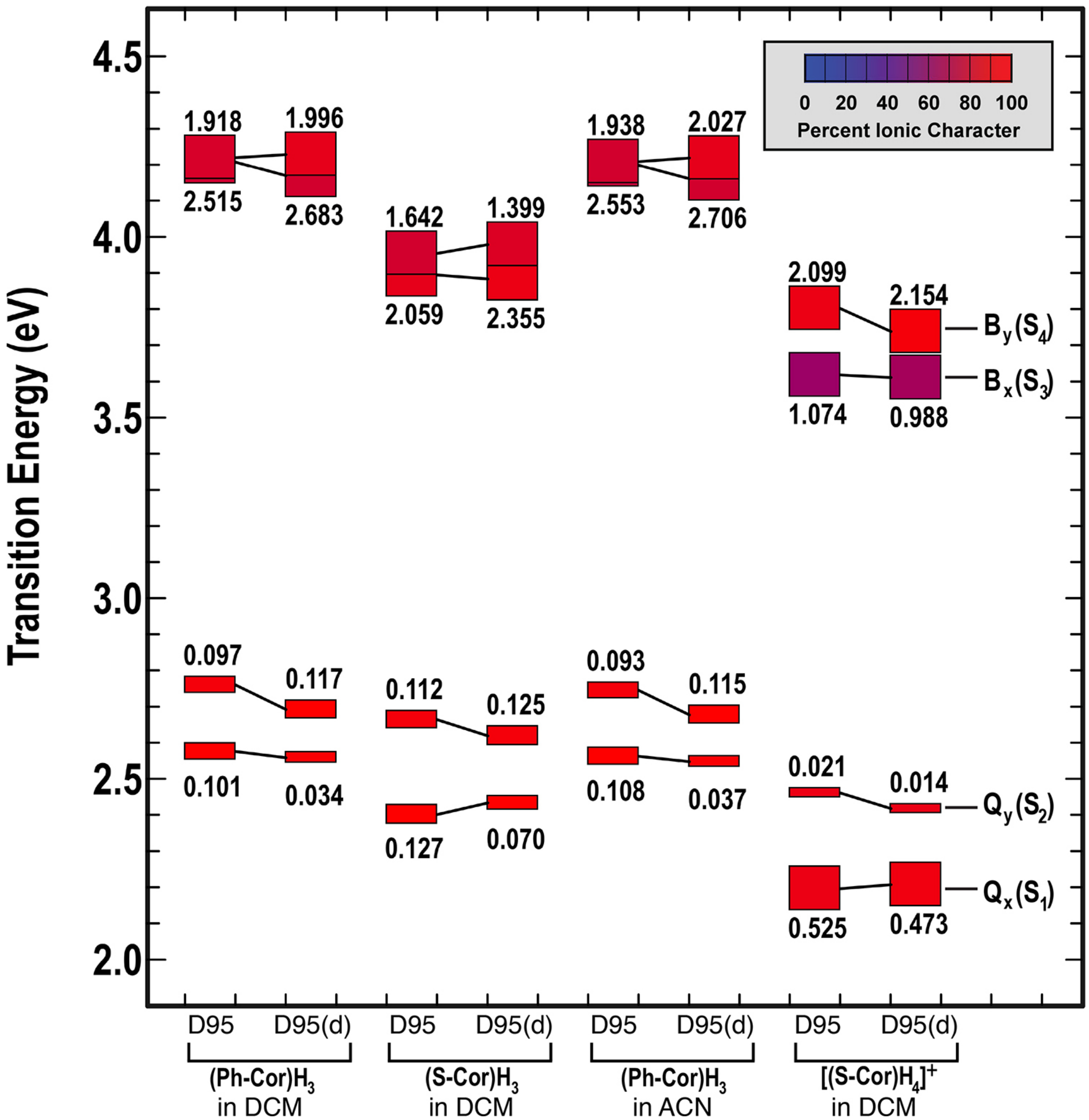

Figure 4.1. Excited singlet state level ordering of the first 4 excited states of **(Ph-Cor)H$_3$**, **(S-Cor)H$_3$**, and **[(S-Cor)H$_4$]$^+$** using Dunning basis sets without polarization functions (D95) and with polarization functions (D95(d)). The labeling scheme is as shown in Figure 4.6.

Table 4.3. Analysis of the Orbital Composition of Various Basis Sets

Basis Set	Row	Atoms	Primary Orbitals	Polarization Orbitals	Diffuse Orbitals	BFs[a]	PGs[b]
D95V	1	H-He	1s,1s'	*none*	*none*	2	4
	2	Li-Ne	1s,2s, 2s',2px, 2px',2py,2py',2pz,2pz'	*none*	*none*	9	25
D95	1	H-He	1s,1s'	*none*	*none*	2	4
	2	Li-Ne	1s,1s', 2s,2s', 2px, 2px',2py,2py',2pz,2pz'	*none*	*none*	10	24
	3	Na-Ar	1s,1s',2s, 2s',3s,3s', 2px, 2px',2py,2py', 2pz,2pz',3px,3px',3py,3py',3pz,3pz'	*none*	*none*	18	36
D95(d)	1	H-He	1s,1s'	*none*	*none*	2	4
	2	Li-Ne	1s,1s',2s, 2s',2px, 2px',2py,2py',2pz,2pz'	3d(x^2,y^2,z^2,xy,xz,yz)	*none*	16	30
	3	Na-Ar	1s,1s',2s, 2s',3s,3s', 2px, 2px',2py,2py', 2pz,2pz',3px, 3px',3py,3py',3pz,3pz'	4d(x^2,y^2,z^2,xy,xz,yz)	*none*	24	42
6-31G(d)	1	H-He	1s,1s'	*none*	*none*	2	4
	2	Li-Ne	1s, 2s, 2s', 2px, 2px', 2py, 2py', 2pz, 2pz'	3d(x^2,y^2,z^2,xy,xz,yz)	*none*	15	28
	3	Na-Ar	1s,2s, 3s,3s', 2px,2py,2pz, 3px,3px', 3py,3py', 3pz,3pz'	4d(x^2,y^2,z^2,xy,xz,yz)	*none*	19	52
6-31+G(d,p)	1	H-He	1s,1s'	2px, 2py, 2pz	*none*	5	7
	2	Li-Ne	1s, 2s, 2s', 2px, 2px', 2py, 2py', 2pz, 2pz'	3d(x^2,y^2,z^2,xy,xz,yz)	2s,2px,2py,2pz	19	32
	3	Na-Ar	1s, 2s, 3s,3s', 2px,2py,2pz, 3px,3px', 3py,3py', 3pz,3pz'	4d(x^2,y^2,z^2,xy,xz,yz)	3s,3px,3py,3pz	23	56
6-311++G(2d,p)	1	H-He	1s,1s',1s"	2px, 2py, 2pz	1s	7	9
	2	Li-Ne	1s, 2s,2s',2s", 2px,2px',2px", 2py,2py',2py", 2pz,2pz',2pz"	3d(0,+1,-1,+2,-2) 3d'(0,+1,-1,+2,-2)	2s,2px,2py,2pz	27	42
	3	Na-Ar	1s, 2s,2s', 3s,3s',3s", 2px, 2px', 2py, 2py', 2pz, 2pz' 3px,3px',3px",3py,3py',3py",3pz,3pz',3pz"	4d(0,+1,-1,+2,-2) 4d'(0,+1,-1,+2,-2)	3s,3px,3py,3pz	35	56

[a]BF = Basis functions
[b]PG = Primitive Gaussians

state electron densities and have an excellent history in examining porphyrin systems.[99-103] The EOM-CCSD results were plotted in Figure 4.6 to demonstrate the relative level-ordering of the investigated molecules in various charge states, while SAC-CI analyses in Figures 4.5, 4.7, and 4.8 were incorporated to observe the transition energies and transition dipole moments of the first four excited states. We found that the combined use of EOM-CCSD and SAC-CI methods provided a good perspective on the excited state properties of these molecules.

4.3. Results and Discussion

4.3.1. Synthesis

The synthesis of the triarylcorroles investigated was accomplished using an established methodology (Scheme 4.2).[90] A dipyrromethane **2**, prepared from pyrrole and an arylaldehyde, **1**, is converted to a triaryl-tetrapyrrane **3** that is, without prior isolation, oxidatively ring-closed to the corresponding corrole.[90] The *meso*-tris(5-methyl-thien-2-yl)corrole (**(S-Cor)H$_3$**) thus prepared from 5-methyl-thienyl-2-aldehyde (**S-1**) and pyrrole showed all the expected spectroscopic and analytical properties. The corrole and the intermediate 5-(5-methyl-thien-2-yl)dipyrromethane (**S-2**) are both similar to the parent non-methylated thienyl derivatives firstly prepared by Churchill.[80,82] We chose the 5-methyl substituted derivative because we have shown that the 5-methyl group lead to a further red-shift of the optical spectra in *meso*-thienyl-substituted porphyrins.[59] Also, the substitution of the thienyl α-position shuts down possible degradation processes at this reactive position.

4.3.2. Empirical UV-visible Spectra of the Corroles

The conventional approach of describing the steady-state absorption spectra of corroles is to assign the transitions in the UV-visible domain as those observed for the parent porphyrin

complexes.[28] Thus, absorption bands in the 400 nm region are assigned as B-bands (i.e., Soret-like transitions), and all those of lower energy (500-700 nm) are considered as Q bands. Accordingly, transitions to the S_1, S_2, S_3, and S_4 energy levels of triarylcorroles will be considered analogous to the transitions of porphine to be the Q_x, Q_y, B_x, and B_y bands, respectively. We follow this labeling scheme hereafter to describe the empirical designation of the electronic transitions.

The UV-visible spectra of **(Ph-Cor)H$_3$** and **(S-Cor)H$_3$** in the non-polar solvent dichloromethane (CH_2Cl_2, DCM) and in the polar solvent acetonitrile (CH_3CN, ACN) are presented in Figure 4.2. Both porphyrins and corroles are dominated by $\pi^* \leftarrow \pi$ transitions, contain an intense Soret band at ~400 nm, and exhibit a set of Q transitions at energies lower than 500 nm. As was described before, electronic transitions of corroles tend to be of lower energy than of the related porphyrin macrocycles.[28] Furthermore, a relative decrease in the extinction coefficient of the Soret bands with respect to the Q bands are commonly observed in corrole spectra due to the decreased symmetry of the macrocycle.

The absorption spectra of the *meso*-phenyl derivative, **(Ph-Cor)H$_3$**, and *meso*-thienyl derivative, **(S-Cor)H$_3$**, in DCM contain similar transitions and relative ratios between the Soret and Q bands, but there are some notable differences. The Soret band of **(S-Cor)H$_3$** is red-shifted by 17 nm compared to that of **(Ph-Cor)H$_3$** (433 and 416 nm, respectively), and it is significantly broader. As described before, the Q band region of **(Ph-Cor)H$_3$** consists of three primary bands, at 574, 617, and 651 nm.[28] In comparison, the Q bands in the **(S-Cor)H$_3$** spectrum at 592, 647, and 682 nm, with a possible feature appearing at 754 nm, are 18-31 nm red-shifted and far less discrete. There is also a noticeable increase in oscillator strength of these bands relative to the

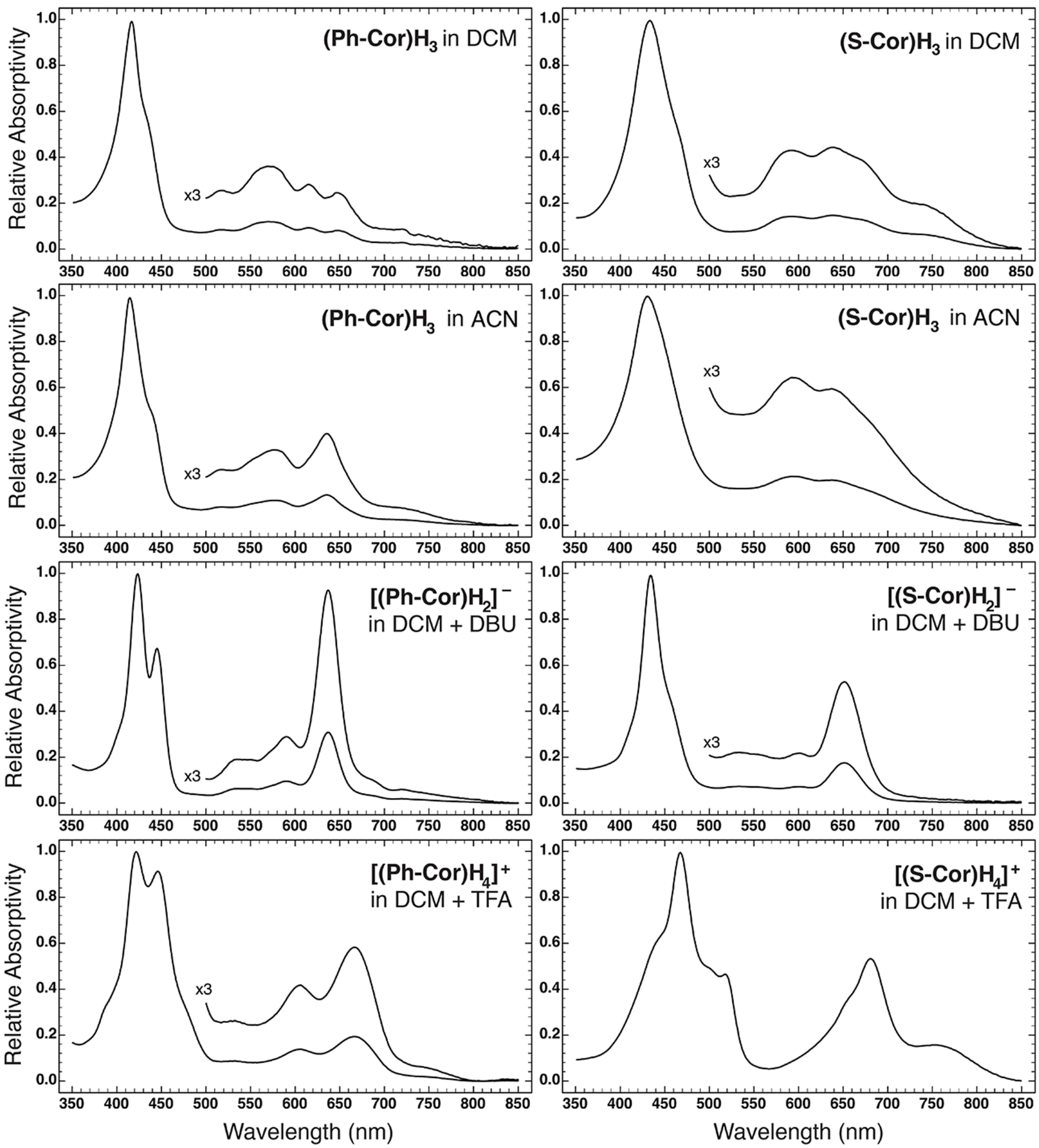

Figure 4.2. Experimental absorption spectra of **(Ph-Cor)H$_3$** and **(S-Cor)H$_3$** in the solvents indicated. All spectra are normalized to the absorption maximum of the Soret band.

Soret band. These differences are consistent with previous findings that corrole absorption spectra are characteristically subject to *meso*-substituent-dependent shifts.[28]

Corrole absorption spectra (and also a number of other physical and chemical properties) are also prone to significant solvatochromic effects[26-28,108,109] that were described and rationalized before. Thus, for both corroles a significant red shift of the Q band region is observed in the strongly polar solvent ACN relative to the non-polar solvent DCM. **(Ph-Cor)H_3** demonstrates an altered Q band structure with two distinct absorption peaks at 580 and 638 nm, in which the 638 nm band has a higher relative oscillator strength than any other feature in the non-polar solvent. The Q band region of **(S-Cor)H_3** also exhibits an intense two band structure (591 and 641 nm). This difference in the absorption spectra is interesting and we will present below a theoretical investigation to elucidate the role the thienyl groups play in the solvatochromism of the thienylcorroles. The position of the Soret bands of **(Ph-Cor)H_3** and **(S-Cor)H_3**, however, are immune to any solvatochromic effect in these solvents.

The acid-base equilibria of corroles were also well described before.[15,23,26,110] Scheme 4.3 describes this acid-base equilibrium, and establishes the nomenclature for the mono-anionic and mono-cationic forms of the triarylcorroles. Corroles are intrinsically much more acidic than porphyrins.[23] Consequently, even mild bases were shown to be capable of generating the anionic form of triarylcorroles.[15,23,26,110] This high acidity can be attributed to the relief of steric hindrance upon the loss of a hydrogen within the inner core of the corrole. This acidity is solvent dependent and is sensitive to the nature of the *meso*-substituents.[15,23,25,110] Addition of the non-nucleophilic strong base, 1,8-diazabicyclo[5.4.0]undec-7-ene (DBU), to **(Ph-Cor)H_3** and **(S-Cor)H_3** in DCM invariably leads to the formation of the anionic forms **[(Ph-Cor)H_2]$^-$** and **[(S-Cor)H_2]$^-$**, as indicated by the appearance of an intense band at 639 and 652 nm, respectively.

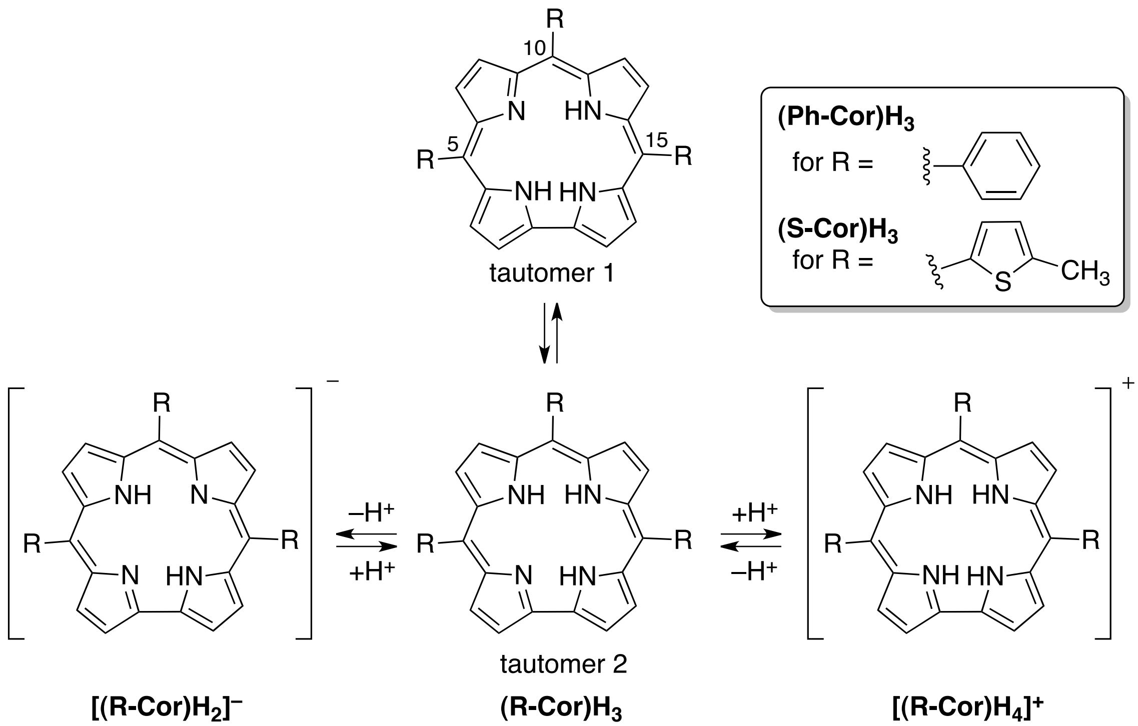

Scheme 4.3. Tautomers and protonation states of the triarylcorroles investigated.

Electronic differences between the corroles carrying the two different types of *meso*-substituents are apparent in the Soret band of **[(Ph-Cor)H$_2$]$^-$**, which is split into two distinct peaks.

On the other hand, addition of the strong organic acid, TFA, mono-protonates the triarylcorroles, creating **[(Ph-Cor)H$_4$]$^+$** and **[(S-Cor)H$_4$]$^+$**.[10,23,111] The cationic configuration of the molecules produce an absorption band in the Q band region that has a larger bathochromic shift, with an intense peak for the phenyl- and thienyl-containing molecules at 666 and 679 nm, respectively. Again, significant differences for the two different corroles are visible. For instance, **[(S-Cor)H$_4$]$^+$** exhibits a dramatically decreased Soret band to Q band ratio, whereas the **[(Ph-Cor)H$_4$]$^+$** Soret band again splits into two peaks.

Below we examine the important conformational influences with regard to the formation of both the mono-anionic and mono-cationic species, as well as the relevance of acid-base chemistry in the solvatochromism of the corroles. We also investigate the apparent differences between the formations of these ions in **(Ph-Cor)H$_3$** and **(S-Cor)H$_3$** to determine the influence of the thienyl substituents on the formation of the anionic/cationic forms.

4.3.3. Structural and Conformational Investigations of Triarylcorroles

The neutral forms of the triarylcorroles are characterized by a trivalent cavity that is in dynamic equilibrium between the two distinct tautomers, 1 and 2 (Scheme 4.3).[25,27,111] The tautomeric equilibrium is solvent and temperature dependent.[25,27] Ding *et al.* investigated the crystal structure of **(Ph-Cor)H$_3$** and found that tautomer 2 is the preferred configuration.[111] Our own ground state geometric analyses also suggested that tautomer 2 is universally more stable, both *in vacuo* and within all solvent environments, irrespective of the nature of the *meso*-aryl groups (here, phenyl or thienyl). Hence, the hydrogen configuration corresponding to tautomer 2 will be used in all subsequent discussions of the neutral triarylcorroles. Similarly, while the two

hydrogens of the anionic core are capable of arranging in multiple configurations, our calculated group state energies predicted that the hydrogen atoms are oriented diagonal from each other in the macrocycle core. This conformation is also the preferred arrangement in the analogous free-base porphyrin structures.[112] The mono-cationic species, of course, is capable of only one configuration with respect to the core hydrogen atoms.

Because each of the three *meso*-aryl substituents on the corrole macrocycle are able to rotate around the *meso*-*ipso*-bond, there are a number of local energy minima available to the molecule. This effect is particularly critical for **(S-Cor)H$_3$**, where the relative positions of the three non-axial symmetric aryl groups influence the planarity of the flexible macrocycle core and the total dipole moment of the molecule, and thus, the spectroscopic properties of the corrole. Thus, potential energy surface (PES) scans were performed to determine the lowest energy ground state geometry of both **(Ph-Cor)H$_3$** and **(S-Cor)H$_3$**.

The PES scans were first carried out *in vacuo*, with 12 varying starting positions of the substituents. Figure 4.3a illustrates the three C^{β}(thienyl)-C^{α}(thienyl)-C^{meso}(corrole)-C^{α}(corrole) dihedral angles ϕ_1 through ϕ_3 that were monitored throughout the three possible PES scans. Because of the asymmetry of the corrole macrocycle, the rotational itineraries for all three thienyl groups vary from each other (Figure 4.3b). These curves are also highly reliant on the relative position of the other two groups of the molecule, which have an impact on the macrocycle conformation. Consequently, the PES scans presented in Figure 4.3b are only one combinatorial example of the energetics of this molecule.

Table 4.1 shows the results of a series of PES scans that were undertaken, which systematically investigated the possible combinations of starting orientations of the thienyl groups. The data shows the lowest energy conformation of each PES scan, or a selection of 12

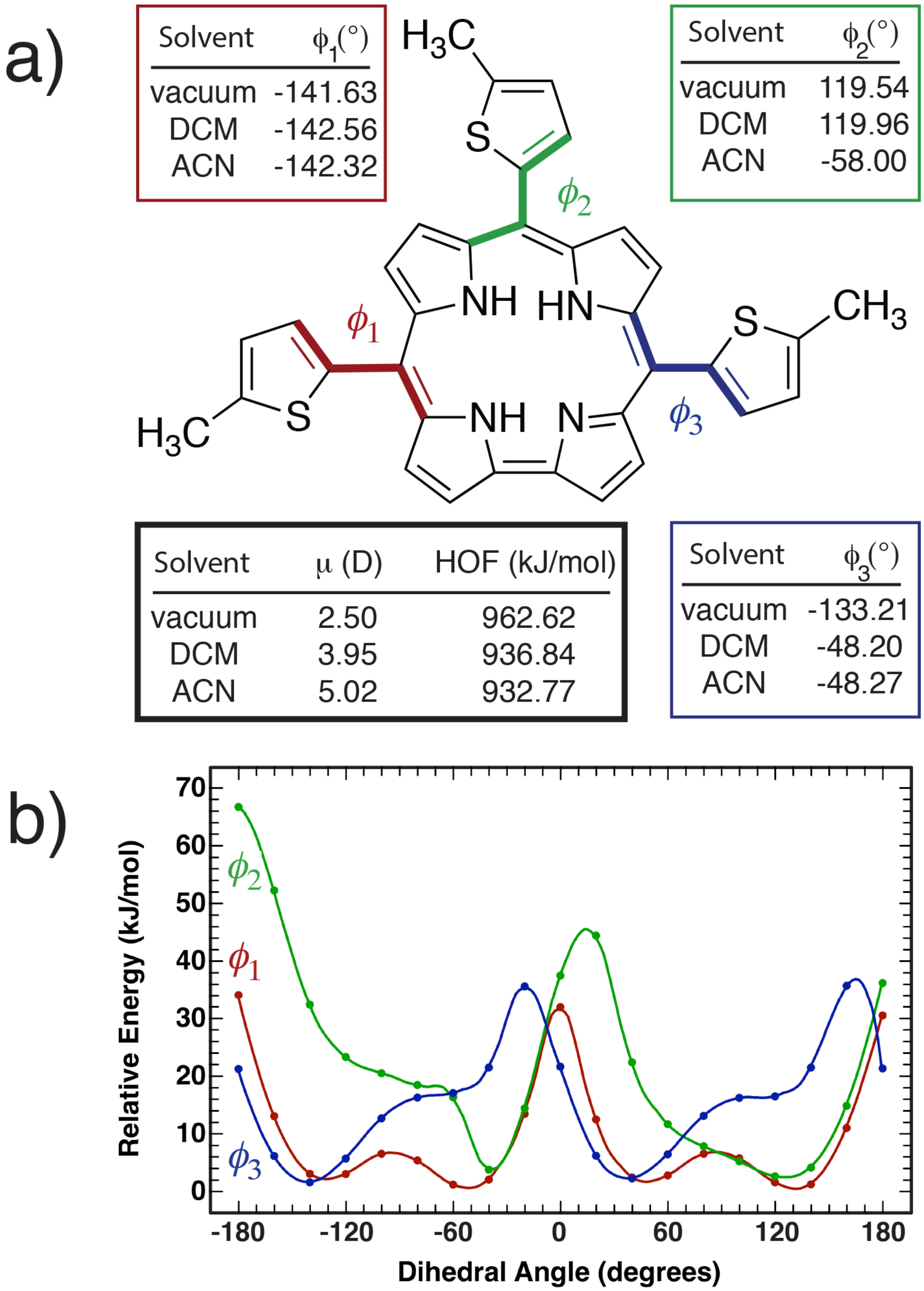

Figure 4.3. Potential energy surface (PES) scans were performed for the three thienyl groups of **(S-Cor)H$_3$** to determine a global minimum of the structure. The resulting minima in vacuum, DCM, and ACN are presented in (A). The curves presented in (B) provide an example of the PES of groups 1 (red), 2 (green), and 3 (blue). See text for further details regarding the high variability of energetics due to inherent asymmetry.

local energy minima (molecules **1-12** in Table 4.1). *In vacuo*, the **(S-Cor)H_3** molecule with the lowest energy conformation has a calculated heat of formation (HOF) of ~963 kJ/mol. Table 4.2 lists the global minima found. Subsequently, the 12 local energy minima conformations were minimized in solvent (DCM and ACN) by using PCM solvent methods. Figure 4.3a tabulates the thienyl group conformations (expressed as the dihedral angles ϕ_1 through ϕ_3) corresponding to the global minima in the solvents indicated. It also lists the dipole moment and HOF for each molecule. Note that while the addition of non-polar solvent did not have a significant impact on the lowest energy geometry, the inclusion of ACN showed that the lowest energy conformation molecule had, as expected, the highest dipole moment.

The 12 local energy minima derived from the *in vacuo* optimizations were also used as starting conformations to determine the lowest energy conformations of the mono-anionic and mono-cationic forms of the triarylcorroles. Table 4.2 lists the ground state energies of these molecules in solvent used for the excited state calculations.

Overall, two major findings can be derived. Firstly, the ground state energy of the molecule is largely dependent on the relative orientation of each of the three thienyl groups, and thus, is strongly coupled to the permanent dipole moment of the structure. Thus, the dipole moment and ground state energy have a strong relationship with the solvent environment, particularly in polar solvents. Secondly, the conformations selected in Table 4.2 delineate reasonable global minima in varying solvents for the subsequent theoretical investigations.

The relative acidity and basicity of the triarylcorroles depends on the electronic interaction of the *meso*-substituents with the macrocycle core. However, the difference in electron withdrawing effects between the thienyl and phenyl substituents is small and likely inconsequential to relative acidities (Table 4.4). The acidity of the core is tied more closely to the

Table 4.4. Summation of the Mulliken Charges Around the Aromatic Components of the Substituents (based on Figure 4.3) of **(Ph-Cor)H$_3$** and **(S-Cor)H$_3$**

		Solvent	
Compound	Group	DCM	CH_3CN
(Ph-Cor)H$_3$	1	0.019958	0.021494
	2	-0.009508	-0.00842
	3	0.008436	0.0089
(S-Cor)H$_3$	1	-0.122131	-0.036061
	2	-0.138458	-0.076862
	3	-0.120922	-0.05808

constrained nature of the corrole, the planarity of the macrocycle, and the co-planarity of the substituents with the macrocycle. Figure 4.4 presents a linear display of the deviation of the 23 atoms that comprise the macrocycle framework from a mean plane defined by the three C^{meso} atoms. The conformation of the pyrrole rings is strongly dependent on the rotational freedom of the tri-substituted corroles, and it is the magnitude of the deviation that is of interest here, not necessarily the directionality of the deviation.

The modes of deviation from planarity of the computed neutral **(Ph-Cor)H$_3$** and **(S-Cor)H$_3$** are similar in magnitude and are characteristic of what is also commonly observed in the crystal structures of triarylcorroles.[80,81,111] The contracted macrocycle core and the presence of three hydrogen atoms introduces a steric clash in the center of the macrocycle. To relieve this, the macrocycle plane takes up a saddling distortion.

Removal of a hydrogen results in a large decrease of the steric clash and results in the formation of strong intramolecular H-bonds. This planarization and overall energy release is at the origin of the high acidity of corroles.[23] Deprotonation also planarizes the macrocycles in **[(Ph-Cor)H$_2$]$^-$** and **[(S-Cor)H$_2$]$^-$** and significantly lowers the energy of the molecules (cf. Table 4.2). Notably, **[(Ph-Cor)H$_2$]$^-$** is significantly more planar than **[(S-Cor)H$_2$]$^-$**. Considering the smaller steric interaction of the thienyl groups with the parent macrocycle, this finding is counter-intuitive.

The conformation of the mono-protonated forms of the corroles also shows a strong dependence on the nature of the *meso*-substituents. The protonated form of the *meso*-thienyl-substituted corrole, **[(S-Cor)H$_4$]$^+$**, is significantly more non-planar than the phenyl-containing corrole, yet its energy increase relative to the non-protonated form is 26/28 kJ/mol less than for the phenyl-derivative (in vacuum/DCM). This difference between the phenyl- and thienyl-

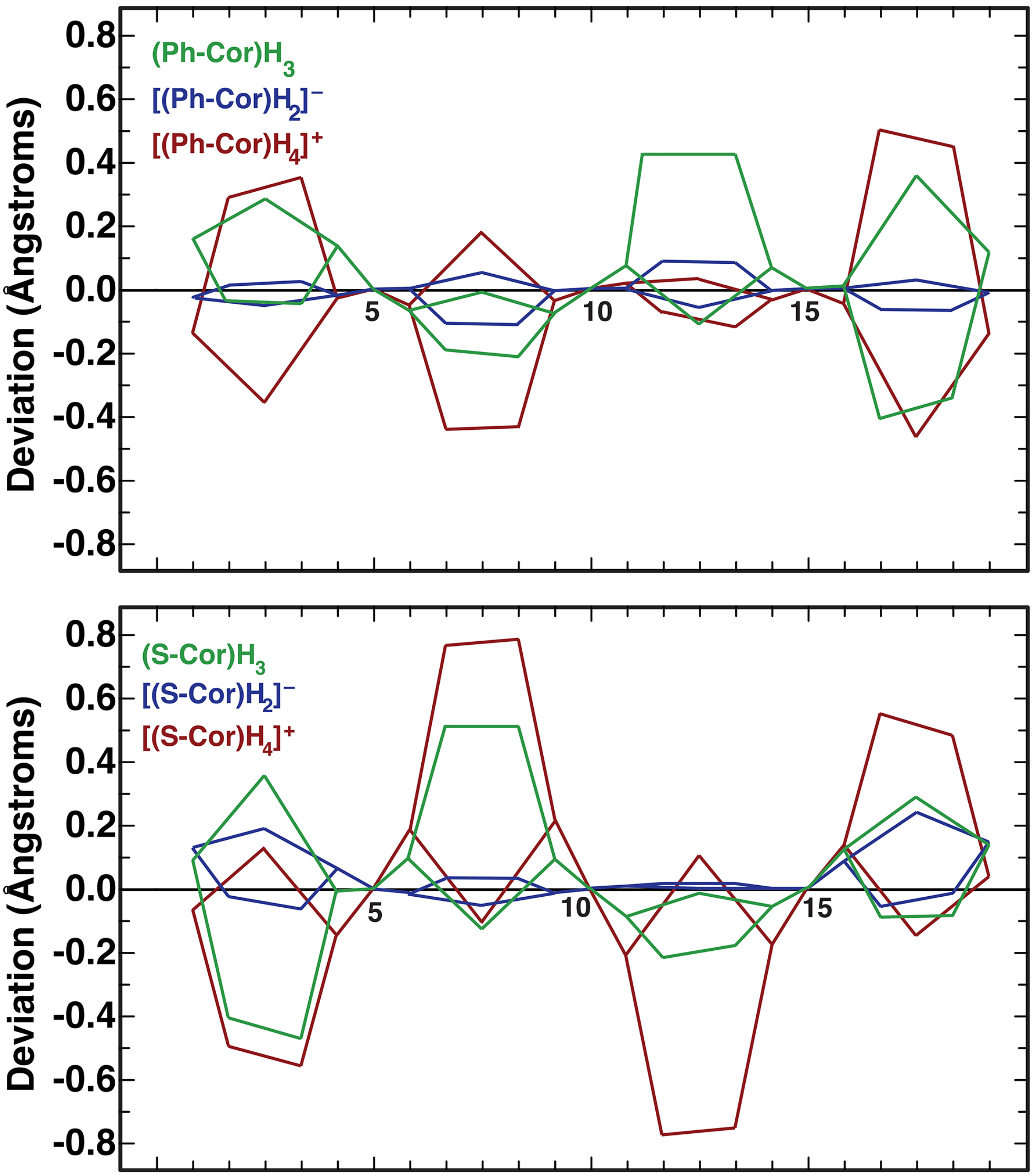

Figure 4.4. A linear display of the deviation of the 23 macrocycle framework atoms. For the assignment of the 5, 10, and 15 positions, see Scheme 3. These three *meso*-carbon atoms served to define the zero-point plane against which the relative deviation were plotted.

substituted mono-protonated corroles is also reflected in the UV-visible absorption spectra of **[(S-Cor)H$_4$]$^+$** and **[(Ph-Cor)H$_4$]$^+$** (Figure 4.2), particularly in terms of the relative oscillator strengths of the Soret and Q bands and the bathochromic shift of the Q-bands. Table 4.5 lists the dihedral angles of the mono-cationic forms of **(Ph-Cor)H$_3$** and **(S-Cor)H$_3$**. The thienyl groups are more co-planar with the corrole chromophore than the phenyl groups are, thus allowing a strong coupling of the thienyl π-system with that of the corrole. In general, corroles exhibit an increase in the extinction coefficients of the Q bands due to the reduction of alternancy symmetry.[113] The out-of-plane conformation of **[(S-Cor)H$_4$]$^+$** further reduces the chromophore symmetry. This, together with the added charge through protonation and the extended π-system involving the thienyl groups (see also below) rationalize the unique spectral features of this species.

Again, we like to highlight the counter-intuitive finding that the sterically less encumbered thienyl groups lead to a more non-planar chromophore. However, this finding is mirrored by precedence. Protonated thienyl-substituted porphyrins were also observed to be significantly more deplanarized than the corresponding protonated phenyl-substituted derivative.[59] We attribute this to an effect where the larger (but presumably still small) loss of π-conjugation induced by the non-planar conformation is balanced by the increased π-conjugation with the thienyl groups this conformation enables. On the other hand, the larger phenyl groups will not, even at the highly non-planar conformations, be allowing an equivalent co-planarity of the π-systems, thus not providing to such an extent a stabilizing π-overlap. The fact that this effect is most prominent in the protonated cases might be due to the additional driving forces of the accumulated charges in the center of the macrocycles, the dissipation of which is also assisted by the π-conjugation effects evoked. The charge density maps of the Soret transitions of

Table 4.5. Dihedral Angles for the Lowest Energy Ground State Geometries of the Neutral (DCM), Mono-Anionic (ACN), and Mono-Cationic (DCM) Forms of **(Ph-Cor)H$_3$** and **(S-Cor)H$_3$**

	Dihedral Angles		
Compound	ϕ_1 (°)	ϕ_2 (°)	ϕ_3 (°)
(Ph-Cor)H$_3$	135.66	-118.20	53.17
(S-Cor)H$_3$	-141.63	119.54	-48.98
[(Ph-Cor)H$_2$]$^-$	127.32	63.32	-53.23
[(S-Cor)H$_2$]$^-$	127.30	101.90	50.97
[(Ph-Cor)H$_4$]$^+$	136.41	66.87	45.41
[(S-Cor)H$_4$]$^+$	-143.89	-43.40	37.70

[(S-Cor)H$_4$]$^+$ (Figure 4.5) show this conjugative stabilization. The conjugation effects of the thienyl groups with porphyrins was also cited by Bhyrappa *et al.* to rationalize the optical properties of *meso*-thienyl-substituted porphyrins.[63]

4.3.4. The Excited State Properties of Triarylcorroles

To describe the nature of the electronic transitions of **(Ph-Cor)H$_3$** and **(S-Cor)H$_3$**, a combination of SAC-CI and EOM-CCSD excited state calculations were used to determine relative level ordering, transition energies, and transition dipole moments of the molecules.

Figure 4.6 shows the predicted level ordering of the first 4 excited states of **(Ph-Cor)H$_3$** and **(S-Cor)H$_3$** in neutral, mono-anionic, and mono-cationic forms, as predicted by using EOM-CCSD coupled-cluster methods and PCM solvent (DCM and ACN) environments. It is evident that all of the computed energy levels of the thienyl derivative, **(S-Cor)H$_3$**, are lower in energy than the corresponding levels of the phenyl derivative **(Ph-Cor)H$_3$**. The energy drop is concomitant with a reduction of the HOMO–LUMO gap. This is also supported experimentally by their UV-visible spectra (see Figure 4.2). Furthermore, the computed oscillator strengths of the Q bands of **(S-Cor)H$_3$** are larger, the S_3 and S_4 transitions are further separated in energy (i.e., the Soret band is broader), and the general Soret-band to Q band ratio is also consistently smaller for the neutral molecules. Again, this is supported by the experimental UV-visible spectra.

What is striking, however, is the seemingly small solvatochromatic effect that was computed for both **(Ph-Cor)H$_3$** and **(S-Cor)H$_3$**. The energy level ordering and oscillator strengths of the transitions are essentially identical between **(Ph-Cor)H$_3$** in DCM and ACN and between **(S-Cor)H$_3$** in the same solvent set. Figure 4.7 includes a SAC-CI analysis of the first 4 excited states of **(Ph-Cor)H$_3$** and **(S-Cor)H$_3$**. Here, it also becomes apparent that the thienyl-

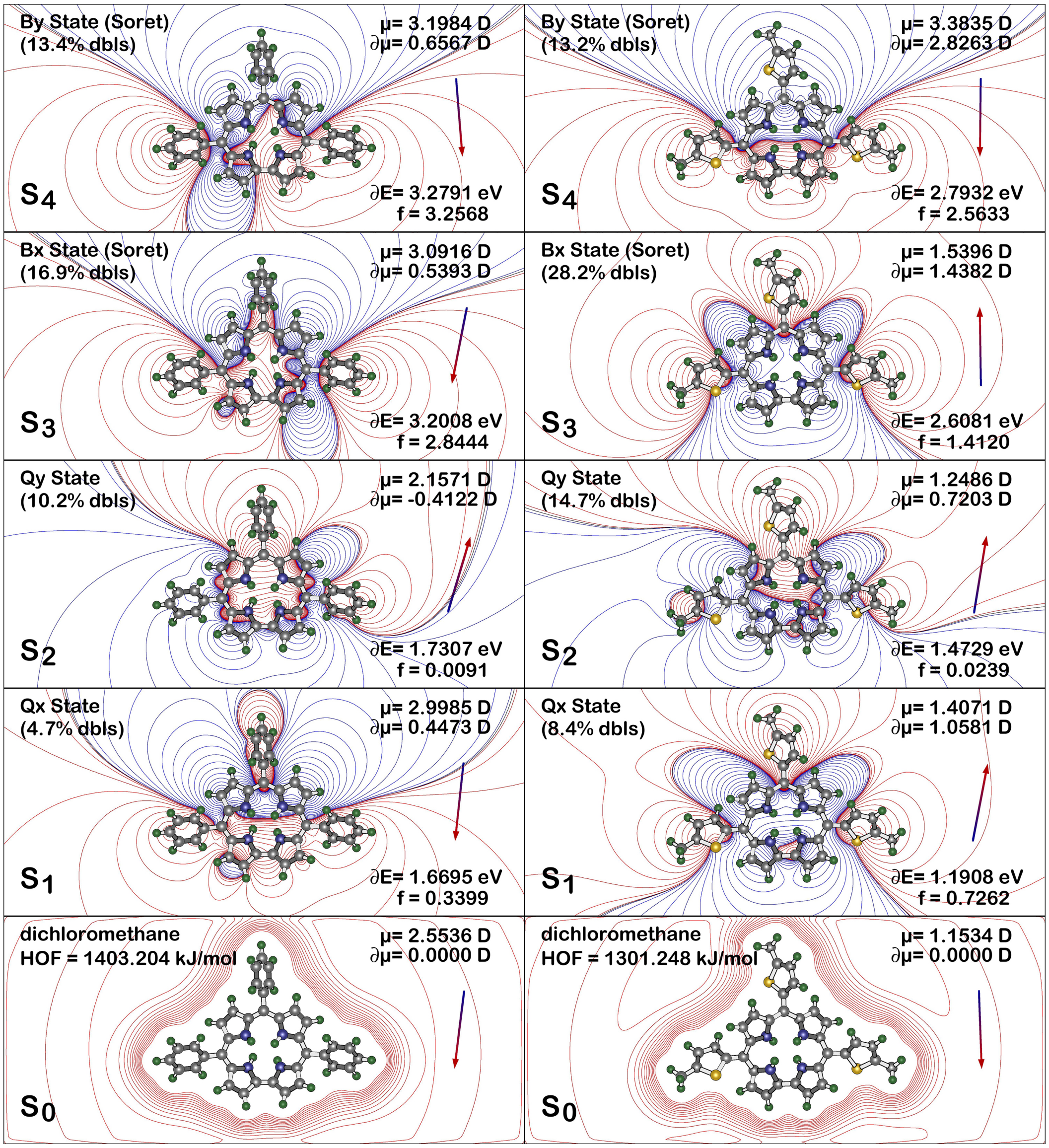

Figure 4.5. Comparison of the electrostatic properties of **[(Ph-Cor)H$_4$]$^+$** and **[(S-Cor)H$_4$]$^+$** in DCM based on SAC-CI methods. The ground state contours display the approximate electrostatic field surrounding the molecule where red contours indicate regions of excess positive charge and blue contours indicate regions of excess negative charge. The contours associated with the excited states (S$_1$, S$_2$, S$_3$ and S$_4$) represent the shift in charge induced by excitation into these states where red contours indicate increased positive charge and blue contours indicate increased negative charge following excitation. The arrows display the dipole moment direction, and the transition energies (δE in electron volts relative to uncorrelated ground state), oscillator strengths (f) and dipole moments (μ in Debye) are shown at the upper right of each panel. The contribution of doubly excited configurations (dbls) is shown as a percentage at upper left of each excited state.

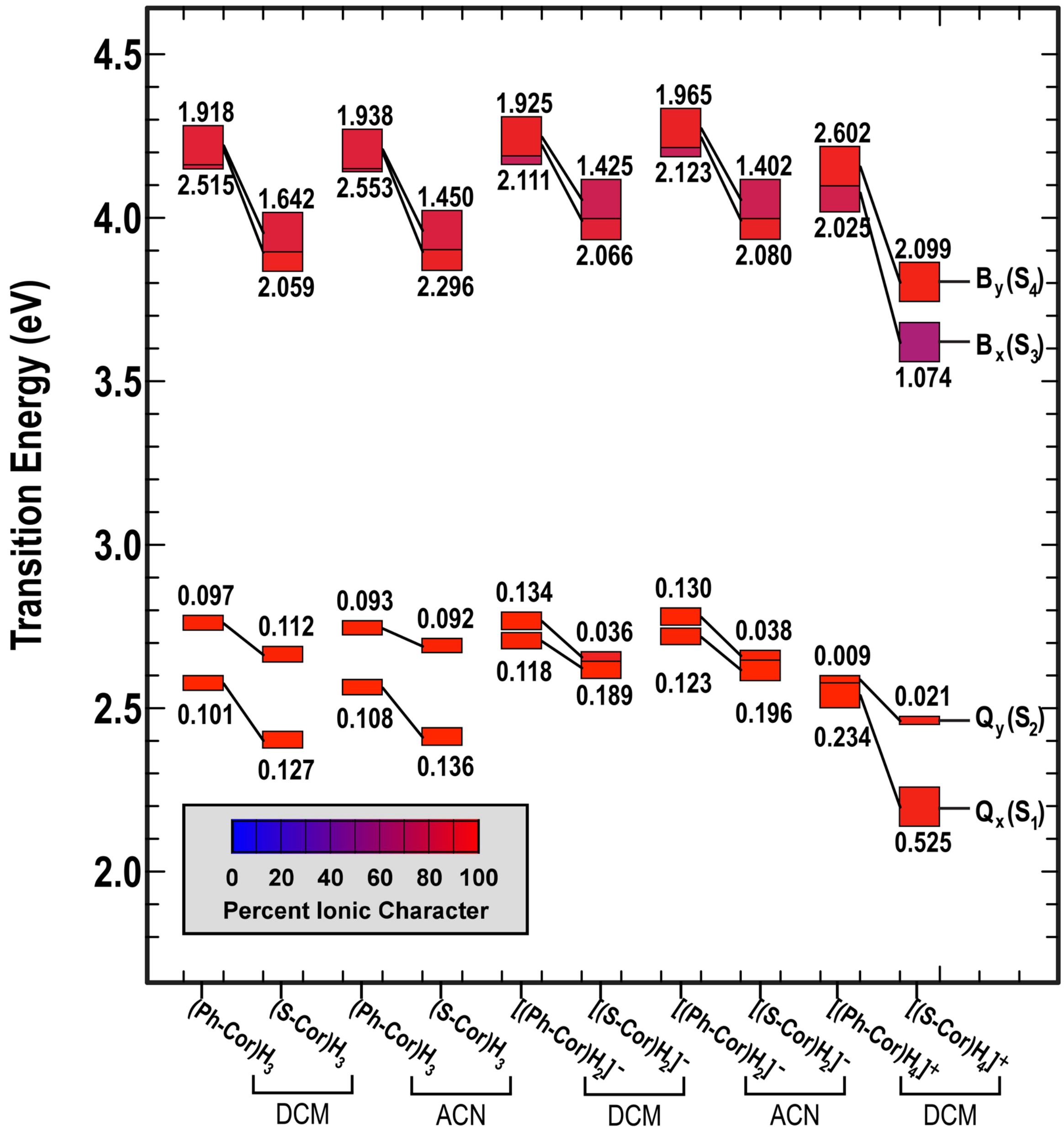

Figure 4.6. Excited singlet state level ordering of the first 4 excited states of **(Ph-Cor)H$_3$** and **(S-Cor)H$_3$** in the neutral, anionic, and cationic states, in DCM and ACN, as calculated using EOM-CCSD methods. The oscillator strengths are given directly above or below each state rectangle, and the thickness of the rectangles are proportional to this value. The ionic versus covalent character of each state follows the colorimetric scheme shown at the lower left.

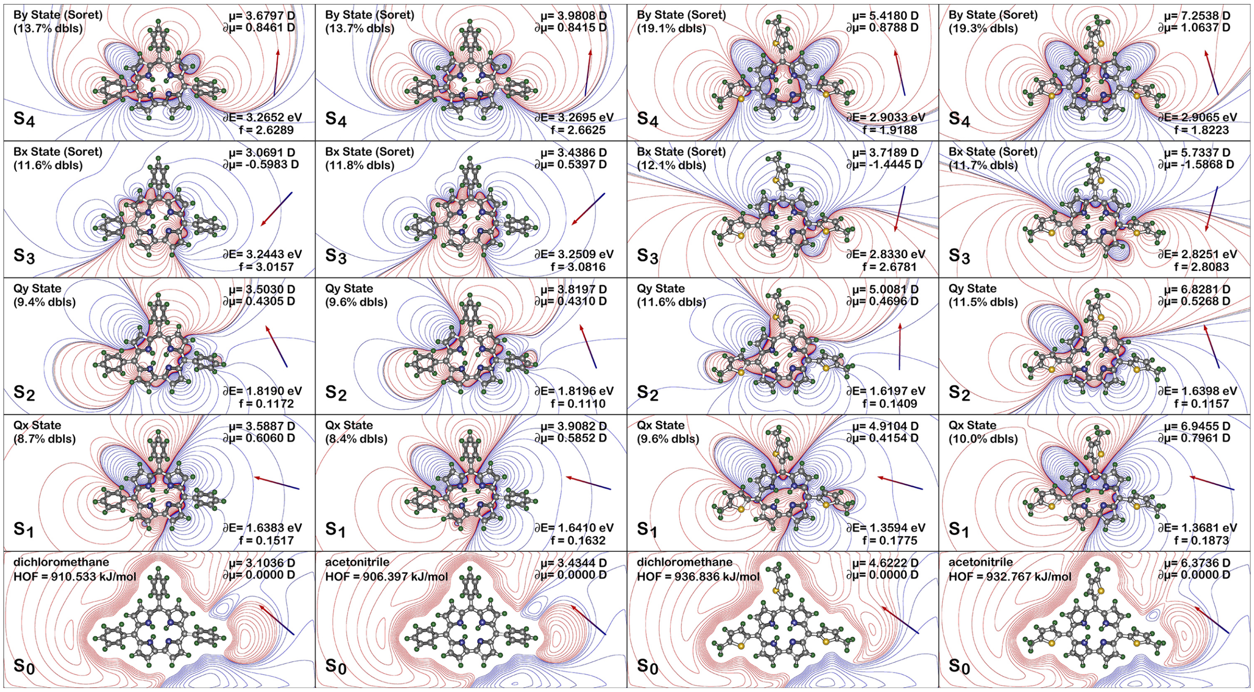

Figure 4.7. Electrostatic properties of the ground state (S_0) and the charge shifts induced by excitation into the first four excited singlet states for **(Ph-Cor)H$_3$** and **(S-Cor)H$_3$** in DCM and in ACN based on SAC-CI methods. The two left panels and the two right panels illustrate **(Ph-Cor)H$_3$** and **(S-Cor)H$_3$**, respectively, with the solvents labeled within each panel. The contours and characteristics are as shown in Figure 4.5.

containing molecules have lower transition energies than the phenyl analogue, however, the transition energies are similar when comparing each molecule in non-polar and polar solvents. These results are consistent with a recent study using Time-Dependent Density Functional Theory (TD-DFT), which also predicted that there is little solvatochromism for the $\pi^* \leftarrow \pi$ transitions for triarylcorroles.[17] Acetonitrile enhances the transition dipole moments of the molecules, with a much greater effect observed for **(S-Cor)H$_3$** than the triphenyl derivative. Furthermore, both molecules are energetically stabilized in ACN (Table 4.2) (for conformers with high dipole moments). However, predictions suggest little solvent effect on the photochemistry of the neutral molecules.

Although the excited state calculations indicate little solvatochromism, the experimental data in Figure 4.2 paint a different picture, particularly for **(Ph-Cor)H$_3$**. The absorption spectrum of **(Ph-Cor)H$_3$** in ACN contains a strongly absorbing peak at 639 nm, which is not observed in DCM. We suggest that the formation of the anionic species **[(Ph-Cor)H$_2$]$^-$** is the source of the observed solvatochromic shift.[26] **[(Ph-Cor)H$_2$]$^-$** is more planar in ACN than **[(S-Cor)H$_2$]$^-$**, thus making the phenyl-containing corrole more acidic (i.e., more likely to deprotonate).

Figure 4.8 presents a collection of SAC-CI excited state analyses, in which the transition energies, transition dipole moments, and relative electrostatic characteristics are tabulated for the mono-anionic species in both DCM and ACN. In addition to the HOF analysis in the discussion above (Table 4.2), the transition energies of **[(Ph-Cor)H$_2$]$^-$** in ACN are generally lower than the transition energies observed for **(Ph-Cor)H$_3$** in the same solvent. On the other hand, the opposite is true of **[(S-Cor)H$_2$]$^-$** and **(S-Cor)H$_3$** in ACN, where the transition energies are roughly equivalent or lower for the neutral molecule. This provides further evidence that the solvent and electronic nature of **(Ph-Cor)H$_3$** make this corrole derivative more acidic than **(S-Cor)H$_3$** in the

same solvent, and that the apparent solvatochromism results from apparent deprotonation events.[26]

The theoretical mono-cationic data is consistent with empirical observations (see Figures 4.2 and 4.6). While the Q_x band of **$[(Ph\text{-}Cor)H_4]^+$** is characterized by a relatively high oscillator strength (f = 0.234), **$[(S\text{-}Cor)H_4]^+$** exhibits a dramatically amplified oscillator strength (f = 0.525). Additionally, the Soret bands of **$[(S\text{-}Cor)H_4]^+$** stray from all other experimental observations for the triarylcorroles, in which the S_3 transition is much lower in oscillator strength (f = 1.074) and contains significantly less ionic character. These optical effects have much to do with the loss of planarity and the accommodation of π-overlap, thereby enhancing the electronic interaction between the thienyl groups and macrocycle. The loss of ionic character is linked to the degeneration of the pseudoparity of the molecular orbitals along the macrocycle, which has already significantly diminished when going from the porphyrin parent compounds to the corrole structure.[113] This loss of alternancy symmetry is intensified by the molecular structure of the mono-cation and has severe optical consequences. The S_3 transition, specifically, is characterized by large doubly excited configurational character (Figures 4.8 and 4.9), which suggests that this state is more covalent in nature and has less charge separation of the molecular orbitals. Moreover, the SAC-CI analysis in Figure 4.5 indicates that **$[(S\text{-}Cor)H_4]^+$** has diminished transition dipole moments relative to all other molecules in this investigation, which is further evidence of decreased ionic character of the molecule.

In order to determine the source of the unique spectroscopic properties that are observed and predicted for **$(S\text{-}Cor)H_3$**, the configurational character of the triarylcorroles must be considered. Ziegler *et al*. have recently studied free-base triarylcorroles by using TD-DFT and magnetic circular dichroism (MCD) to examine the optical properties and solvatochromic

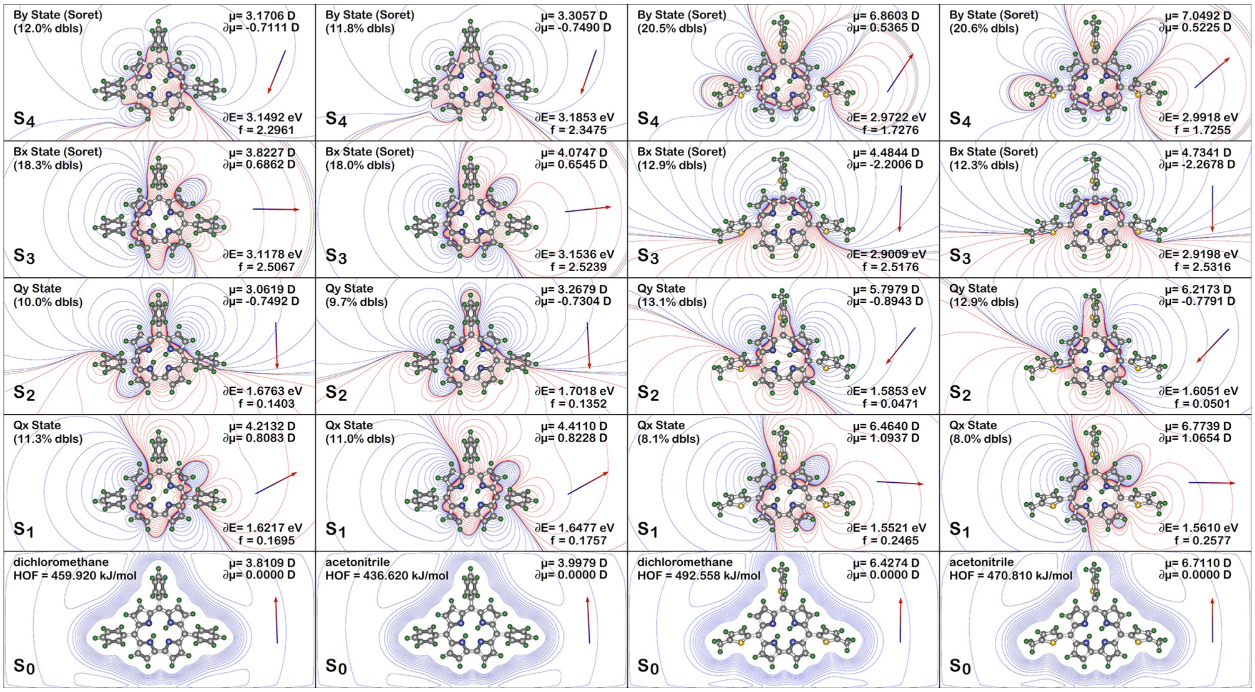

Figure 4.8. Comparison of the electrostatic properties of **[(Ph-Cor)H$_2$]$^-$** and **[(S-Cor)H$_2$]$^-$** in DCM and ACN. The contours and characteristics are as shown in Figure 4.5.

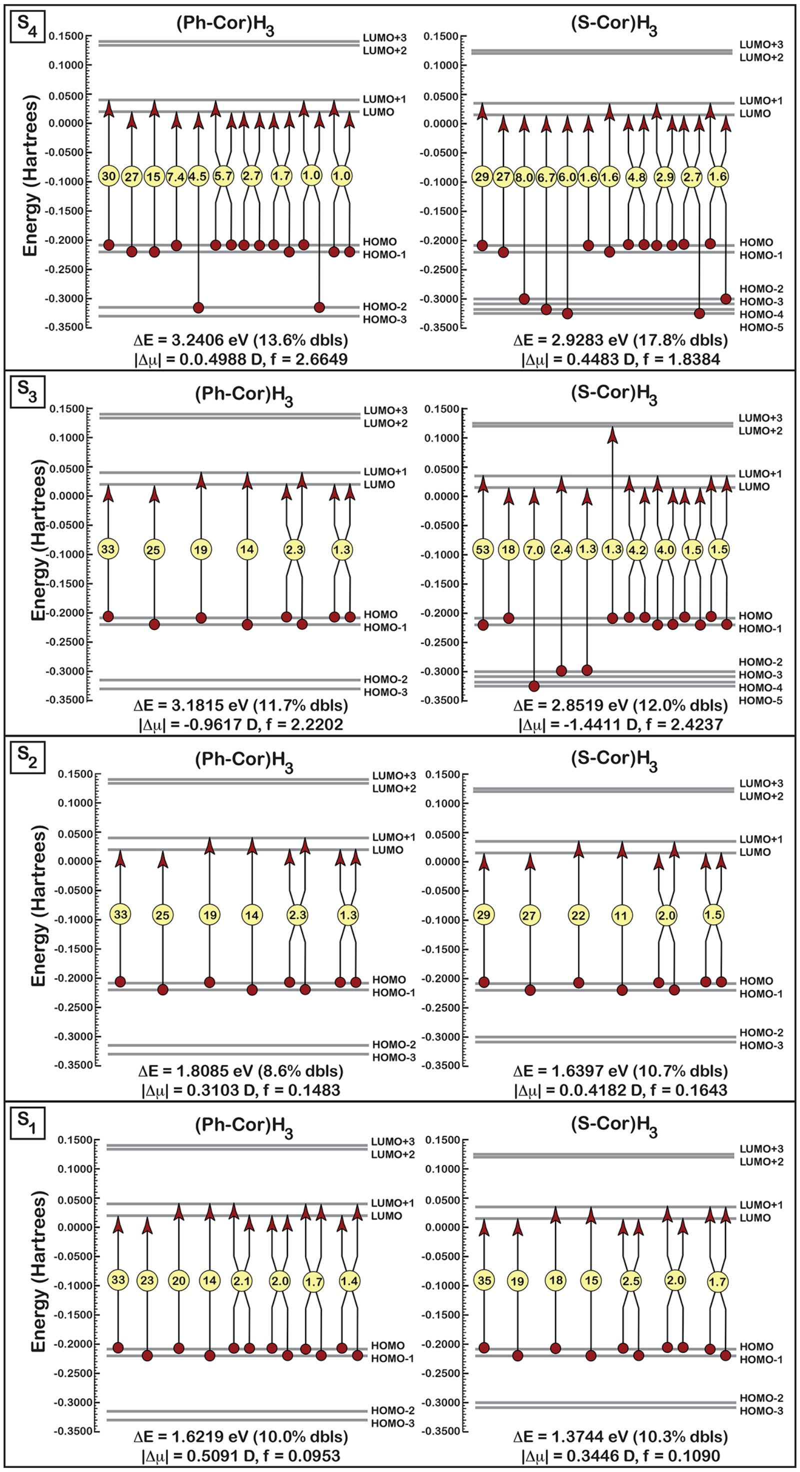

Figure 4.9. Configurational analysis of the four lowest-lying excited singlet states of **(Ph-Cor)H$_3$** and **(S-Cor)H$_3$** based on SAC-CI molecular orbital theory. Each excited state is described as a linear combination of single or double excitations, with the percent contribution of each configuration shown in the yellow circles. Only configurations contributing 1% or more are shown. Doubly excited configurations have two source (circles) and destination (arrows) symbols.

effects.[17] This study has found a rare relationship within the π and π^* molecular orbitals (MOs) of the free-base corrole core, in which there is a larger energy difference between LUMO and LUMO+1 π^* MOs (ΔLUMO) compared to HOMO and HOMO-1 π MOs (ΔHOMO). This scheme is opposite that of Gouterman's four orbital model of porphyrins.[114] Figure 4.9 depicts the configurational properties of the first four excited states of **(Ph-Cor)H$_3$** and **(S-Cor)H$_3$**, as predicted by SAC-CI MO theory. The ΔHOMO < ΔLUMO relationship is confirmed in using this model, however, analysis of the configurational character of the two molecules reveal a higher complexity over simple porphyrins.

The four orbital model works generally well with these molecules, however, there is significant mixing between the energy levels and a large contribution from double excitations. The configurational description of the Q band region for **(Ph-Cor)H$_3$** and **(S-Cor)H$_3$** are surprisingly similar. The character of the Soret bands of **(S-Cor)H$_3$** differ more significantly compared to **(Ph-Cor)H$_3$**. The thienyl-substituted molecule has a large degree of mixing and doubly excited character in the Soret region, and an even larger deviation from the four orbital model. The MO configurations of **(S-Cor)H$_3$**, as well as the enhanced π-overlap of the substituents, indicate a complex electronic structure that is subject to unique chromatic shifts and sensitivities to acidic and basic solvent environments.

4.4. Conclusions

The photophysical properties of free-base *meso*-trithienylcorroles were investigated in direct comparison to *meso*-triphenylcorroles, which have a broad history of investigations throughout the literature. The origin of the unique electronic characteristics of the trithienylcorrole were described using a combinational approach of spectroscopic and theoretical

methodologies. This work complements a number of other reports that elucidated other aspects of the electronic structure of *meso*-arylcorroles and the much increased electronic cross-talk between the *meso*-substituents and the chromophore when compared to *meso*-arylporphyrins. This study is the first to implement EOM-CCSD and SAC-CI excited state calculations. The ground state and excited state calculations generally support experimental findings, wherein the trithienylcorroles posses red-shifted optical spectra compared to the corresponding triphenylcorroles, irrespective of whether they are in the neutral, deprotonated, or protonated states. Theoretical approaches by using PES scans were incorporated into a series of ground state minimizations, in an attempt to delineate reasonable global energy minima for molecules that are highly flexible, rotationally variable, and sensitive to solvent environments. Solvatochromic behavior is rationalized based on conformational and dipole effects, although it was found that the formation of the mono-anionic molecules are energetically favorable and likely explain the dramatic shifts in the optical spectra. At the same charge state, it was found that **(S-Cor)H$_3$** adopts a more non-planar conformation than **(Ph-Cor)H$_3$**, thus allowing a larger degree of co-planarity and electronic interaction of the thienyl groups with the corrole chromophore. The key differences in the configurational character of the two molecules of interest were also explained. The experimental differences can be rationalized once this data is coupled with the relative MO energies and the structural characteristics described above. The complex nature of the configurational character of the Soret bands and the large degree of mixing also provide insight into the unique optical effects observed of **(S-Cor)H$_3$** in this investigation.

In conclusion, thienylcorroles are interesting corrole derivatives in that the thienyl groups have a profound effect on the electronic properties of the chromophore. The reactivity of the thiophene moiety presumably allows the thienylcorroles, like its porphyrin congeners, to be

incorporated into conducting polymer networks but that might benefit from the tight coupling of the *meso*-substituents with the corrole chromophore. We look forward to the ongoing developments in this and related fields.

4.5. References

(1) Battersby, A. R. Tetrapyrroles: The Pigments of Life. *Nat. Prod. Rep.* **2000**, *17*, 507-526.

(2) Toganoh, M.; Furuta, H. Synthesis and Metal Coordination of N-Confused and *N*-Fused Porphyrinoids. In *Handbook of Porphyrin Science*; Kadish, K. M., Smith, K. M., Guilard, R., Eds.; World Scientific: Singapore, 2010; Vol. 2, pp 295-367.

(3) Lash, T. D. Carbaporphyrins and Related Systems. Synthesis, Characterization, Reactivity and Insights into Porphyrinoid Aromaticity. In *Handbook of Porphyrin Science*; Kadish, K. M., Smith, K. M., Guilard, R., Eds.; World Scientific: Singapore, 2010; Vol. 16, pp 1–330.

(4) Kadish, K. M.; Smith, K. M.; Guilard, R.*The Porphyrin Handbook, Vol. 2 - Heteroporphyrins, Expanded Porphyrins and Related Macrocycles*; Academic Press: San Diego, 2000; Vol. 2.

(5) Fox, S.; Boyle, R. W. Synthetic Routes to Porphyrins Bearing Fused Rings. *Tetrahedron* **2006**, *62*, 10039-10054.

(6) Gupta, I.; Ravikanth, M. Recent Developments in Heteroporphyrins and their Analogues. *Coord. Chem. Rev.* **2006**, *250*, 468-518.

(7) Stepien, M.; Latos-Grazynski, L. Benziporphyrins: Exploring Arene Chemistry in a Macrocyclic Environment. *Acc. Chem. Res.* **2005**, *38*, 88-98.

(8) Stepien, M.; Latos-Grazynski, L. Aromaticity and Tautomerism in Porphyrins and Porphyrinoids. *Top. Heterocycl. Chem.* **2009**, *19*, 83-153.

(9) Pawlicki, M.; Latos-Grazynski, L. Carbaporphyrinoids – Synthesis and Coordination Properties In *Handbook of Porphyrin Science*; Kadish, K. M., Smith, K. M., Guilard, R., Eds.; World Scientific: Singapore, 2010; Vol. 2, pp 103-192.

(10) Aviv-Harel, I.; Gross, Z. Aura of Corroles. *Chem. Eur. J.* **2009**, *15*, 8382-8394.

(11) Gross, Z.; Galili, N.; Saltsman, I. The First Directed Synthesis of Corroles from Pyrrole. *Angew. Chem. Int. Ed. Engl.* **1999**, *38*, 1427-1429.

(12) Gross, Z.; Galili, N.; Simkhovich, L.; Saltsman, I.; Botoshansky, M.; Bläser, D.; Boese, R.; Goldberg, I. Solvent-Free Condensation of Pyrrole and Pentafluorobenzaldehyde: A Novel Synthetic Pathway to Corrole and Oligopyrromethenes. *Org. Lett.* **1999**, *1*, 599-602.

(13) Gryko, D. T. Recent Advances in the Synthesis of Corroles and Core-Modified Corroles. *Eur. J. Org. Chem.* **2002**, 1735-1743.

(14) Gryko, D. T.; Fox, J. P.; Goldberg, D. P. Recent Advances in the Chemistry of Corroles and Core-Modified Corroles. *J. Porphyrins Phthalocyanines* **2004**, *8*, 1091-1105.

(15) Nardis, S.; Monti, D.; Paolesse, R. Novel Aspects of Corrole Chemistry. *Mini-Rev. Org. Chem.* **2005**, *2*, 355-374.

(16) Gryko, D. T. Adventures in the Synthesis of *meso*-Substituted Corroles. *J. Porphyrins Phthalocyanines* **2008**, *12*, 906−917.

(17) Ziegler, C. J.; Sabin, J.; Geier III, G. R.; Nemykin, V. N. The First TDDFT and MCD Studies of Free Base Triarylcorroles: A Closer Look into Solvent-Dependent UV-Visible Absorption. *Chem. Commun.* **2012**, *48*, 4743-4745.

(18) Alemayehu, A.; Conradie, J.; Ghosh, A. A First TDDFT Study of Metallocorrole Electronic Spectra: Copper *meso*-Triarylcorroles Exhibit Hyper Spectra. *Eur. J. Inorg. Chem.* **2011**, *2011*, 1857-1864.

(19) Ghosh, A.; Steene, E. High-Valent Transition Metal Centers and Noninnocent Ligands in Metalloporphyrins and Related Molecules: A Broad Overview Based on Quantum Chemical Calculations. *J. Biol. Inorg. Chem.* **2001**, *6*, 740-751.

(20) Rovira, C.; Kunc, K.; Hutter, J.; Parrinello, M. Structural and Electronic Properties of Co-Corrole, Co-Corrin, and Co-Porphyrin. *Inorg. Chem.* **2001**, *40*, 11-17.

(21) Steene, E.; Wondimagegn, T.; Ghosh, A. Resonance Raman Spectroscopy and Density Functional Theoretical Calculations of Manganese Corroles. A Parallelism Between High-Valent Metallocorroles and Metalloporphyrins, Relevant to Horseradish Peroxidase and Chloroperoxidase Compound I and II Intermediates. *J. Inorg. Biochem.* **2002**, *88*, 113-118.

(22) Wasbotten, I. H.; Wondimagegn, T.; Ghosh, A. Electronic Absorption, Resonance Raman, and Electrochemnical Studies of Planar and Saddled Copper(III) *meso*-Triarylcorroles. Highly Substituent-Sensitive Soret Bands as a Distinctive Feature of High-Valent Transition Metal Corroles. *J. Am. Chem. Soc.* **2002**, *124*, 8104-8116.

(23) Mahammed, A.; Weaver, J. J.; Gray, H. B.; Abdelas, M.; Gross, Z. How Acidic are Corroles and Why? *Tetrahedron Lett.* **2003**, *44*, 2077-2079.

(24) Ghosh, A.; Wondimagegn, T.; Parusel, B. J. Electronic Structure of Gallium, Copper, and Nickel Complexes of Corrole. High-Valent Transition Metal Centers Versus Noninnocent Ligands. *J. Am. Chem. Soc.* **2000**, *122*, 5100-5104.

(25) Ivanova, Y. B.; Savva, V. A.; Mamardashvili, N. Z.; Starukhin, A. S.; Ngo, T. H.; Dehaen, W.; Maes, W.; Kruk, M. M. Corrole NH Tautomers: Spectral Features and Individual Protonation. *J. Phys. Chem. A* **2012**, *116*, 10683-10694.

(26) Kruk, M.; Ngo, T. H.; Savva, V.; Starukhin, A.; Dehaen, W.; Maes, W. Solvent-Dependent Deprotonation of *meso*-Pyrimidinylcorroles: Absorption and Fluorescence Studies. *J. Phys. Chem. A* **2012**, *116*, 10704-10711.

(27) Kruk, M.; Ngo, T. H.; Verstappen, P.; Starukhin, A.; Hofkens, J.; Dehaen, W.; Maes, W. Unraveling the Fluorescence Features of Individual Corrole NH Tautomers. *J. Phys. Chem. A* **2012**, *116*, 10695-10703.

(28) Ding, T.; Alemán, E. A.; Modarelli, D. A.; Ziegler, C. J. Photophysical Properties of a Series of Free-Base Corroles. *J. Phys. Chem. A* **2005**, *109*, 7411-7417.

(29) Wagnert, L.; Berg, A.; Stavitski, E.; Berthold, T.; Kothe, G.; Goldberg, I.; Mahammed, A.; Simkhovich, L.; Gross, Z.; Levanon, H. Exploring the Photoexcited Triplet States of Aluminum and Tin Corroles by Time-Resolved Q-Band EPR. *Appl. Magn. Reson.* **2006**, *30*, 591-604.

(30) Rozenshtein, V.; Wagnert, L.; Berg, A.; Stavitski, E.; Berthold, T.; Kothe, G.; Saltsman, I.; Gross, Z.; Levanon, H. Probing the Photoexcited States of Rhodium Corroles by Time-Resolved Q-Band EPR. Observation of Strong Spin-Orbit Coupling Effects. *J. Phys. Chem. A* **2008**, *112*, 5338-5343.

(31) Wagnert, L.; Berg, A.; Saltsman, I.; Gross, Z.; Rozenshtein, V. Time-Resolved Electron Paramagnetic Resonance Study of Rhodium(III) Corrole Excited States. *J. Phys. Chem. A* **2010**, *114*, 2059-2072.

(32) Wagnert, L.; Rubin, R.; Berg, A.; Mahammed, A.; Gross, Z.; Levanon, H. Photoexcited Triplet State Properties of Brominated and Nonbrominated Ga(III)-Corroles as Studied by Time-Resolved Electron Paramagnetic Resonance. *J. Phys. Chem. B* **2010**, *114*, 14303-14308.

(33) Tanabe, M.; Matsuoka, H.; Ohba, Y.; Yamauchi, S.; Sugisaki, K.; Toyota, K.; Sato, K.; Takui, T.; Goldberg, I.; Saltsman, I.; Gross, Z. Time-Resolved Electron Paramagnetic Resonance and Phosphorescence Studies of the Lowest Excited Triplet States of Rh(III) Corrole Complexes. *J. Phys. Chem. A* **2012**, *116*, 9662-9673.

(34) Yang, Y.; Jones, D.; von, H. T.; Linke, M.; Wagnert, L.; Berg, A.; Levanon, H.; Zacarias, A.; Mahammed, A.; Gross, Z.; Heyne, K. Assignment of Aluminum Corroles Absorption Bands to Electronic Transitions by Femtosecond Polarization Resolved VIS-Pump IR-Probe Spectroscopy. *J. Phys. Chem. A* **2012**, *116*, 1023-1029.

(35) Brückner, C. The Silver Complexes of Porphyrins, Corroles and Carbaporphyrins: Silver in the Oxidation States +II and +III. *J. Chem. Educ.* **2004**, *81*, 1665-1670.

(36) Gross, Z.; Gray, H. B. How Do Corroles Stabilize High Valent Metals? *Comments Inorg. Chem.* **2006**, *27*, 61-72.

(37) McGown, A. J.; Badiei, Y. M.; Leeladee, P.; Prokop, K. A.; DeBeer, S.; Goldberg, D. P. Synthesis and Reactivity of High-Valent Transition Metal Corroles and Corrolazines. In *Handbook of Porphyrin Science*; Kadish, K. M., Smith, K. M., Guilard, R., Eds.; World Scientific Publishing: Singapore, 2011; Vol. 14, pp 525-599.

(38) Gross, Z.; Golubkov, G.; Simkhovich, L. Epoxidation Catalysis by a Manganese Corrole and Isolation of an Oxomanganese(V) Corrole. *Angew. Chem., Int. Ed.* **2000**, *39*, 4045-4047.

(39) Simkhovich, L.; Mahammed, A.; Goldberg, I.; Gross, Z. Synthesis and Characterization of Germanium, Tin, Phosphorus, Iron, and Rhodium Complexes of Tris(pentafluorophenyl)corrole, and the Utilization of the Iron and Rhodium Corroles as Cyclopropanation Catalysts. *Chem. Eur. J.* **2001**, *7*, 1041-1055.

(40) Aviv, I.; Gross, Z. Iron Corroles and Porphyrins as Very Efficient and Highly Selective Catalysts for the Reactions of α-Diazo Esters with Amines. *Synlett* **2006**, 951-953.

(41) Mahammed, A.; Gross, Z. Iron and Manganese Corroles are Potent Catalysts for the Decomposition of Peroxynitrite. *Angew. Chem., Int. Ed.* **2006**, *45*, 6544-6547.

(42) Eckshtain, M.; Zilbermann, I.; Mahammed, A.; Saltsman, I.; Okun, Z.; Maimon, E.; Cohen, H.; Meyerstein, D.; Gross, Z. Superoxide Dismutase Activity of Corrole Metal Complexes. *Dalton Trans.* **2009**, 7879-7882.

(43) Kumar, A.; Goldberg, I.; Botoshansky, M.; Buchman, Y.; Gross, Z. Oxygen Atom Transfer Reactions from Isolated (Oxo)Manganese(V) Corroles to Sulfides. *J. Am. Chem. Soc.* **2010**, *132*, 15233-15245.

(44) Schechter, A.; Stanevsky, M.; Mahammed, A.; Gross, Z. Four-Electron Oxygen Reduction by Brominated Cobalt Corrole. *Inorg. Chem.* **2012**, *51*, 22-24.

(45) Aviv, I.; Gross, Z. Corrole-Based Applications. *Chem. Commun.* **2007**, 1987-1999.

(46) Aviv-Harel, I.; Gross, Z. Coordination Chemistry of Corroles with Focus on Main Group Elements. *Coord. Chem. Rev.* **2011**, *255*, 717-736.

(47) Walker, D.; Chappel, S.; Mahammed, A.; Brunschwig, B. S.; Winkler, J. R.; Gray, H. B.; Zaban, A.; Gross, Z. Corrole-Sensitized TiO_2 Solar Cells. *J. Porphyrins Phthalocyanines* **2006**, *10*, 1259-1262.

(48) Kim, K.; Kim, I.; Maiti, N.; Kwon, S. J.; Bucella, D.; Egorova, O. A.; Lee, Y. S.; Kwak, J.; Churchill, D. G. A Study of Nerve Agent Model Organophosphonate Binding with Manganese-A_2B-Corrole and -A_2B_2-Porphyrin Systems. *Polyhedron* **2009**, *28*, 2418-2430.

(49) Aviezer, D.; Cotton, S.; David, M.; Segev, A.; Khaselev, N.; Galili, N.; Gross, Z.; Yayon, A. Porphyrin Analogues as Novel Antagonists of Fibroblast Growth Factor and Vascular Endothelial Growth Factor Receptor Binding that Inhibit Endothelial Cell Proliferation, Tumor Progression, and Metastasis. *Cancer Res.* **2000**, *60*, 2973-2980.

(50) Wang, Y.; Akhigbe, A.; Ding, Y.; Brückner, C.; Lei, Y. *meso*-Tritolylcorrole-Functionalized Single-Walled Carbon Nanotube Donor-Accepter Nanocomposites for NO_2 Gas Detection. *Electroanalysis* **2012**, *24*, 1348–1355.

(51) Haber, A.; Aviram, M.; Gross, Z. Protecting the Beneficial Functionality of Lipoproteins by 1-Fe, a Corrole-Based Catalytic Antioxidant. *Chem. Sci.* **2011**, *2*, 295-302.

(52) Hwang, J. Y.; Wachsmann-Hogiu, S.; Ramanujan, V. K.; Ljubimova, J.; Gross, Z.; Gray, H. B.; Medina-Kauwe, L. K.; Farkas, D. L. A Multimode Optical Imaging System for Preclinical Applications In Vivo: Technology Development, Multiscale Imaging, and Chemotherapy Assessment. *Mol. Imaging Biol.* **2012**, *14*, 431-442.

(53) Lim, P.; Mahammed, A.; Okun, Z.; Saltsman, I.; Gross, Z.; Gray, H. B.; Termini, J. Differential Cytostatic and Cytotoxic Action of Metallocorroles Against Human Cancer Cells: Potential Platforms for Anticancer Drug Development. *Chem. Res. Toxicol.* **2012**, *25*, 400-409.

(54) Haber, A.; Angel, I.; Mahammed, A.; Gross, Z. Combating Diabetes Complications by 1-Fe, a Corrole-Based Catalytic Antioxidant. *J. Diabetes Complications* **2013**, *27*, 316-321.

(55) Ojadi, E. C. A.; Linschitz, H.; Gouterman, M.; Walter, R. I.; Lindsey, J. S.; Wagner, R. W.; Droupadi, P. R.; Wang, W. Sequential Protonation of *meso*-[*p*-(dimethylamino)phenyl]porphyrins: Charge-Transfer Excited States Producing Hyperporphyrins. *J. Phys. Chem.* **1993**, *97*, 13192-13197.

(56) Vitasovic, M.; Gouterman, M.; Linschitz, H. Calculations on the Origin of Hyperporphyrin Spectra in Sequentially Protonated *meso*-(dimethylaminophenyl) Porphyrins. *J. Porphyrins Phthalocyanines* **2001**, *5*, 191-197.

(57) Thomas, D. W.; Martell, A. E. Absorption Spectra of *para*-Substituted Tetraphenylporphines. *J. Am. Chem. Soc.* **1956**, *78*, 1338-1343.

(58) Senge, M. O. Database of Tetrapyrrole Crystal Structure Determinations. In *Porphyrin Handbook*; Kadish, K. M., Smith, K. M., Guilard, R., Eds.; Academic Press: San Diego, CA, USA, 2000; Vol. 10, pp 1-218.

(59) Brückner, C.; Foss, P. C. D.; Sullivan, J. O.; Pelto, R.; Zeller, M.; Birge, R. R.; Crundwell, G. Origin of the Bathochromically Shifted Optical Spectra of *meso*-Tetrathien-2- and 3-ylporphyrins as Compared to *meso*-Tetraphenylporphyrin *Phys. Chem. Chem. Phys* **2006**, *8*, 2402 - 2412.

(60) Ono, N.; Miyagawa, H.; Ueta, T.; Ogawa, T.; Tani, H. Synthesis of 3,4-Diarylpyrroles and Conversion into Dodecaarylporphyrins; A New Approach to Porphyrins with Altered Redox Potentials. *J. Chem. Soc., Perkin Trans.* **1998**, *1*, 1595-1601.

(61) Gupta, I.; Hung, C.-H.; Ravikanth, M. Synthesis and Structural Characterization of *meso*-Thienyl Core-Modified Porphyrins. *Eur. J. Org. Chem.* **2003**, 4392-4400.

(62) Shi, D.-F.; Wheelhouse, R. T. A Novel, High-Yielding Synthesis of *meso*-Substituted Porphyrins Via the Direct Arylation of Porphine. *Tetrahedron Lett.* **2002**, *43*, 9341-9342.

(63) Bhyrappa, P.; Bhavana, P. *Meso*-Tetrathienylporphyrins: Electrochemical and Axial Ligation Properties. *Chem. Phys. Lett.* **2001**, *349*, 399-404.

(64) Odobel, F.; Suresh, S.; Blart, E.; Nicolas, Y.; Quintard, J.-P.; Janvier, P.; Le Questel, J.-Y.; Illien, B.; Rondeau, D.; Richomme, P.; Häupl, T.; Wallin, S.; Hammarström, L. Synthesis of Oligothiophene-Bridged Bisporphyrins and Study of the Linkage Dependence of the Electronic Coupling. *Chem. Eur. J.* **2002**, *8*, 3027-3046.

(65) Medforth, C. J.; Haddad, R. E.; Muzzi, C. M.; Dooley, N. R.; Jaquinod, L.; Shyr, D. C.; Nurco, D. J.; Olmstead, M. M.; Smith, K. M.; Ma, J.-G.; Shelnutt, J. A. Unusual Aryl-Porphyrin Rotational Barriers in Peripherally Crowded Porphyrins. *Inorg. Chem.* **2003**, *42*, 2227-2241.

(66) Shimidzu, T.; Segawa, H.; Wu, F.; Nakayama, N. Approaches to Conducting Polymer Devices with Nanostructures: Photoelectrochemical Function of One-Dimensional and Two-Dimensional Porphyrin Polymers with Oligothienyl Molecular Wire. *J. Photochem. Photobiol. A* **1995**, *92*, 121-127.

(67) Collis, G. E.; Campbell, W. M.; Officer, D. L.; Burrell, A. K. The Design and Synthesis of Porphyrin/Oligothiophene Hybrid Monomers. *Org. Biomol. Chem.* **2005**, *3*, 2075-2084.

(68) Vollmer, M. S.; Würthner, F.; Effenberger, F.; Emele, P.; Meyer, D. U.; Stümpfig, T.; Port, H.; Wolf, H. C. Anthyloligothienylporphyirns: Energy Transfer and Light-Harvesting Systems. *Chem. Eur. J.* **1998**, *4*, 260-269.

(69) Friedlein, R.; Kieseritzky, F. v.; Braun, S.; Linde, C.; Osikowicz, W.; Hellberg, J.; Salaneck, W. R. Solution-Processed, Highly-Oriented Supramolecular Architectures of Functionalized Porphyrins with Extended Electronic States. *Chem. Comm.* **2005**, *15*, 1974-1976.

(70) Lau, K. S. F.; Zhao, S.; Ryppa, C.; Jockusch, S.; Turro, N. J.; Zeller, M.; Gouterman, M.; Khalil, G. E.; Brückner, C. Synthesis, Structure, and Optical Properties of the Platinum(II) Complexes of Indaphyrin and Thiaindaphyrin. *Inorg. Chem.* **2009**, *48*, 4067-4074.

(71) You, Y.; Gibson, S. L.; Hilf, R.; Ohulchanskyy, T. Y.; Detty, M. R. Core-Modified Porphyrins. Part 4: Steric Effects on Photophysical and Biological Properties In Vitro. *Bioorg. Med. Chem.* **2005**, *13*, 2235-2251.

(72) Li, G.; Bhosale, S.; Tao, S.; Guo, R.; Bhosale, S.; Li, F.; Zhang, Y.; Wang, T. Y.; Fuhrhop, J.-H. Very Stable, Highy Electroactive Polymers of Zinc(II)-5,15-Bisthienylphenyl Porphyrin Exhibiting Charge-Trapping Effects. *Polymer* **2005**, *46*, 5299-5307.

(73) Maruyama, H.; Segawa, H.; Sodota, S.; Sato, T.; Kosai, N.; Sagisaka, S.; Shimidzu, T.; Tanaka, K. Electrochemical Construction of Ultrathin Film Composed of Quasi Two-Dimensional Poprhyrin Polymers. *Synth. Met.* **1998**, *96*, 141-149.

(74) Chen, W.; Akhigbe, J.; Brückner, C.; Li, C. M.; Lei, Y. Electrocatalytic Four-Electron Reduction of Dioxygen by Electrochemically Deposited Poly{[*meso*-tetrakis(2-thienyl)porphyrinato]cobalt(II)}. *J. Phys. Chem. C* **2010**, *114*, 8633-8638.

(75) Chen, W.; Ding, Y.; Akhigbe, J.; Brückner, C.; Li, C. M.; Lei, Y. Enhanced Electrochemical Oxygen Reduction-Based Glucose Sensing Using Glucose Oxidase on Nanodendritic Poly[*meso*-tetrakis(2-thienyl)porphyrinato]cobalt(II)-SWNTs Composite Electrodes. *Biosens. Bioelectron.* **2010**, *26*, 504-510.

(76) Chen, W.; Wang, Y.; Brückner, C.; Li, C. M.; Lei, Y. Poly[*meso*-tetrakis(2-thienyl)porphyrin] for the Sensitive Electrochemical Detection of Explosives. *Sens. Actuators, B* **2010**, *147*, 191-197.

(77) Steene, E.; Wondimagegn, T.; Ghosh, A. Electrochemical and Electronic Absorption Spectroscopic Studies of Substituent Effects in Iron(IV) and Manganese(IV) Corroles. Do the Compounds Feature High-Valent Metal Centers or Noninnocent Corrole Ligands? Implications for Peroxidase Compound I and II Intermediates. *J. Phys. Chem. B* **2002**, *106*, 5312-5312.

(78) Gryko, D. T.; Piechota, K. E. Straightforward Route to Teans-A_2B-Corroles Bearing Substituents with Basic Nitrogen Atoms. *J. Porphyrins Phtalocyanines* **2002**, *6*, 81-97.

(79) Gryko, D. T.; Koszarna, B. Refined Methods for the Synthesis of *meso*-Substituted A_3- and *trans*-A_2B-Corroles. *Org. Biomol. Chem.* **2003**, *1*, 350-357.

(80) Maiti, N.; Lee, J.; Kwon, S. J.; Kwak, J.; Do, Y.; Churchill, D. G. Synthetic, Crystallographic and Electrochemical Studies of Thienyl-Substituted Corrole Complexes of Copper and Cobalt. *Polyhedron* **2006**, *25*, 1519-1530.

(81) Egorova, O. A.; Tsay, O. G.; Khatua, S.; Meka, B.; Maiti, N.; Kim, M.-K.; Kwon, S. J.; Huh, J. O.; Bucella, D.; Kang, S.-O.; Kwak, J.; Churchill, D. G. Synthetic, Cyclic Voltammetric, Structural, EPR, and UV-Vis Spectroscopic Studies of Thienyl-Containing *meso*-A_2B-Cor(Cr^V=O) Systems: Consideration of Three Interrelated Molecular Detection Modalities. *Inorg. Chem.* **2010**, *49*, 502-512.

(82) Maiti, N.; Lee, J.; Do, Y.; Shin, H. S.; Churchill, D. G. Synthesis and Structures of Thienyl-Substituted 5-Dipyrromethane Isomers. *J. Chem. Crystallogr.* **2005**, *35*, 949-955.

(83) Egorova, O. A.; Tsay, O. G.; Khatua, S.; Huh, J. O.; Churchill, D. G. A Chiral *meso*-ABC-Corrolatochromium(V) Complex. *Inorg. Chem.* **2009**, *48*, 4634-4636.

(84) Choi, S. H.; Pang, K.; Kim, K.; Churchill, D. G. Cu^{2+} Colorimetric Sensing and Fluorescence Enhancement and Hg^{2+} Fluorescence Diminution in "Scorpionate"-like Tetrathienyl-Substituted Boron-Dipyrrins. *Inorg. Chem.* **2007**, *46*, 10564-10577.

(85) Choi, S. H.; Kim, K.; Jeon, J.; Meka, B.; Bucella, D.; Pang, K.; Khatua, S.; Lee, J.; Churchill, D. G. Optical Effects of *s*-Oxidation and Mn^+ Binding in *meso*-Thienyl Dipyrrin Systems and of Stepwise Bromination of 4,4-difluoro-8-(2,5-dibromo-3-thienyl)-4-bora-3*a*,4*a*-diaza-*s*-indacene. *Inorg. Chem.* **2008**, *47*, 11071-11083.

(86) Kim, K.; Jo, C.; Easwaramoorthi, S.; Sung, J.; Kim, D. H.; Churchill, D. G. Crystallographic, Photophysical, NMR Spectroscopic and Reactivity Manifestations of the "8-Heteroaryl Effect" in 4,4-difluoro-8-(C_4H_3X)-4-bora-3*a*,4*a*-diaza-*s*-indacene (X = O, S, Se) (BODIPY) Systems. *Inorg. Chem.* **2010**, *49*, 4881-4894.

(87) Singh, A. P.; Lee, K. M.; Murale, D. P.; Jun, T.; Liew, H.; Suh, Y.-H.; Churchill, D. G. Novel Sulphur-Rich BODIPY Systems that Enable Stepwise Fluorescent O-Atom Turn-On and H_2O_2 Neuronal System Probing. *Chem. Commun.* **2012**, *48*, 7298-7300.

(88) Singh, A. P.; Murale, D. P.; Ha, Y.; Liew, H.; Lee, K. M.; Segev, A.; Suh, Y.-H.; Churchill, D. G. A Novel, Selective, and Extremely Responsive Thienyl-Based Dual Fluorogenic Probe for Tandem Superoxide and Hg^{2+} Chemosensing. *Dalton Trans.* **2013**, *42*, 3285-3290.

(89) Singh, A. P.; Tsay, O. G.; Murale, D. P.; Jun, T.; Liew, H.; Suh, Y.-H.; Churchill, D. G. Extremely Selective "Turn-On" Fluorescence Detection of Hypochlorite Confirmed by Proof-of-Principle Neurological Studies Via Esterase Action in Living Cells. *Analyst* **2013**, *138*, 2829-2832.

(90) Briñas, R. P.; Brückner, C. Triarylcorroles by Oxidative Coupling of Triaryltetrapyrranes. *Synlett* **2001**, *3*, 442-444.

(91) Becke, A. D. Density-Functional Thermochemistry. III. The Role of Exact Exchange. *J. Phys. Chem.* **1993**, *98*, 5648-5652.

(92) Frisch, M. J.; Trucks, G. W.; Schlegel, H. B.; Scuseria, G. E.; Robb, M. A.; Cheeseman, J. R.; Scalmani, G.; Barone, V.; Mennucci, B.; Petersson, G. A.; Nakatsuji, H.; Caricato, M.; Li, X.; Hratchian, H. P.; Izmaylov, A. F.; Bloino, J.; Zheng, G.; Sonnenberg, J. L.; Hada, M.; Ehara, M.; Kitao, O.; Nakai, H.; Vreven, T.; Montgomery, J., J. A.; Peralta, J. E.; Ogliaro, F.; Bearpark, M.; Heyd, J. J.; Brothers, E.; Kudin, K. N.; Staroverov, V. N.; Kobayashi, R.; Normand, J.; Raghavachari, K.; Rendell, A.; Burant, J. C.; Iyengar, S. S.; Tomasi, J.; Cossi, M.; Rega, N.; Millam, J. M.; Klene, M.; Knox, J. E.; Cross, J. B.; Bakken, V.; Adamo, C.; Jaramillo, J.; Gomperts, R.; Stratmann, R. E.; Yazyev, O.; Austin, A. J.; Cammi, R.; Pomelli, C.; Ochterski, J. W.; Martin, R. L.; Morokuma, K.; Zakrzewski, V. G.; Voth, G. A.; Salvador, P.; Dannenberg, J. J.; Dapprich, S.; Daniels, A. D.; Farkas, O.; Foresman, J. B.; Ortiz, J. V.; Cioslowski, J.; Fox, D. J.. *Gaussian 09*, revision D.01; Gaussian, Inc., Wallingford, CT, 2009.

(93) Barone, V.; Cossi, M.; Tomasi, J. Geometry Optimization of Molecular Structures in Solution by the Polarizable Continuum Model. *J. Comput. Chem.* **1998**, *19*, 404-417.

(94) Tomasi, J.; Mennucci, B.; Cammi, R. Quantum Mechanical Continuum Solvation Models. *Chem. Rev.* **2005**, *105*, 2999-3093.

(95) Clark, T.; Chandrasekhar, J.; Spitznagel, G. W.; Schleyer, P. V. R. Efficient Diffuse Function-Augmented Basis-Sets for Anion Calculations. 3. The 3-21+G Basis Set for 1st-Row Elements, LI-F. *J. Comput. Chem.* **1983**, *4*, 294-301.

(96) Stanton, J. F.; Bartlett, R. J. Equation of Motion Coupled-Cluster Method: A Systematic Biorthogonal Approach to Molecular Excitation Energies, Transition Probabilities, and Excited State Properties. *J. Chem. Phys.* **1993**, *98*, 7029-7039.

(97) Koch, H.; Kobayashi, R.; Sánchez de Merás, A.; Jørgensen, P. Calculation of Size-Intensive Transition Moments from the Coupled Cluster Singles and Doubles Linear Response Function. *J. Chem. Phys.* **1994**, *100*, 4393-4400.

(98) Kállay, M.; Gauss, J. Calculation of Excited-State Properties Using General Coupled-Cluster and Configuration-Interaction Models. *J. Chem. Phys.* **2004**, *121*, 9257-9269.

(99) Nakatsuji, H.; Hirao, K. Cluster Expansion of the Wavefunction. Symmetry-Adapted-Cluster Expansion, its Variational Determination, and Extension of Open-Shell Orbital Theory. *J. Chem. Phys.* **1978**, *68*, 2053-2065.

(100) Nakatsuji, H. Cluster Expansion of the Wave Function: Calculation of Electron Correlations in Ground and Excited States by SAC and SAC CI Theories.*Chem. Phys. Lett.* **1979**, *67*, 334-342.

(101) Nakatsuji, H. Description of Two- and Many-Electron Processes by the SAC-CI Method. *Chem. Phys. Lett.* **1991**, *177*, 331-337.

(102) Ishida, M.; Toyota, K.; Ehara, M.; Frisch, M. J.; Nakatsuji, H. Analytical Energy Gradient of the Symmetry-Adapted-Cluster Configuration-Interaction General-R Method for Singlet to Septet Ground and Excited States. *J. Chem. Phys.* **2004**, *120*, 2593-2605.

(103) Nakajima, T.; Nakatsuji, H. Energy Gradient Method for the Ground, Excited, Ionized, and Electron-Attached States Calculated by the SAC (Symmetry-Adapted Cluster)/SAC-CI (Configuration Interaction) Method. *Chem. Phys.* **1999**, *242*, 177-193.

(104) Dunning Jr., T. H.; Hay, P. J. Modern Theoretical Chemistry. In *Modern Theoretical Chemistry*; Schaefer, H. F., Ed.; Plenum, New York, NY, USA: 1976; Vol. 3, pp 1-28.

(105) Caricato, M.; Mennucci, B.; Scalmani, G.; Trucks, G. W.; Frisch, M. J. Electronic Excitation Energies in Solution at Equation of Motion CCSD Level Within a Specific Polarizable Continuum Model Approach. *J. Chem. Phys.* **2010**, *132*, 0841021-0841027.

(106) Wagner, N. L.; Greco, J. A.; Enriquez, M. M.; Frank, H. A.; Birge, R. R. The Nature of the Intramolecular Charge Transfer State in Peridinin. *Biophys. J.* **2013**, *104*, 1314-1325.

(107) Enriquez, M. M.; Hananoki, S.; Hasegawa, S.; Kajikawa, T.; Katsumura, S.; Wagner, N. L.; Birge, R. R.; Frank, H. A. Effect of Molecular Symmetry on the Spectra and Dynamics of the Intramolecular Charge Transfer (ICT) State of Peridinin. *J. Phys. Chem. B* **2013**, *116*, 10748-10756.

(108) Bhattacharya, D.; Singh, P.; Sarkar, S. Synthesis, X-Structure and Solvent Induced Electronic States Tuning of Meso-Tris(4-nitrophenyl)Corrolato-Copper Complex. *Inorg. Chim. Acta* **2010**, *363*, 4313-4318.

(109) Palmer, J. H.; Durrell, A. C.; Gross, Z.; Winkler, J. R.; Gray, H. B. Near-IR Phosphorescence of Iridium(III) Corroles at Ambient Temperature. *J. Am. Chem. Soc.* **2010**, *132*, 9230-9231.

(110) Shen, J.; Shao, J.; Ou, Z.; E, W.; Koszarna, B.; Gryko, D. T.; Kadish, K. M. Electrochemistry and Spectroelectrochemistry of Meso-Substituted Free-Base Corroles in Nonaqueous Media: Reactions of (Cor)H3, [(Cor)H4]+, and [(Cor)H2]. *Inorg. Chem.* **2006**, *45*, 2251-2265.

(111) Ding, T.; Harvey, J. D.; Ziegler, C. J. N-H Tautomerization in Triaryl Corroles. *J. Porphyrins Phthalocyanines* **2005**, *9*, 22-27.

(112) Fleischer, E. B. The Structure of Porphyrins and Metalloporphyrins. *Acc. Chem. Res.* **1970**, *3*, 105-112.

(113) Hashimoto, T.; Choe, Y.-K.; Nakano, H.; Hirao, K. Theoretical Study of the Q and B Bands of Free-Base, Magnesium, and Zinc Porphyrins, and their Derivatives. *J. Phys. Chem. A* **1999**, *103*, 1894-1904.

(114) Gouterman, M. Spectra of Porphyrins. *J. Mol. Spectrosc.* **1961**, *6*, 138-163.

Chapter 5

Low-Temperature Trapping of Photointermediates of the Rhodopsin E181Q Mutant

Selected portions of the material presented in this chapter are published in: Sandberg, M. N.*, Greco, J. A.*, Wagner, N. L., Amora, T. L., Ramos, L. A., Chen, M.-H., Knox, B. E., and Birge, R. R. (2014) Low-Temperature Trapping of Photointermediates of the Rhodopsin E181Q Mutant. *SOJ Biochem.* **2014**, *1*, 1-12. **These authors contributed equally to this work.*

5.0. Abstract

Three active-site components in rhodopsin play a key role in the stability and function of the protein: 1) the counter-ion residues which stabilize the protonated Schiff base, 2) water molecules, and 3) the hydrogen-bonding network. The ionizable residue Glu-181, which is involved in an extended hydrogen-bonding network with Ser-186, Tyr-268, Tyr-192 and key water molecules within the active site of rhodopsin, has been shown to be involved in a complex counter-ion switch mechanism with Glu-113 during the photobleaching sequence of the protein. Herein we examine the photobleaching sequence of the E181Q rhodopsin mutant by using cryogenic UV-visible spectroscopy to further elucidate the role of Glu-181 during photoactivation of the protein. We find that lower temperatures are required to trap the early photostationary states of the E181Q mutant compared to native rhodopsin. Additionally, a blue-shifted intermediate (BSI, λ_{max} = 498 nm, 100 K) is observed after the formation of E181Q bathorhodopsin (Batho, λ_{max} = 556 nm, 10 K) but prior to formation of E181Q lumirhodopsin (Lumi, λ_{max} = 506 nm, 220 K). A potential energy diagram of the observed photointermediates suggests the E181Q Batho intermediate has an enthalpy value 7.99 kJ/mol higher than E181Q BSI, whereas in rhodopsin, the BSI is 10.02 kJ/mol higher in enthalpy than Batho. Thus, the Batho to BSI transition is enthalpically driven in E181Q and entropically driven in native rhodopsin. We conclude that the substitution of Glu-181 with Gln-181 results in a significant perturbation of the hydrogen-bonding network within the active site of rhodopsin. In addition, the removal of a key electrostatic interaction between the chromophore and the protein destabilizes the protein in both the dark state and Batho intermediate conformations while having a stabilizing effect on the BSI conformation. The observed destabilization upon this substitution

further supports that Glu-181 is negatively charged in the early intermediates of the photobleaching sequence of rhodopsin.

5.1. Introduction

Rhodopsin, a member of the G protein-coupled receptor (**GPCR**) visual opsins, is located in the rod photoreceptor cells, which are responsible for scotopic (low-light) vision.[1] The visual pigment consists of a seven transmembrane helical apoprotein and an organic chromophore covalently bound to a conserved lysine residue (Lys-296) in helix VII via a protonated Schiff base (**PSB**) linkage. Upon absorption of light, the chromophore, 11-*cis* retinal, isomerizes to an all-*trans* conformation, initiating a series of conformational changes within the protein, which are associated with the formation of a series of spectrally discrete photointermediates with known lifetimes [order of magnitude shown for 298 K]: bathorhodopsin (**Batho**) [ns], blue-shifted intermediate (**BSI**) [ns], lumirhodopsin (**Lumi**) [μs], metarhodopsin I (**Meta I**) [ms], and metarhodopsin II (**Meta II**). The Meta II intermediate is stable on the timescale of minutes and activates the heterotrimeric G protein, transducin.[2-4]

The photointermediate Batho is the first intermediate stable at low temperatures and stores the energy needed (~32 kcal/mol photon energy) to propagate the structural and conformational changes necessary to form the active state of the protein (Meta II), which in turn catalyzes the visual transduction process.[5-7] Although the exact mechanism of energy storage is unknown, it has been proposed that the energy storage in Batho involves conformational strain within the chromophore and electrostatic interactions between the chromophore and the protein.[8] At low temperatures, Batho is converted directly to Lumi by gradually warming rhodopsin in the dark. However, at room temperature, the formation of a BSI is observed after formation of Batho and prior to the formation of Lumi.[9] The first observation of a BSI during the Batho to Lumi transition occurred during nanosecond photolysis experiments on various artificial visual pigments, including 13-desmethyl rhodopsin and 5,6-dihydrorhodopsin.[10,11] These rhodopsin

analogs displayed a destabilization in the Batho intermediate as well as the accumulation of the BSI to sufficient concentrations as to be observed at low temperatures.[8,10-13] Time-resolved resonance Raman analysis suggests the Batho → BSI transition involves the relaxation of the chromophore in the C_{10}-C_{11}=C_{12}-C_{13} region,[14] and it is important to note that Glu-181 is located directly above this region of the chromophore. The formation of the BSI in native rhodopsin has only been observed at room temperature, which is due to the equilibrium constant shifting towards the Batho intermediate resulting in too little formation of the BSI to be experimentally observed at low temperatures.[8,9] While changes in the steric and/or electrostatic interactions between the chromophore and the protein have been associated with the formation of BSI, the decay rate appears to be largely dependent on conformational changes within the protein, or protein relaxation.[8]

Models of rhodopsin developed from recent crystal structure data provide evidence of an extended hydrogen-bonding network around the PSB involving residues Glu-113, Glu-181, Ser-186, Tyr-192, Tyr-268 and select water molecules,[15,16] which has been shown to stabilize the dark state conformation of rhodopsin.[17] The spectral shifts observed during the early photointermediates (dark state, Batho, BSI, and Lumi) are due to modulations of the retinal PSB structure in and around this hydrogen-bonding network, in addition to the eletrostatic influence of the charged residues (Glu-113 and Glu-181), π-stacking, and van der Waals interactions with surrounding residues within the protein-binding pocket.[18] Titration experiments on native rhodopsin and site-directed mutants reveal that the primary counter-ion to the PSB in Meta I is Glu-181, implying there is a switch in the primary counter-ion from Glu-113 in the dark state to Glu-181 in the Meta I state via a rearrangement of the active site hydrogen-bonding network[19-21] and a rotation of helix VI to accommodate this shift.[22] During the transition from Meta I to Meta

II, the PSB is deprotonated and the ionic interaction between the PSB and Glu-113, which serves to lock the protein in an inactive conformation, is broken.[23] This deprotonation of the PSB has been shown to be largely influenced by an enhanced torsional flexibility of the retinal polyene chain and a shift in the relative orientation of the β-ionone ring.[24-27]

The ionizable residue Glu-181, which is located within the binding pocket along extracellular loop II connecting transmembrane helices IV and V, is directly involved in a hydrogen-bonding network with Tyr-268, Tyr-192, Ser-186, and water molecule 14 (**Wat-14**).[28] The protonation state of the carboxylic acid side chain of this residue during the early intermediates has been debated through numerous experimental and theoretical investigations.[20,29-45] Original models of the counter-ion switch predict that a proton is transferred from Glu-181 to Glu-113 during the Lumi to Meta I transition (Figures 5.1A – 5.1D), however, our recent report on the excited state manifold of the rhodopsin mutant with a glutamine substitution at position 181 (**E181Q**) strongly supports a negatively charged Glu-181 during Batho.[42] Figures 5.1E – 5.1H demonstrate that the counter-ion switch model is still applicable with a negatively charged Glu-181 during the dark state and Batho. Previous time-resolved studies on several Glu-181 mutants also suggest the residue plays a significant role in the early stages of the photobleaching sequence of rhodopsin.[39] At room temperature, the E181Q mutation results in the destabilization of the Batho intermediate and subsequently an accelerated decay from Batho to BSI (<30 ns), resulting in the formation of a considerable amount of BSI.[39]

Herein, the consequence of the mutational exchange of residue Glu-181 with Gln-181 on the structural stability and photoactivation mechanism of rhodopsin is explored using low-temperature trapping methods.[46-48] The mutant pigment E181Q was genetically engineered and spectroscopically characterized at cryogenic temperatures following purification. The formation

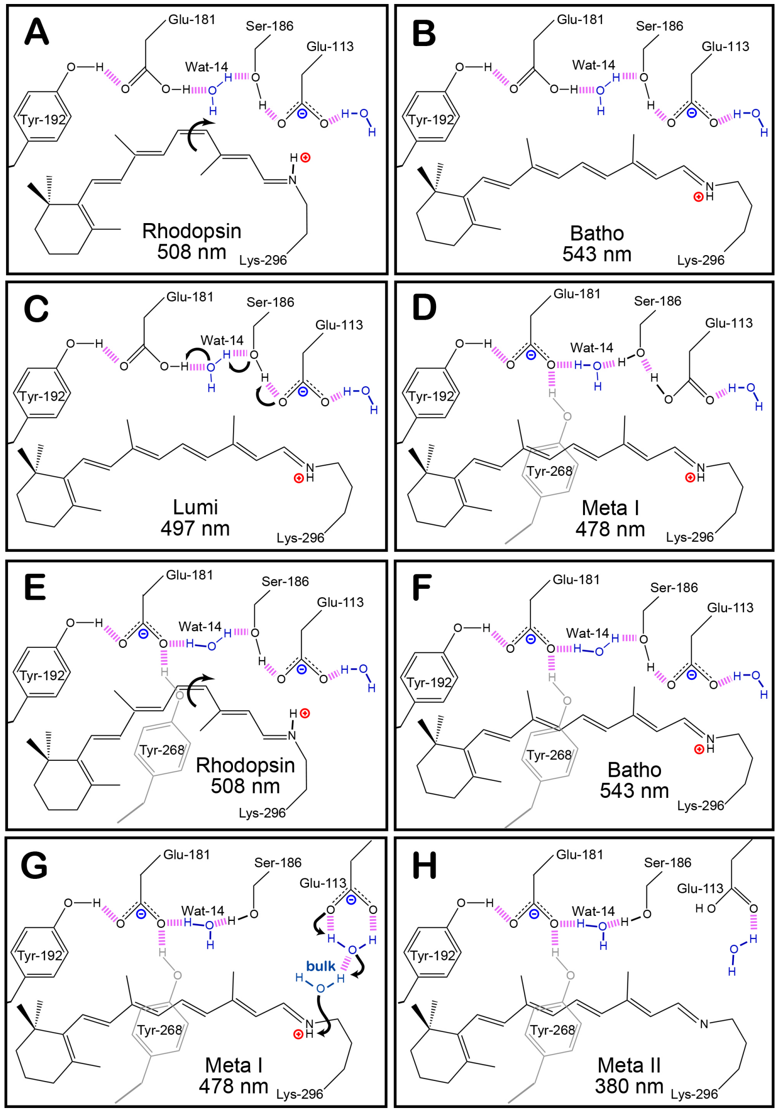

Figure 5.1. The hydrogen-bonding network of the protein-binding site of native rhodopsin at select intermediates during the photobleaching sequence. Panels A – D depict the original model of the counter-ion switch, in which Glu-181 is initially neutral. The primary photochemical event involves the isomerization of 11-*cis* retinal in rhodopsin (A) to all-*trans* retinal in Batho (B). During these early intermediates, Glu-113 serves as the primary counter-ion for the PSB. The transition from Lumi (C) to Meta I (D) is characterized by the transfer of a proton from Glu-181 to the hydrogen bonding network, which subsequently leads to the protonation of Glu-113. Panels E – H demonstrates our model,[42] which predicts that Glu-181 is also negatively charged during the early intermediates (E and F), and the hydrogen-bonding network rearranges to allow Glu-181 to serve as the primary counter-ion after the transition to Meta I (G). During the Meta II state (H), the PSB is deprotonated within the protein-binding site and the protein is activated in order to catalyze the visual transduction cascade. The purple dashed lines represent hydrogen bonding, and the positively and negatively charged species are indicated using red and blue labels, respectively.

and decay of each photointermediate was analyzed using UV-visible spectroscopy and notable differences were observed between the photobleaching sequences of E181Q and native rhodopsin. Plotting the potential energy surface of each intermediate of the photobleaching sequences provides insight into the observation of BSI in the rhodopsin mutant E181Q at low temperatures and possible mechanisms of BSI stability are discussed. The combination of experimental and theoretical data shown below lead us to conclude a negatively charged carboxylic acid side chain at position 181 is crucial for the stability of the Batho and Lumi states in rhodopsin.

5.2. Materials and Methods

5.2.1. Visual Pigment Expression and Purification

The pigment was constructed and isolated as previously reported.[49] The E181Q mutant was expressed in mammalian COS1 cells and purified by immunoaffinity chromatography techniques. The pigment was eluted in buffer Y1 [50 mM HEPES, 140 mM NaCl, 3 mM $MgCl_2$, pH 6.6] with 20 % glycerol and 0.1 % *N*-dodecyl-β-D-maltoside (**DM**) and stored at 193 K until used.

5.2.2. Cryogenic Experiments

The spectra of each photointermediate in the photobleaching sequence of rhodopsin and E181Q were measured using standard methods.[42,47,48,50,51] The samples were prepared in 67 % glycerol, buffer Y1 [50 mM HEPES, 140 mM NaCl, 3 mM $MgCl_2$, pH 6.8], and 0.05 % DM. Low-temperature experiments were conducted from 10 K to 220 K in a closed-cycle helium-refrigerated cryostat (APD Cryogenics) coupled to a Cary 50 UV-visible spectrophotometer (Varian, Inc.). For the mutant E181Q, a temperature below 20 K was required due to the

instability of the E181Q Batho photoproduct. The 10 K temperature was chosen to prevent formation of any intermediates other than Batho. To generate each photostationary state (**PSS**), samples were equilibrated to 10 K prior to illumination with a Photomax system equipped with a 200 W arc lamp and a monochromator (Oriel Instruments) tuned 20 nm to the blue of the absorption maximum ($\boldsymbol{\lambda_{max}}$) of the dark state. Once photoconversion to the Batho photoproduct was complete, the temperature was then raised to 220 K in increments of 10 K. To avoid artifacts arising from temperature-dependent baseline shifts, the temperature of the sample was cooled down to the starting temperature (10 K) before each spectrum was recorded. Semi-low temperature experiments were carried out from 233 K to 293 K in a Cary 5000 UV-visible spectrophotometer (Varian, Inc.) equipped with a temperature controlled sample holder (Quantum Northwest, Inc.). Samples were illuminated with 495 nm light until no further spectral shift was observed. The temperature of the sample was then raised to 293 K in increments of 5 K once photoconversion was completed.

Two methods were used in combination to determine the composition of each PSS. The first method involved warming the sample to ambient temperature to allow for the formation of Meta II, which has a λ_{max} for both rhodopsin and E181Q rhodopsin of approximately 380 nm. The spectrum of the resulting sample contains a mixture of the dark state and Meta II, separated in wavelength to a sufficient extent to allow reliable spectral deconvolution. The integral of the λ_{max} band, when compared to that observed for the pure dark state at the same temperature, permits accurate assignment of the amount of rhodopsin converted. Additionally, retinal oximes were extracted and analyzed using high-performance liquid chromatography (**HPLC**) following the methods and procedures reported previously[50] and described below. The isomeric compositions of each PSS are then used to deconvolute the measured spectra and determine the

λ_{max} of the photointermediates of E181Q. The pure dark state is assumed to be comprised of 100% 11-*cis* retinal for spectral deconvolution, as previously described.[52-54] All absorption spectra presented are the average of three spectra normalized with respect to the protein aromatic residue band at 280 nm. Each difference spectrum was calculated by subtracting the selected PSS from the corresponding dark state or relevant PSS.

5.2.3. Chromophore Extraction

The isomeric ratio of the chromophore was determined as follows. A mixture of 150 μL of ice-cold 1.0 M hydroxylamine (pH 7) solution, 1 mL of methanol, and 1 mL of dichloromethane was added to each glycerol/protein sample. The mixture was shaken vigorously for 1 min and put on ice. Hexane (1 mL) was then added and the sample was shaken and spun in a clinical centrifuge for 45 s. The hexane layer was removed, and another 5 mL hexane extraction was performed. The combined hexane layers were then dried (Na_2SO_4), filtered through a 0.2 μm filter, and evaporated in a clean tube under vacuum. The total volume of the hexane layer was brought to 100 μL.

A portion of the hexane layer (50 μL) was injected into an HPLC instrument (Waters Corporation), which was equipped with two HPLC columns (Waters Prep Nova-Pak HR silica columns, 3.9 × 300 mm, Waters catalog no. WAT038501) and a Waters 2487 dual wavelength absorbance detector monitoring at 360 nm. The mobile phase used to separate the retinal isomers was composed of 96 % hexane, 3 % *tert*-butyl methyl ether, 0.5 % 1-octanol, and 0.5 % 1,4-dioxane. All solvents used were HPLC grade (Fisher Scientific). The flow rate was fixed at 2.5 mL/min. Retinal oxime standards (all-*trans*, 11-*cis* and 9-*cis* retinal oxime) were used to assign the retention times of the peaks observed following the chromophore extractions. The *syn* oxime enantiomers were favored due to the low temperature and concentrations used for the extraction,

and these peaks were used exclusively to determine the isomeric ratios of retinal within the chromatograms. The *anti* oxime enantiomers were observed, however, these species were found at longer retention times and were ignored for this analysis.

5.2.4. Computational Methods

All molecular orbital calculations were carried out using Gaussian 09.[55] The heavy atom coordinates for dark state rhodopsin, Batho, Lumi, and Meta II were taken from the 1U19,[16] 2G87,[56] 2HPY,[57] and 2I37[58] crystal structures of rhodopsin, respectively. Hydrogen atoms were added to all relevant atoms of residues within 5.6 Å of the chromophore by using Anamol 5.6.4. The hydrogen atoms and these local residues, in addition to the chromophore, were optimized by using the Parameterized Model 3 (**PM3**) methods[59,60] in Gaussian 09, while holding all other heavy atoms at the crystal geometry coordinates. During these optimizations, the oxygen atoms of the nearby water molecules were locked while the hydrogen atoms were allowed to fully optimize. Subsequently, seven iterations of B3LYP/6-31G(d) procedures[61,62] in Gaussian 09 were used to generate the ground state structures of the photointermediates. The configuration of the glutamine residue was optimized by minimizing the two possible rotational geometries and selecting the geometry with the lowest energy. The electrostatic charge shifts of the protein-binding sites were generated in Mathscriptor 3.5.0 (www.mathscriptor.org).

The rhodopsin photobleaching energy surface was taken from Ref. 63, and was generated based on photocalorimetry as the primary experimental method. The E181Q energy surface was generated by reference to the rhodopsin surface using the temperature ramping experiments to assign the barriers, and the theoretical calculations to estimate the energy minima. The energy barriers separating the various intermediates in E181Q, $E_{barrier}^{\mathrm{E181Q}}$, were assigned by reference to the temperature of appearance, $T_{obsvd}^{\mathrm{E181Q}}$, of the next intermediate:

$$E_{barrier}^{\mathrm{E181Q}} \approx \frac{E_{barrier}^{\mathrm{RHO}} \times T_{obsvd}^{\mathrm{E181Q}}}{T_{obsvd}^{\mathrm{RHO}}} \tag{5.1}$$

where $E_{barrier}^{\mathrm{RHO}}$ and T_{obsvd}^{RHO} are the corresponding barrier and temperatures in the rhodopsin photobleaching sequence. Because the above method and the theoretical models are approximate, the E181Q surface should be viewed as qualitative.

5.3. Results

The raw spectra of the low-temperature and semi-low temperature spectroscopy studies of native rhodopsin and E181Q are described in detail below. At room temperature, E181Q displayed a significant red-shift in absorption maximum (λ_{max} = 508 nm) relative to native rhodopsin (λ_{max} = 499 nm).[42] Lowering the temperature to 10 K resulted in a negligible shift for E181Q and a bathochromic shift of 4 nm for native rhodopsin (λ_{max} = 503 nm) at 70 K (Figure 5.2). Illumination of E181Q with 500 nm light initiated the formation of the first PSS, a mixture of resting state and Batho, which was red-shifted to a λ_{max} of 522 nm (**PSS522**). Figures 5.2A – 5.2D demonstrate that the photoconversion to Batho for native rhodopsin and E181Q was complete in 1 hour at 70 K and 10 K, respectively, and involved the formation of a single species with the disappearance of the dark state. As the temperature of PSS522 was raised in 10 K increments, no spectral shift was observed from 10 K to 50 K (Figure 5.3). At 60 K, the spectrum begins to shift to form a second PSS at 498 nm (**PSS498**). The temperature was then gradually raised to 220 K, and the formation of a third intermediate was observed at 506 nm (**PSS506**). No further spectral change was measured after 200 K, indicating the formation of PSS506 was complete. HPLC analysis of PSS506 (Figure 5.4) revealed a retinal composition of 32 % 11-*cis*, 61% all-*trans*, and 7% 9-*cis* retinal isomers.

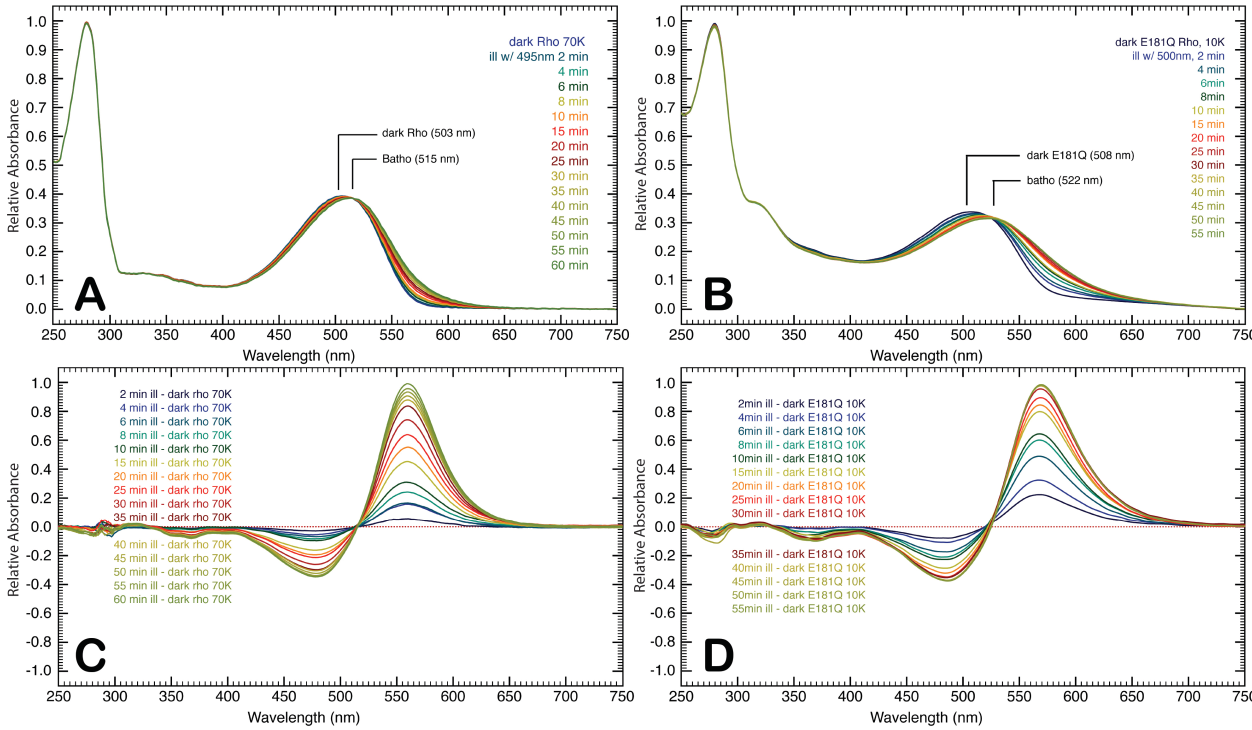

Figure 5.2. Time-resolved absorption spectra of rhodopsin at 70 K (A) and E181Q at 10 K (B) following illumination by using a 495 nm and 500 nm light source, respectively. The absorption spectra were collected at the given time points following illumination. The difference spectra of the absorption profiles are provided for rhodopsin (C) and E181Q (D) and were obtained by subtracting the respective spectra of the dark state from the corresponding time point throughout the experiment.

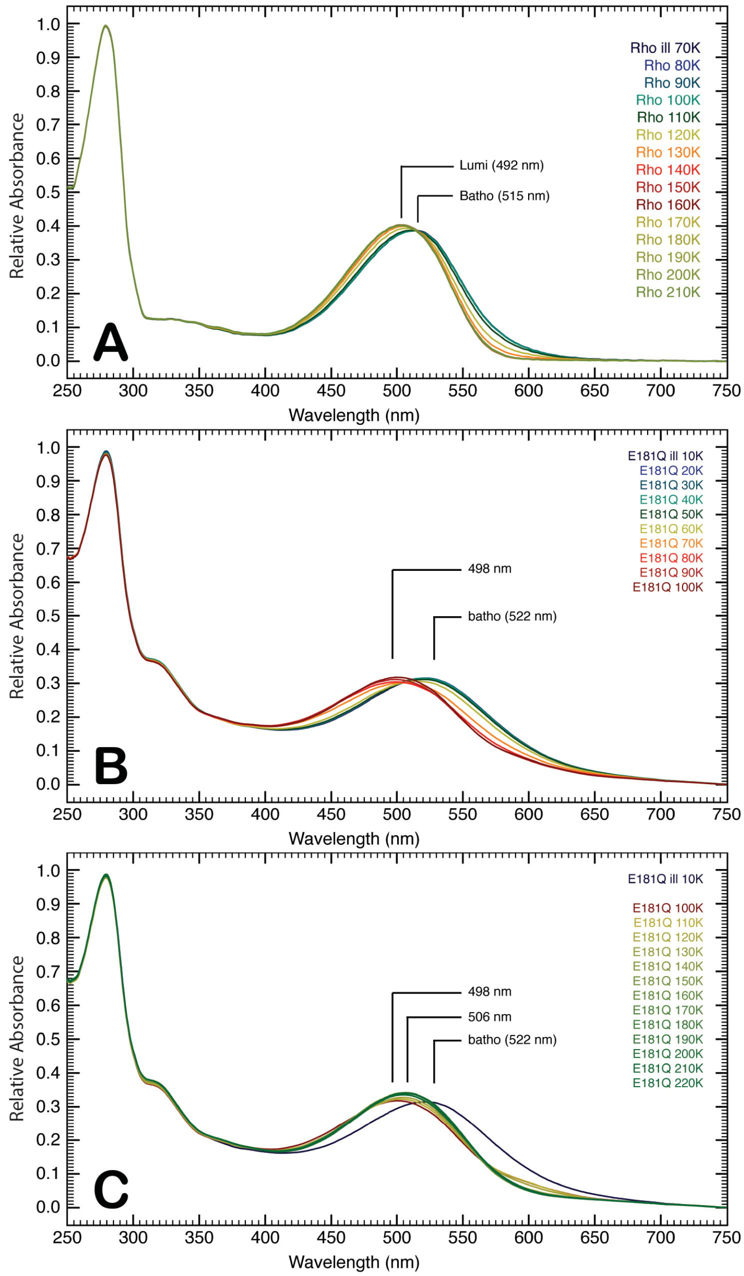

Figure 5.3. Absorption spectra of rhodopsin (A) and E181Q (B and C) post-illumination as the temperature is ramped to 220 K via 10 K increments. The initial formation of the Batho photointermediate for native rhodopsin was achieved at 70 K (A), and as the temperature was increased, the formation of a single Lumi photointermediate (492 nm) was observed. The absorption spectra for E181Q was first collected at 10 K, in which the PSS522 consisted of a mixture of the dark and Batho states of the mutant protein (B). As the temperature was increased, a second PSS formed (PSS498) at 60 K. The E181Q sample was then allowed to warm to 220 K (C), where a third PSS (PSS506) evolved. The PSS498 was found to be a mixture of Batho and BSI, whereas the PSS506 was a Lumi photointermediate of the mutant protein (see text).

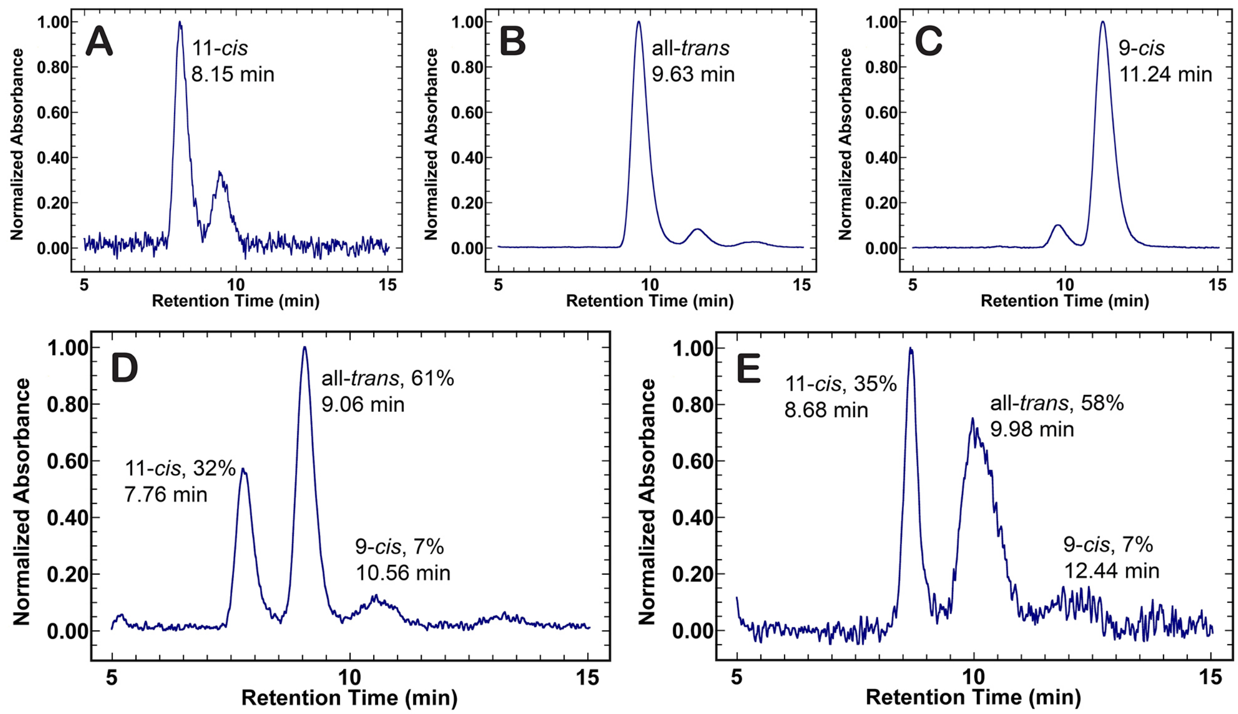

Figure 5.4. HPLC chromatograms of retinal oxime standards and retinal oxime extractions of PSS506 and PSS383. Panels A, B, and C show the chromatograms for the 11-*cis*, all-*trans*, and 9-*cis* retinal oxime standards, respectively. Each standard peak represents the retention time for the *syn* oxime enantiomer of the retinal isomers. The percent of retinal isomers formed for PSS506 (D) and PSS383 (E) were determined by integrating under each peak.

The formation and decay of the late photointermediates (Lumi, Meta I, and Meta II) for rhodopsin and E181Q were studied using semi-low temperature spectroscopy, from 233 K to 293 K. Irradiation of E181Q with 495 nm light at 233 K promoted the formation of Lumi (λ_{max} = 495 nm) and no spectral shift was observed after 85 min of continuous illumination (Figure 5.5A). During the formation of Lumi, the formation and decay of a red-shifted difference spectrum species (λ_{max} = 575 nm) is seen along with the formation of a blue-shifted difference spectrum species (λ_{max} = 385 nm) (Figure 5.5B). Further temperature ramping experiments illustrated in Figure 5.6 indicate that the transition to the Meta I intermediate (λ_{max} = 480 nm) began at 238 K and was complete by 243 K. The Meta I spectrum is very broad and may be a mixture of Meta I and Lumi intermediate that has not decayed completely at 233 K. With increasing temperature (in 5 K increments), the spectrum continues to blue shift until the formation of Meta II (λ_{max} = 383 nm; **PSS383**) is complete. HPLC analysis of the retinal composition of PSS383 (Figure 5.4) shows the presence of 11-*cis* (35%), all-*trans* (58%), and 9-*cis* (7%) retinal isomers.

5.4. Discussion

Time-resolved UV-visible spectroscopy has been instrumental in determining the formation and decay of discrete photointermediates of rhodopsin, as well as elucidating the photobleaching pathway of the protein.[9] However, a key disadvantage of room-temperature time-resolved UV-visible spectroscopy for the rhodopsin mutant E181Q is the simultaneous formation and decay of multiple intermediates. Low-temperature trapping experiments, which slow down the photobleaching process and ensure that each photointermediate is observed individually, were performed to avoid this problem.[46-48] In the photobleaching sequence of native rhodopsin,

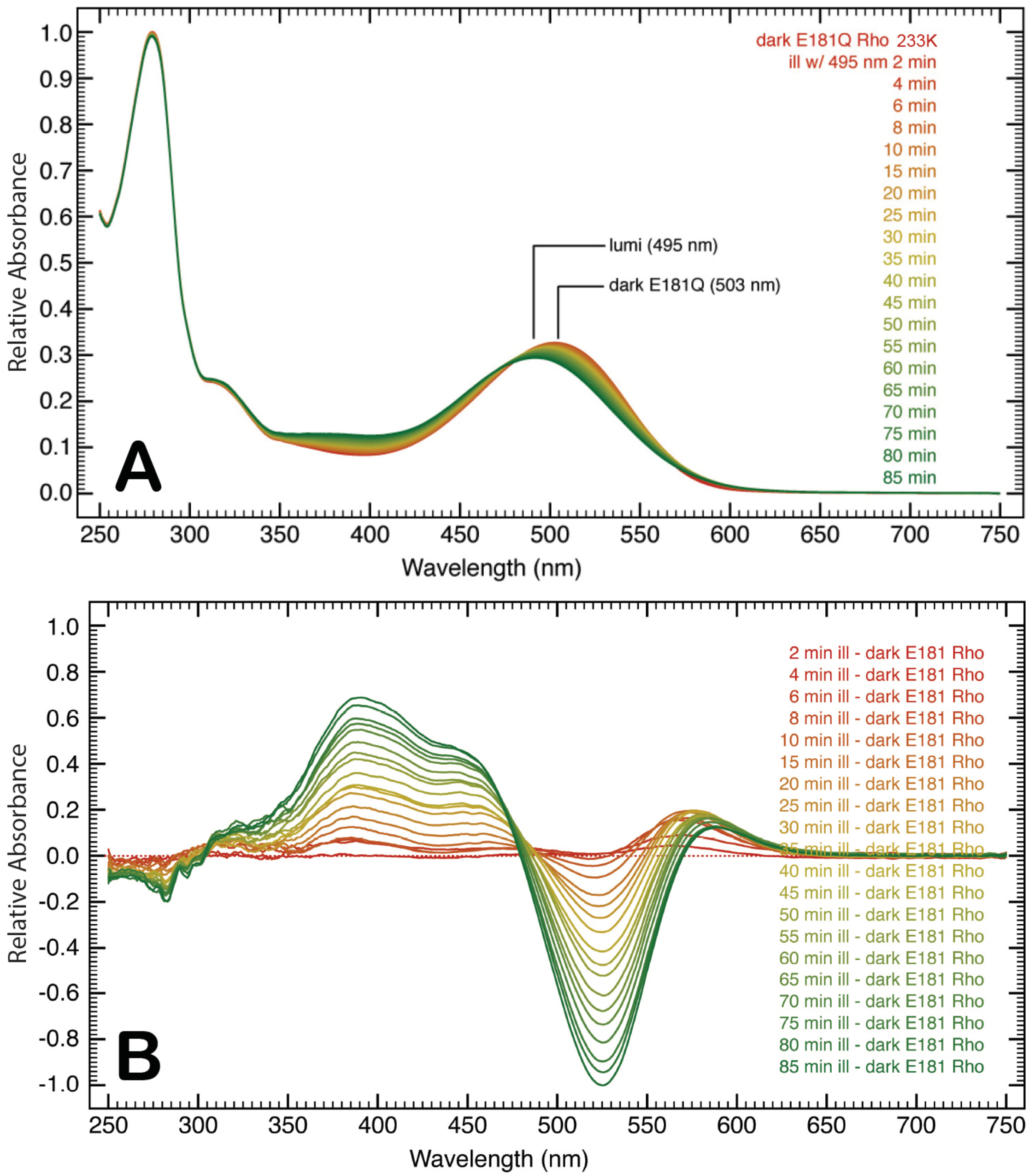

Figure 5.5. Time-resolved absorption spectra of E181Q at 233 K following illumination with 495 nm light (A). The difference spectra presented in panel (B) was obtained by subtracting the dark state spectrum from the spectra of each time point. While the blue-shifted species is accounted for by the evolution of Lumi (495 nm) over 85 min, the origin of the red-shifted species with a difference spectrum maximum at 575 nm is currently unknown.

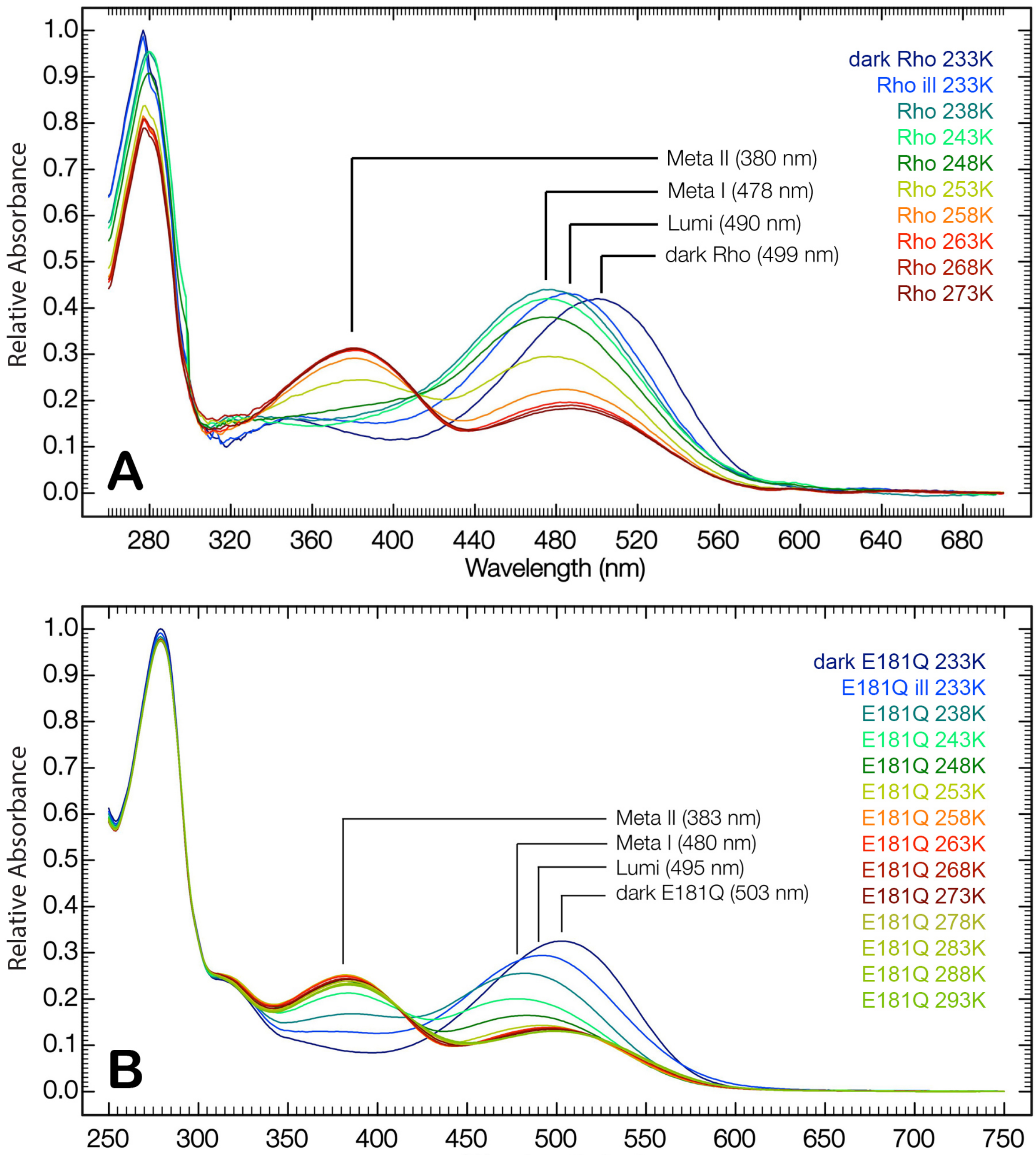

Figure 5.6. Absorption spectra of rhodopsin (A) and E181Q (B) at semi-low temperatures (233 K to 293 K) following illumination of the dark state to initiate the photobleaching sequence. The higher temperatures allowed for the formation and trapping of the late photointermediates (Meta I and Meta II), in addition to a single Lumi photointermediate.

Batho is stable at 70 K and decays directly to Lumi upon gradual warming (Figure 5.3A). However, in the photobleaching sequence of E181Q, Batho is only stable at temperatures lower than 50 K and thermally equilibrates with BSI when the temperature is raised above 60 K. The final equilibrium mixture (PSS498), which is comprised mainly of BSI, is not established until 90 K. Spectral deconvolution was used to determine that pure BSI for E181Q has a λ_{max} of 479 nm. Raising the temperature to 220 K results in decay of the mixture to Lumi (PSS506), the identity of which is confirmed through the chromophore extraction of the PSS and HPLC analysis. The isomeric composition of PSS506 was found to be 32% 11-*cis* retinal, 61% all-*trans* retinal, and 7% 9-*cis* retinal. Pure Lumi is found to have a λ_{max} of 510 nm (at 220 K) by adding back 32% of the dark state spectrum of E181Q to the difference spectrum of PSS506 minus the dark state spectrum. Contributions from the 9-*cis* chromophore were ignored for this spectral deconvolution because so little is formed (7%). In comparison to the native rhodopsin spectral data, these observations suggest that the retinylidene binding pocket environment has been significantly perturbed during the early stages of the photoactivation mechanism.

In the semi-low temperature experiments, a single Lumi intermediate is seen for native rhodopsin (λ_{max} = 490 nm) at 233 K. Previous studies have shown that at low temperatures, the equilibrium constant between Lumi I and Lumi II for native rhodopsin is significantly shifted towards Lumi II and thus only one Lumi intermediate is observed.[64] Similarly, we observe the formation of a single E181Q Lumi intermediate (λ_{max} = 495 nm). However, during the formation of E181Q Lumi, the formation and decay of a red-shifted difference spectrum species (λ_{max} = 575 nm) is observed (Figure 5.5). This species is not seen during Lumi formation in native rhodopsin and warrants further investigation. While the absorption spectra of the later intermediates of E181Q and native rhodopsin are similar (Figure 5.6), the Meta I and Meta II

photointermediates of E181Q form more readily at lower temperatures compared to native rhodopsin. Recall that a negatively charged Glu-181 serves as the primary counter-ion during the late photointermediates,[19-21] and thus the substitution with Gln-181 will serve to destabilize the retinal binding site during Meta I and Meta II. The isomeric composition of PSS383 (35% 11-*cis* retinal, 58% all-*trans* retinal, and 7% 9-*cis* retinal) is used in a similar fashion as for PSS506 in order to determine the λ_{max} of pure Meta II (λ_{max} = 384 nm at 273 K).

Lewis *et al.*[39] investigated the room temperature time-resolved spectra of Glu-181 mutants and observed a destabilization of the Batho intermediate, as well as a significant shift in equilibrium towards BSI in E181Q. During the late stages of the photoactivation mechanism, they also note the absence of a Lumi I to Lumi II transition for the E181Q mutant.[39] Because the formation of these photointermediates are temperature dependent, only the formation of photointermediates that accumulate to appreciable amounts at room temperature are expected to form at low temperatures in observable concentrations. The notion that only a single Lumi intermediate was produced for this mutant at room temperature allows us to predict that we are observing a transition from BSI to Lumi at low temperatures (< 200 K) in E181Q and not a Lumi I to Lumi II transition. The proposed photobleaching sequence pathways of native rhodopsin and E181Q are summarized in Figure 5.7.

Recall that a destabilized Batho may result from a change in ionization or a disruption in the complex hydrogen-bonding network involving several binding pocket residues. Because Batho and BSI are in equilibrium, changes that destabilize Batho would result in the stabilization of BSI. While Lewis *et al.*[39] found that E181Q and other Glu-181 mutants lead to an accelerated decay of Batho, replacing Glu-181 with aspartic acid (**E181D**) resulted in a Batho lifetime

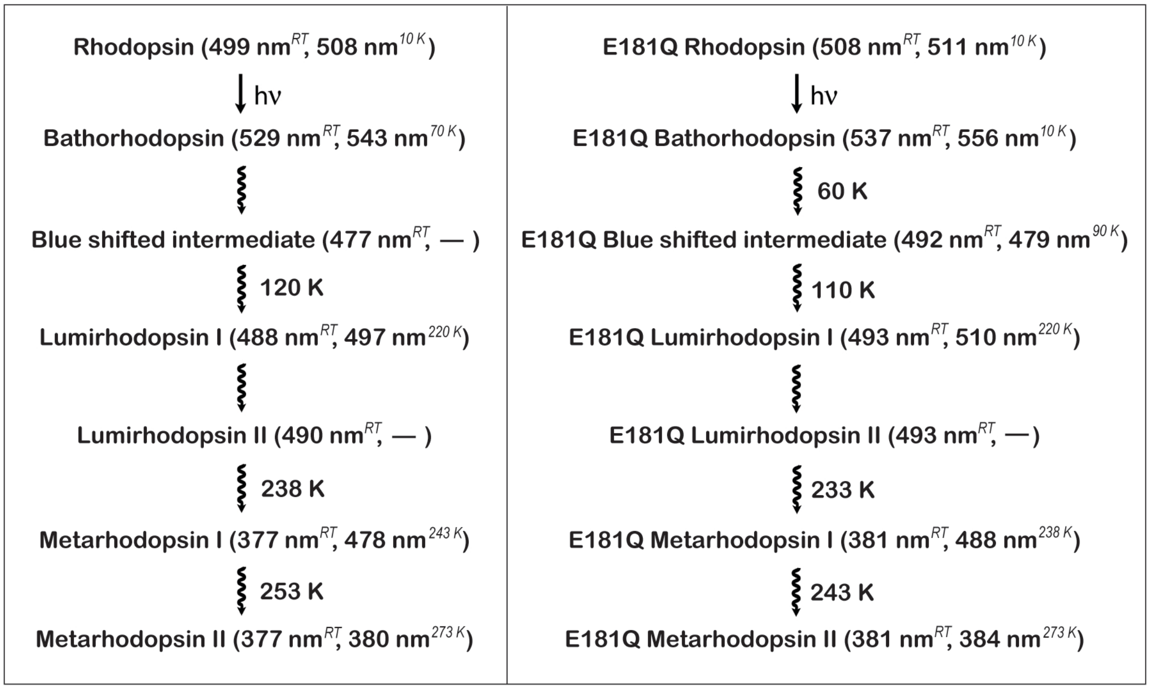

Figure 5.7. Photobleaching sequences of rhodopsin and E181Q rhodopsin. For each photointermediate, the λ_{max} is shown at both room temperature and low temperatures. The room temperatures are based on the values obtained by Lewis *et al.*,[39] and the low-temperature data is based on the deconvolution of the spectra presented in this study. At low temperatures, no BSI was observed for rhodopsin, and no Lumi II was observed for either rhodopsin or E181Q.

similar to that of native rhodopsin. Aspartic acid is one carbon atom shorter than glutamic acid, however, the carboxyl group is maintained. Therefore, it is reasonable to predict that the stability of Batho relies on the presence of the carboxyl atoms. Although there is no clear agreement on the protonation state of Glu-181,[20,29-45] if we assume it is negatively charged in the dark state, then replacing Glu-181 with the neutral residue Gln-181 may provide insight into why the mutant E181Q leads to a faster decay of Batho and stabilizes the BSI. During the primary event, the distance between the C_{13}-methyl group and residue Glu-181 decreases from a distance of 5.7 Å to 3.0 Å.[16,56] The removal of a charged residue near the highly strained C_9-C_{13} portion of retinal may provide an increased flexibility in the polyene chain of the chromophore, which would allow the chromophore to more readily adopt a planar conformation and shift the equilibrium towards the BSI.

Moreover, substitution of Glu-181 with Gln-181 may also result in a destabilized Batho via perturbation of the active site hydrogen-bonding network. The notion that this mutational change would alter the hydrogen-bonding network is not surprising because the functional groups on these two residues contain different hydrogen-bonding character. Further support for a hydrogen-bonding rearrangement being responsible for the observed destabilized Batho comes from the fact that Wat-14, which is in a direct path of the C_{13}-methyl group of the chromphore during the primary event, is believed to contribute to the stability of Batho.[65] Thus, any perturbation of Wat-14 may also result in a destabilization of Batho. In addition to E181Q, a destabilized Batho intermediate has been observed in several artificial pigments, as well as select rhodopsin mutants and cone-type visual pigments.[10,11,66-68] Previous studies have shown the decay of Batho is dependent on the rotation barrier of the C_6-C_7 bond, which in turn depends on the steric interaction between the C_5-methyl and the C_8-hydrogen. In E181Q, a rearrangement in

the hydrogen-bonding network during the photobleaching sequence causes a shift in the position of Tyr-268 towards Gln-181 and Tyr-192 (Figure 5.8). The repositioning of Tyr-268 may lower the barrier to BSI by decreasing the steric interaction between the C_5-methyl and C_8-H groups. While the E181Q rhodopsin mutant is not the first to display a destabilized Batho,[68] it is interesting to note that replacing Ser-186 with an alanine residue results in a normal Batho intermediate, despite the fact that Ser-186 is hydrogen-bonded to Glu-181 via Wat-14 in the dark state and early photointermediates of rhodopsin (Figures 5.1 and 5.8).[28] Thus, in the case of E181Q, the observed destabilization of Batho may be caused in part by a rearrangement of the hydrogen-bonding network involving Tyr-268 and Tyr-192 rather than perturbations in the active site hydrogen-bonding network involving Wat-14 and Ser-186. Although the exact mechanism of Batho destabilization remains unclear, these results demonstrate that the carboxyl group at residue 181 is required for the stabilization of Batho in native rhodopsin. Furthermore, the dramatic influence of the glutamine substituion on the photobleaching kinetics suggests that this carboxyl group is likely negatively charged during the dark and Batho states.

Plotting the potential energy surface of the photobleaching pathway for both rhodopsin and E181Q provides further insight into the stabilization of BSI in E181Q (Figure 5.9). Our calculations, which utilize the temperature of appearance of the photointermediates and the calculated energies (Equation 1), are in agreement with the literature and predict the BSI in rhodopsin lies higher in energy than Batho.[8,63] When we overlay the energies of the E181Q photointermediates, shown in dashes, it is immediately apparent that the E181Q mutant is less stable than native rhodopsin throughout the photobleaching sequence. All measured photointermediates of E181Q first appeared at lower temperatures than for the corresponding intermediates of native rhodopsin, which correlates with the predicted destabilization. This

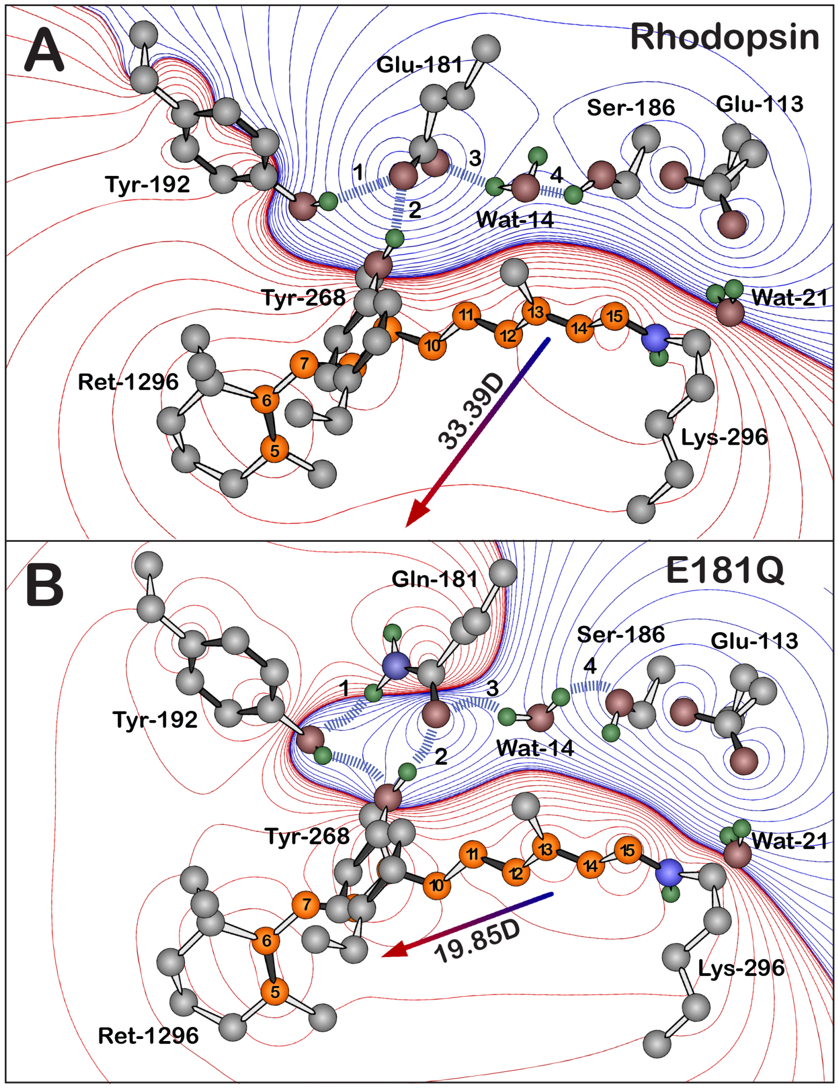

Figure 5.8. The hydrogen-bonding network of the negatively charged Glu-181 residue of native rhodopsin (A) and of the Gln-181 residue of E181Q (B), both during the Lumi photointermediate. The blue dashed lines and the labels **1–4** highlight the key hydrogen-bonding network between residue 181, Ser-186, Tyr-192, Tyr-268, and Wat-14, which is perturbed upon the glutamine substitution. The Lumi structure (A) is based off of the 2HPY crystal structure[57] and a relaxed conformation of the Lumi photointermediate of E181Q (B) was obtained by minimizing the crystal structure with Gln-181. Polyene atoms of retinal (**Ret-1296**) are indicated in orange, and the numbering system shown here is used in the text. The water molecules are labeled using the Protein Data Bank (**PDB**) numbers minus 2000. All hydrogen atoms were included in the calculations and were optimized by using B3LYP/6-31G(d) methods, although only polar hydrogens are shown in the figure. Red and blue contours indicate regions of increased positive and negative charge, respectively. The contours are drawn by using the following first-order electrostatic energies: 0 (black), ± 0.282, ± 2.26, ± 7.63, ± 18, ± 35.3, ± 61, ± 96.9, ± 144, ± 206, ± 282, ± 376, ± 488, ± 621, ± 755 kJ/mol.

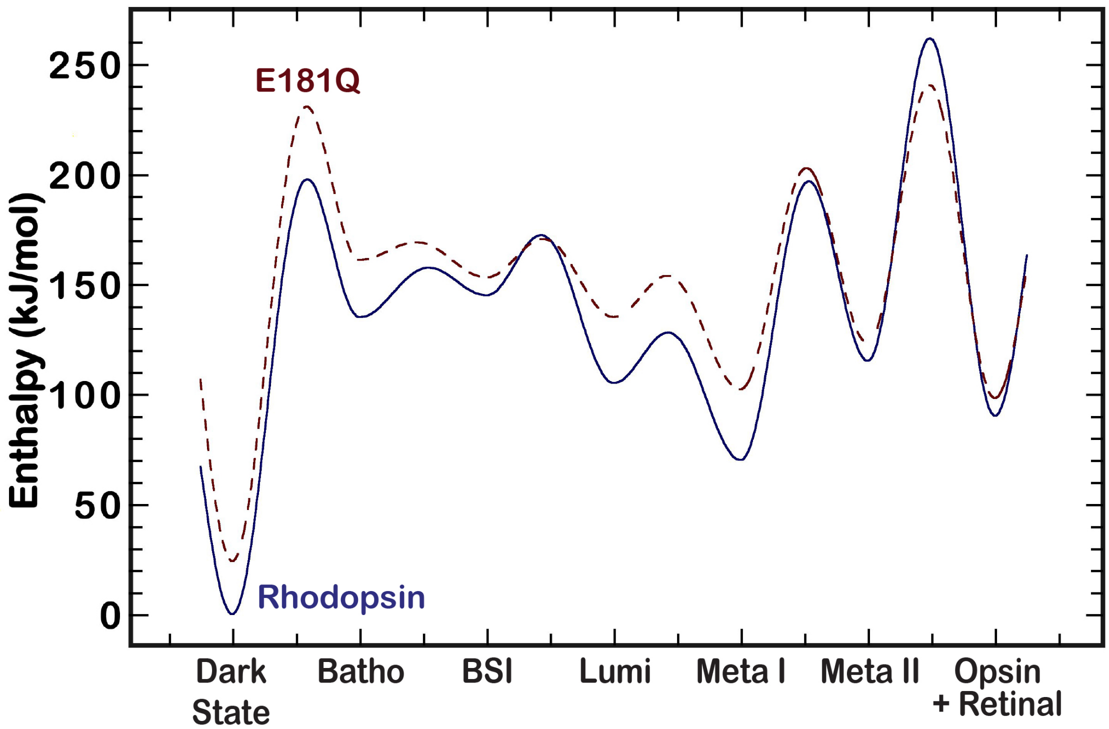

Figure 5.9. A potential energy surface of the photobleaching sequence of native rhodopsin (solid blue) and E181Q (dashed red). The rhodopsin surface is adopted from reference [63]. The E181Q surface is approximate and was generated using the methods described in the text.

destabilization is further supported in the model of the Lumi photointermediate for both rhodopsin and E181Q provided in Figure 5.8, which indicates a significant modulation in the hydrogen-bonding network around the chromophore for the mutant. Most importantly, our model predicts the E181Q Batho intermediate has an enthalpy value 7.99 kJ/mol higher than E181Q BSI, whereas in rhodopsin, the BSI has an enthalpy that is 10.02 kJ/mol higher than Batho. From these results, we conclude the Batho to BSI transition is enthalpically driven in E181Q and entropically driven in native rhodopsin. Note, however, that these enthalpy differences and the potential energy surfaces depicted in Figure 5.9 are very approximated because they are based on Equation 1. A more rigorous theoretical study using a hybrid quantum mechanics/molecular mechanics (**QM/MM**) approach is currently being undertaken for further analysis of these models.

5.5. Conclusions

The photobleaching sequence of the rhodopsin mutant E181Q has been investigated by cryogenic studies in an attempt to further elucidate the role of Glu-181 during the photoactivation process of rhodopsin. We conclude that the photobleaching sequence of E181Q at low temperatures involves a two-step sequential decay from Batho to Lumi that includes an equilibrium between Batho and a subsequent BSI. The present study supports conclusions of other studies that have suggested Batho is destabilized in E181Q and that the Batho to BSI equilibrium lies toward the BSI.[39] The stabilization of the BSI in E181Q can be explained by the thermodynamics of the photobleaching process, which shows the Batho to the BSI transition is enthalpically driven in the rhodopsin mutant. Three key differences are noted for the photobleaching sequence of E181Q compared to rhodopsin collected at cryogenic temperatures:

1) lower temperatures are required to trap the primary photointermediate Batho in E181Q compared to native rhodopsin, 2) the decay of Batho occurs much more rapidly compared to native rhodopsin, and 3) the formation of the BSI is observed during low temperature experiments. Additionally, the formation of the later intermediates (Meta I and Meta II) of E181Q all occur at lower temperatures compared to the formation of the later intermediates of native rhodopsin. We conclude that these differences in the photobleaching sequence of E181Q compared to native rhodopsin provide strong evidence that the negatively charged carboxylic acid side chain of residue Glu-181 plays a critical role in the early intermediates of the photobleaching sequence of native rhodopsin by maintaining the integrity of the active site hydrogen-bonding network which serves to stabilize the protein in the dark state and the primary photointermediate, Batho. Furthermore, by replacing the Glu-181 residue with Gln-181, a key electrostatic interaction is altered concurrent with a rearrangement of the hydrogen-bonding network within the binding pocket, thus allowing for the formation of the BSI to accumulate to concentrations observable at low temperatures.

5.6. References

(1) Baylor, D. How Photons Start Vision. *Proc. Natl. Acad. Sci. U.S.A.* **1996**, *93*, 560-565.

(2) Kwok-Keung Fung, B.; Stryer, L. Photolyzed Rhodopsin Catalyzes the Exchange of GTP for Bound GDP in Retinal Rod Outer Segments. *Proc. Natl. Acad. Sci. U.S.A.* **1980**, *77*, 2500-2504.

(3) Hofmann, K. P.; Jäger, S.; Ernst, O. P. Structure and Function of Activated Rhodopsin. *Isr. J. Chem.* **1995**, *35*, 339-355.

(4) Smith, S. O. Structure and Activation of the Visual Pigment Rhodopsin. *Annu. Rev. Biophys.* **2010**, *39*, 309-328.

(5) Boucher, F.; Leblanc, R. M. Energy Storage in the Primary Photoreaction of Bovine Rhodopsin. A Photoacoustic Study. *Photochem. Photobiol.* **1985**, *41*, 459-465.

(6) Cooper, A. Energy Uptake in the First Step of Visual Excitation. *Nature* **1979**, *282*, 531-533.

(7) Schick, G. A.; Cooper, T. M.; Holloway, R. A.; Murray, L. P.; Birge, R. R. Energy Storage in the Primary Photochemical Events of Rhodopsin and Isorhodopsin. *Biochemistry* **1987**, *26*, 2556-2562.

(8) Hug, S. J.; Lewis, J. W.; Einterz, C. M.; Thorgeirsson, T. E.; Kliger, D. S. Nanosecond Photolysis of Rhodopsin: Evidence for a New, Blue Shifted Intermediate. *Biochemistry* **1990**, *29*, 1475-1485.

(9) Lewis, J. W.; Kliger, D. S. Photointermediates of Visual Pigments. *J. Bioenerg and Biomembr.* **1992**, *24*, 201-210.

(10) Einterz, C. M.; Hug, S. J.; Lewis, J. W.; Kliger, D. S. Early Photolysis Intermediates of the Artificial Visual Pigment 13-demethyl Rhodopsin. *Biochemistry* **1990**, *29*, 1485-1491.

(11) Albeck, A.; Friedman, N.; Ottolenghi, M.; Sheves, M.; Einterz, C.M.; Hug, S.J.; Lewis, J.W.; Kliger, D.S. Photolysis Intermediates of the Artificial Visual Pigment Cis-5,6-dihydro-Isorhodopsin. *Biophys. J.* **1989**, *55*, 233-241.

(12) Shichida, Y.; Kropf, A.; Yoshizawa, T. Photochemical Reactions of 13-demethyl Visual Pigment Analogues at Low Temperatures. *Biochemistry* **1981**, *20*, 1962-1968.

(13) Randall, C. E.; Lewis, J. W.; Hug, S. J.; Björling, S. C.; Eisner-Shanas, I.; Ottolenghi, M.; Sheves, M.; Friedman, N.; Kliger, D. S. A New Photolysis Intermediate in Artificial and Native Visual Pigments. *J. Am. Chem. Soc.* **1991**, *113*, 3473-3485.

(14) Pan, D.; Ganim, Z.; Kim, J. E.; Verhoeven, M. A.; Lugtenburg, J.; Mathies, R. A. Time-Resolved Resonance Raman Analysis of Chromophore Structural Changes in the Formation and Decay of Rhodopsin's BSI Intermediate. *J. Am. Chem. Soc.* **2002**, *124*, 4857-4864.

(15) Palczewski, K.; Kumasaka, T.; Hori, T.; Behnke, C. A.; Motoshima, H.; Fox, B. A.; Le Trong, I.; Teller, D. C.; Okada, T.; Stenkamp, R. E.; Yamamoto, M., Miyano, M. Crystal Structure of Rhodopsin: A G Protein-Coupled Receptor. *Science* **2000**, *289*, 739-745.

(16) Okada, T.; Sugihara, M.; Bondar, A.; Elstner, M.; Entel, P.; Buss, V. The Retinal Conformation and its Environment in Rhodopsin in Light of a New 2.2 å Crystal Structure. *J. Mol. Biol.* **2004**, *342*, 571-583.

(17) Liu, J.; Liu, M. Y.; Nguyen, J. B.; Bhagat, A.; Mooney, V.; Yan, E. C. Y. Thermal Decay of Rhodopsin: Role of Hydrogen Bonds in Thermal Isomerization of 11-cis Retinal in the Binding Site and Hydrolysis of Protonated Schiff Base. *J. Am. Chem. Soc.* **2009**, *131*, 8750-8751.

(18) Campomanes, P.; Neri, M.; Horta, B. A. C.; Röhrig, U. F.; Vanni, S.; Tavernelli, I.; Rothlisberger, U. Origin of the Spectral Shifts Among the Early Intermediates of the Rhodopsin Photocycle. *J. Am. Chem. Soc.* **2014**, *136*, 3842-3851.

(19) Terakita, A.; Yamashita, T.; Shichida, Y. Highly Conserved Glutamic Acid in the Extracellular IV-V Loop in Rhodopsins Acts as the Counterion in Retinochrome, a Member of the Rhodopsin Family. *Proc. Natl. Acad. Sci. U.S.A.* **2000**, *97*, 14263-14267.

(20) Yan, E. C. Y.; Kazmi, M. A.; Ganim, Z.; Hou, J.M.; Pan, D.; Chang, B. S. W.; Sakmar, T. P.; Mathies, R. A. Retinal Counterion Switch in the Photoactivation of the G Protein-Coupled Receptor Rhodopsin. *Proc. Natl. Acad. Sci. U.S.A.* **2003**, *100*, 9262-9267.

(21) Yan, E. C. Y.; Kazmi, M. A.; De, S.; Chang, B. S. W.; Seibert, C.; Marin, E. P.; Mathies, R. A.; Sakmar, T. P. Function of Extracellular Loop 2 in Rhodopsin: Glutamic Acid 181 Modulates Stability and Absorption Wavelength of Metarhodopsin II. *Biochemistry* **2002**, *41*, 3620-3627.

(22) Eilers, M.; Goncalves, J. A.; Ahuja, S.; Kirkup, C.; Hirshfeld, A.; Simmerling, C.; Reeves, P. J.; Sheves, M.; Smith, S. O. Structural Transitions of Transmembrane Helix 6 in the Formation of Metarhodopsin i. *J. Phys. Chem. B* **2012**, *116*, 10477-10489.

(24) Zhu, S.; Brown, M. F.; Feller, S. E. Retinal Conformation Governs pKa of Protonated Schiff Base in Rhodopsin Activation. *J. Am. Chem. Soc.* **2013**, *135*, 9391-9398.

(25) Leioatts, N.; Mertz, B.; Martínez-Mayorga, K.; Romo, T. D.; Pitman, M. C.; Feller, S. E.; Grossfield, A.; Brown, M. F. Retinal Ligand Mobility Explains Internal Hydration and Reconciles Active Rhodopsin Structures. *Biochemistry* **2014**, *53*, 376-385.

(26) Ahuja, S.; Eilers, M.; Hirshfeld, A.; Yan, E. C. Y.; Ziliox, M.; Sakmar, T. P.; Sheves, M.; Smith, S. O. 6-*s-cis* Conformation and Polar Binding Pocket of the Retinal Chromophore in the Photoactivated State of Rhodopsin. *J. Am. Chem. Soc.* **2009**, *131*, 15160-15169.

(27) Bartl, F. J.; Fritze, O.; Ritter, E.; Herrmann, R.; Kuksa, V.; Palczewski, K.; Hofmann, K. P.; Ernst, O. P. Partial Agonism in a G Protein-Coupled Receptor: Role of the Retinal Ring Structure in Rhodopsin Activation. *J. Biol. Chem.* **2005**, *280*, 34259-34267.

(28) Yan, E. C. Y.; Epps, J.; Lewis, J. W.; Szundi, I.; Bhagat, A.; Sakmar, T. P.; Kliger, D. S. Photointermediates of the Rhodopsin S186A Mutant as a Probe of the Hydrogen-Bond Network in the Chromophore Pocket and the Mechanism of Counterion Switch. *J. Phys. Chem. C* **2007**, *111*, 8843-8848.

(29) Birge, R. R.; Murray, L. P.; Pierce, B. M.; Akita, H.; Balogh-Nair, V.; Findsen, L. A.; Nakanishi, K. Two-photon spectroscopy of locked-11-cis rhodopsin: Evidence for a Protonated Schiff Base in a Neutral Protein Binding Site. *Proc. Natl. Acad. Sci. U.S.A.* **1985**, *82*, 4117-4121.

(30) Yan, E. C. Y.; Ganim, Z.; Kazmi, M. A.; Chang, B. S. W.; Sakmar, T. P.; Mathies, R. A. Resonance Raman Analysis of the Mechanism of Energy Storage and Chromophore Distortion in the Primary Visual Photoproduct. *Biochemistry* **2004**, *43*, 10867-10876.

(31) Sekharan, S.; Buss, V. Glutamic Acid 181 is Uncharged in Dark-Adapted Visual Rhodopsin. *J. Am. Chem. Soc.* **2008**, *130*, 17220-17221.

(32) Mollevanger, L. C.; Kentgens, A. P.; Pardoen, J. A.; Courtin, J. M.; Veeman, W. S.; Lugtenburg, J.; de Grip, W. J. High-Resolution Solid-State 13c-NMR Study of Carbons C-5 and C-12 of the Chromophore of Bovine Rhodopsin. Evidence for a 6-s-cis Conformation with Negative-Charge Perturbation Near C-12. *Eur. J. Biochem.* **1987**, *163*, 9-14.

(33) Smith, S. O.; Palings, I.; Miley, M. E.; Courtin, J. M.; de Groot, H.; Lugtenburg, J.; Mathies, R. A.; Griffin, R. G. Solid State NMR Studies of the Mechanism of the Opsin Shift in the Visual Pigment Rhodopsin. *Biochemistry* **1990**, *29*, 8158-8164.

(34) Han, M.; Smith, S. O. NMR Constraints on the Location of the Retinal Chromophore in Rhodopsin and Bathorhodopsin. *Biochemistry* **1995**, *34*, 1425-1432.

(35) Honig, B.; Dinur, U.; Nakanishi, K.; Balogh-Nair, V.; Gawinowicz, M. A.; Arnaboldi, M.; Motto, M. G. An External Point-Charge for Wavelength Regulation in Visual Pigments. *J. Am. Chem. Soc.* **1979**, *101*, 7084-7086.

(36) Nagata, T.; Terakita, A.; Kandori, H.; Shichida, Y.; Maeda, A. The Hydrogen-Bonding Network of Water Molecules and the Peptide Backbone in the Region Connecting Asp 83, Gly 120, and Glu 113 in Bovine Rhodopsin. *Biochemistry* **1998**, *37*, 17216-17222.

(37) Lüdeke, S.; Beck, M.; Yan, E. C. Y.; Sakmar, T. P.; Siebert, F.; Vogel, R. The Role of Glu181 in the Photoactivation of Rhodopsin. *J. Mol. Biol.* **2005**, *353*, 345-356.

(38) Röhrig, U. F.; Guidoni, L.; Rothlisberger, U. Early Steps of the Intramolecular Signal Transduction in Rhodopsin Explored by Molecular Dynamics Simulations. *Biochemistry* **2002**, *41*, 10799-10809.

(39) Lewis, J. W.; Szundi, I.; Kazmi, M. A.; Sakmar, T. P.; Kliger, D. S. Time-Resolved Photointermediate Changes in Rhodopsin Glutamic Acid 181 Mutants. *Biochemistry* **2004**, *43*, 12614-12621.

(40) Martinez-Mayorga, K.; Pitman, M. C.; Grossfield, A.; Feller, S. E.; Brown, M. F. Retinal Counterion Switch Mechanism in Vision Evaluated by Molecular Simulations. *J. Am. Chem. Soc.* **2006**, *128*, 16502-16503.

(41) Frähmcke, J. S.; Wanko, M.; Phatak, P.; Mroginski, M. A.; Elstner, M. The Protonation State of Glu181 in Rhodopsin Revisited: Interpretation of Experimental Data on the Basis of QM/MM Calculations. *J. Phys. Chem. B* **2010**, *114*, 11338-11352.

(42) Sandberg, M. N.; Amora, T. L.; Ramos, L. S.; Chen, M.-H.; Knox, B. E.; Birge, R. R. Glutamic Acid 181 is Negatively Charged in the Bathorhodopsin Photointermediate of Visual Rhodopsin. *J. Am. Chem. Soc.* **2011**, *133*, 2808-2811.

(43) Tomasello, G.; Olaso-González, G.; Altoè, P.; Stenta, M.; Serrano-Andrés, L.; Merchán, M.; Orlandi, G.; Bottoni, A.; Garavelli, M. Electrostatic Control of the Photoisomerization Efficiency and Optical Properties in Visual Pigments: On the Role of Counterion Quenching. *J. Am. Chem. Soc.* **2009**, *131*, 5172-5186.

(44) Grossfield, A.; Pitman, M. C.; Feller, S. E.; Soubias, O.; Gawrisch, K. Internal Hydration Increases During Activation of the G-Protein-Coupled Receptor Rhodopsin. *J. Mol. Biol.* **2008**, *381*, 478-486.

(45) Hall, K. F.; Vreven, T.; Frisch, M. J.; Bearpark, M. J. Three-Layer Oniom Studies of the Dark State of Rhodopsin: The Protonation State of Glu181. *J. Mol. Biol.* **2008**, *383*, 106-121.

(46) Yoshizawa, T.; Shichida, Y. Low-Temperature Spectroscopy of Intermediates of Rhodopsin. *Methods Enzymol.* **1982**, *81*, 333-354.

(47) Kusnetzow, A.; Dukkipati, A.; Babu, K. R.; Singh, D.; Vought, B. W.; Knox, B. E.; Birge, R. R. The Photobleaching Sequence of a Short-Wavelength Vsual Pigment. *Biochemistry* **2001**, *40*, 7832-7844.

(48) Ramos, L. S.; Chen, M.-H.; Knox, B. E.; Birge, R. R. Regulation of Photoactivation in Vertebrate Short Wavelength Visual Pigments: Protonation of the Retinylidene Schiff Base and a Counterion Switch. *Biochemistry* **2007**, *46*, 5330-5340.

(49) Babu, K. R.; Dukkipati, A.; Birge, R. R.; Knox, B. E. Regulation of Phototransduction in Short Wavelength Cone Visual Pigments via the Retinylidene Schiff Base Counterion. *Biochemistry* **2001**, *40*, 13760-13766.

(50) Vought, B. W.; Dukkipati, A.; Max, M.; Knox, B. E.; Birge, R. R. Photochemistry of the Primary Event in Short-Wavelength Visual Opsins at Low Temperature. *Biochemistry* **1999**, *38*, 11287-11297.

(51) Kusnetzow, A. K.; Dukkipati, A.; Babu, K. R.; Ramos, L.; Knox, B. E.; Birge, R. R. Vertebrate Ultraviolet Visual Pigments: Protonation of the Retinylidene Schiff Base and a Counterion Switch During Photoactivation. *Proc Natl Acad Sci U.S.A.* **2004**, *101*, 941-946.

(52) Birge, R. R.; Einterz, C. M.; Knapp, H. M.; Murray, L. P. The Nature of the Primary Photochemical Events in Rhodopsin and Isorhodopsin. *Biophys. J.* **1988**, *53*, 367-385.

(53) Suzuki, T.; Callender, R. H. Primary Photochemistry and Photoisomerization of Retinal at 77°K in Cattle and Squid Rhodopsins. *Biophys. J.* **1981**, *34*, 261-270.

(54) Vought, B. W.; Dukkipatti, A.; Max, M.; Knox, B. E.; Birge, R. R. Photochemistry of the Primary Event in Short-Wavelength Visual Opsins at Low Temperature. *Biochemistry* **1999**, *38*, 11287-11297.

(55) Frisch, M. J.; Trucks, G. W.; Schlegel, H. B.; Scuseria, G. E.; Robb, M. A.; Cheeseman, J. R.; Scalmani, G.; Barone, V.; Mennucci, B.; Petersson, G. A.; Nakatsuji, H.; Caricato, M.; Li, X.; Hratchian, H. P.; Izmaylov, A. F.; Bloino, J.; Zheng, G.; Sonnenberg, J. L.; Hada, M.; Ehara, M.; Kitao, O.; Nakai, H.; Vreven, T.; Montgomery, J., J. A.; Peralta, J. E.; Ogliaro, F.; Bearpark, M.; Heyd, J. J.; Brothers, E.; Kudin, K. N.; Staroverov, V. N.; Kobayashi, R.; Normand, J.; Raghavachari, K.; Rendell, A.; Burant, J. C.; Iyengar, S. S.; Tomasi, J.; Cossi, M.; Rega, N.; Millam, J. M.; Klene, M.; Knox, J. E.; Cross, J. B.; Bakken, V.; Adamo, C.; Jaramillo, J.; Gomperts, R.; Stratmann, R. E.; Yazyev, O.; Austin, A. J.; Cammi, R.; Pomelli, C.; Ochterski, J. W.; Martin, R. L.; Morokuma, K.; Zakrzewski, V. G.; Voth, G. A.; Salvador, P.; Dannenberg, J. J.; Dapprich, S.; Daniels, A. D.; Farkas, O.; Foresman, J. B.; Ortiz, J. V.; Cioslowski, J.; Fox, D. J.. *Gaussian 09*, revision D.01; Gaussian, Inc., Wallingford, CT, 2009.

(56) Nakamichi, H.; Okada, T. Crystallographic Analysis of Primary Visual Photochemistry. *Angew. Chem. Int. Ed.* **2006**, *45*, 4270-4273.

(57) Nakamichi, H.; Okada, T. Local Peptide Movement in the Photoreaction Intermediate of Rhodopsin. *Proc. Natl. Acad. Sci. U.S.A.* **2006**, *103*, 12729-12734.

(58) Salom, D.; Lodowski, D. T.; Stenkamp, R. E.; Le Trong, I.; Golczak, M.; Jastrzebska, B.; Harris, T.; Ballesteros, J. A.; Palczewski, K. Crystal Structure of a Photoactivated Deprotonated Intermediates of Rhodopsin. *Proc. Natl. Acad. Sci. U.S.A.* **2006**, *103*, 16123-16128.

(59) Stewart, J. J. P. Optimization of Parameters for Semiempirical Methods. I. Method. *J. Comput. Chem.* **1989**, *10*, 209-220.

(60) Stewart, J. J. P. Optimization of Parameters for Semiempirical Methods. II. Applications. *J. Comput. Chem.* **1989**, *10*, 221-264.

(61) Becke, A. D. Density-Functional Thermochemistry. III. The Role of Exact Exchange. *J. Chem. Phys.* **1993**, *98*, 5648-5652.

(62) Lee, C.; Yang, W.; Parr, R. G. Development of the Colle-Salvetti Correlation-Energy Formula into a Functional of the Electron Density. *Phys. Rev. B: Condens. Matter Mater. Phys.* **1988**, *37*, 785-789.

(63) Birge, R. R.; Vought, B. W. Energetics of Rhodopsin Photobleaching: Photocalorimetric Studies of Energy Storage in the Early and Later Intermediates. *Methods Enzymol.* **2000**, *315*, 143-163.

(64) Szundi, I.; Epps, J.; Lewis, J. W.; Kliger, D. S. Temperature Dependence of the Lumirhodopsin I - Lumirhodopsin II Equilibrium. *Biochemistry* **2010**, *49*, 5852-5858.

(65) Lewis, J. W.; Fan, G.-B.; Sheves, M.; Szundi, I.; Kliger, D. S. Steric Barrier to Bathorhodopsin Decay in 5-demethyl and Mesityl Analogues of Rhodopsin. *J. Am. Chem. Soc.* **2001**, *123*, 10024-10029.

(66) Lewis, J. W.; Liang, J.; Ebrey, T. G.; Sheves, M.; Kliger, D. S. Chloride Effect on the Early Photolysis Intermediates of a Gecko Cone-Type Visual Pigment. *Biochemistry* **1995**, *34*, 5817-5823.

(67) Shichida, Y.; Okada, T.; Kandori, H.; Fukada, Y.; Yoshizawa, T. Nanosecond Laser Photolysis of Iodopsin, a Chicken Red-Sensitive Cone Visual Pigment. *Biochemistry* **1993**, *32*, 10832-10838.

(68) Jäger, S.; Han, M.; Lewis, J. W.; Szundi, I.; Sakmar, T. P.; Kliger, D. S. Properties of Early Photoylsis Intermediates of Rhodopsin are Affected by Glycine 121 and Phenylalanine 261. *Biochemistry* **1997**, *36*, 11804-11810.

Appendix A

Permissions

Copyright Clearance Center RightsLink®

Home | Create Account | Help | Live Chat

ACS Publications
Most Trusted. Most Cited. Most Read.

Title: Two-Photon Spectroscopy of the Q-Bands of meso-Tetraphenyl-Porphyrin and -Chlorin Framework Derivatives

Author: Jordan A. Greco, Sumie Shima, Nicole L. Wagner, et al

Publication: The Journal of Physical Chemistry C

Publisher: American Chemical Society

Date: Feb 1, 2015

LOGIN

If you're a copyright.com user, you can login to RightsLink using your copyright.com credentials. Already **a RightsLink user** or want to learn more?

PERMISSION/LICENSE IS GRANTED FOR YOUR ORDER AT NO CHARGE

This type of permission/license, instead of the standard Terms & Conditions, is sent to you because no fee is being charged for your order. Please note the following:

- Permission is granted for your request in both print and electronic formats, and translations.
- If figures and/or tables were requested, they may be adapted or used in part.
- Please print this page for your records and send a copy of it to your publisher/graduate school.
- Appropriate credit for the requested material should be given as follows: "Reprinted (adapted) with permission from (COMPLETE REFERENCE CITATION). Copyright (YEAR) American Chemical Society." Insert appropriate information in place of the capitalized words.
- One-time permission is granted only for the use specified in your request. No additional uses are granted (such as derivative works or other editions). For any other uses, please submit a new request.

BACK | CLOSE WINDOW

JOHN WILEY AND SONS LICENSE
TERMS AND CONDITIONS

Dec 03, 2015

This Agreement between Jordan Greco ("You") and John Wiley and Sons ("John Wiley and Sons") consists of your license details and the terms and conditions provided by John Wiley and Sons and Copyright Clearance Center.

License Number	3761470072148
License date	Dec 03, 2015
Licensed Content Publisher	John Wiley and Sons
Licensed Content Publication	Wiley oBooks
Licensed Content Title	Biomolecular Electronics and Protein-Based Optical Computing
Licensed Content Author	Jordan A. Greco,Nicole L. Wagner,Matthew J. Ranaghan,Sanguthevar Rajasekaran,Robert R. Birge
Licensed Content Date	Dec 21, 2012
Pages	27
Type of use	Dissertation/Thesis
Requestor type	Author of this Wiley chapter
Format	Print and electronic
Portion	Full chapter
Will you be translating?	No
Title of your thesis / dissertation	Spectroscopic and Theoretical Characterization of Retinylidene Proteins and Biological Chromophores for Use in Biophotonic Applications
Expected completion date	Dec 2015
Expected size (number of pages)	278
Requestor Location	Jordan Greco 55 North Eagleville Road STORRS MANSFIELD, CT 06269 United States Attn: Jordan A Greco
Billing Type	Invoice
Billing Address	Jordan A Greco 55 North Eagleville Road STORRS MANSFIELD, CT 06269 United States Attn: Jordan A Greco
Total	0.00 USD

JOHN WILEY AND SONS LICENSE
TERMS AND CONDITIONS

Dec 03, 2015

This Agreement between Jordan Greco ("You") and John Wiley and Sons ("John Wiley and Sons") consists of your license details and the terms and conditions provided by John Wiley and Sons and Copyright Clearance Center.

License Number	3761461245389
License date	Dec 03, 2015
Licensed Content Publisher	John Wiley and Sons
Licensed Content Publication	Photochemistry and Photobiology
Licensed Content Title	A Spectroscopic and Theoretical Investigation of a Free-Base meso-Trithienylcorrole
Licensed Content Author	Jordan A. Greco,Alison Rossi,Robert R. Birge,Christian Brückner
Licensed Content Date	Dec 5, 2013
Pages	13
Type of use	Dissertation/Thesis
Requestor type	Author of this Wiley article
Format	Print and electronic
Portion	Full article
Will you be translating?	No
Title of your thesis / dissertation	Spectroscopic and Theoretical Characterization of Retinylidene Proteins and Biological Chromophores for Use in Biophotonic Applications
Expected completion date	Dec 2015
Expected size (number of pages)	278
Requestor Location	Jordan Greco 55 North Eagleville Road STORRS MANSFIELD, CT 06269 United States Attn: Jordan A Greco
Billing Type	Invoice
Billing Address	Jordan A Greco 55 North Eagleville Road STORRS MANSFIELD, CT 06269 United States Attn: Jordan A Greco
Total	0.00 USD
Terms and Conditions	

TERMS AND CONDITIONS

This copyrighted material is owned by or exclusively licensed to John Wiley & Sons, Inc. or one of its group companies (each a"Wiley Company") or handled on behalf of a society with which a Wiley Company has exclusive publishing rights in relation to a particular work (collectively "WILEY"). By clicking "accept" in connection with completing this licensing transaction, you agree that the following terms and conditions apply to this transaction (along with the billing and payment terms and conditions established by the Copyright Clearance Center Inc., ("CCC's Billing and Payment terms and conditions"), at the time that you opened your RightsLink account (these are available at any time at http://myaccount.copyright.com).

Terms and Conditions

- The materials you have requested permission to reproduce or reuse (the "Wiley Materials") are protected by copyright.

- You are hereby granted a personal, non-exclusive, non-sub licensable (on a stand-alone basis), non-transferable, worldwide, limited license to reproduce the Wiley Materials for the purpose specified in the licensing process. This license, **and any CONTENT (PDF or image file) purchased as part of your order,** is for a one-time use only and limited to any maximum distribution number specified in the license. The first instance of republication or reuse granted by this license must be completed within two years of the date of the grant of this license (although copies prepared before the end date may be distributed thereafter). The Wiley Materials shall not be used in any other manner or for any other purpose, beyond what is granted in the license. Permission is granted subject to an appropriate acknowledgement given to the author, title of the material/book/journal and the publisher. You shall also duplicate the copyright notice that appears in the Wiley publication in your use of the Wiley Material. Permission is also granted on the understanding that nowhere in the text is a previously published source acknowledged for all or part of this Wiley Material. Any third party content is expressly excluded from this permission.

- With respect to the Wiley Materials, all rights are reserved. Except as expressly granted by the terms of the license, no part of the Wiley Materials may be copied, modified, adapted (except for minor reformatting required by the new Publication), translated, reproduced, transferred or distributed, in any form or by any means, and no derivative works may be made based on the Wiley Materials without the prior permission of the respective copyright owner.**For STM Signatory Publishers clearing permission under the terms of the STM Permissions Guidelines only, the terms of the license are extended to include subsequent editions and for editions in other languages, provided such editions are for the work as a whole in situ and does not involve the separate exploitation of the permitted figures or extracts,** You may not alter, remove or suppress in any manner any copyright, trademark or other notices displayed by the Wiley Materials. You may not license, rent, sell, loan, lease, pledge, offer as security, transfer or assign the Wiley Materials on a stand-alone basis, or any of the rights granted to you hereunder to any other person.

- The Wiley Materials and all of the intellectual property rights therein shall at all times remain the exclusive property of John Wiley & Sons Inc, the Wiley Companies, or their respective licensors, and your interest therein is only that of having possession of

and the right to reproduce the Wiley Materials pursuant to Section 2 herein during the continuance of this Agreement. You agree that you own no right, title or interest in or to the Wiley Materials or any of the intellectual property rights therein. You shall have no rights hereunder other than the license as provided for above in Section 2. No right, license or interest to any trademark, trade name, service mark or other branding ("Marks") of WILEY or its licensors is granted hereunder, and you agree that you shall not assert any such right, license or interest with respect thereto

- NEITHER WILEY NOR ITS LICENSORS MAKES ANY WARRANTY OR REPRESENTATION OF ANY KIND TO YOU OR ANY THIRD PARTY, EXPRESS, IMPLIED OR STATUTORY, WITH RESPECT TO THE MATERIALS OR THE ACCURACY OF ANY INFORMATION CONTAINED IN THE MATERIALS, INCLUDING, WITHOUT LIMITATION, ANY IMPLIED WARRANTY OF MERCHANTABILITY, ACCURACY, SATISFACTORY QUALITY, FITNESS FOR A PARTICULAR PURPOSE, USABILITY, INTEGRATION OR NON-INFRINGEMENT AND ALL SUCH WARRANTIES ARE HEREBY EXCLUDED BY WILEY AND ITS LICENSORS AND WAIVED BY YOU.

- WILEY shall have the right to terminate this Agreement immediately upon breach of this Agreement by you.

- You shall indemnify, defend and hold harmless WILEY, its Licensors and their respective directors, officers, agents and employees, from and against any actual or threatened claims, demands, causes of action or proceedings arising from any breach of this Agreement by you.

- IN NO EVENT SHALL WILEY OR ITS LICENSORS BE LIABLE TO YOU OR ANY OTHER PARTY OR ANY OTHER PERSON OR ENTITY FOR ANY SPECIAL, CONSEQUENTIAL, INCIDENTAL, INDIRECT, EXEMPLARY OR PUNITIVE DAMAGES, HOWEVER CAUSED, ARISING OUT OF OR IN CONNECTION WITH THE DOWNLOADING, PROVISIONING, VIEWING OR USE OF THE MATERIALS REGARDLESS OF THE FORM OF ACTION, WHETHER FOR BREACH OF CONTRACT, BREACH OF WARRANTY, TORT, NEGLIGENCE, INFRINGEMENT OR OTHERWISE (INCLUDING, WITHOUT LIMITATION, DAMAGES BASED ON LOSS OF PROFITS, DATA, FILES, USE, BUSINESS OPPORTUNITY OR CLAIMS OF THIRD PARTIES), AND WHETHER OR NOT THE PARTY HAS BEEN ADVISED OF THE POSSIBILITY OF SUCH DAMAGES. THIS LIMITATION SHALL APPLY NOTWITHSTANDING ANY FAILURE OF ESSENTIAL PURPOSE OF ANY LIMITED REMEDY PROVIDED HEREIN.

- Should any provision of this Agreement be held by a court of competent jurisdiction to be illegal, invalid, or unenforceable, that provision shall be deemed amended to achieve as nearly as possible the same economic effect as the original provision, and the legality, validity and enforceability of the remaining provisions of this Agreement shall not be affected or impaired thereby.

- The failure of either party to enforce any term or condition of this Agreement shall not constitute a waiver of either party's right to enforce each and every term and condition of this Agreement. No breach under this agreement shall be deemed waived or

excused by either party unless such waiver or consent is in writing signed by the party granting such waiver or consent. The waiver by or consent of a party to a breach of any provision of this Agreement shall not operate or be construed as a waiver of or consent to any other or subsequent breach by such other party.

- This Agreement may not be assigned (including by operation of law or otherwise) by you without WILEY's prior written consent.

- Any fee required for this permission shall be non-refundable after thirty (30) days from receipt by the CCC.

- These terms and conditions together with CCC's Billing and Payment terms and conditions (which are incorporated herein) form the entire agreement between you and WILEY concerning this licensing transaction and (in the absence of fraud) supersedes all prior agreements and representations of the parties, oral or written. This Agreement may not be amended except in writing signed by both parties. This Agreement shall be binding upon and inure to the benefit of the parties' successors, legal representatives, and authorized assigns.

- In the event of any conflict between your obligations established by these terms and conditions and those established by CCC's Billing and Payment terms and conditions, these terms and conditions shall prevail.

- WILEY expressly reserves all rights not specifically granted in the combination of (i) the license details provided by you and accepted in the course of this licensing transaction, (ii) these terms and conditions and (iii) CCC's Billing and Payment terms and conditions.

- This Agreement will be void if the Type of Use, Format, Circulation, or Requestor Type was misrepresented during the licensing process.

- This Agreement shall be governed by and construed in accordance with the laws of the State of New York, USA, without regards to such state's conflict of law rules. Any legal action, suit or proceeding arising out of or relating to these Terms and Conditions or the breach thereof shall be instituted in a court of competent jurisdiction in New York County in the State of New York in the United States of America and each party hereby consents and submits to the personal jurisdiction of such court, waives any objection to venue in such court and consents to service of process by registered or certified mail, return receipt requested, at the last known address of such party.

WILEY OPEN ACCESS TERMS AND CONDITIONS
Wiley Publishes Open Access Articles in fully Open Access Journals and in Subscription journals offering Online Open. Although most of the fully Open Access journals publish open access articles under the terms of the Creative Commons Attribution (CC BY) License only, the subscription journals and a few of the Open Access Journals offer a choice of Creative Commons Licenses. The license type is clearly identified on the article.
The Creative Commons Attribution License
The Creative Commons Attribution License (CC-BY) allows users to copy, distribute and transmit an article, adapt the article and make commercial use of the article. The CC-BY